

UNCLASSIFIED

AD NUMBER

ADB000384

LIMITATION CHANGES

TO:

Approved for public release; distribution is unlimited.

FROM:

Distribution authorized to U.S. Gov't. agencies only; Test and Evaluation; SEP 1974. Other requests shall be referred to Materials and Mechanics Research Center, ATTN: AMXMR-PL, Watertown MA 02172.

AUTHORITY

DARPA ltr, 19 Dec 1974

THIS PAGE IS UNCLASSIFIED

THIS REPORT HAS BEEN DELIMITED
AND CLEARED FOR PUBLIC RELEASE
UNDER DOD DIRECTIVE 5200.20 AND
NO RESTRICTIONS ARE IMPOSED UPON
ITS USE AND DISCLOSURE.

DISTRIBUTION STATEMENT A

APPROVED FOR PUBLIC RELEASE,
DISTRIBUTION UNLIMITED.

AD B 000384



AD

AMMRC CTR 74-59

BRITTLE MATERIALS DESIGN, HIGH TEMPERATURE GAS TURBINE

Technical Report By:

Arthur F. McLean, Ford Motor Company, Dearborn, Michigan 48121
Eugene A. Fisher, Ford Motor Company, Dearborn, Michigan 48121
Raymond J. Bratton, Westinghouse Electric Corporation, Pittsburgh,
Pennsylvania 15235

September, 1974

Interim Report Number 6, January 1, 1974 to June 30, 1974

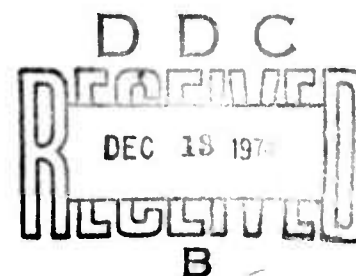
Contract Number DAAG 46-71-C-0162

Sponsored by the Advanced Research Projects Agency

ARPA Order Number 1849

Project Code Number 1D10

Agency Accession Number DA OD 4733



Distribution limited to U.S. Government agencies only: Test and Evaluation data; Sept., 1974. Other requests for this document must be referred to the Director, Army, Materials and Mechanics Research Center, ATTN: AMXMR-PL, Watertown, Massachusetts 02172

Prepared for

ARMY MATERIALS AND MECHANICS RESEARCH CENTER
Watertown, Massachusetts 02172

The findings in this report are not to be construed as an official Advanced Research Projects Agency, Department of the Army, or U.S. Government position, either expressed or implied, unless so designated by other authorized documents.

Mention of any trade names or manufacturers in this report shall not be construed as advertising nor as an official indorsement or approval of such products or companies by the United States Government.

DISPOSITION INSTRUCTIONS

Destroy this report when it is no longer needed. Do not return it to the originator.

AMMRC CTR 74-59

BRITTLE MATERIALS DESIGN, HIGH TEMPERATURE GAS TURBINE

Technical Report By:

Arthur F. McLean, Ford Motor Company, Dearborn, Michigan 48121
Eugene A. Fisher, Ford Motor Company, Dearborn, Michigan 48121
Raymond J. Bratton, Westinghouse Electric Corporation, Pittsburgh,
Pennsylvania 15235

September, 1974

Interim Report Number 6, January 1, 1974 to June 30, 1974

Contract Number DAAG 46-71-C-0162

Sponsored by the Advanced Research Projects Agency

ARPA Order Number 1849

Project Code Number 1D10

Agency Accession Number DA OD 4733

Distribution limited to U.S. Government agencies only: Test and Evaluation data; Sept., 1974. Other requests for this document must be referred to the Director, Army, Materials and Mechanics Research Center, ATTN: AMXMR-PL, Watertown, Massachusetts 02172

Prepared for:

ARMY MATERIALS AND MECHANICS RESEARCH CENTER
Watertown, Massachusetts 02172

ABSTRACT

The "Brittle Materials Design, High Temperature Gas Turbine" program is to demonstrate successful use of brittle materials in demanding high temperature structural applications. A small vehicular gas turbine and a large stationary gas turbine, each utilizing uncooled ceramic components, will be used in this iterative design and materials development program. Both the contractor, Ford Motor Company, and the subcontractor, Westinghouse Electric Corporation, have had in-house research programs in this area prior to this contract.

In the vehicular turbine project, three dimensional stress analysis programs are being developed and applied to turbine rotors and stators. Improvements have been made in the fabrication of duo density silicon nitride rotors. A major objective was reached with the completion of a 50 hour cyclic engine test of ceramic hot flow path components. A silicon carbide combustor tube was tested in a combustor rig for 50 hours, including 6 hours at an outlet temperature of 2500°F. Non-destructive evaluation techniques have been applied to the fabrication of ceramic components resulting in the elimination of defective parts at an early stage in processing.

In the stationary turbine project, considerable design effort was expended on the modification of the rotating test turbine for the high temperature testing to meet program objectives. The static test rig was rebuilt for 2500°F peak temperature operation, and five cycles were run to 2300°F to establish control parameters. Damage to the new ceramic duct section and to the mixer caused testing to be stopped. The silicon nitride and silicon carbide stator vane assemblies being tested were apparently undamaged. A rotor blade configuration was analyzed by the three dimensional stress analysis program and the results are presented.

FORWARD

This report is the sixth semi-annual technical report of the "Brittle Materials Design, High Temperature Gas Turbine" program initiated by the Advanced Research Projects Agency, ARPA Order Number 1849, and monitored by the Army Materials and Mechanics Research Center, under Contract Number DAAG-46-71-C-0162. This is an incrementally-funded five year program.

Since this is an iterative design and materials development program, design concepts and materials selection and/or properties presented in this report will probably not be those finally utilized. Thus all design and property data contained in the semi-annual reports must be considered tentative, and the reports should be considered to be illustrative of the design, materials, processing, and NDT techniques being developed for brittle materials.

The principal investigator of this program is Mr. A. F. McLean, Ford Motor Company, and the technical monitor is Dr. A. E. Gorum, AMMRC. The authors would like to acknowledge the valuable contributions in the performance of this work by the following people:

Ford Motor Company

D. Alexander, R. R. Baker, P. Beardmore, D. J. Cassidy, J. C. Caverly, H. A. Cikanek, D. A. Davis, G. C. DeBell, A. Ezis, W. A. Fate, R. R. Fogoros, M. U. Goodyear, E. T. Grostick, D. L. Hartsock, P. H. Havstad, D. W. Huser, R. A. Jeryan, C. F. Johnson, K. H. Kinsman, J. T. Kovach, J. G. LaFond, J. A. Mangels, W. E. Meyer, M. E. Milberg, J. J. Mittman, T. G. Mohr, P. F. Nicholls, A. Paluszny, N. P. Peters, J. J. Schuldies, J. R. Secord, K. H. Styhr, L. Swank, W. Trela, T. J. Whalen, W. Wu

Westinghouse Electric Corporation

J. Allen, G. W. Bauserman, D. Boes, C. R. Booher, Jr., E. S. Diaz, A. N. Holden, R. Kossowsky, T. Lam, F. F. Lange, S. Y. Lee, W. Malchman, E. L. Shenoway, D. G. Miller, S. Mumford, J. Owensby, T. J. Rahaim, S. C. Sanday, S. C. Singhal, J. P. Smed, L. C. Szema, W. Van Buren, C. Visser, R. Weidenbacker, J. H. White

Army Material and Mechanics Research Center

E. M. Lenoe, R. N. Katz, D. R. Messier, H. Priest

TABLE OF CONTENTS

	<u>Page No.</u>
Title Page	i
Abstract	ii
Forward	iii
Table of Contents	iv
List of Illustrations	v
List of Tables	xiii
1. Introduction	1
2. Summary of Progress	11
2.1 Vehicular Turbine Project	11
2.2 Stationary Turbine Project	13
2.3 Materials Technology - Vehicular & Stationary Turbine Projects	14
3. Progress on the Vehicular Turbine Project	15
3.1 Ceramic Rotor Development	15
3.1.1 Design and Analysis	17
3.1.2 Materials and Fabrication	32
3.1.3 Testing	42
3.2 Ceramic Stators, Rotor Shrouds, Nose Cones, and Combustors	55
3.2.1 Design and Analysis	56
3.2.2 Materials and Fabrication	64
3.2.3 Testing	67
3.3 Gas Bearings	81
3.3.1 Gas Bearing Design and Analysis	82
4. Progress on the Stationary Turbine Project	87
4.1 Stator Vane Development	87
4.1.1 Design	88
4.1.2 The Stress Analysis of Stator Vanes	92
4.1.3 Static Rig Tests	94
4.1.4 Vane Fabrication	102
4.2 Rotor Blade Development	105
4.2.1 WISEC Rotor Blade Analysis	106
5. Progress on Materials Technology - Vehicular and Stationary Turbine Projects	115
5.1 Materials Engineering Data	115
5.1.1 Properties of Hot-Pressed Materials	116
5.1.2 Physical Properties of Reaction-Sintered Silicon Nitride	136
5.2 Material Science	147
5.2.1 Microstructure of Hot-Pressed Silicon Nitride and Silicon Carbide	148
5.2.2 Solid State Reactions	150
5.2.3 Slow Crack Growth Studies	152
5.2.4 Sialon Development	156
5.3 Non Destructive Evaluation of Materials	157
5.3.1 Ultrasonic NDE	158
5.3.2 Acoustic Emission	165
5.3.3 X-Ray Radiography	168
5.3.4 NDE in the Fabrication of Ceramic Components	170
5.3.5 Summary of NDE Applications	172
6. References	179

LIST OF ILLUSTRATIONS

		<u>Page No.</u>
Figure 1.1	Flow Path Schematic of Vehicular Gas Turbine	2
Figure 1.2	30 Mw Test Turbine Flow Path	3
Figure 1.3	Brittle Material Design/High Temperature Gas Turbine - Breakdown of Major Elements Reported	4
Figure 1.4	Brittle Material Design/High Temperature Gas Turbine - Block Diagram Flow Chart of Iterative Development	6
Figure 3.1	Front View of the Three Dimensional Model of a First Stage Rotor Blade, Platform, and Disk Portion Extending to the Throat Region	18
Figure 3.2	Side View of the Three Dimension Model of a First Stage Rotor Blade, Platform, and Disk Portion Extending to the Throat Region	19
Figure 3.3	Front View of First Stage Turbine Rotor Showing Portion Being Modeled	20
Figure 3.4	Generation of Blade Model Nodes	21
Figure 3.5	Computer Output Coordinates Which Define the Overall Cross-Section of the Platform	22
Figure 3.6	Program Input Data Used to Generate the Coordinates for the Overall Cross-Section of the Platform	22
Figure 3.7	Manually Chosen Elements and Nodal Points That Define the Platform Cross-Section	23
Figure 3.8	Failure Distribution of Single Blades and Complete Rings on Type C-M Silicon Nitride	25
Figure 3.9	Failure Distribution of Single Blades and Complete Rings for Type C Silicon Nitride	26
Figure 3.10	Failure Distribution of Single Blades for Type C-M Silicon Nitride	27
Figure 3.11	Failure Distribution of Single Blades for Type C Silicon Nitride	28
Figure 3.12	Common Profile Rotor Disk	29
Figure 3.13	Maximum Principal Stresses (psi) in Second Stage Disk, 110% Speed Centrifugal Loading, Hot Pressed Si_3N_4 Disk and Blades	30

LIST OF ILLUSTRATIONS

		<u>Page No.</u>
Figure 3.14	Maximum Principal Stresses (psi) in Second Stage Disk, 110% Speed Centrifugal Loading, Hot Pressed Si_3N_4 Disk, Reaction Sintered Si_3N_4 Blades	31
Figure 3.15	Maximum Principal Stresses (psi) in Second Stage Disk, 110% Speed Centrifugal Loading, Triple-Density Design	33
Figure 3.16	Maximum Principal Stresses (psi) in First Stage Disk, 110% Speed Centrifugal Loading, Hot Pressed Si_3N_4 Disk and Blades	34
Figure 3.17	Finite Element Grid Used for Stress Determinations in First Stage Common Rotor Disk	35
Figure 3.18	Finite Element Grid Used for Stress Determinations in Second Stage Common Rotor Disk	36
Figure 3.19	Duo-Density and Triple-Density Ceramic Rotor Concepts	37
Figure 3.20	Molded Silicon Nitride Rotor Blade Ring Showing First Blade Fill	38
Figure 3.21	Duo-Density Silicon Nitride Rotor Assembled Prior to Press Bonding Showing Second Blade Fill	38
Figure 3.22	Hot-Press Bonding Assembly	40
Figure 3.23	Press Bonded Silicon Nitride Rotor Showing Bond	41
Figure 3.24	Fracture Surface of Rotor Ring Showing Typical Flaw Caused by Entrapped Gas During Molding	41
Figure 3.25	Fracture Surface at Base of Rotor Blade Showing Folds or Knit Lines	42
Figure 3.26	X-Ray Radiograph Showing As-Molded Rotor Ring With No Apparent Flaws	43
Figure 3.27	X-Ray Radiograph Showing As-Molded Rotor Ring With a Major Void in Disk at 2:00 O'Clock and Indications of Low Density Areas	44
Figure 3.28	Rotor Blade Fabrication Steps	44
Figure 3.29	Triggering Device for Photography of Bursts During Spin Testing	45
Figure 3.30	Rotor Placement Within the Photographic Triggering Device	46
Figure 3.31	A Segment of a Molded Silicon Nitride Rotor Blade Ring and the Metal Test Hub	48

LIST OF ILLUSTRATIONS

		<u>Page No.</u>
Figure 3.32	A Complete Molded Silicon Nitride Rotor Blade Ring Ready for Bonding to the Metal Test Hub	49
Figure 3.33	First Stage Rotor Blade Segments at Instant of Failure at 61,900 rpm	50
Figure 3.34	Second Stage Rotor Blade Segments at Instant of Failure at 56,840 rpm	51
Figure 3.35	Thermal Shock Testing of Blade Fillet Area of Molded Silicon Nitride Rotor Blade Rings	52
Figure 3.36	Rotor Thermal Response as Measured on Hot Side of Blade During 1930 ^o F Thermal Shock Testing	53
Figure 3.37	Rotor Thermal Response as Measured on Cool Side of Blade During 1930 ^o F Thermal Shock Testing	54
Figure 3.38	Rotor Thermal Response as Measured on Hot Side of Blade During 2300 ^o F Thermal Shock Testing	54
Figure 3.39	Schematic of the Three Dimensional Stress Analysis Process	57
Figure 3.40	Film Coefficients for the First Stage Stator Vane at Radius of 1.7 Inches	60
Figure 3.41	Film Coefficients for the First Stage Stator Vane at Radius of 1.95 Inches	61
Figure 3.42	Film Coefficients for the First Stage Stator Vane at Radius of 2.2 Inches	62
Figure 3.43	Average Film Coefficients for the Surfaces of the Inner and Outer Shrouds of the First Stage Stator	63
Figure 3.44	Three Dimensional Computer Model of the Second Stage Stator	63
Figure 3.45	One Piece First Stage Stator Made From Molded Reaction Sintered Silicon Nitride	65
Figure 3.46	Gap Changes in Second Stage Slip Cast Silicon Nitride Rotor Shrouds at Various Stages in the Heat Treatment Cycle	66
Figure 3.47	Combustor Test Rig	68
Figure 3.48	"Refel" Silicon Carbide Combustor Tube After Testing	69
Figure 3.49	Durability Duty Cycle for Ceramic Components Using Metal Turbine Rotors	71

LIST OF ILLUSTRATIONS

		<u>Page No.</u>
Figure 3.50	Turbine Inlet Temperature vs Time for a Cold Light Transient	72
Figure 3.51	Turbine Inlet Temperature vs Time for a Hot Light Transient	73
Figure 3.52	Turbine Inlet Temperature vs Time for a Hot Shut-down Transient	74
Figure 3.53	Turbine Inlet Temperature vs Time for a Cold Shut-down Transient	75
Figure 3.54	Durability Duty Cycle for Ceramic Components Using Ceramic Turbine Rotors	76
Figure 3.55	Molded Reaction Sintered Silicon Nitride Nose Cone After 50 Hour Durability Test	76
Figure 3.56	Slip Cast Reaction Sintered Silicon Nitride Turbine Rotor Shrouds After 50 Hour Durability Test	77
Figure 3.57	Molded Reaction Sintered Silicon Nitride First Stage Stator After 50 Hour Durability Test	77
Figure 3.58	Inverted Channel Reaction Sintered Silicon Nitride Second Stage Stator After 50 Hour Durability Test	78
Figure 3.59	Statistical Interpretation of the Results of Ceramic Nose Cone Testing	79
Figure 3.60	Single Leaf HYDRESIL Foil Bearing	83
Figure 3.61	Rotor-Bearing Dynamics Simulator Rig	84
Figure 3.62	High Speed Rotor Simulator	84
Figure 3.63	Three Leaf HYDRESIL Foil Bearing	85
Figure 4.1	W-251 Rotating Test Turbine	89
Figure 4.2	Tapered-Twisted Airfoil Section - Stator Vane Assembly for Rotating Turbine Test	90
Figure 4.3	Effect of Loading Area on the Maximum Principal Stress	92
Figure 4.4	Second Generation Airfoil Cross Section at the End Cap Surface	96
Figure 4.5	Finite Element Model of Airfoil Section	96

LIST OF ILLUSTRATIONS

		<u>Page No.</u>
Figure 4.6	Modified Finite Element Model	97
Figure 4.7	Vane Cross Section Showing Elliptical Contact Surface Projections for the Worst Contact Conditions at the Inner Vane-End Cap Interface	98
Figure 4.8	The Effects of Parameter Variation on Contact Tensile Stress at the Airfoil-End Cap Interface Under Start Up Conditions	99
Figure 4.9	The Effects of Parameter Variation on Contact Tensile Stress at the Airfoil-End Cap Interface Under Shut Down Conditions	100
Figure 4.10	Second Generation Silicon Carbide and Silicon Nitride Stator Vane Assemblies	103
Figure 4.11	Computer Plot of Ceramic Rotor Blade	106
Figure 4.12	Material Orientation for Orthotropic Analysis	108
Figure 4.13	Inlet Temperature Profile	109
Figure 4.14	Film Convection Coefficients for the Ceramic Rotor Blade	109
Figure 4.15	Temperature Distribution for Ceramic Rotor Blade at Section 300	110
Figure 4.16	Temperature Distribution for Ceramic Rotor Blade at Section 700	110
Figure 4.17	Steady State Radial Thermal Stress Distribution for Ceramic Rotor Blade at Section 300	111
Figure 4.18	Steady State Radial Thermal Stress Distribution for Ceramic Rotor Blade at Section 700	111
Figure 4.19	Radial Stress Distribution for Ceramic Rotor Blade Under Centrifugal Loading at Section 300	112
Figure 4.20	Radial Stress Distribution for Ceramic Rotor Blade Under Centrifugal Loading at Section 700	112
Figure 4.21	Combined Steady State Thermal and Centrifugal Stress Distribution for Ceramic Rotor Blade at Section 300	113

LIST OF ILLUSTRATIONS

		<u>Page No.</u>
Figure 4.22	Combined Steady State Thermal and Centrifugal Stress Distribution for Ceramic Rotor Blade at Section 700	113
Figure 5.1	Tensile Strength of Norton HS-130 Silicon Nitride	116
Figure 5.2	The Tensile Strength of Norton Hot-Pressed Silicon Carbide	118
Figure 5.3	The Effect of Temperature on the Elastic Modulus of Norton Hot-Pressed Silicon Nitride and Silicon Carbide	119
Figure 5.4	Schematic Diagram of Time Dependent Deformation	120
Figure 5.5	Schematic Diagram of the Stress-Strain Behavior Showing the Time Dependent Outer Fiber Curve and Two Instantaneous Curves	121
Figure 5.6	Bending of a Bar in Four Point Flexure	122
Figure 5.7	Deflection-Time Relationship for Proposed Time Dependent Flexural Test	124
Figure 5.8	Moment-Time Relationship for the Proposed Time Dependent Flexural Test	124
Figure 5.9	The Stress-Strain Relationship for the Proposed Flexural Test	125
Figure 5.10	The Stress-Strain Relationships for the Proposed Flexural Test for Time Dependent Tensile and Elastic Compressive Deformation	126
Figure 5.11	The Moment-Strain Relationship for the Time Dependent Flexural Test	127
Figure 5.12	Moment-Time Curves for Equivalent Time Dependent Tensile and Compressive Deformation (a) and Time-Dependent Tensile and Elastic Compressive Deformation (b)	129
Figure 5.13	Outer Fiber Tensile Stress-Strain Relationships for Equivalent Tensile and Compressive Deformation as Determined from Elastic Beam Theory (a), Time-Dependent Deformation Theory (b) and Time-Independent Deformation Theory (c)	129
Figure 5.14	Outer Fiber Stress-Strain Relationships for Non-Linear Tensile and Linear Compressive Deformation as Determined from Elastic Beam Theory (a), Time-Dependent Deformation Theory (b), and Time-Independent Deformation Theory (c)	130

LIST OF ILLUSTRATIONS

		<u>Page No.</u>
Figure 5.15	Molten Metal-Metal Oxide Silicon Carbide Reaction in High Temperature Stress Rupture Test	131
Figure 5.16	Creep of Norton HS-130 Silicon Nitride at 2300°F in Air	132
Figure 5.17	Silicon Nitride (Left) and Silicon Carbide (Right) Specimen as Tested in Turbine Passage at 2500°F	133
Figure 5.18	Silicon Nitride (Right) and Silicon Carbide (Left) Specimens from Turbine Passage Test at 2500°F After Sandblast	134
Figure 5.19	Schematic of Fatigue Response in HS-130 Si ₃ N ₄ at 2300°F in Air	135
Figure 5.20	Bend Strength vs Temperature of Norton NC-350 Reaction Sintered Silicon Nitride	137
Figure 5.21	Steady State Strain Rate vs Applied Stress for Reaction Sintered Silicon Nitride	137
Figure 5.22	Steady State Strain Rate vs Temperature for Reaction Sintered Silicon Nitride	138
Figure 5.23	Steady State Strain Rate vs Calcium Content of Reaction Sintered Silicon Nitride	139
Figure 5.24	Steady State Strain Rate vs Grain Boundary Viscosity of Reaction Sintered Silicon Nitride	140
Figure 5.25	Longitudinal Modulus vs Temperature for Various Silicon Nitrides	142
Figure 5.26	Shear Modulus vs Temperature for Various Silicon Nitrides	143
Figure 5.27	Young's Modulus vs Temperature for Various Silicon Nitrides	143
Figure 5.28	Poisson's Ratio vs Temperature for Various Silicon Nitrides	144
Figure 5.29	Room Temperature Elastic Constant Data for Silicon Nitride Compared With Budiansky Theory	145
Figure 5.30	(a) Sample Pre-cracking Schematic of Crack Configuration Emplaced by Hardness Indenter	152
	(b) Appearance of Typical Surface Crack in Norton HS-130 Hot Pressed Si ₃ N ₄	

LIST OF ILLUSTRATIONS

		<u>Page No.</u>
Figure 5.31	Plot of Fracture Stress as a Function of Crack Size	153
Figure 5.32	Comparison of Temperature Dependence of Fracture Stress in Nominally Unflawed Material to that Containing 90 μ Flaws	154
Figure 5.33	Appearance of Surface Crack After Subcritical Crack Growth	154
Figure 5.34	Temperature Dependence of the Extent of Subcritical Crack Growth Shown by Optical Microscopy. (b) is a Higher Magnification View by SEM of (c)	155
Figure 5.35	Sensitivity Comparison of the Conventional and the Computer Aided System on a Disk of HS-110 Hot Pressed Silicon Nitride	159
Figure 5.36	Method of Testing Radiographic Test Block, Where Each Large Step Contains a Smaller Step Which is 2% of the Thickness of the Large Step	160
Figure 5.37	Step-Block Resolution of the Computer-Aided Ultrasonic System	161
Figure 5.38	Step-Block Resolution of the Conventional Ultrasonic System	162
Figure 3.39	Reflections From the Back Surface of a HS-130 Silicon Nitride Disk, Showing the Differences Between (a) The Conventional System and (b) The Computer-Aided System	163
Figure 5.40	Strength of A Scan Ultrasonic Reflection vs Depth of Hole	164
Figure 5.41	Acoustic Emission vs Time For a Second Stage Stator Assembly	165
Figure 5.42	Acoustic Emission vs Time For a Second Stage Stator Assembly	166
Figure 5.43	Acoustic Emission vs Time For a Second Stage Stator Assembly	167
Figure 5.44	Acoustic Emission vs Time For a Second Stage Stator Assembly	167
Figure 5.45	Radiographic Reversal Print of Injection Molded Second Stage Stator Vanes, Showing (a) Flawed Vanes and (b) Good Vanes	169
Figure 5.46	Schematic of Ceramic Component Fabrication Sequence Indicating Points in the Process Where NDE is Utilized	171

LIST OF TABLES

		<u>Page No.</u>
Table 3.1	Effect of Tool and Material Temperature on Quality of Molded Rotor Rings	39
Table 3.2	Test Data, Second Stage Rotor Blades	46
Table 3.3	Operating Conditions During 50 Hour Combustor Test	69
Table 3.4	Best Life on Ceramic Components	80
Table 5.1	Tensile Properties of Norton HS-130 Silicon Nitride	117
Table 5.2	Tensile Properties of Norton Hot Pressed Silicon Carbide	118
Table 5.3	Creep Properties of Hot-Pressed Silicon Nitride and Silicon Carbide	131
Table 5.4	Effect of Corrosion-Erosion At 2500°F in Air	134
Table 5.5	Static Coefficient of Friction for Hot-Pressed Silicon Carbide	134
Table 5.6	Stress-Rupture Properties of Reaction Sintered Silicon Nitride	138
Table 5.7	Auger Analysis of Fracture Surfaces	139
Table 5.8	Creep of Slip Cast Silicon Nitride	141
Table 5.9	Comparison of Creep Data, Bending Creep Results	141
Table 5.10	Spectrographic Analysis of Norton HS-130 Silicon Nitride	148
Table 5.11	Detection of Defects by A-Scan Ultrasonics	164
Table 5.12	Detection of Defects by X-Radiography	169
Table 5.13	Sensitivity/Resolution Limits	172

1. INTRODUCTION

As stipulated by the Advanced Research Projects Agency of the Department of Defense, the major purpose of this program is to demonstrate that brittle materials can be successfully utilized in demanding high temperature structural applications. The gas turbine engine, utilizing uncooled ceramic components in the hot flow path, was chosen as the vehicle for this demonstration. Two hundred hours of operation over a representative duty cycle at ceramic temperatures up to 2500°F is required for the demonstration.

It is the further purpose of this program to develop design technology for ceramic materials on a systems basis requiring close integration of design, engineering, materials selection, materials processing and fabrication, testing and evaluation.

The progress of the gas turbine engine has been closely related to the development of materials capable of withstanding the engine's environment at high operating temperature. Since the early days of the jet engine, new metals have been developed which have allowed a gradual increase in operating temperatures. Today's nickel-chrome superalloys are in use without cooling at turbine inlet gas temperatures of 1800° to 1900°F. However, there is considerable incentive to further increase turbine inlet temperature to improve specific air and fuel consumptions. The use of ceramics in the gas turbine engine as a demonstration vehicle for this program promises to make a major step in increasing turbine inlet temperature. Success will offer significant advances in engine efficiency, power per unit weight, cost, pollution abatement, and fuel utilization.

This program will demonstrate the use of ceramics in two demanding gas turbine applications:

- (1) A small-vehicular type of engine (Ford). Such an engine would have a major impact on the technology of mobile field power units, military vehicles and craft. As a consequence of its significantly increased operating temperature it would not only provide more horsepower/unit weight than current engines, but would also provide improved fuel economy. In addition, the benefits of low emissions and multi-fuel capability are attained. A simplified schematic of the flow path of this regenerative type of engine is shown in Figure 1.1. A brief explanation of this flow path will be given to familiarize the reader with the various components considered for ceramics. Air is induced through an intake silencer and filter into a radial compressor, and then is compressed and ducted through one side of each of two rotary regenerators. The hot compressed air is then supplied to a combustion chamber where fuel is added and combustion takes place.

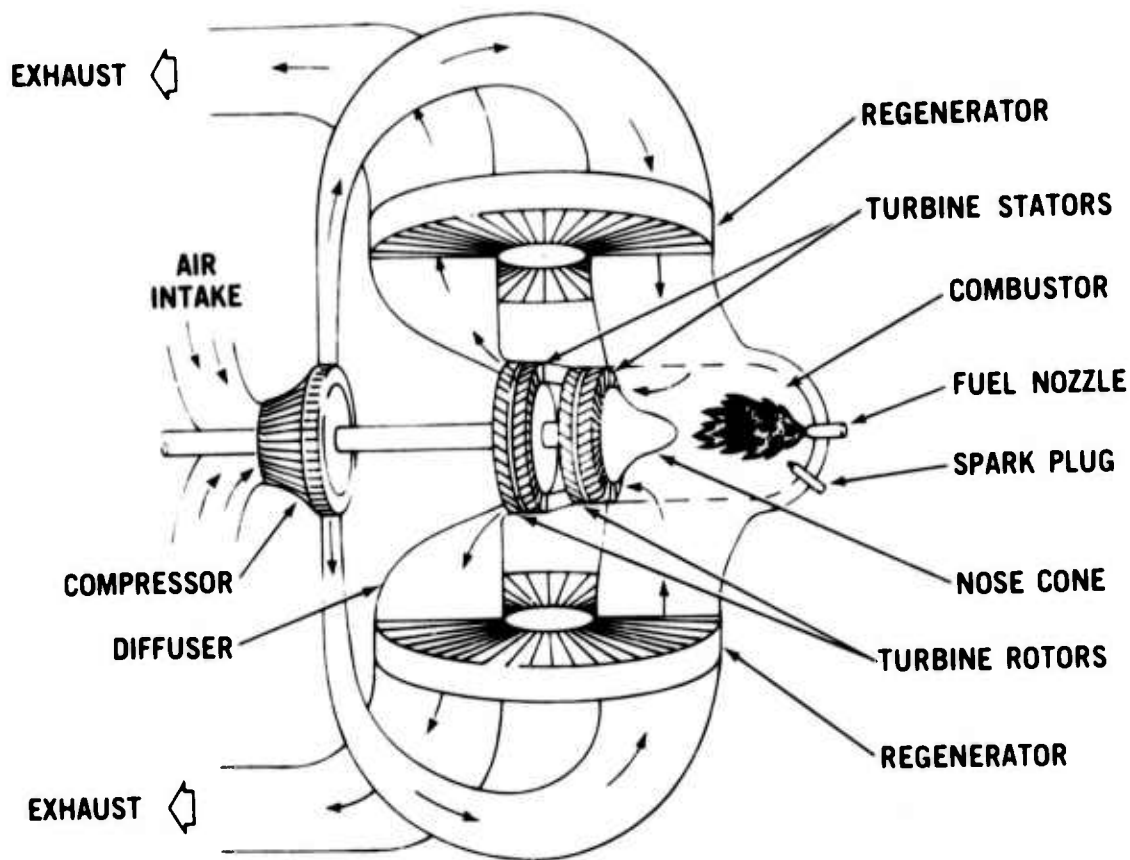


Figure 1.1 - Flow Path Schematic of Vehicular Gas Turbine

The hot gas discharging from the combustor is then directed into the turbine stages by a turbine inlet structure, in this case shown as a nose cone. The gas then passes through the turbine stages which comprise two turbine stators, each having stationary airfoil blades which direct the gas onto each corresponding turbine rotor. In passing through the turbine, the gas expands and generates work to drive the compressor and supply useful power. The expanded turbine exhaust gas is then ducted through the hot side of each of the two regenerators which, to conserve fuel consumption, transfer much of the exhaust heat back into the compressed air.

The parts which are subject to the peak cycle temperature and are made out of superalloys in today's gas turbine are the combustor, the turbine inlet nose cone, the turbine stators and the turbine rotors. These are areas where ceramics could be exploited to the fullest and have been selected for application in the vehicular turbine project.

- (2) A large-stationary gas turbine for electric power production (Westinghouse). Such an engine would be most desirable for DOD installations requiring on site power generation. Not only will ceramics facilitate significantly increased operating temperatures with attendant improvement in power and fuel economy, but, because of their improved corrosion-erosion resistance they will also facilitate use of low cost residual fuel. In addition, the environmental benefits of low emissions and lack of cooling water (with its attendant thermal pollution problems) are attained. A simplified sketch of the hot flow path of the engine is shown in Figure 1.2. As with the vehicular turbine project, a brief explanation of the flow path of the stationary turbine will be given to help the reader understand the function of the components to be made from ceramic materials.

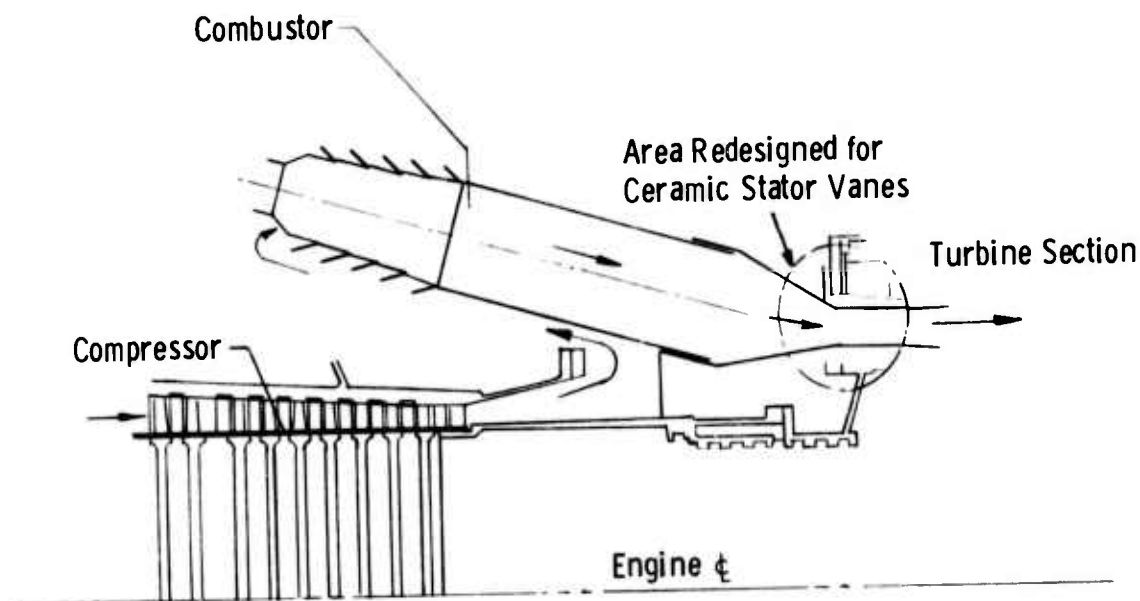


Figure 1.2 - 30 Mw Test Turbine Flow Path

Air is induced through a large intake silencer and filter into an 18 stage axial compressor where it is compressed before entering the combustor housing. The combustor housing supplies air at 650°F to combustion cans assembled in a circumferential array. Air is mixed with distillate fuel or natural gas and ignited in the primary combustion zone. The gas passes down stream through the combustors mixing with secondary air. Flow continues from the combustion section, through the transition zone, and enters the power turbine at a gas temperature of 2500°F. The hot gases expand through the three stage turbine section and are either exhausted through a stack or ducted into a reheat boiler as part of a combined cycle power generating unit.

The parts, where ceramics could be exploited to the fullest, selected for application in the stationary turbine project are the first stage turbine stator vanes and the first stage turbine rotor.

To maintain coherence, progress on the vehicular and stationary turbine projects are reported separately. Also reported separately is the common link between these two programs, materials technology. Information presented under materials technology is general, and does not specifically apply to one or the other of the gas turbine engines. On the other hand, items reported under the vehicular and stationary turbine projects are categorized by components and therefore relate directly to those projects (even these items, however, are indirectly related when it comes to such considerations as design techniques, etc.). Figure 1.3 has been prepared to help the reader understand the interrelationship between the major elements of the report.

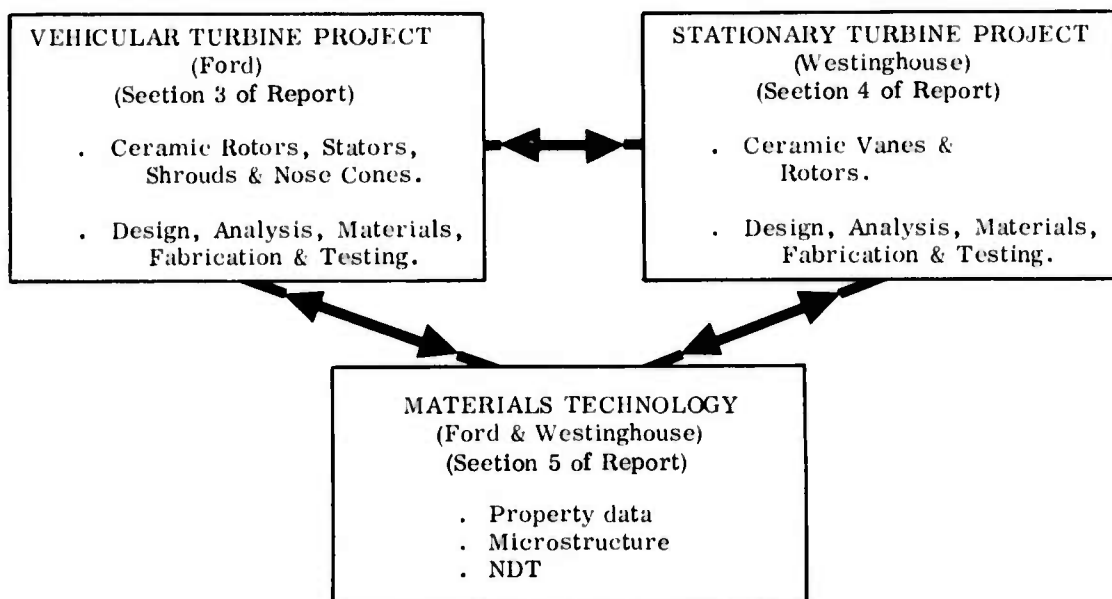


Figure 1.3 - Brittle Material Design/High Temperature Gas Turbine - Breakdown of Major Elements Reported

Successful demonstration of a high temperature gas turbine engine will involve a complex iterative development. One cannot divorce the development of ceramic materials from processes for making parts; no more so can one isolate the design of those parts from how they are made or from what they are made. Likewise, the design of mountings and attachments between metal and ceramic parts within the engine are equally important. Innovation in the control of the environment of critical engine components is another link in the chain. Each of these factors has a relationship with the others, and to obtain success in any one may involve compromises in the others. Testing plays an important role during the iterative development since it provides a positive, objective way of evaluating the various combinations of factors involved. If successful, the test forms the credibility to move on to the next link in the development chain. If unsuccessful, the test flags a warning and prompts feedback to earlier developments to seek out and solve the problem which has resulted in failure. Finally, all of the links in the chain are evaluated by a complete engine test, by which means the ultimate objective of the program will be demonstrated.

One difference in philosophy between the two turbine projects is worth noting. Because the science of ceramic materials, fabrication processes and designs is not fully developed, the vehicular turbine engine was designed as a test bed, and features ease of replacement of ceramic components. New ideas in a component's material, process, or design can therefore be engine-evaluated fairly rapidly. This work can then parallel and augment the time consuming efforts on material and component characterization, stress analysis, heat transfer analysis, etc. Some risk of damage to other components is present when following this approach, but this is considered outweighed by the more rapid acquisition of actual test information. On the other hand, the stationary gas turbine engine is so large, so expensive to test, and contains many costly components which could be damaged or lost by premature failure, that very careful material and design work must be performed to minimize the possibility of expensive, time-consuming failures.

Figure 1.4 shows a block diagram flow chart of the major factors involved including the feedback loops, which serves to illustrate this complex and comprehensive iterative development program. The starting point is the concept of a design to use brittle materials. From this, a design layout is prepared and analyzed leading to the detailed design and analysis of the gas turbine engine components made of or involving ceramics. In parallel with the design phase, ceramic materials are developed and screened for application to the gas turbine engine. Process development of candidate ceramics then takes place and material science and property evaluation are used to improve materials and processes, and to feed information back into the design phase. Next, with the first detailed designs completed and with the process for the selected ceramics reasonably developed, tooling can be designed and fabrication development started to make actual ceramic turbine engine components. Non-destructive testing of these parts will be developed to form a feedback for improving material and fabrication methods. In conjunction with non-destructive evaluation, techniques will be developed for proof testing ceramic components prior to use in engines. In parallel with ceramic part fabrication, proof testing, and non-destructive evaluation, metal parts for the ceramic turbine engine and test rigs are made per the detailed design requirements. The ceramic and metal parts are then dimensionally inspected and instrumented for engine testing. Assembly techniques for brittle materials are developed, and testing and durability development in both test rigs and engines is performed. Failure analysis from test rig and engine testing forms the feedback loops for corrective action; almost all of the factors involved in the development could be affected by experience learned in the test phase of the program. Finally, when engine durability has reached a given level of development, the 200 hour demonstration test will be conducted to meet the program objective.

It should be noted that both the contractor and subcontractor had in-house research programs in this area prior to the initiation of this program. Many ceramic materials were extensively tested and screened leading to the selection of silicon nitride and silicon carbide. In the stationary turbine program, preliminary design concepts were in existence before the award of the

Figure 1.4 — Brittle Material Design/High Temperature Gas Turbine - Block Diagram Flow Chart of Iterative Development

contract. In the vehicular turbine program, development was fairly well along and at least one pass had been completed through all of the factors shown in Figure 1.4 prior to the initiation of this program. This one pass, involving many minor iterations, led to a vehicular turbine hot flow path having all ceramic stationary components and designated Design A. Based on further experience gained during engine testing, a modified flow path was generated and designated Design B.

Since initiation of this program with AMMRC and ARPA, work on both the vehicular and stationary gas turbine projects was accelerated. Work accomplished during the first reporting period ⁽¹⁾ included, for the vehicular turbine project, initial fabrication development and preliminary testing of Design B turbine stators and nose cones made of reaction sintered silicon nitride. Design studies of ceramic turbine rotors showed that computed operating stresses can be withstood by dense silicon carbide and dense silicon nitride. Development programs were started to explore several approaches to fabricate rotors in these materials.

Accomplishments on the stationary turbine project during the first reporting period included obtaining physical property data of hot pressed silicon nitride and identifying microstructural details of this material. The initial design of ceramic stator vanes was completed and calculated vane stresses were reduced 40% by decreasing the stator vane chord.

The results of work accomplished during the second reporting period ⁽²⁾ included, for the vehicular turbine project, continued fabrication development as well as rig and engine testing of the second generation design (Design B) turbine stators and inlet nose cones. Ceramic turbine rotor design studies were performed on an expanded two-dimensional heat transfer computer program to include rotor attachment designs. Progress was reported on the multi-approaches being explored to fabricate a one-piece, intricately-shaped turbine rotor from candidate high strength ceramic materials.

The results of work accomplished on the stationary turbine project included the stress analysis and design of first stage vanes as well as a preliminary report on the rig for statically testing the stator vanes. Progress on the development of a new three-dimensional, finite-element, stress analysis computer program for subsequent use in ceramic rotor blade design was also reported.

Development in materials technology for both the vehicular and stationary gas turbines was reported and included continued compilation of material property data, continued characterization of material structure, and development of non-destructive evaluation techniques such as ultrasonics, radiography and acoustic emission.

The results of work accomplished during the third reporting period ⁽³⁾ included, for the vehicular turbine project, considerable emphasis on the development of the ceramic turbine rotor. Development was started on a new concept for a silicon nitride rotor, termed "duo-density". Progress was made on the stress analysis and the development of machining techniques for fabricating monolithic rotors from high-strength

hot-pressed materials. A cracking problem in the first stage stator blade appeared solved with the aid of a thermal shock test rig.

On the stationary turbine project, a full scale model of the first generation stator vane assembly showed that the design was functional when subjected to differential motions well in excess of design limits. Using improved physical property data, the transient thermal stresses in the first stage stator vane were recalculated. The three-dimensional stress analysis program was applied to a dense silicon nitride rotor blade.

Work on materials technology resulted in additional property data on candidate ceramic materials, and further relationships of microstructure to properties were uncovered. A number of processing parameters were examined for reaction-sintered silicon nitride.

The work accomplished during the fourth reporting period ⁽⁴⁾ included, for the vehicular turbine project, the continued development of methods for fabricating duo-density silicon nitride turbine rotors during which several rotors were made; the best of these was spin-tested to 50,500 rpm before failure. A refined stress analysis of a monolithic silicon nitride rotor was completed, and the effects of a severe flame-out transient on the duo-density rotor was analyzed. Design revisions have been made to both stator stages, which resulted in the elimination of most but not all cracking.

Work accomplished on the stationary turbine project included stator vane design modifications with improvements to aerodynamics and methods of mounting. Additional stress analyses have been performed at critical interfaces. The static test rig, for evaluation of ceramic stator vanes under realistic gas turbine conditions, has been completed and installed. Design concepts and stress analyses of rotating turbine blades continued to be investigated.

Work on materials technology was continued, and a considerable amount of mechanical and thermal property data on silicon nitride and silicon carbide was determined. The microstructure of hot pressed silicon carbide was studied, and further process improvements were made for reaction sintered silicon nitride.

During this fifth reporting period, work on the vehicular turbine project included an investigation and experimental evaluation of the use of Weibull theory for predicting probability of failure of turbine rotors. Processing development was concentrated on multi-density silicon nitride rotors, a number of which were cold spin tested. The thermal response of first stage stator vanes during engine testing was determined by direct observation through a quartz window, and correlated with thermal response data obtained on the thermal shock test rig.

Work on the stationary turbine project passed a major milestone with the completion of the first static rig testing of silicon nitride vanes at temperatures up to 2200°F. All silicon nitride vanes which met design specifications successfully survived more than 100 thermal transient cycles. Parts which did not meet design specifications cracked in a non-catastrophic manner due to an edge loading condition.

Work on materials technology explored the effect of impurities in hot pressed silicon nitride as well as oxidation-sulfidation testing of hot pressed silicon nitride and improvements in the properties of both injection molded and slip cast reaction sintered silicon nitride.

Accomplishments on the vehicular turbine project during this sixth reporting period included progress on the development and application of three dimensional stress analysis programs to ceramic rotors and stators. Improvements were made in the method of supporting molded blade rings during the press-bonding of duo-density rotors, and preliminary experiments on an investment casting approach to fabricating Si_3N_4 rotor blades were successful. A major milestone was reached with the completion of a 50 hour dynamic engine test of the hot flow path ceramic components under cyclic load conditions at 1930°F. All the components except for eight second stage stator vanes were in excellent condition following the test. A "REFEL" silicon carbide combustor also survived a 50 hour cyclic durability test.

On the stationary turbine project, work is well along on the design modifications for the rotating test rig for peak temperatures of 2500°F. Silicon nitride and silicon carbide stator vanes of two designs will be tested. The static test rig was rebuilt for 2500°F operation. During testing at 2300°F, the ceramic duct failed catastrophically, resulting in a delay in further testing. The ceramic vanes being evaluated were not damaged. The three dimensional finite element stress analysis code was demonstrated on a ceramic rotor blade operating at 3600 rpm.

Development and evaluation of ceramic materials was continued. Additional property data was determined, and x-ray radiography was found to be an extremely valuable tool for inspecting ceramic components during processing.

Summarizing the current program status, it appears that the vehicular gas turbine engine stationary flow path components will meet the final 200 hour goal with further expected improvements in design, materials, and processing. The completion of the 50 hour durability test further enhances this optimism. Nose cones and rotor shroud rings of current designs and materials should be capable of reaching this goal now, although further improvements are expected to improve reliability. It is also felt that design and processing modifications currently in progress will sufficiently improve stator durability to achieve the final goal. The ceramic turbine rotor development is the most critical area and requires solution to several major engineering problems. Improvements in material strength, fabrication, and processing are needed in order to develop satisfactory rotors, and work is proceeding in these areas. On the stationary gas turbine engine, results to date indicate that a viable stator design has been achieved. Continued effort on quality control and material reliability should result in successful program completion, requiring only minor future modifications.

This report covers the progress in the period January 1, 1974, through June 30, 1974.

2. SUMMARY OF PROGRESS

2.1 VEHICULAR TURBINE PROJECT

The vehicular turbine project is composed of three primary section -- design, materials, and testing. Within these primary areas there exist many tasks which must be accomplished in order to achieve the program goal of 200 hours of turbine engine operation over a representative duty cycle at ceramic temperatures up to 2500°F. Each semi-annual report is a progress report detailing the results of work over a six month time increment, and reporting on the individual accomplishments on the tasks which will culminate in the final program objective.

Work is in progress concurrently in areas of turbine engine component design and analysis, ceramic material and process development, material and engine testing, materials technology, and nondestructive evaluation of ceramic engine components. Progress, made in several of these areas in this reporting period, is summarized in this section of the report.

(1) A three dimensional finite element model of the first stage rotor blade and platform areas has been generated. This model will be used for complete heat transfer and stress analyses which, together with the two dimensional analyses of the disks that have already been performed, will complete the task of rotor stress analysis. Refer to Section 3.1.1 of this report for more information.

(2) A method of supporting the blade ring during press bonding was developed for the duo-density Si_3N_4 turbine rotors. Because of this development and problems with the triple density approach, the latter was de-emphasized in favor of the duo density concept. A systematic study of injection molding parameters resulted in the fabrication of Si_3N_4 blade rings free of those detectable flaws which had been found to be crack initiation sites when the blades were spin tested. A method of slip casting Si_3N_4 blades based upon investment casting principles has shown initial success. Section 3.1.2 contains the details of work in these areas.

(3) A method was developed for spin testing of molded Si_3N_4 rotor blade rings at room temperature without requiring the fabrication of a complete press bonded ceramic rotor. Test results showed the best first stage blade ring achieved 61,900 rpm while the best second stage blade ring achieved 56,840 rpm. Details of this testing is contained in Section 3.1.3.

(4) Progress has been made in developing a three dimensional stress analysis system for all ceramic turbine components, utilizing a series of interacting computer programs. The initial steps in applying this system to the stress analysis of Si_3N_4 stators is explained in Section 3.2.1.

(5) Several of the newly designed one piece first stage stators have been fabricated in reaction sintered silicon nitride by injection molding. A previous dimensional instability problem involving slip cast Si_3N_4 rotor shroud rings appears to have been solved. Refer to Section 3.2.2 for more details.

(6) A combustor tube made of "REFEL" silicon carbide was evaluated for 50 hours, including six hours at an outlet temperature of 2500°F, without failure. This evaluation was performed in a test rig closely simulating turbine engine conditions, and is described in Section 3.2.3.

(7) A major program milestone was reached with the successful completion of a fifty hour cyclic engine durability test of the hot flow path ceramic components. The test was conducted at a steady state temperature of 1930° F due to the limitations imposed by the use of metal rotors. Section 3.2.3 contains the details of the test cycle and the results of the performance of the ceramic components.

(8) A program to develop gas bearings for the high speed turbine shaft has been initiated and is described in Section 3.3.1.

2.2 STATIONARY TURBINE PROJECT

The stationary turbine project is a design study of brittle materials in a high temperature gas turbine application, culminating in a demonstration of uncooled ceramic stator vanes in an advanced power turbine operating for 200 hours. This operation will consist of 100 sequences of peaking cycle service. A performance simulation of ceramic rotor blades will also be performed by computer. Work is currently in progress in areas of stator vane design and analysis; rotor blade analysis based on the development of 3-dimensional finite element stress analysis codes; component fabrication and performance evaluation; and material technology. Progress is summarized in this section of the report.

(1) Layout drawings and design specifications have been prepared for the modification of the W-251 test turbine. An average turbine inlet temperature of 2300°F was selected to meet the peak temperature requirement of 2500°F on the first stage ceramic stator vanes. The air-cooled metal rotor (first stage) and cooling for all subsequent metal components downstream are discussed in section 4.1.1 of the report.

(2) Stress analysis confirmed the effects of edge loading and the contact stress problem as contributors to premature airfoil failure in the static rig tests at 2200°F. For contact areas of 0.003, 0.006, and 0.012 in², for example, the maximum principal stress decreases from 95 through 60 to 38 x 10³ psi, respectively. Minimum loading areas at the airfoil tenon-end cap interface actually degenerated to point or line contact as a result of out of tolerance machining and/or poor vane assembly element matching. The second generation vane design was proposed as an aerodynamic optimization of the three piece ceramic stator vane assembly. Finite element stress analysis indicates too great a compromise in the mechanical aspects, however, since the maximum principal stress is expected to reach 125 x 10³ psi in the fillet transition area where the airfoil is blended into the enlarged tenon. These results reflect boundary conditions characteristic of emergency shutdown from a steady state peak temperature of 2500°F.

(3) Static rig testing of Si₃N₄ and SiC stator vane assemblies was resumed with calibration runs for the 2500°F peak temperature test schedule, reaching 2300°F. Damage to the ceramic duct and mixer sections of the static rig will delay further testing until September, 1974. Details are reported in section 4.1.3 of this report.

(4) The Norton Company completed the rework on sixteen Noralide NC-203 silicon carbide end caps to eliminate edge loading in the elements as assembled. Sixteen stator vane assemblies of second generation design were also delivered. Vane fabrication is discussed in section 4.1.4 of this report.

(5) The WISEC three-dimensional finite element code is demonstrated by a ceramic rotor blade analysis of a typical geometry at 3600 rpm. Anisotropic and temperature sensitive material properties are represented in the discussion appearing in section 4.2.1 of this report.

2.3 MATERIALS TECHNOLOGY - VEHICULAR AND STATIONARY PROJECTS

Complete property characterization of the ceramic materials for turbine engine use is an enormous task, which will proceed throughout the life span of the contract. This task is complicated by the fact that many of the materials being investigated are in the developmental stage. Improvements in properties are anticipated, which will require that some, if not all of the physical properties will be re-determined eventually. Progress in materials technology is summarized in this section of the report.

(1) Additional tensile, flexural, and creep data are used to supplement existing engineering property compilations of Norton HS-130 Si_3N_4 (NC-132) and NC-203 SiC. Refer to section 5.1.1 of this report for detailed information.

(2) Reversible low cycle fatigue data indicated a finite life for hot-pressed silicon nitride at 2300°F. Experimental results appear in section 5.1.1 of this report.

(3) Additional creep testing of reaction sintered Si_3N_4 has shown that material nitrided in an atmosphere of hydrogen plus nitrogen has improved creep resistance. Refer to section 5.1.2 for more information.

(4) Initial stress-rupture testing of molded reaction sintered Si_3N_4 has shown good life. One sample was tested for over 800 hours at 2300°F and 10,000 psi load without failure, and another sample has exceeded 50 hours at 2500°F and 20,000 psi load. Test results are given in section 5.1.2.

(5) The elastic constants for silicon nitride of four different densities have been determined from room temperature to 1830°F. These properties appear to vary with density, as shown in Section 5.1.2.

(6) A complete chemical analysis of all remaining billets of HS-130 silicon nitride is reported. The calcium concentration was below 0.05 w/o. Results are tabulated in section 5.2.1 of this report.

(7) The combined effects of oxidation and sulfidation on weight gains in hot-pressed silicon carbide are equivalent to oxidation alone. Refer to section 5.2.2 of this report for a complete discussion.

(8) Fracture mechanics studies on hot pressed silicon nitride have shown the presence of slow crack growth. A low fracture energy value (18,000 ergs/cm²) is obtained, indicating the pre-cracking method used produces a very sharp crack. Temperature dependence of fracture strength in flawed vs unflawed material is discussed in section 5.2.3.

(9) The computer-aided ultrasonic defect detection system was used to evaluate hot pressed Si_3N_4 . This system proved capable of higher resolution and sensitivity than has been shown by conventional systems, as shown in section 5.3.1.

(10) X-ray radiography was found to be a useful tool for evaluating the quality of as-molded rotors and stators. Subsurface flaws were readily detected, making it possible to discard faulty components at a very early stage of processing, avoiding wasted time and preventing possible future failures. Refer to Section 3.1.2 and Section 5.3.3 for more information.

(11) A special summary section, 5.3.5, is provided in this report which summarizes the current state-of-the-art in the application of NDE to ceramic materials in this project. Applications, limitations, and sensitivity limits are discussed.

3. PROGRESS ON THE VEHICULAR TURBINE PROJECT

3.1 CERAMIC ROTOR DEVELOPMENT

SUMMARY

A three-dimensional analytical model of the blade and throat area of the first stage turbine rotor has been generated. Combining this model with existing computer programs provides a complete analytical tool for stress and heat transfer analysis of turbine rotors.

A rotor disk has been designed with a symmetrical profile and with sufficiently low stress levels to be used for both first and second stage turbine rotors. The common disk reduces the inventory of parts and eliminates possible errors in assembly prior to press bonding.

Development of multi-density silicon nitride turbine rotors continues. The major effort during this reporting period was concentrated on developing fabrication techniques for triple density rotors. However, problems with fracture of the rim and inconsistencies in bonding, plus the development of a suitable blade fill material for duo-density bonding development resulted in de-emphasis of the triple density concept in favor of work on duo-density rotors.

A double blade fill technique for supporting the blades of low density rotors during press bonding was developed which provides adequate support while still providing easy removal of the fill material after press bonding.

Considerable effort was expended on improving the quality of injection molded silicon nitride blade rings. Spin testing showed that blade failures have initiated from molding flaws. Detectable molding flaws were eliminated through variations in molding and processing parameters.

Development of an investment casting technique for forming complex ceramic shapes is continuing. Airfoil sections have been cast, as well as three blade segments which simulate a turbine rotor blade ring. Excellent fill of the shell mold with silicon metal slip has been obtained. The mold can be easily removed from the part after nitriding in the mold.

Spin test evaluation of ceramic blade rings was continued, with the best results showing a first stage blade failure at 96% of design speed and a second stage blade failure at 88% of design speed. Data obtained from cold spin testing of blades made from two different grades of reaction sintered Si_3N_4 was analyzed statistically to determine the distribution of failure speeds, characteristic speed, and Weibull modulus (m).

Additional thermal shock tests have been conducted on rotor blades. Four first and second stage blade rings were tested in a manner simulating the engine light-off transient condition, and survived 2462 cycles without damage.

In assessing the current status of ceramic turbine rotor development, the primary candidate continues to be the duo-density Si_3N_4 approach. Several duo-density turbine rotors have been fabricated with improved bond integrity; work is underway to resolve remaining bonding problems. Cold spin testing showed an improvement in blade strength; however, the rotors tested to date did not reach the full top speed goal. Elimination of defects plus expected material strength improvements should produce blade rings capable of full speed

operation. Development of slip casting processes to produce high density high strength blade rings should provide additional speed capability. Although the confidence level of achievement of a ceramic turbine rotor capable of meeting the program goals within the time limit of the program remains lower than the confidence in the stationary components, recent accomplishments in development of duo-density rotors and blade ring fabrication processes have provided encouragement.

3.1.1 DESIGN AND ANALYSIS

Introduction

The three dimensional finite element model to be used for thermal stress analysis of the first stage rotor is presented along with an explanation of the methods used to build the model. A probability analysis of blade failures under various test conditions is also included in this section. The first and second stage rotor disks have been redesigned to utilize a common geometry, and the results of stress analyses are presented. The use of dissimilar metals in the rotor attachment bolt was shown to reduce the stiffness of the folded bolt arrangement and lower the bolt clamping loads.

Previous reports (2,3,4,5) have presented thermal stress analyses of the ceramic turbine rotors modeled as axisymmetric bodies. However, this representation is not valid for analysis of the rotor blades and rotor platform areas at the blade roots. A full three dimensional analysis is required in these areas. The computer codes used for this work are general finite element heat transfer (TAP) and stress (SAP) codes. These codes would be applicable for both rotor and stator analysis.

The heat transfer (TAP) and stress programs (SAP) were purchased by Ford for the development of 3-D techniques to analyze ceramic components such as rotors and stators. The programs required modification, both for the specific application and the specific computer installation (Honeywell 6080).

The heat transfer program (TAP) is currently limited to the use of materials with constant thermal properties. Experience with ceramics necessitates modifying the code to allow for analysis of a non-linear thermal problem, since thermal conductivity varies appreciably with temperature. This modification to the computer code has been worked on during this reporting period.

The three dimensional stress code (SAP) required modification to conveniently analyze transient thermal stress problems. This modification has also been in progress during this reporting period. As mentioned in the last report (5), the code also required considerable modification in order to analyze the rotor or stator economically. The code has been modified to allow modeling of a circumferentially repeatable structure such as the rotor or stator by using one typical segment of the structure.

Three Dimensional Stress Analysis of Ceramic Rotors

To reduce analytical modeling and computational costs, the model was constructed using the principle of repeatability (6). The entire rotor was modeled by one typical segment of the rotor. The model is shown in Figures 3.1 and 3.2. It represents one blade and the corresponding platform and disk segment down to the throat, as shown in Figure 3.3.

The basic element being used for the stress analysis is the eight node brick with incompatible displacement nodes developed by E. L. Wilson (7). A combination of automatic element generation for the blade and disk and manual selection grid-point locations for the blade-platform region was used in developing the complete 3-D first stage rotor model.

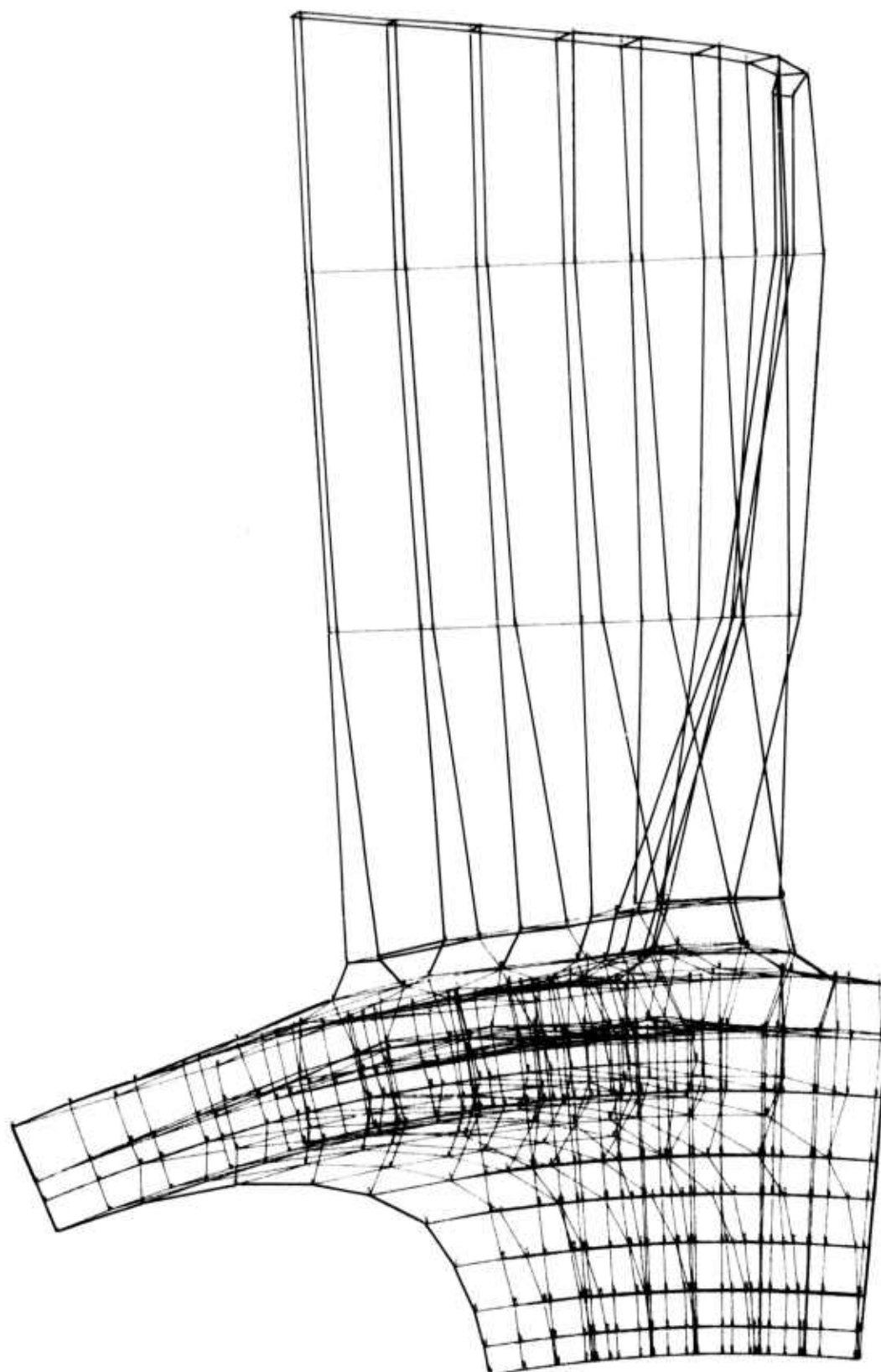


Figure 3.1 Front View of the Three Dimensional Model of a First Stage
Rctor Blade, Platform, and Disk Portion Extending to the
Throat Region

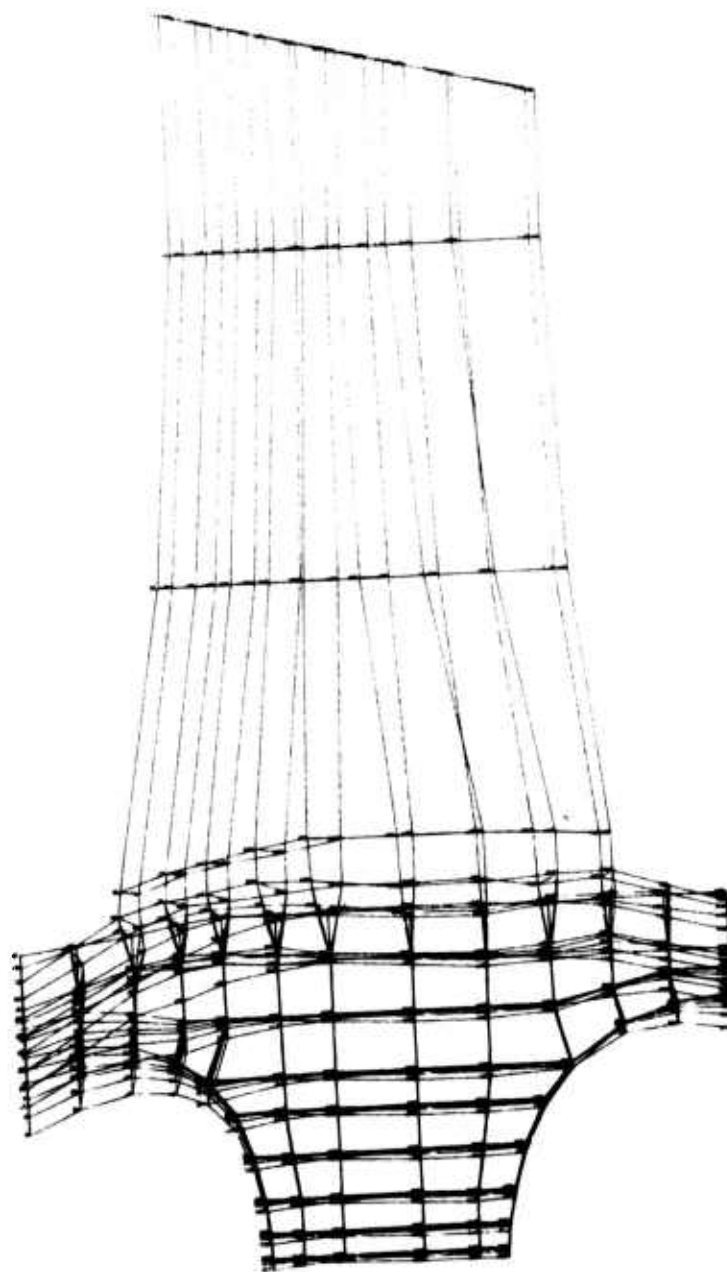
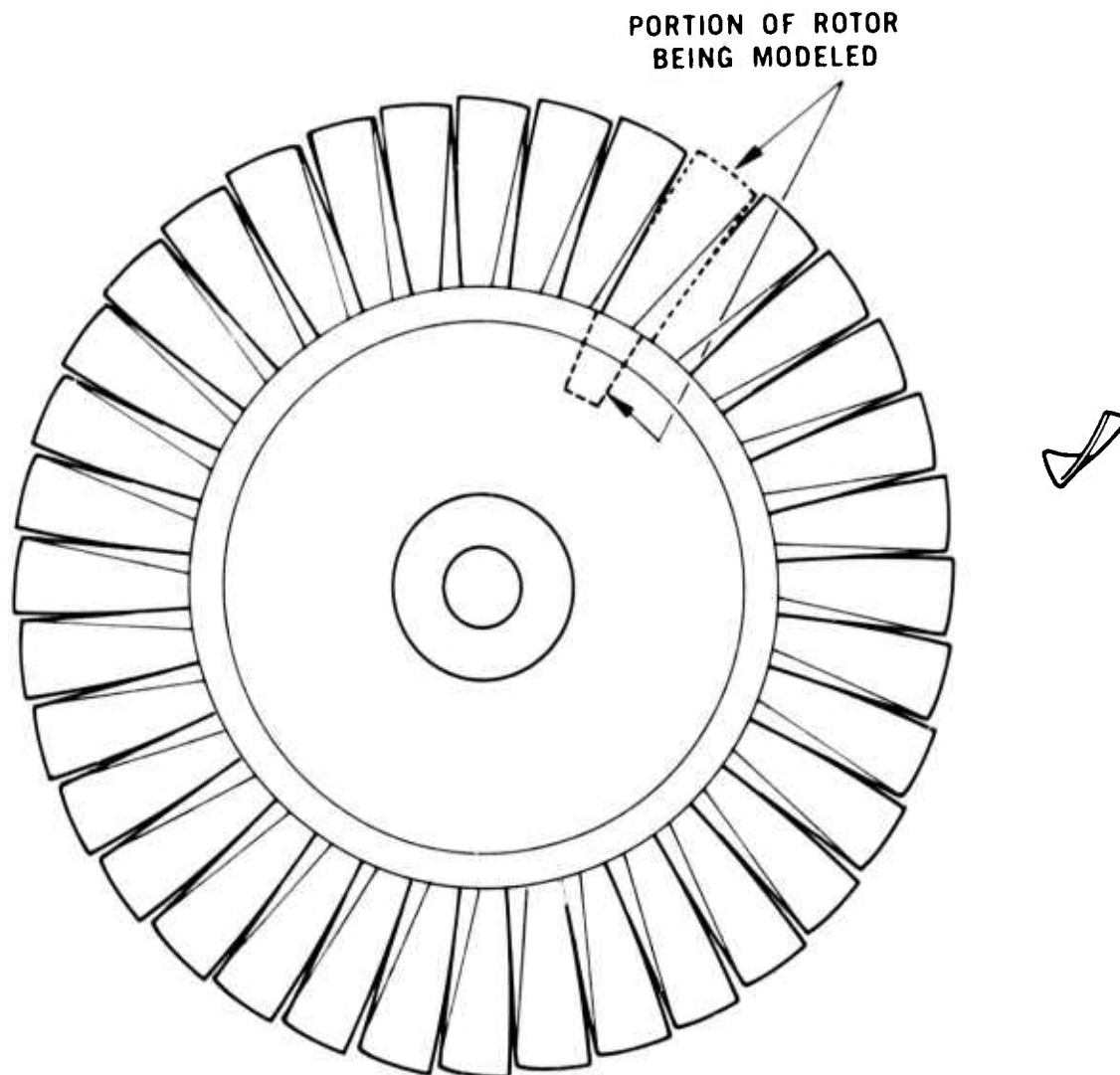


Figure 3.2 Side View of the Three Dimensional Model of a First Stage Rotor Blade, Platform, and Disk Portion Extending to the Throat Region



FIRST STAGE TURBINE ROTOR (FRONT VIEW)

Figure 3.3 Front View of First Stage Turbine Rotor Showing Portion Being Modeled

To generate the blade portion of the model, a computer program was written which used as input previously defined airfoil sections. These sections are depicted as Aero 1, 2, and 3 in Figure 3.4. The location of a fixed number of reference nodal points on the pressure and suction sides of each section was chosen. By fitting second order curves through corresponding reference nodal points on the aerodynamic airfoil sections the shape of the blade was defined. Next, the airfoil planes used for the blade model were selected. The intersection of those planes with the second order curves defined the nodal points in the blade model as shown in Figure 3.4. In addition, this program generates coordinates which define the overall cross-sections of the platform, as shown in Figure 3.5. The inputs used for this generation are blade hub radius, the axial distances (X-direction) from the stacking axis (Z-Axis) to the front and rear surfaces of the platform, the radius to the underside of the platform, and the number of blades on the rotor, as illustrated in Figure 3.6.

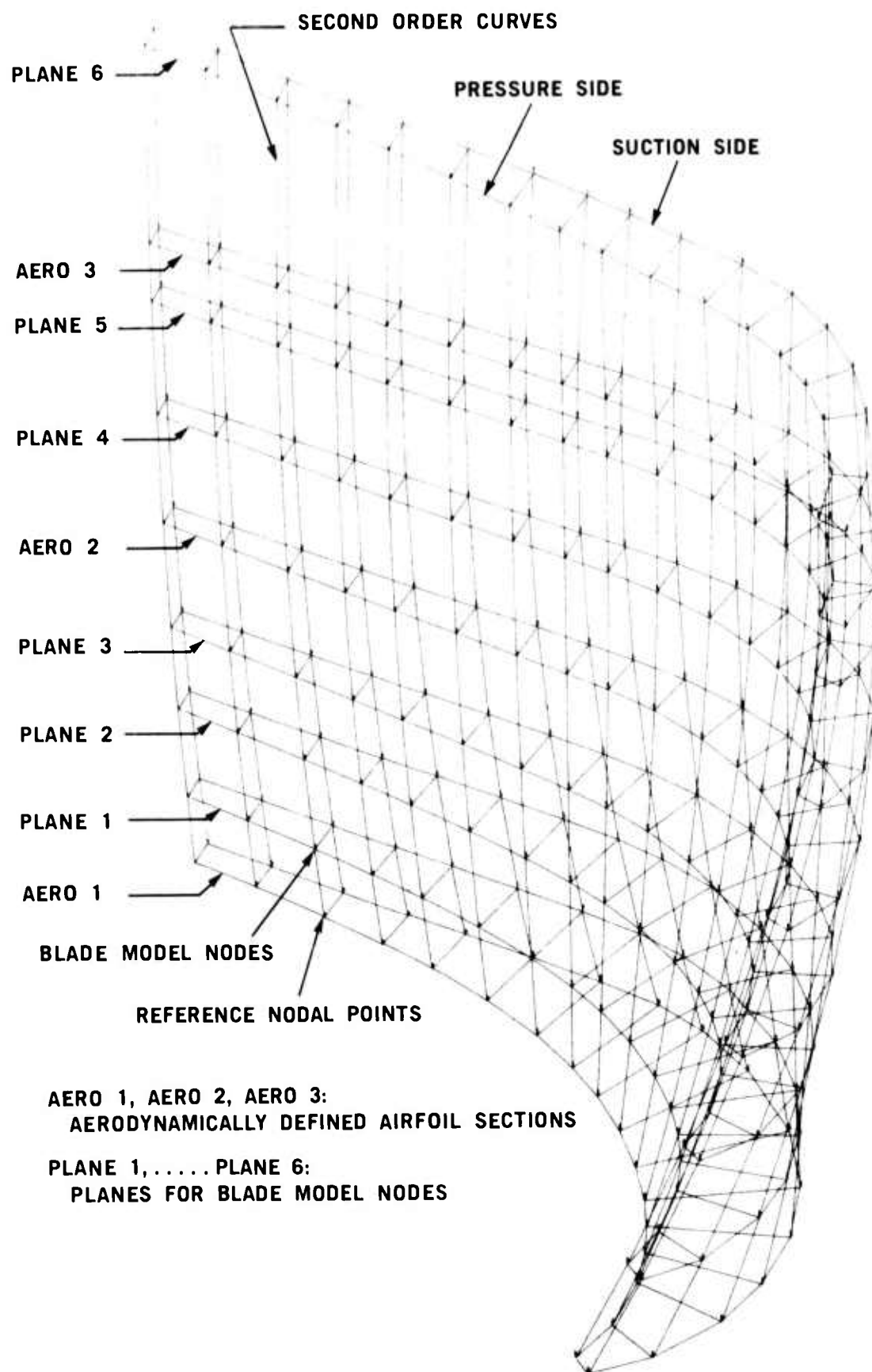


Figure 3.4 Generation of Blade Model Nodes

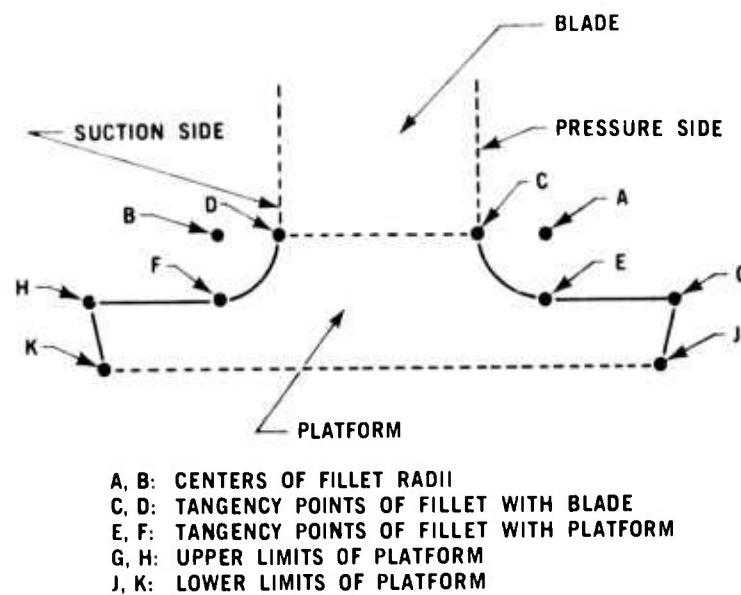


Figure 3.5 Computer Output Coordinates Which Define the Overall Cross-Section of the Platform

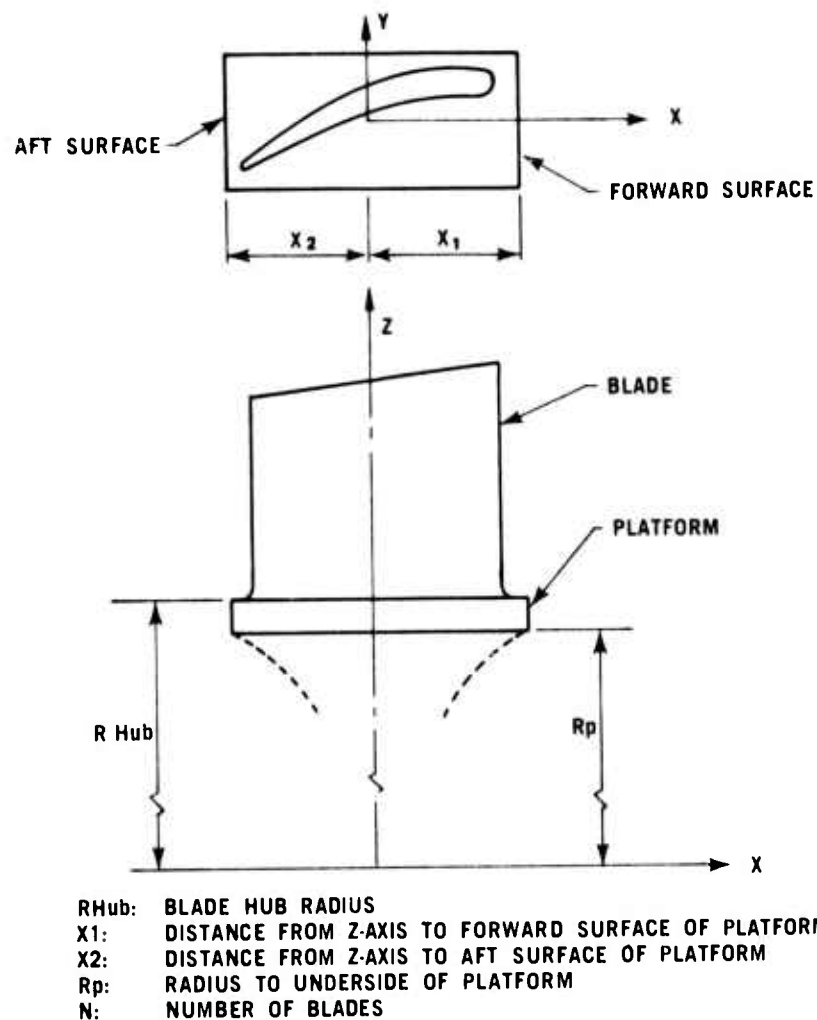


Figure 3.6 Program Input Data Used to Generate the Coordinates for the Overall Cross-Section of the Platform

The blade-platform intersection is a critical region in the turbine rotor since it is the junction of an abrupt geometric change from a plate-type structure (blade) to a cylindrical structure (disk periphery). Such abrupt changes result generally in severe stress concentrations. In this particular case the junction is located within the major thermal boundary of the disk, which adds to the complexity of loading during thermal transients such as cold starts or shut-downs. With these factors in mind, the blade-platform transition portion of the model is done manually by building individual elements to best represent the actual geometry as shown in Figure 3.7. The selected nodes are then digitized and incorporated with the blade nodes.

To generate the remaining disk portion of the model, another computer program was written which defines a radial line from every node on the underside of the platform to the engine centerline (X-Axis). The angles that these radial lines make in their respective Y-Z planes are calculated and stored along with the corresponding X-coordinates. By supplying the true radial dimensions and the X-coordinates of the desired two-dimensional disk contour, the program automatically generates the X, Y, and Z coordinates of the nodes in the disk portion of the 3-D model.

To reduce the three-dimensional analytical costs as much as possible, the construction of the disk portion of the model utilized the principle of Saint-Venant in which the effects of discrete blade loadings are expected to be damped out within the rim region above the throat of the disk. Below that region it is believed that the axisymmetric 2-D analysis provides a valid representation of temperature and stress states. This will allow axisymmetric analysis to be used to determine realistic boundary conditions (displacement) at the disk throat, i.e. the junction of the 2-D and 3-D models. This assumption will be verified by comparing stresses and deformations obtained from this model with those obtained from a purely 3-D model of a disk segment.

The addition of the three-dimensional modeling techniques to the existing SAP, TAP and axisymmetric computer programs provides the designer with a complete set of analytical tools required for mechanical and thermal stress analysis of complex ceramic structures such as turbine rotors under both steady-state and transient loadings.

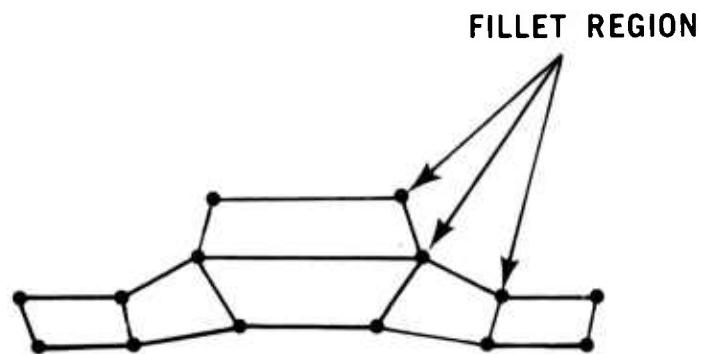


Figure 3.7 Manually Chosen Elements and Nodal Points That Define the Platform Cross-Section

Rotor Disk Redesign

A redesign has been completed on the rotor disks, making them common to both the first and second stage rotors. The purpose of this redesign was to reduce stresses and to reduce the number of parts required during the development phase of the duo-density rotor program. The revised disk also has the same profile on the front and back faces so that it is reversible. The common profile disk is shown in Figure 3.8. Also shown in Figure 3.8 are the portions of both the first and second stage blade ring platforms which are bonded to the common disk.

The non-symmetrical features of the rotor, not common to the first and second stage, will be machined after the bonding operation. The balance rings have been eliminated and the platform has been thickened to allow for removal of balance stock. The thicker platform also gives more support to the blade ring during hot press bonding. Elimination of the balance ring has improved the quality of the hot pressed Si_3N_4 rotor hub by removing a troublesome change in section.

The results of the design study are shown in Figures 3.9 through 3.11. The figures show the isostress contours, in increments of 5,000 psi, of the maximum principal stress for centrifugal loading at 110% speed. These may be compared to the same operating conditions for dissimilar rotor profiles in previous reports (3,4,5). The finite element outline used to simulate the blade's mass distribution is shown on the rotor platform. The axial load of the attachment bolt was not included in this analysis, and the local stresses due to the curvic coupling teeth and the blades were neglected.

Figure 3.9 shows the stress distribution for the common profile rotor of fully dense Si_3N_4 with second stage blade loading. Figure 3.10 shows the stress distribution of the duo-density configuration. The blade ring is molded reaction sintered Si_3N_4 and the disk is hot pressed Si_3N_4 . Stresses are slightly reduced due to the use of lower density material in the blades. Figure 3.11 shows the stress distribution of the triple-density configuration, utilizing a molded blade ring, a slip cast Si_3N_4 ring and a hot pressed hub. The slip cast ring supports the molded blade ring during the press bonding operation. Stresses in the bore are about the same as the duo-density hub, but the stresses in the press-bond region are considerably higher in the triple-density rotor. These stresses reach 20,000 psi versus 10,000 psi for the duo-density design. This may be a problem if bond strengths are low.

Figure 3.12 shows the stress distribution for the common profile of fully dense Si_3N_4 with first stage blade loading. A comparison of Figures 3.9 and 3.12 show that the first stage has slightly lower stresses. Comparison of other first stage configurations, duo-density, triple-density, etc., were not made since the stresses are similar for the fully dense cases. Stress calculations were made with an axisymmetric finite element program. The finite element grids used are shown in Figures 3.13 and 3.14.

Ceramic Rotor Attachment

The folded bolt and the curvic coupling designs for the attachment of the ceramic rotors have been discussed previously (2,4,5). With the introduction of dissimilar materials for the tension and compression members, discussed in

the last report (5), a much softer bolt configuration was achieved. Analysis of this configuration indicates the required bolt load can be reduced to approximately 3900 pounds when the engine is at room temperature. This load increases to 4530 pounds during the startup transient and reduces to 2140 pounds for steady state operation. These installation and transient loads are lower than those originally estimated.

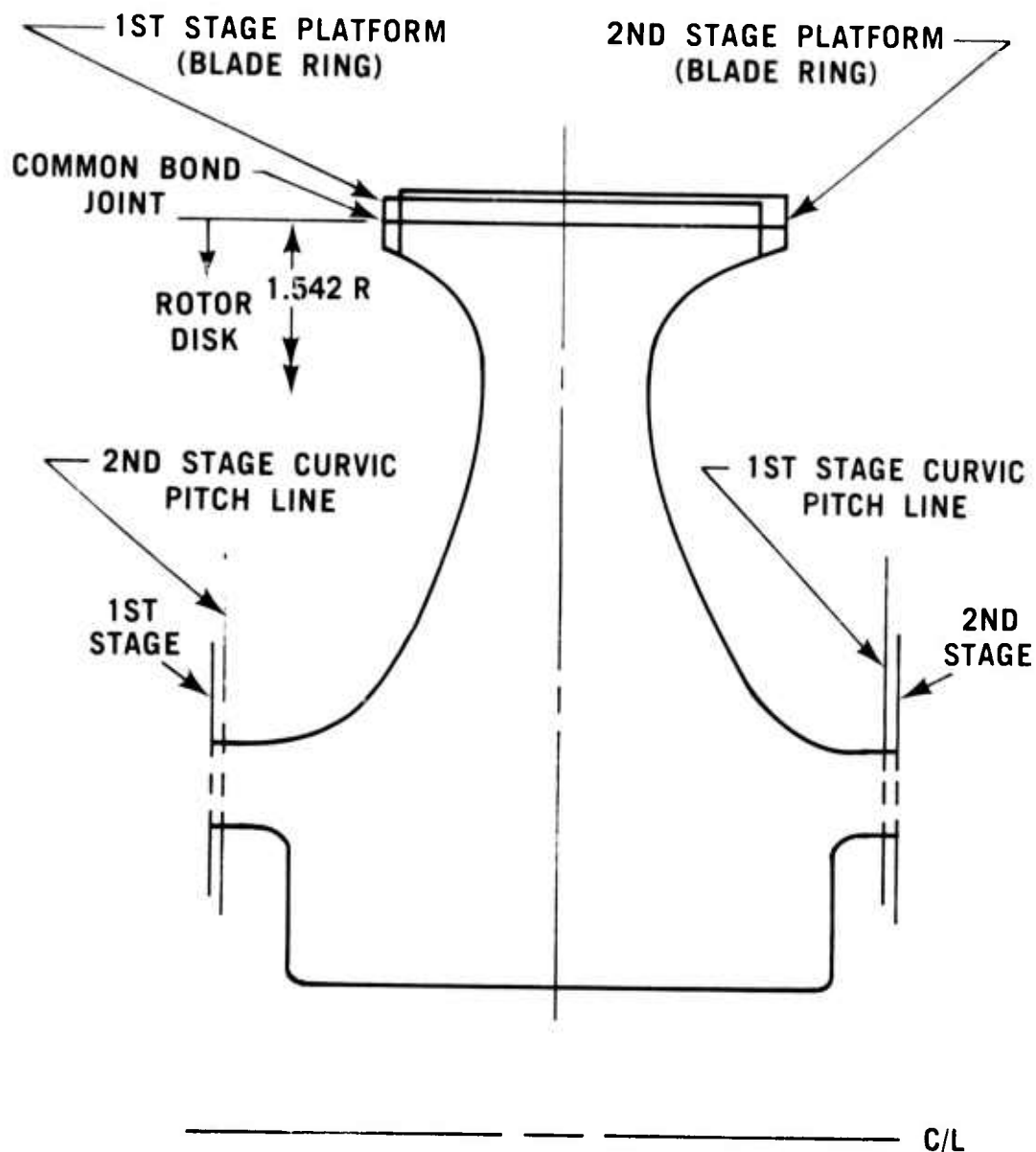


Figure 3.8 Common Profile Rotor Disk

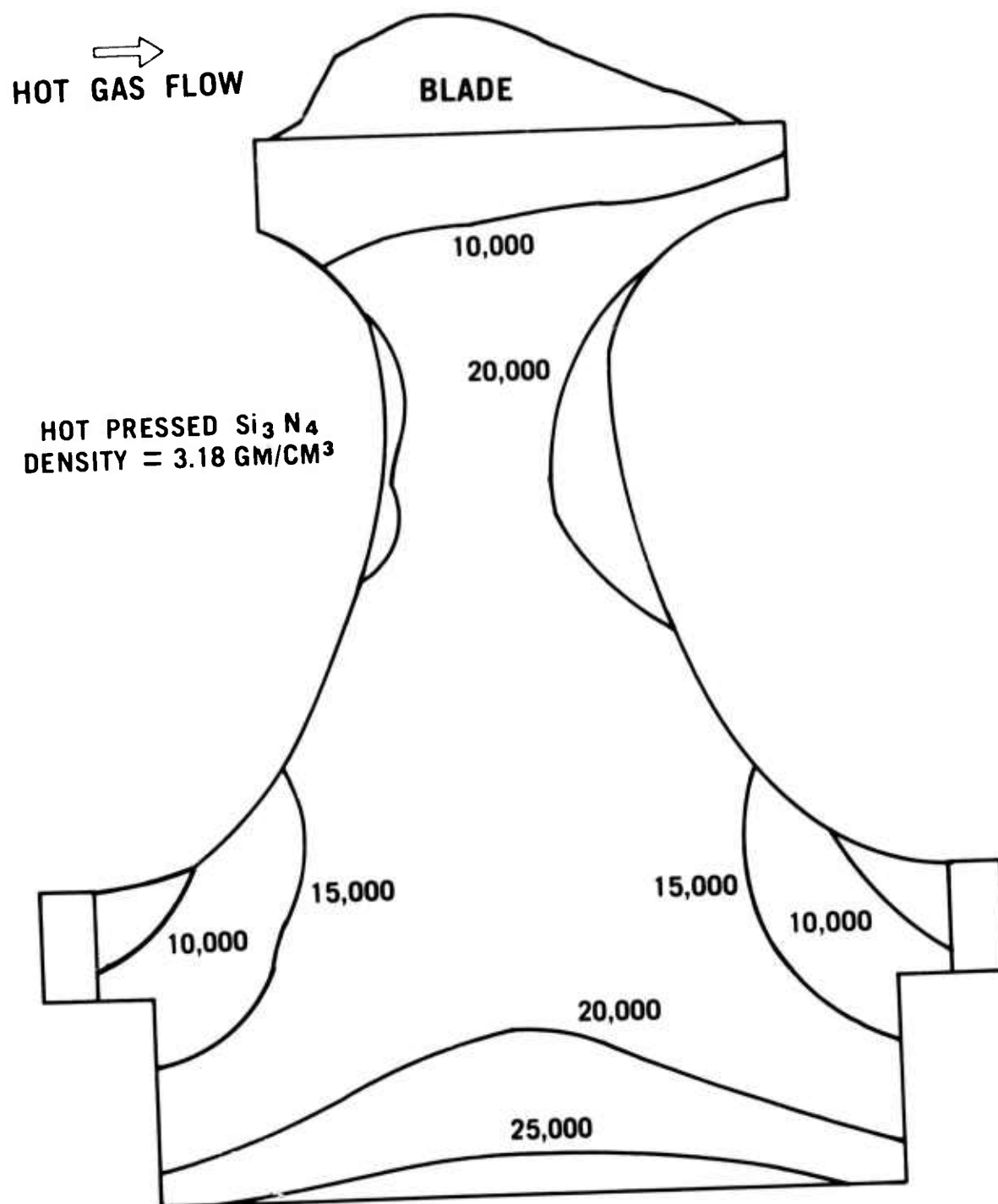


Figure 3.9 Maximum Principal Stresses (psi) in Second Stage Disk, 110% Speed Centrifugal Loading, Hot Pressed Si_3N_4 Disk and Blades

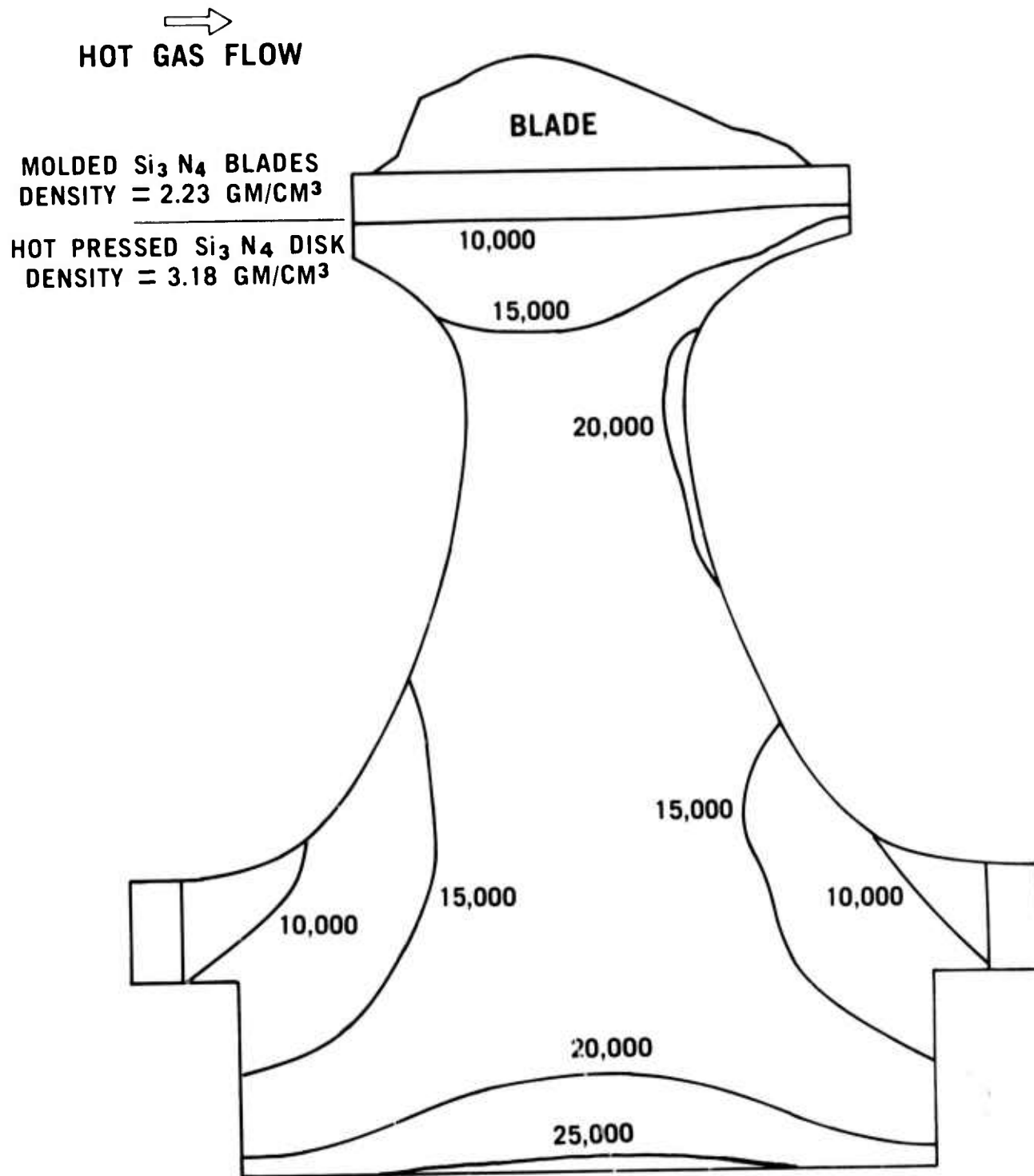


Figure 3.10 Maximum Principal Stresses (psi) in Second Stage Disk, 110%, Speed Centrifugal Loading, Hot Pressed Si_3N_4 Disk, Reaction Sintered Si_3N_4 Blades

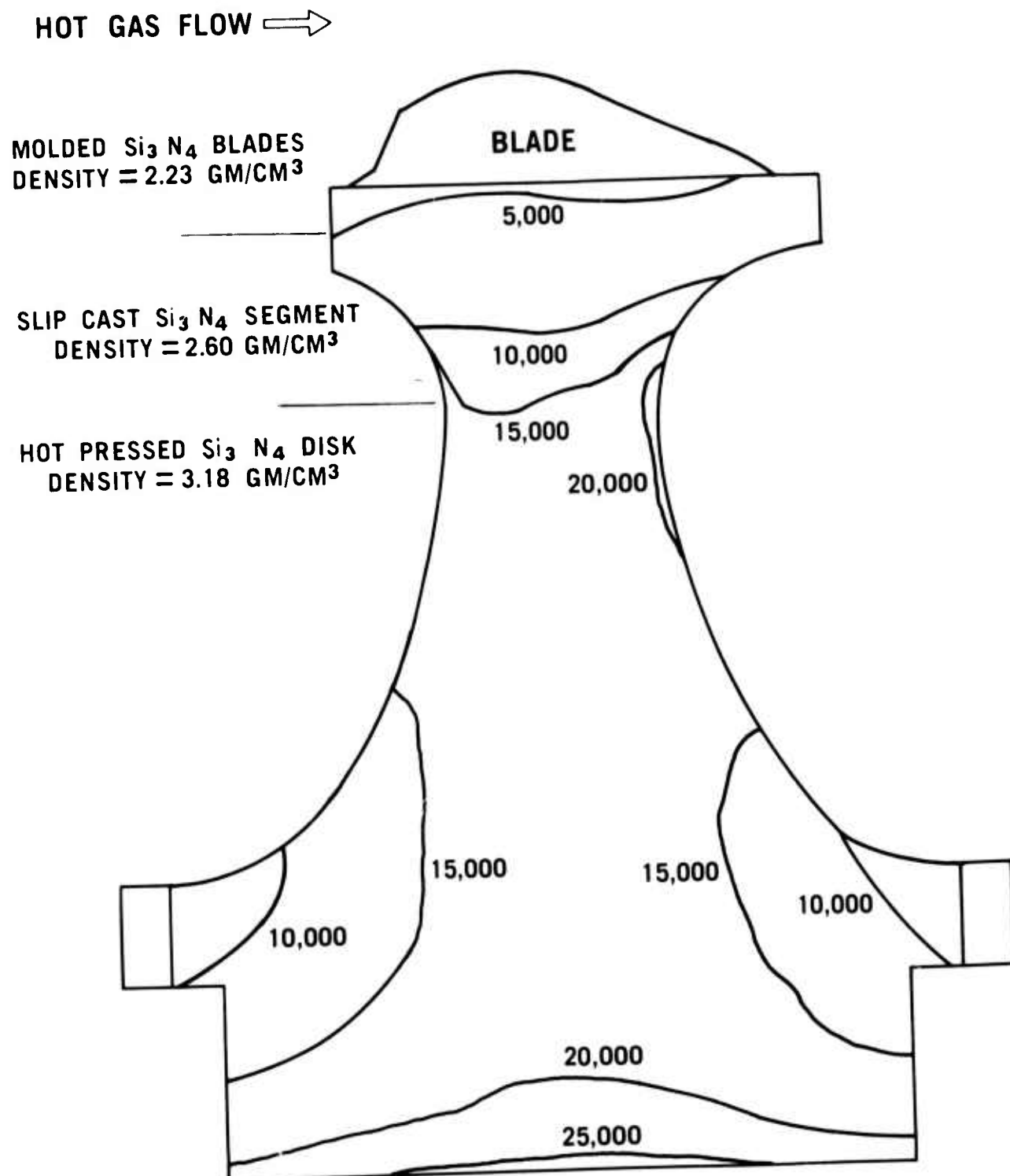


Figure 3.11 Maximum Principal Stresses (psi) in Second Stage Disk, 110%, Speed Centrifugal Loading, Triple-Density Design

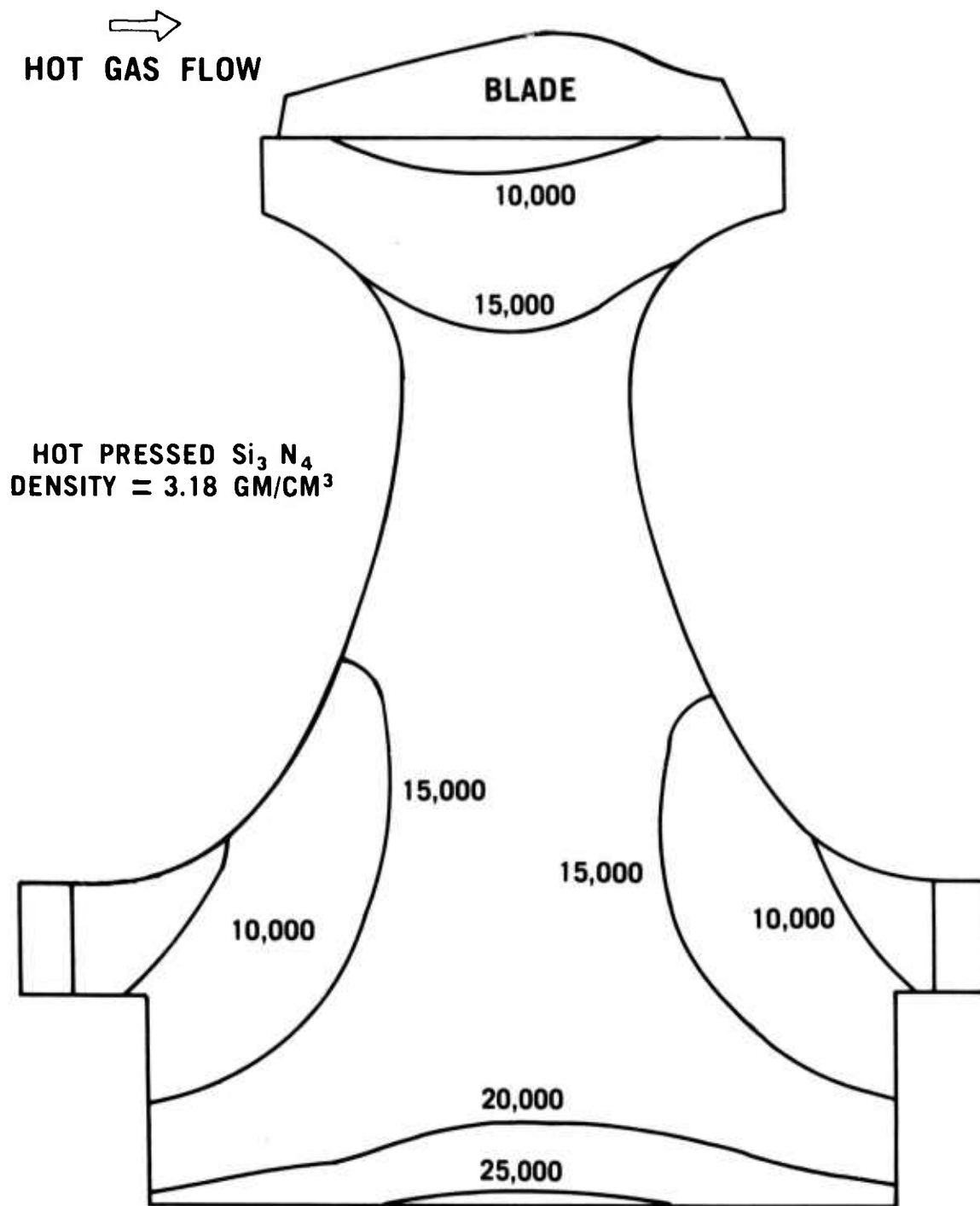


Figure 3.12 Maximum Principal Stresses (psi) in First Stage Disk, 110%, Speed Centrifugal Loading, Hot Pressed Si_3N_4 Disk and Blades

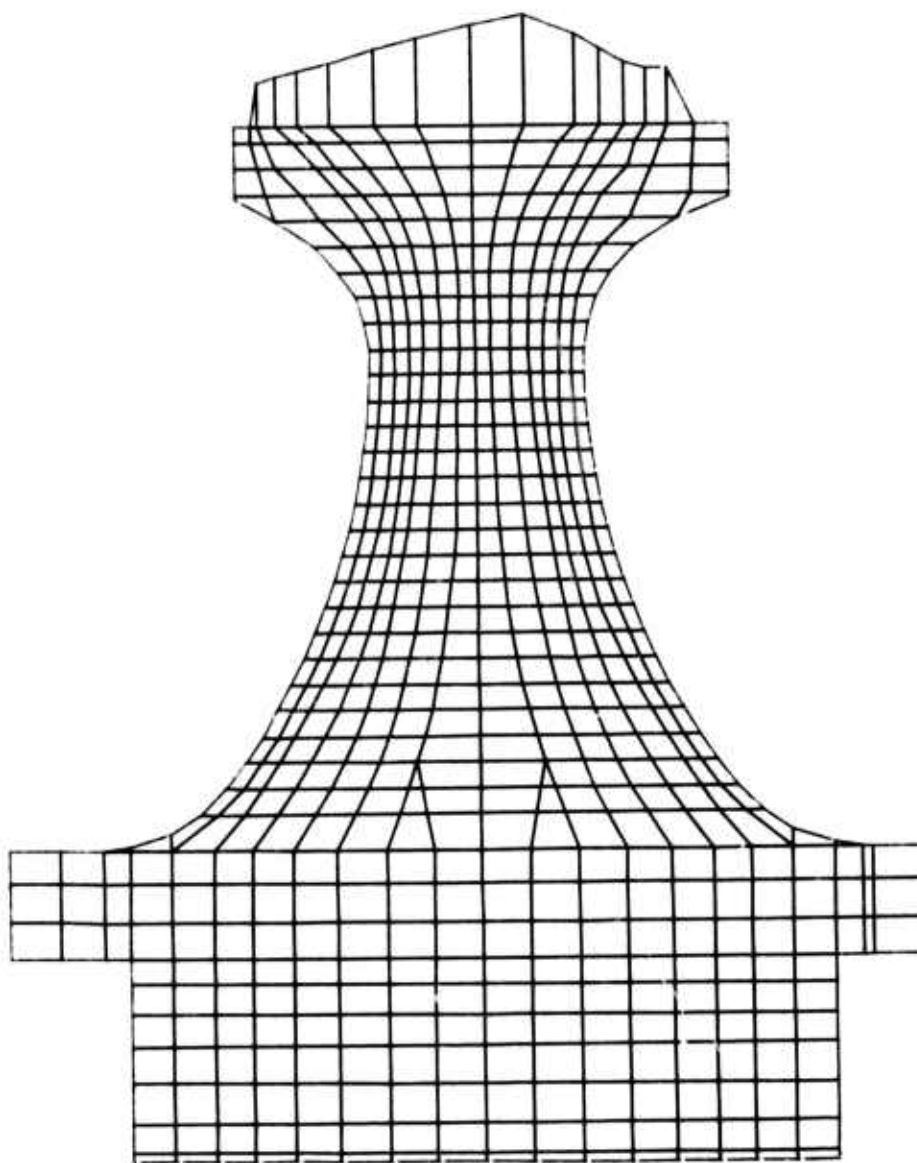


Figure 3.13 Finite Element Grid Used For Stress Determinations in First Stage Common Rotor Disk

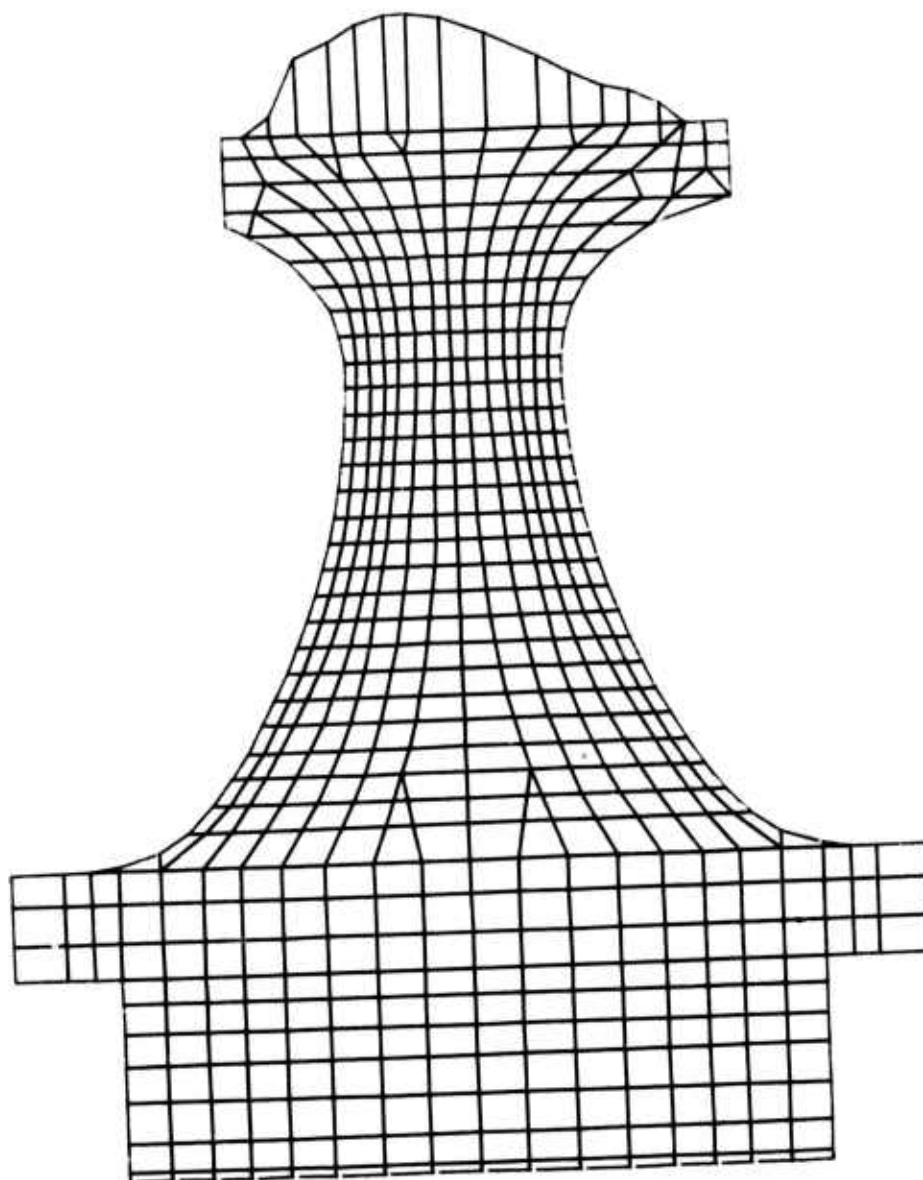


Figure 3.14 Finite Element Grid Used for Stress Determinations in Second Stage Common Rotor Disk

3.1.2 MATERIALS AND FABRICATION

Introduction

The major "in-house" effort continues to be applied to the fabrication of silicon nitride multi-density turbine rotors, especially in the development of assembly and joining techniques. Problem areas in the triple density approach, in which an intermediate density slip cast reinforcement ring is introduced between a lower density injection molded blade ring and a fully dense, hot pressed hub, have been identified. Improvements in blade fill restraint systems and hot press bonding techniques have caused a shifting of emphasis back to the duo-density concept in which only the blade ring and dense hub are combined to form the full rotor.

Spin pit testing of both assembled ceramic rotors and molded reaction-sintered Si_3N_4 blade rings, with correlation by nondestructive evaluation techniques, have identified a molding flaw problem. A study of molding parameters was initiated to improve the quality and consistency of molded blade rings.

An alternate fabrication method for producing ceramic rotors continues to be investigated, involving a modified investment casting technique for producing complex Si_3N_4 blade shapes.

Multi-Density Silicon Nitride

In the duo-density concept ^(4,5) the high strength of hot-pressed Si_3N_4 is utilized in the disk region where stresses are highest but temperatures are moderate and, therefore, creep problems are minimized. Reaction bonded Si_3N_4 , which can be readily formed into complex airfoil blade shapes by injection molding, is utilized for the blades which are exposed to the highest temperatures but the lowest stress levels.

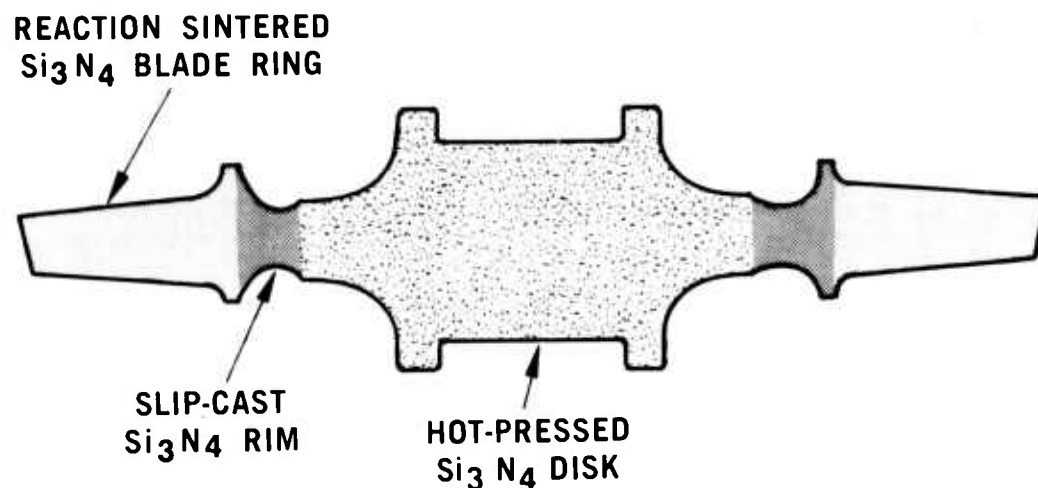
Work on the duo-density approach during this reporting period was directed forward further developing the graphite wedge system ⁽⁵⁾ as the fabrication technique for bonding the reaction-sintered Si_3N_4 blade ring and hot pressed hub together. The blade ring assembly was injection molded in one piece from silicon metal powder and subsequently nitrided to form Si_3N_4 having a density of 2.2 gm/cm^3 . Theoretically dense Si_3N_4 contoured hubs were fabricated by hot-pressing AME alpha Si_3N_4 powder with 2 to 5 w/o MgO added. The MgO is a densification aid which enables the alpha Si_3N_4 powder to be hot pressed to theoretical density. The bond surfaces of all component parts were machined to remove any oxide or reaction surface layers.

The major effort during the last reporting period was directed toward developing fabrication techniques for triple density rotors ⁽⁵⁾. The triple density turbine rotor consisted of an injection molded blade ring bonded to a section of higher density, higher strength slip cast reaction sintered Si_3N_4 as illustrated in Figure 3.15, which compares the duo and triple density concepts. It was believed that this thicker section would prevent deformation and/or fracture of the blade ring during hot press bonding. After many trials and variations, problems of fracture of the rim and inconsistent bonding persisted which resulted in a de-emphasis of this technique in favor of the duo-density concept. Several factors contributed to this decision and are summarized as follows:

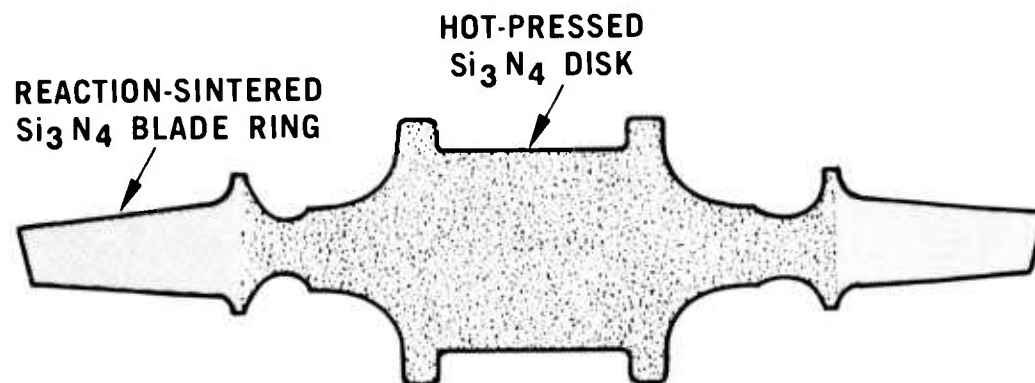
1. Stress analyses indicated that the strength of the present slipcast Si_3N_4 at the neck region of the hub is insufficient to withstand the stresses of top speed operation. On the other hand, in the duo-density rotor concept, the molded reaction sintered Si_3N_4 does not extend beyond the platform into the area where operating stresses exceed the strength of reaction sintered material.

2. Non-uniformity of deformation of the slipcast rim during hot-press bonding resulted in an inconsistent bond at the slipcast-hub interface.

3. Development of a removable blade fill material which made the duo-density rotor fabrication technique more attractive. Based on these factors, the triple density rotor was de-emphasized in favor of further development of the duo-density approach.



TRIPLE DENSITY TURBINE ROTOR



DUO-DENSITY TURBINE ROTOR

Figure 3.15 Duo-Density and Triple-Density Ceramic Rotor Concepts

With regards to bonding the blade ring to the hub, experience has shown that the entire blade rim must be supported during hot-press bonding. Work was started on injecting a low density fill of silicon metal into the blade cavities as the reinforcing media. It was thought that shrinkage during nitriding of the blade fill material would allow easy removal after hot-press bonding. However, it was found that the shrinkage of this blade fill caused it to pull away from the molded rim, thus giving no support to the rim. In order to better control this shrinkage of the silicon blade fill material during nitriding, it was found beneficial during this reporting period to use slipcast rather than injection molded silicon.

A double blade fill technique has been devised to support the blade ring which does enable removal after hot press bonding. The injection molded Si_3N_4 turbine rotor blade ring was first heavily coated with boron nitride. The blade cavities were filled with a "first fill" slipcast silicon, as shown in Figure 3.16, and nitrided. The "first fill" inserts are completely independent of one another as shown by the one partially removed insert. The "first fill" assembly was again coated with boron nitride and a "second fill" of slipcast silicon was used to encase the entire assembly. The assembly was again nitrided to convert the second blade fill to Si_3N_4 . The encased blade ring and the hot-pressed disks were separately machined to a slip fit, as shown in Figure 3.17, and assembled. The assembly was then placed into the hot-press bonding assembly, as shown in Figure 3.18. Graphfoil and boron nitride were used as barrier materials at all graphite- Si_3N_4 interfaces. The hot-press bonding assembly was designed to allow individual control and monitoring of the applied pressure on both the outside graphite wedge and inside hub component.

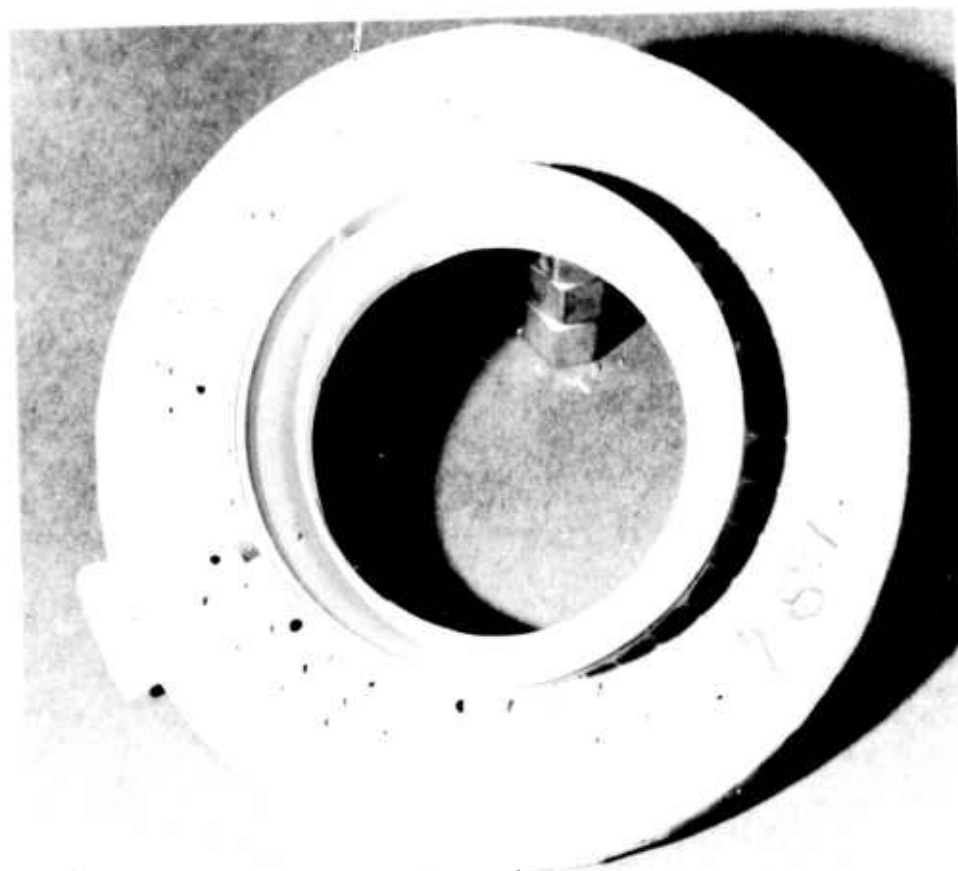


Figure 3.16 Molded Silicon Nitride Rotor Blade Ring Showing First Blade Fill



Figure 3.17 Duo-Density Silicon Nitride Rotor Assembled Prior to Press Bonding Showing Second Blade Fill

Several attempts to fabricate duo-density turbine rotors have been made using this technique. These have led to the following observations regarding duo-density hot press bonding:

1. Alignment of the assembly in the hot-press is critical to prevent distortion, which causes inconsistent bonding and fracture of the blade ring.
2. Encasement of the turbine blade airfoils in reaction sintered Si_3N_4 was notably more effective in preventing reaction to form SiC on the blade surfaces than previous techniques of only encasing the blades in boron nitride powder. This allowed the hot-press bonding temperature to be increased 100°C to 1750°C , which improved bonding without deterioration of the blades.
3. The blade fill can be removed and only occasionally does the first blade fill damage a blade. Further improvements in blade fill technology are anticipated which should eliminate any damage to individual blades.
4. A higher MgO content (5w/o) in the hot pressed disks enables a more even distribution of pressure during hot-press bonding due to the improved flow characteristics of the disk. In addition, the higher MgO content appears to increase magnesium diffusion across the bond interface, thus improving bonding. Smoother and more uniform surface finish of the disk has been achieved with the 5w/o MgO additive which has eliminated expensive and time-consuming contour machining of the disk.

5. Changes in the outer diameter of the rotor platform during press bonding only varied from 0.10 to 0.30 percent, indicating the Si_3N_4 blade fill effectively restrained the blade rim. Although there appears to be excellent bonding between the hot-pressed hub and reaction sintered blade ring, as shown in Figure 3.19, two cracking problems persist. These are identified as axial and circumferential cracks which are believed related to mismatched hub and wedge pressures during hot-press bonding. Adjustments to optimize these pressure relationships will require further experimentation. The higher hot-press bonding temperature may be helpful in permitting lower bonding pressures without sacrificing bond integrity.

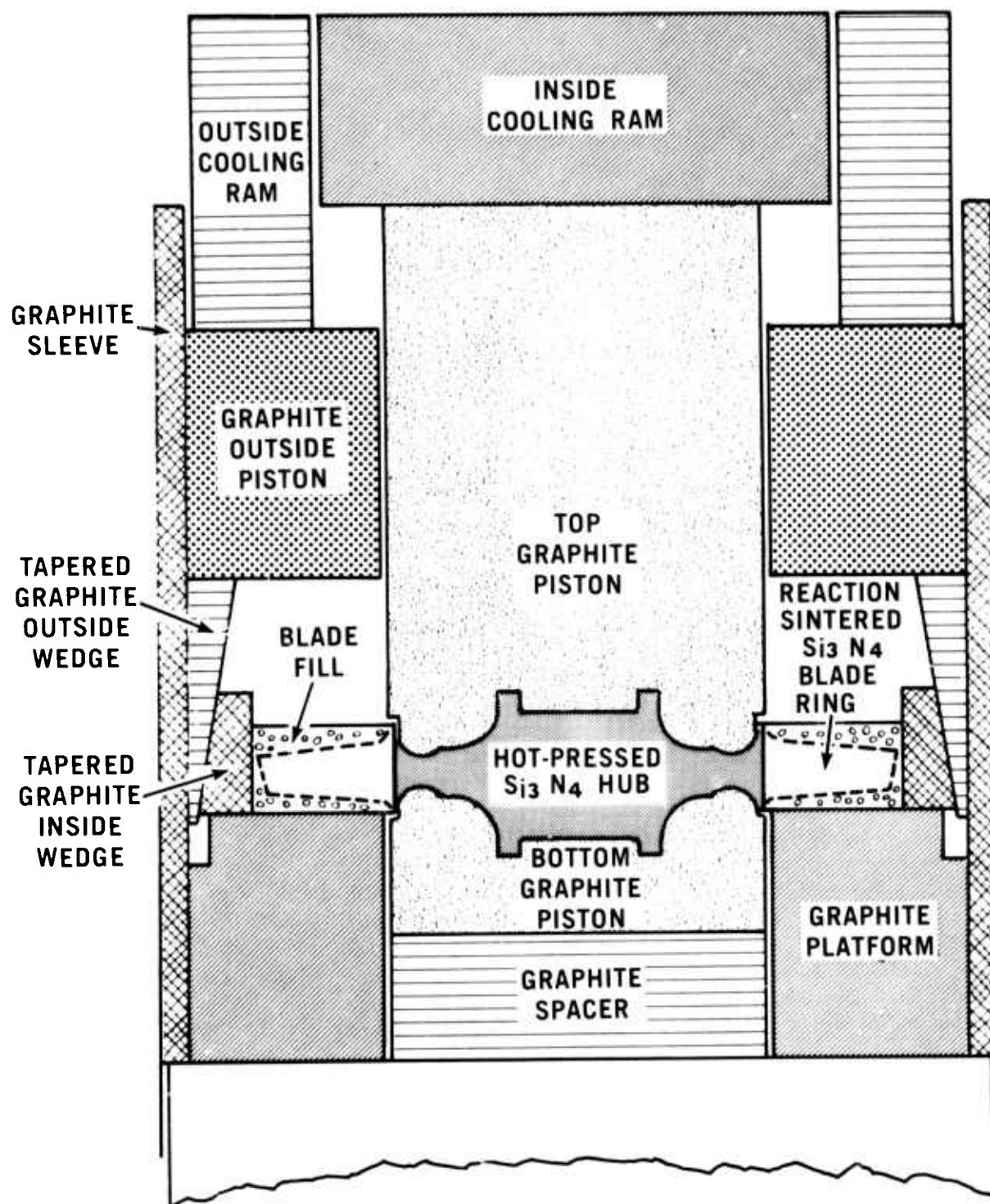
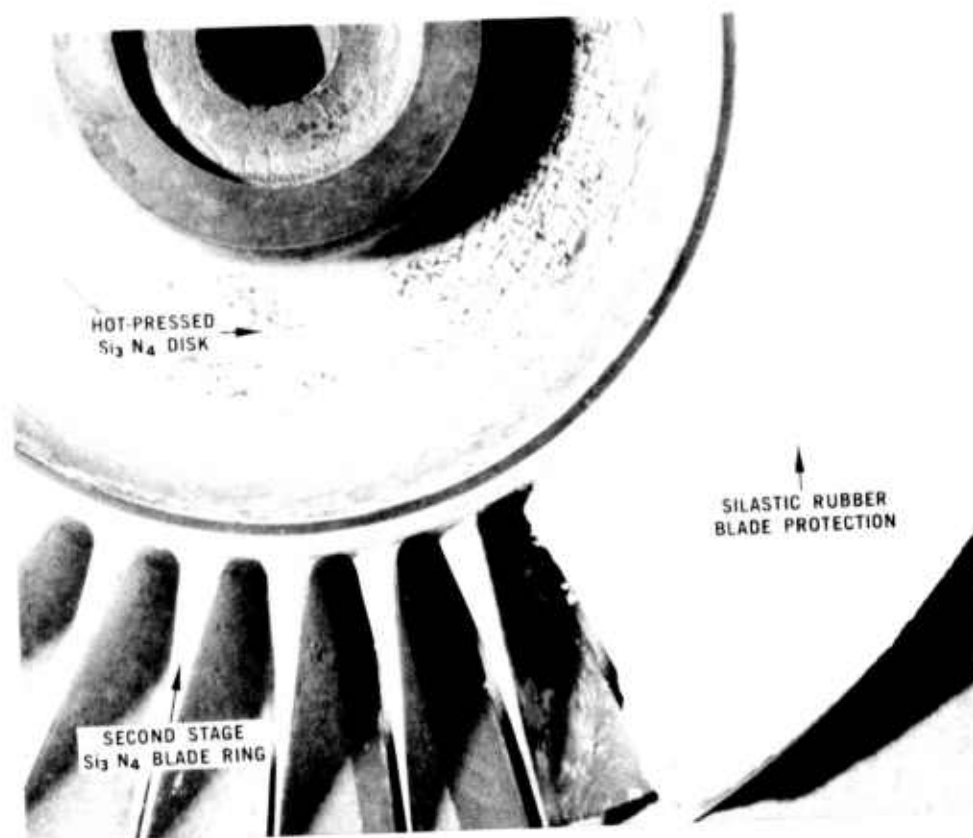


Figure 3.18 Hot-Press Bonding Assembly

Future work will continue to be directed toward optimizing alignment and hot-pressing parameters to improve the bond between the molded and hot-pressed materials.



HOT-PRESS BONDED Si₃N₄ TURBINE ROTOR SHOWING BOND AREA.

Figure 3.19 Press Bonded Silicon Nitride Rotor Showing Bond

Molding of Silicon Nitride Blade Rings

During this reporting period major efforts have been made to improve the quality of injection molded silicon nitride turbine rotor blade rings. Spin testing of rotor rings has revealed that blade failures have resulted from crack initiation at regions of molding flaws. Molding flaws observed in rotor blade rings are entrapped gas voids, shrinkage cracks, and fold or knit lines.

Examples of commonly observed flaws in rotor blade rings are shown in Figures 3.20 and 3.21. Both entrapped gas voids and shrinkage voids appear as a white depression at the fracture surface. Shrinkage cracks are caused by lack of proper temperature control. Fold and knit lines occur when material which has been injected into the die cavity as a liquid solidifies from outer surfaces toward the center. If solidification is not properly controlled, the resulting shrinkage of the cooling material results in a thin interface referred to as a knit line. A knit line can also result when materials is improperly gated into the tool or injected at too low a temperature. Material flowing improperly in the die will cool on the leading edge of the flowing material and form a skin of partially solidified material. When the tool is completely filled, the areas where a skin has been prematurely formed will produce an unbonded interface.

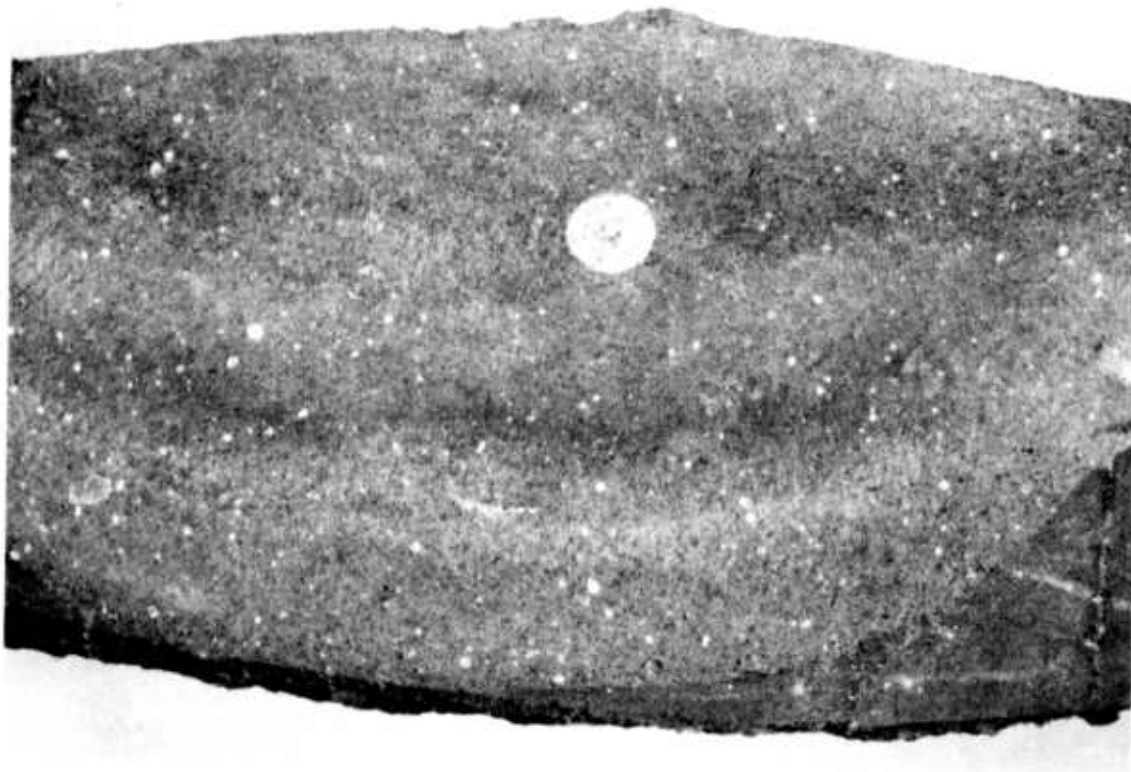


Figure 3.20 Fracture Surface of Rotor Ring Showing Typical Flaw Caused by Entrapped Gas During Molding

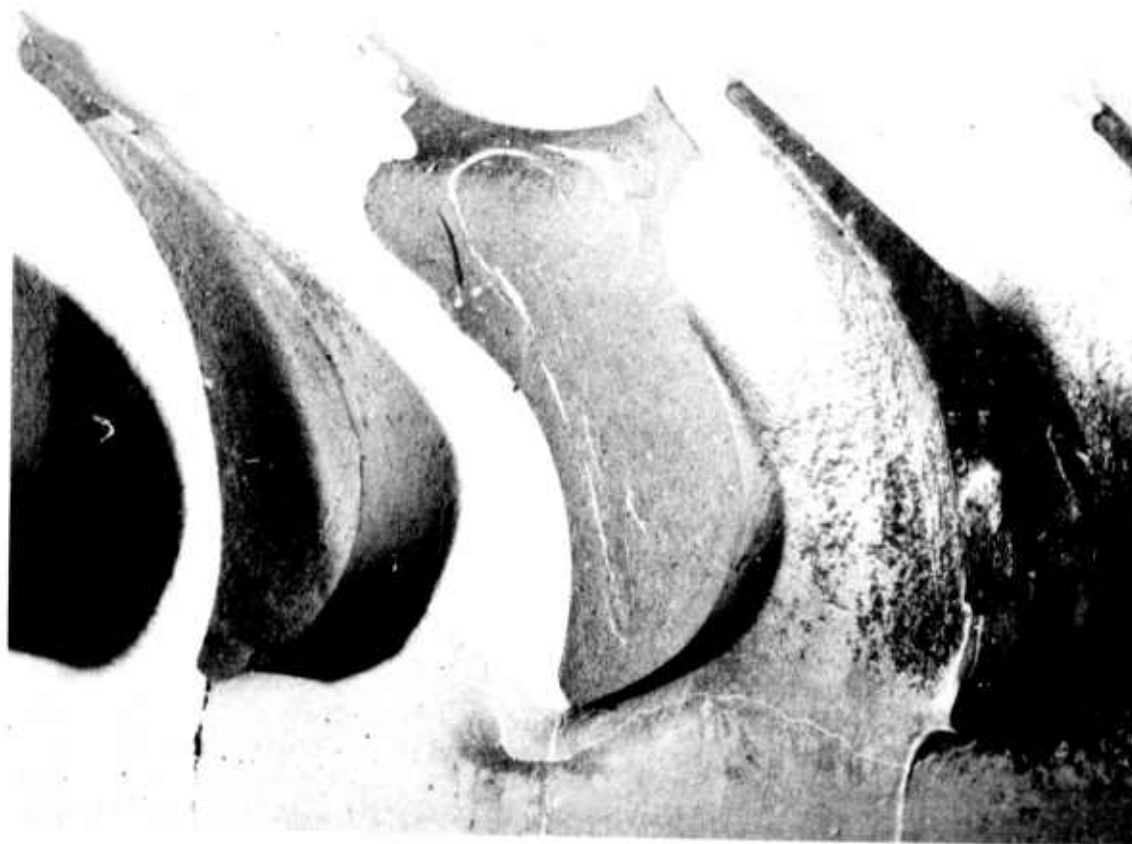


Figure 3.21 Fracture Surface at Base of Rotor Blade Showing Folds or Knit Lines

Previous molding experiments have demonstrated the feasibility of eliminating molding flaws through variations of molding and processing parameters. Variation in power and location of heaters in the first and second stage rotor tools were made in order to improve temperature control during molding. Lower power heaters located further from the center of the tool were found to give more uniform air-foil insert temperatures with less temperature overshoot. A cooling coil was also added to remove heat during the cool mode of temperature control. Better temperature uniformity enabled optimization of tool temperature to achieve blade rings free of molding flaws.

Additional control has also been added to material preparation. A timed procedure is now followed during material mixing and shelf life limits have been established for molding material.

Material used in rotor fabrication is now pre-extruded through the barrel of the molding machine. This additional high shear mixing gives the material increased flow properties and improved homogeneity. All rotor molding now uses a timed cycle for injection and hold times.

A quality assurance program has been completed and has resulted in injection molded blade rings free of detectable flaws. The quality assurance program first standardized all parameters, with the exception of temperature, at optimum values. Temperature was then systematically varied over a range of tool and material temperatures and six rotors were molded at each condition. Table 3.1 summarizes the tool and material temperatures used.

After molding, each rotor was inspected and ranked as good, fair, or poor on the basis of visual quality. To receive a good rating, a rotor was required to be entirely free of visible defects. A fair rotor contained a small number of tolerable defects, and a poor rotor was not useable.

TABLE 3.1

EFFECT OF TOOL AND MATERIAL
TEMPERATURE ON QUALITY OF
MOLDED ROTOR RINGS

Percent Yield of Injection Molded
Rotors Suitable for Engine Use

Material Temperature °F	230	100%	50%	0%	0%
	215	100%	100%	100%	66%
	200	92%	75%	66%	33%
		100	110	120	130
		Tool Temperature °F			

Upon completion of visual ranking all rotors were x-rayed in their as-molded condition to determine the extent of sub-surface flaws. The use of x-ray radiography for determining the quality of as-molded components is discussed in more detail in Section 5.3.3 of this report. The x-ray was optimized for platform rim and vane sections of the rotor and each section was x-rayed separately. Each element of the rotor was rated separately and ranked, using the same scale employed in visual inspection, and the results tabulated with visual ratings in Table 3.1. It was found that in a range of material temperature from 200-215°F and tool temperature of 100-110°F, rotors could be molded with no defects detectable by x-ray. Figures 3.22 and 3.23 show respectively the radiographs of a typical defect-free rotor and a rotor containing defects.

Georgia Institute of Technology Precision Cast Si₃N₄ Program

It has been reported ⁽⁵⁾ that a program had been initiated at the Georgia Institute of Technology Experiment Station directed at the development of investment casting techniques for forming precision cast ceramic shapes. Preliminary experiments, initially conducted on test bars and simple shapes, have now been extended to complex shapes, including individual rotor airfoils.

Figure 3.24 is a photograph of samples at various stages in the fabrication of a single rotor blade in reaction sintered silicon nitride. On the far left is an airfoil blade and blade root of the early "clamped wheel" ⁽²⁾ design, molded in a wax composition commonly used for investment casting patterns. At the upper right of the wax blade is a fused silica shell mold, made by dipping and stucco techniques similar to those used in other "lost wax" investment casting methods. The part shown was made from one of a family of experimental compositions being developed to control porosity, strength, surface finish, and ability to be easily removed after the cast part within the mold is fully reaction sintered to silicon nitride. In the top center of Figure 3.24 is such a silicon

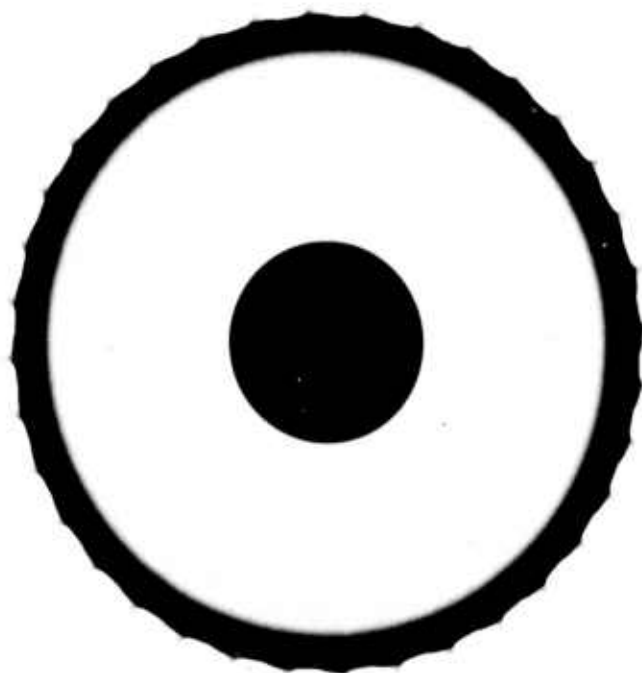


Figure 3.22 X-Ray Radiograph Showing As-Molded Rotor Ring With No Apparent Flaws

nitride blade, duplicating the molded wax, after it has been removed from a silica shell mold following the nitriding heat treatment. Remnants of a shell mold removed from a nitrided blade are shown to the right of and below the silicon nitride blade. This process has been further extended to segments of a rotor having three or more blades.



Figure 3.23 X-Ray Radiograph Showing As-Molded Rotor Ring With a Major Void in Disk at 2:00 O'Clock and Indications of Low Density Areas

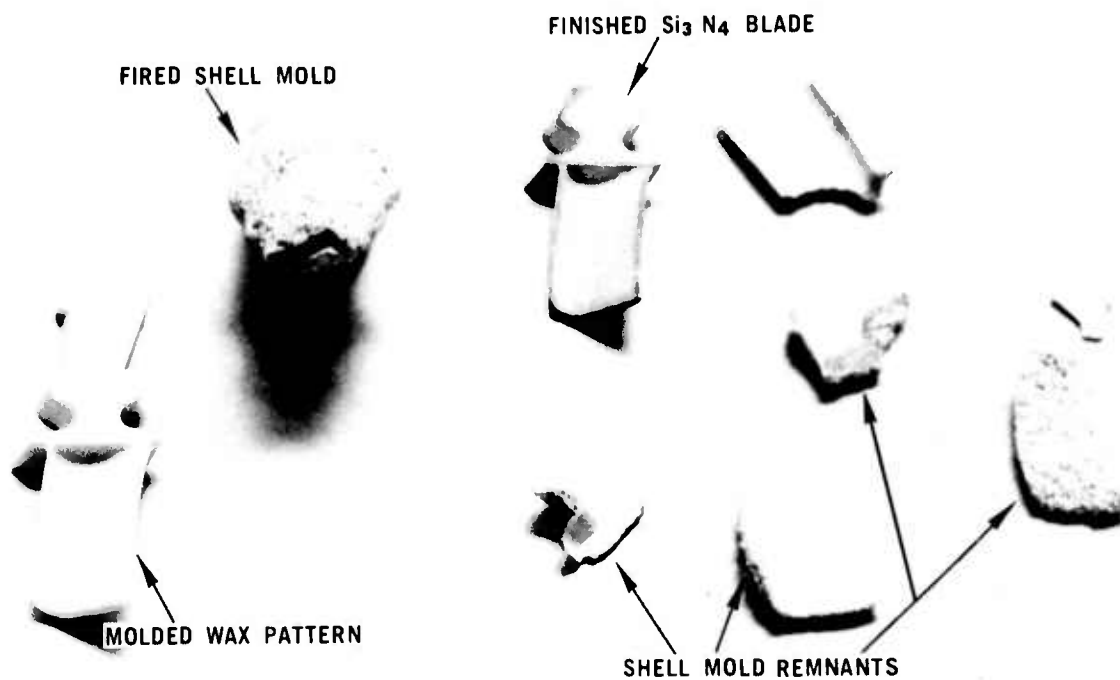


Figure 3.24 Rotor Blade Fabrication Steps

3.1.3 TESTING

Introduction

As noted in the last report (5), much emphasis has been placed on rotor blade testing. Both cold spin pit tests and thermal shock tests have been conducted. The spin pit test procedure has been improved with a new photographic triggering mechanism and revised blade mounting technique. The thermal shock tests have been repeated with the flame impingement at the blade root as compared to the previous tests with flame impingement at mid-span. Two engine thermal conditions were simulated by these tests.

Cold Spin Testing

The details of the spin pit equipment used for testing ceramic turbine rotors have been shown in a previous report (2). All ceramic rotors are spun at room temperature in a partial vacuum at gradually increasing speed until failure occurs.

A new photographic triggering device was added during this reporting period which allows a blade failure to occur without causing damage to the remaining blades on the ring. Figures 3.25 and 3.26 show the new blade failure photographic ring. This ring is made of 18 windings of 0.003 inch diameter copper wire wound around a piece of 1.5 inch wide masking tape, reinforced by a cardboard tube. This assembly is inexpensive, easy to fabricate, and is often reuseable after a blade failure, since a single blade will pass cleanly through the trigger without leaving residual fragments which may damage the remaining blades.

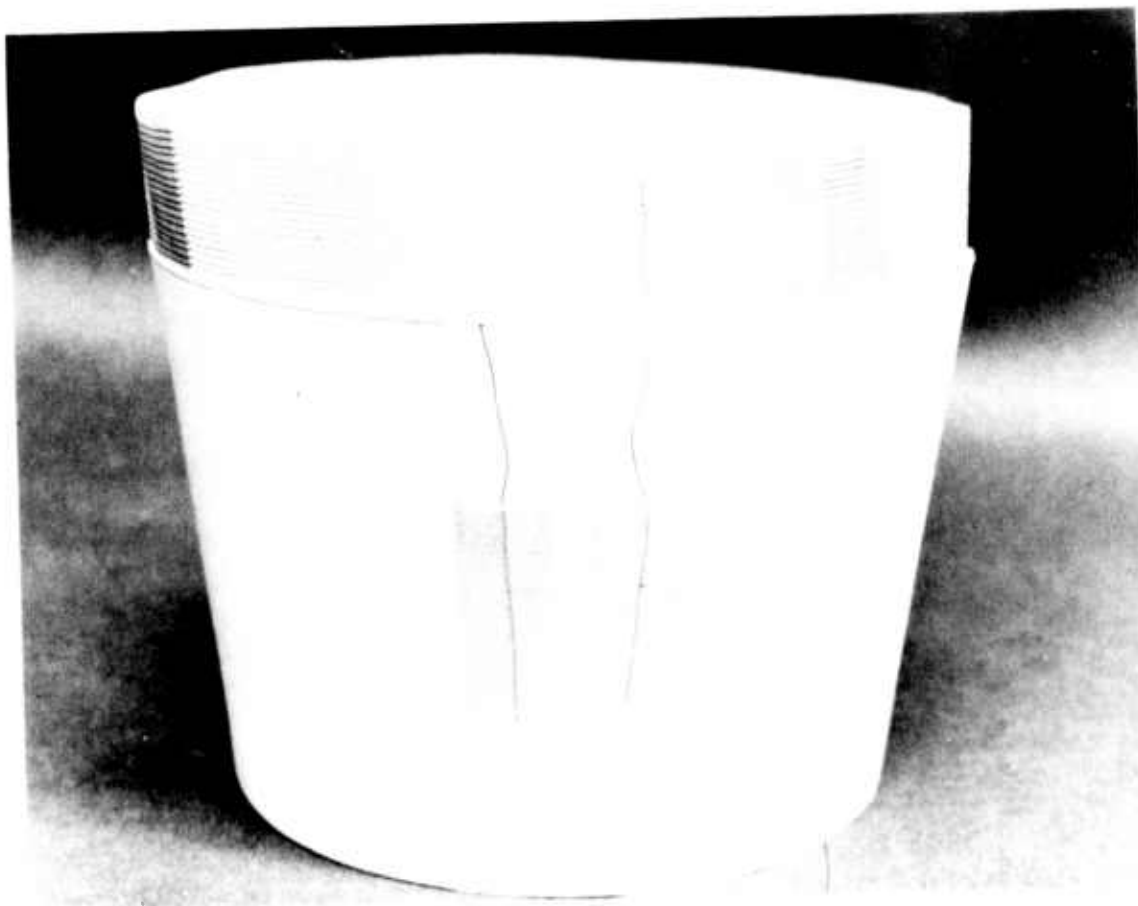


Figure 3.25 Triggering Device For Photography of Bursts During Spin Testing

Experience in using this device has shown it to be effective up to approximately 38,000 rpm. At speeds greater than this, a single failed blade is not able to clear the blade ring without coming in contact with the remaining blades, thereby creating sufficient debris to remove all other blades.

In order to determine the blade strength of various injection molded materials and the effect of different firing cycles, some spin tests were conducted with blade rings which were sectioned into four segments. Each segment consisted of 3 to 4 complete blades. Figure 3.27 shows a metal test hub and a Si_3N_4 blade ring segment, and Figure 3.28 illustrates a complete blade ring ready for bonding to the test hub. The segments were bonded to the metal hub with an epoxy adhesive.

Blade rings used for spin tests were inspected and discarded for cracks or nicks on a blade surface, visible holes or pits, areas indicating low density blade fill, and voids as shown by x-ray of the blade platform or blade interior. First stage blades were spin tested as segments bonded to a metal hub as shown in Figure 3.27. Failure speeds for the Type C ⁽⁵⁾ blades ranged from 46,230 rpm or 72% of design speed to 61,900 rpm or 96% of design speed. Figure 3.29 shows the first stage blade failure at 61,900 rpm.

Second stage rotor spin testing was conducted using various grades of molded silicon nitride materials. Blade rings were made using silicon metal powder starting material of purity levels designated Type A, and Type C ⁽⁵⁾, as were two modifications reflecting process improvements ⁽⁵⁾. The first process improvement is the use of a 40 μ grade of Type C purity silicon, incorporating 1% Fe_2O_3 as a nitriding aid. The further modification, referred to as Type C-M material, was to nitride the 40 μ material containing 1% Fe_2O_3 in a mixture of hydrogen and nitrogen ⁽⁵⁾. Comparative spin tests were conducted to determine the best material.



Figure 3.26 Rotor Placement Within The Photographic Triggering Device

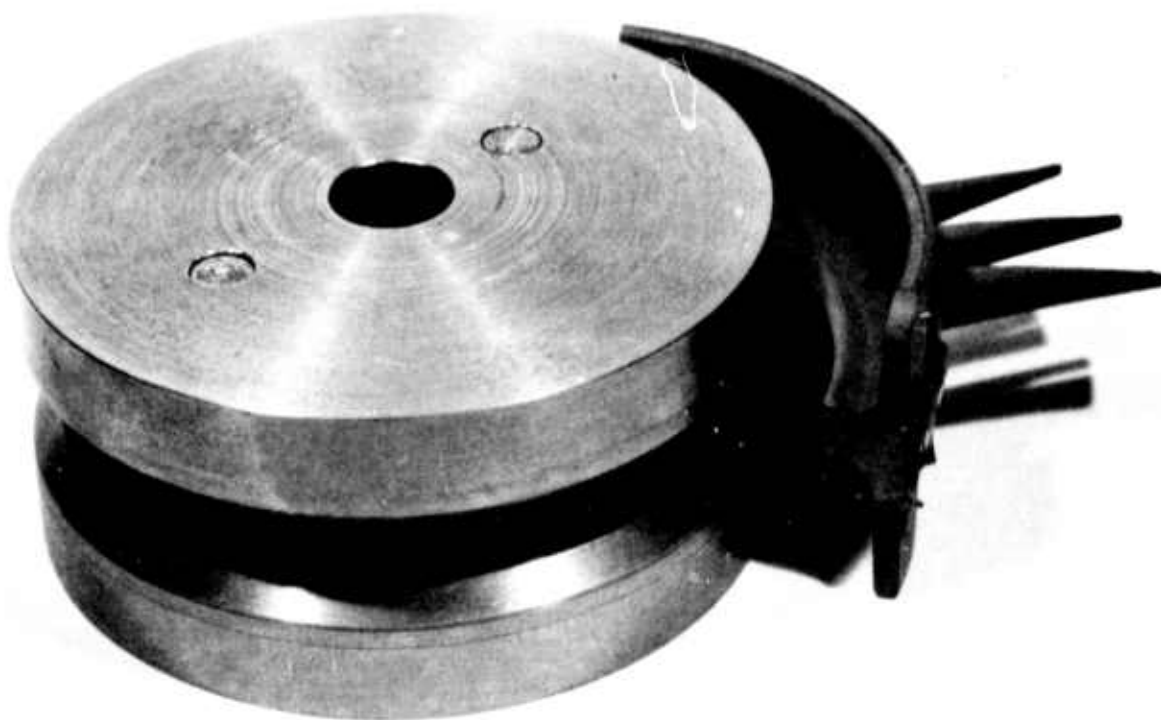


Figure 3.27 A Segment of a Molded Silicon Nitride Rotor Blade Ring and the Metal Test Hub

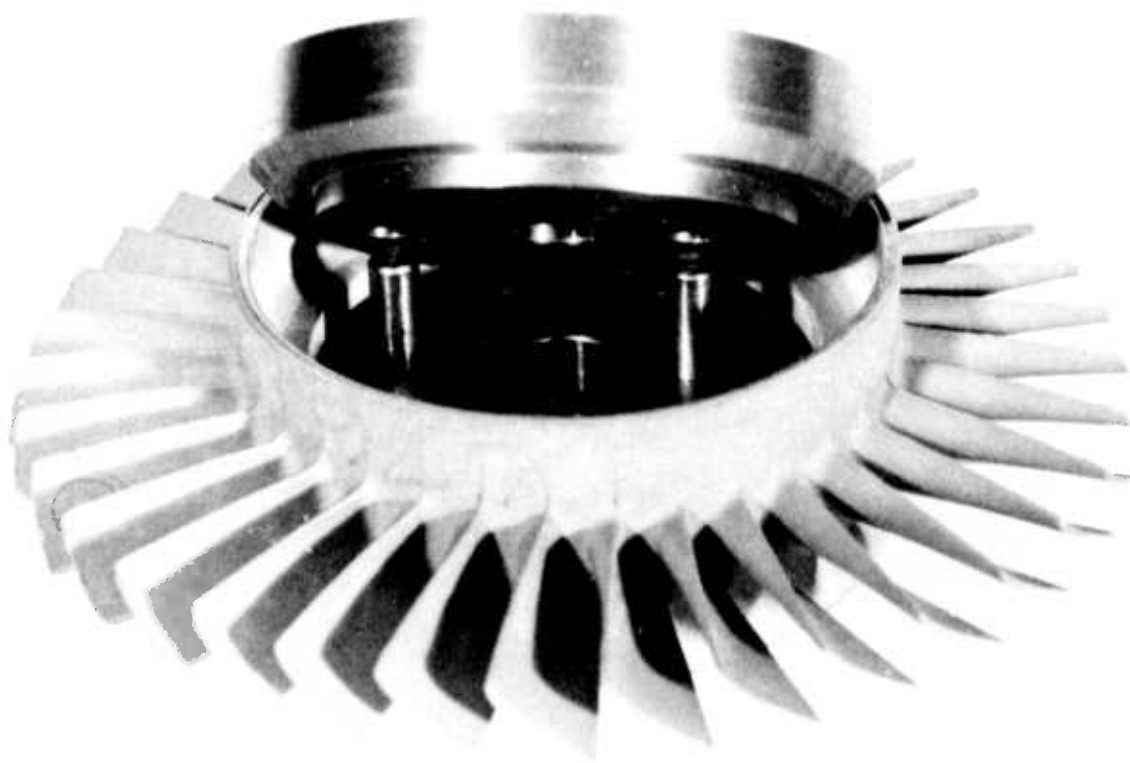


Figure 3.28 A Complete Molded Silicon Nitride Rotor Blade Ring Ready For Bonding to the Metal Test Hub

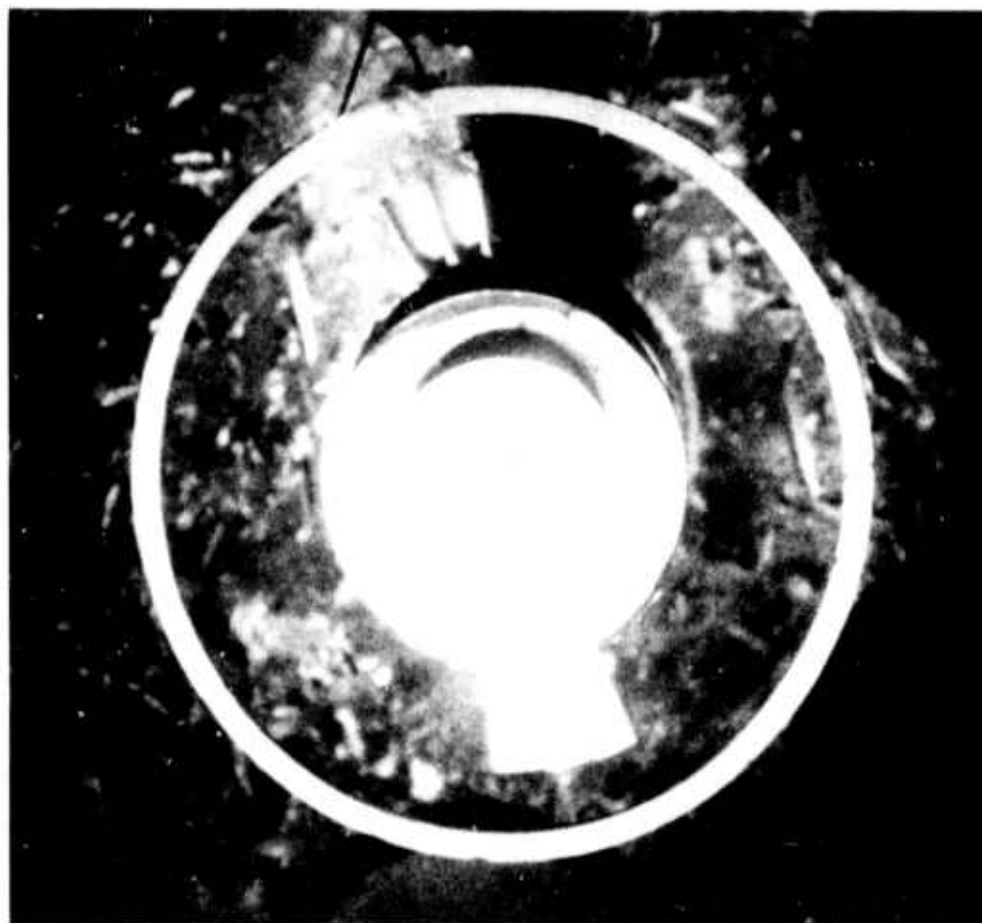


Figure 3.29 First Stage Rotor Blade Segments at Instant of Failure at 61,900 rpm

Failure speeds for Type A material ranged from 18,090 rpm or 35% of design speed to 31,020 rpm or 48% design speed. Failure speeds for the Type C material nitrided in the hydrogen-nitrogen mixture ranged from 32,980 rpm or 51% of design speed to 45,310 rpm or 70% of design speed. The Type C-M blade rings failed at speeds ranging from 30,160 rpm or 48% of design speed to 56,840 rpm or 88% of design speed. Figure 3.30 shows the second stage blade ring failure at 56,840 rpm.

The test data has indicated that the Type C-M material exhibited the highest speed potential. Because of the large scatter in failure speeds, a statistical analysis of rotor blade failures was carried out.

Probability Analysis of Cold Spin Testing Results

The purpose of this effort was to statistically analyze the turbine rotor blade spin test results in order to determine the distribution of failure speeds, characteristic speed, and Weibull modulus, (m) of the blade for different materials. The characteristic speed is the speed at which 63.2 percent of the blades will have failed.

The data for this analysis is shown in Table 3.2, and the test method is discussed in detail in the last section of this report. Segments of test rotors with

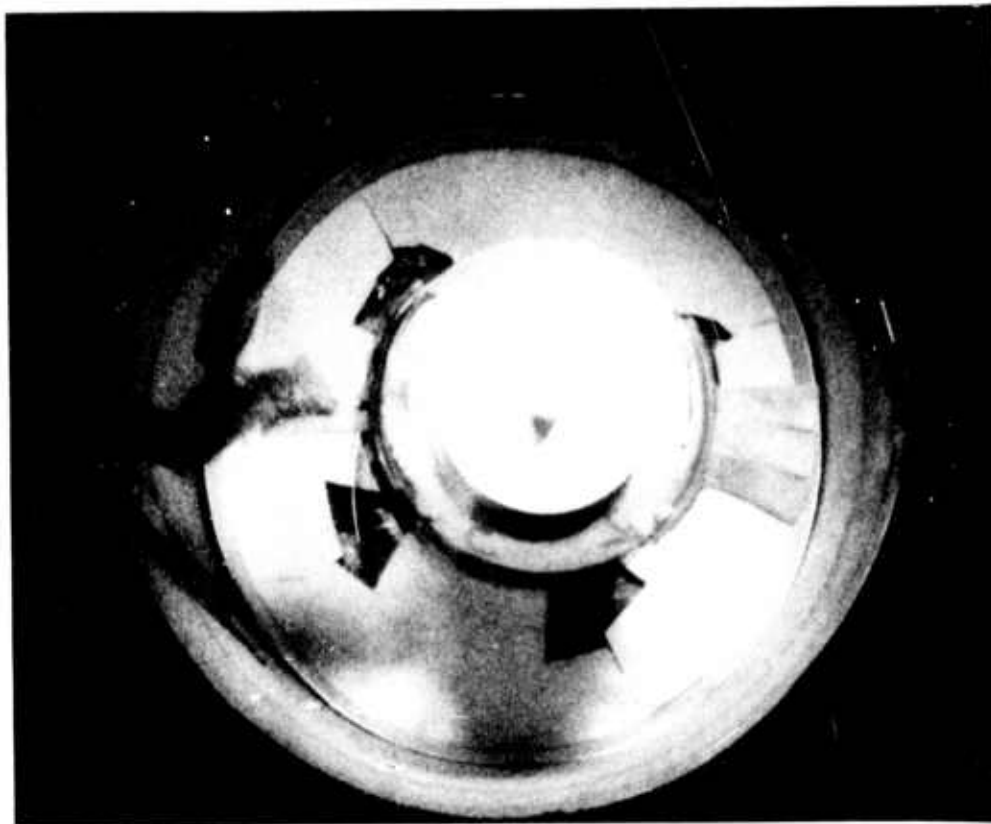


Figure 3.30 Second Stage Rotor Blade Segments at Instant of Failure at 56,840 rpm

TABLE 3.2
TEST DATA
SECOND STAGE ROTOR BLADES

<u>Material</u>	<u>Test Group Size</u>	<u>Failure Speed R.P.M.</u>
Type C	12	32980
	9	37770
	12	43850
	6	45310
Type C-M	6	27320
	6	32220
	6	33100
	6	34370
	5	36730
	3	38280
	6	43160
	6	45870
	6	56840

varying numbers of blades were spun at increasing speed until the first blade failed, destroying the rest of the blades. This test determined the weakest blade in each test group. Spin test results where something other than the blades failed, e.g., the epoxy bond or the disk, were not considered in this analysis.

Two blade materials were analyzed. These were made from Type C ⁽⁵⁾ purity silicon metal which was nitrided in a mixture of hydrogen and nitrogen, and a Type C purity material (C-M) modified to a particle size distribution of -40 microns, nitrided in a mixture of hydrogen and nitrogen with 1% Fe₂O₃ added as a nitriding aid. The Type C material sample was 50 blades, with nine failures. The Type C-M material sample was thirty nine blades with four failures.

Two methods were used to determine the failure distribution of the blades. The first method was the use of order statistics with the Weibull distribution which utilizes the suspended test items to adjust the observed failure distribution to obtain the population failure distribution ⁽⁸⁾. The second method is the use of extreme value statistics to determine the parent population failure distribution from the first failure with unequal size samples ⁽⁹⁾.

The first method requires the assumption that the suspended items are uniformly distributed. The method of extreme values, which does not require uniform distribution, may therefore be more generally applicable.

The second method, which uses $1 - k/(n+1)$ as the estimate of the reliability of the k^{th} item, was modified to use an unbiased estimator, one minus the k^{th} median rank for the reliability ⁽¹⁰⁾. All of the data is presented as percent failed and is plotted on Weibull probability paper. The results of the use of the first method are shown in Figures 3.31 and 3.32 with the 90 percent confidence bands. The results of the use of the second method are shown in Figures 3.33 and 3.34. These graphs represent the failure distributions for a single blade. The probability of failure of a complete blade ring of thirty-six blades, F_r , can be calculated from the failure probability of the single blades, F_b , by:

$$F_r = 1 - (1 - F_b)^{36}$$

The plot of the distribution for the complete rings is shown on Figures 3.31 and 3.32. The characteristic speeds for complete blade rings made from the Type C-M and the Type C materials are 27995 and 34549 rpm, respectively.

An examination of the plots will show that the failure distributions for both materials by either method are very close and statistical tests should be used to determine if a significant difference exists between them. It should also be realized that the limited test data will produce considerable uncertainty in the characterization of the materials. Some experience with graphites and aluminas ⁽¹¹⁾ has indicated that 40 or more samples are necessary to determine the Weibull material constants m and σ_μ .

Future spin testing procedures will be modified to maximize the failure data points and minimize the suspensions. The segments of blades will be equally spaced with three or four per hub. One blade will be on each segment, so that each blade should fail without destroying the other blades on the hub. The hub can then be re-balanced and re-spun to test each remaining blade. Using the present testing procedure, all the blades were destroyed and only one failure point was gathered per test.

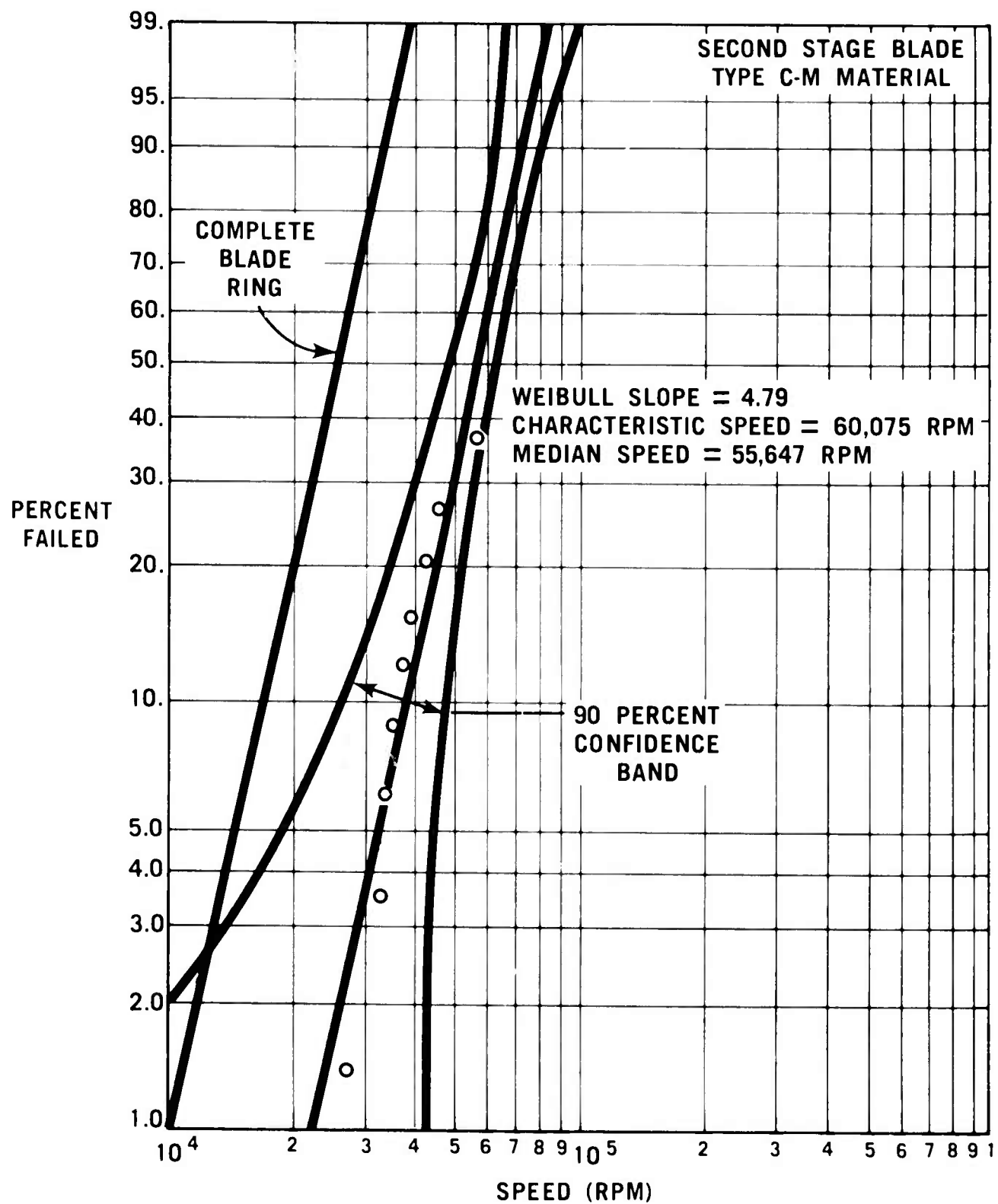


Figure 3.31 Failure Distribution of Single Blades and Complete Rings on Type C-M Silicon Nitride

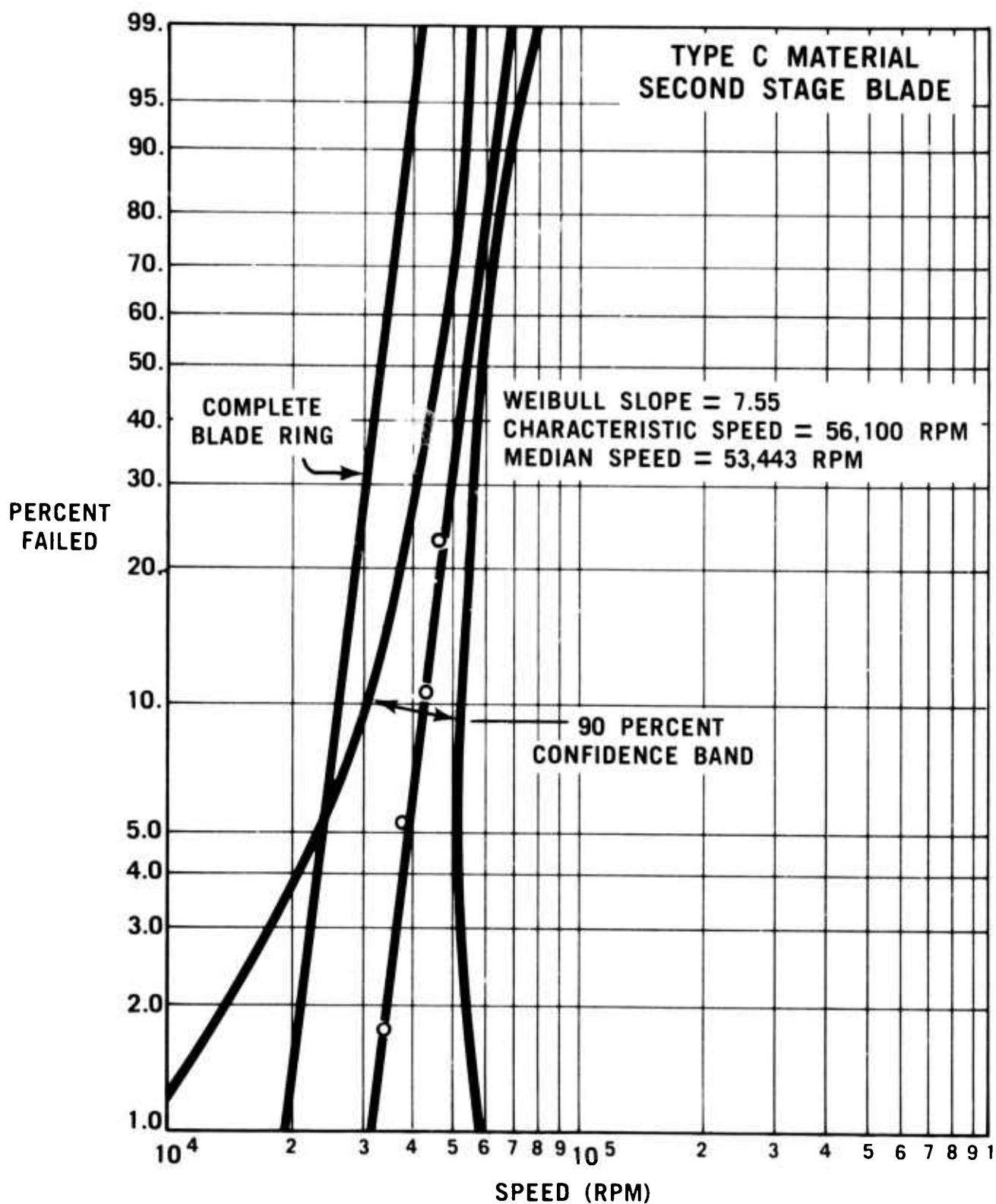


Figure 5.32 Failure Distribution of Single Blades and Complete Rings for Type C Silicon Nitride

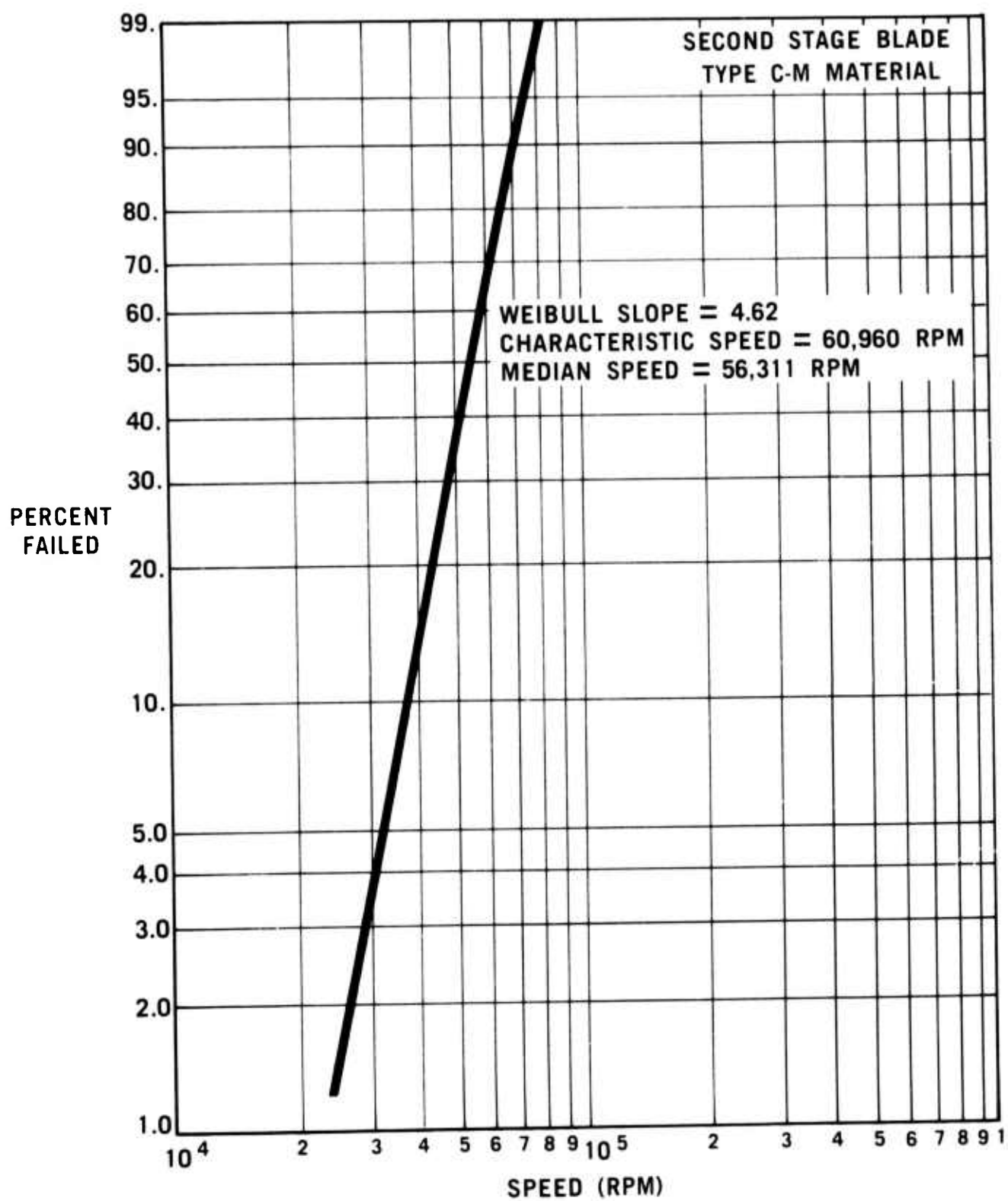


Figure 3.33 Failure Distribution of Single Blades for Type C-M Silicon Nitride

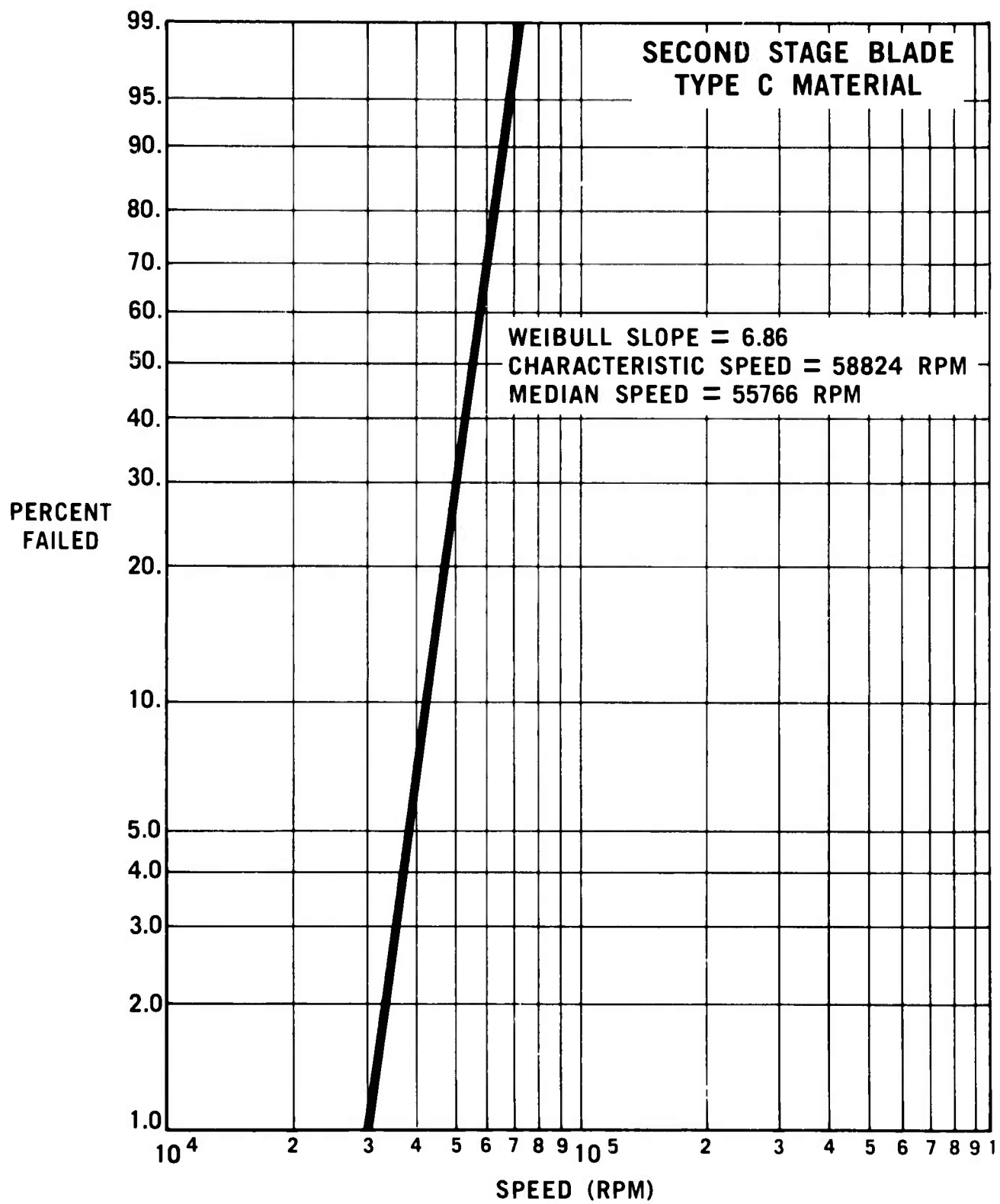


Figure 3.34 Failure Distribution of Single Blades for Type C Silicon Nitride

Thermal Shock Testing of Rotors

The first and second stage rotor blades are subject to thermal shock in engine and turbine rotor test rig operation, caused by rapid heating and cooling of the blades during startup and shutdown. This heating and cooling causes large thermal gradients which place the hottest sections of the blade in compression and the coolest sections in tension. Previous testing to assess the thermal shock resistance of the rotor blades was presented in the last report (5). Those tests were run on the Thermal Shock Test Rig with the flame directed at the mid-span of the blade.

During this reporting period, additional tests were performed with the flame directed at the blade one-quarter inch above the platform. Due to the thermal inertial of the hub as compared to the blade and the high transient heating and cooling of the blade, the fillet area is the location of maximum thermal stress.

The test apparatus and position of the flame with respect to the rotor blade is illustrated in Figure 3.35. The point of impingement was the leading edge, with the flame washing the entire fillet area. The flame primarily followed the concave blade surface, raising this surface to a higher temperature than the convex side. The overall operation of the Thermal Shock Test Rig has been discussed in previous reports (3,4). The blade rings selected for this test were injection molded, reaction bonded silicon nitride, with a density of 2.2 gm/cm^3 . The molded blade rings were bonded onto slip cast rings of 2.6 gm/cm^3 density. The slip cast ring was used to simulate the heat sink effect of the rotor disks.

Four first stage and four second stage rotor blade rings were tested. The blades were first tested on a cycle to simulate the transient between light-off and idle, requiring a blade temperature of 1930°F . In order to reach this temperature in the fillet portion of the blade, a rig flame temperature of 2800°F was required. Figures 3.36 and 3.37 show the thermal response of the blades for the heating cycle portion of this test. Figure 3.36 indicates the thermal response at three locations at the mid-chord point on the concave



Figure 3.35 Thermal Shock Testing of Blade Fillet Area of Molded Silicon Nitride Rotor Blade Rings

or hotter side of the blade. A very sharp temperature gradient was observed between the blade and the fillet. The blade temperature data marked "hot" in Figure 3.36 was measured at the hottest spot mid-chord on the blade. The curve marked "cool" was plotted from temperature measurements at the same mid-chord location in the fillet radius as close as possible to the line of demarcation of the sharp gradient. The temperature of the platform of the rotor blade ring was measured at a point in line with the other two. This data points out the severity of this thermal gradient during the transient simulation.

The sharp gradient noted on the concave side was not nearly as pronounced on the convex side. Temperature measurements of this side, taken at the same relative locations as noted for Figure 3.36, are shown in Figure 3.37. These temperature profiles confirm the visual observations of a less severe thermal gradient.

The eight blade rings tested at this 1930°F condition were not damaged after 2462 cycles. The same test rig conditions were used as reported previously ⁽⁵⁾, namely 130 C.F.H. of cooling air and cycle time of 45 seconds.

A second test was conducted using fresh blades from the same blade rings. The second test was a more severe cycle with a maximum blade temperature of 2300°F obtained by increasing the flame temperature of the burners. A sharp thermal gradient at the fillet was again produced. The thermal response curves for the hot side of the blade are shown in Figure 3.38. Under these conditions, some blade cracking occurred. One first stage blade failed at the fillet after 662 cycles, another cracked at mid-span after 1260 cycles, and a third failed at mid-span after 2028 cycles, at which point testing was terminated. The fourth blade had not failed. One second stage blade failed at mid-span after 1570 cycles, while a second one was cracked at the fillet at 2028 cycles. The remaining two second stage blades were not cracked. As before, a cooling air flow of 130 C.F.H. and a cycle time of 45 seconds was used.

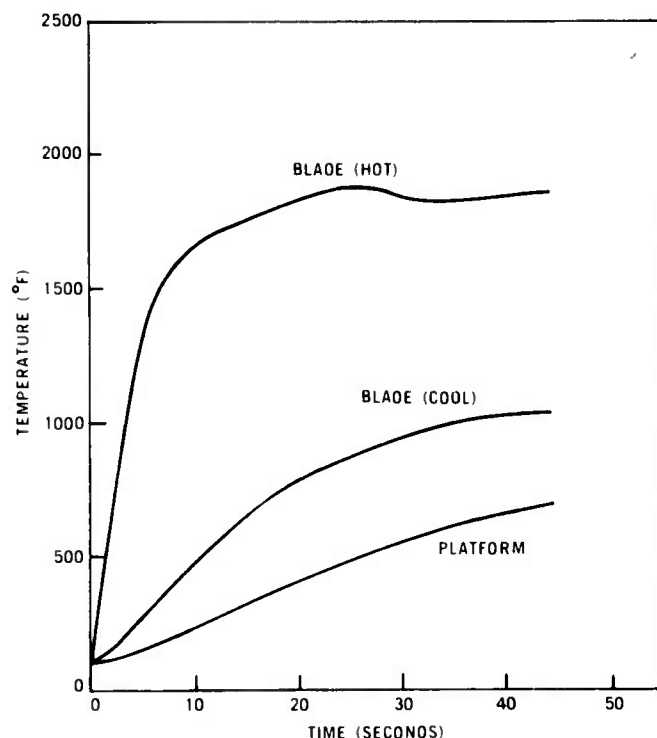


Figure 3.36 Rotor Thermal Response as Measured on Hot Side of Blade During 1930°F Thermal Shock Testing

This thermal shock test was considerably more severe than the test reported previously ⁽⁵⁾, in that higher heating rates and more severe thermal gradients were set up. These blades withstood this test much more successfully than did the blades tested previously. Expected further material improvements should result in significantly better thermal shock resistance.

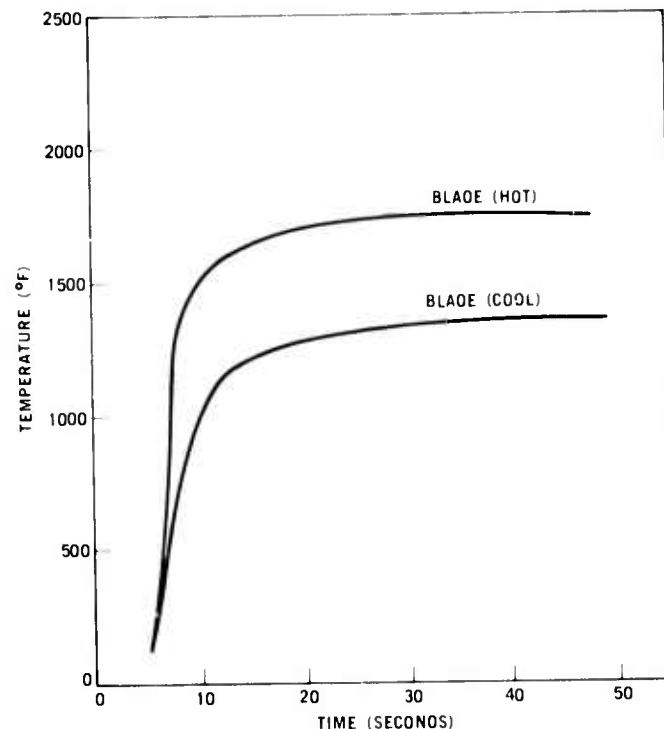


Figure 3.37 Rotor Thermal Response as Measured on Cool Side of Blade During 1930°F Thermal Shock Testing

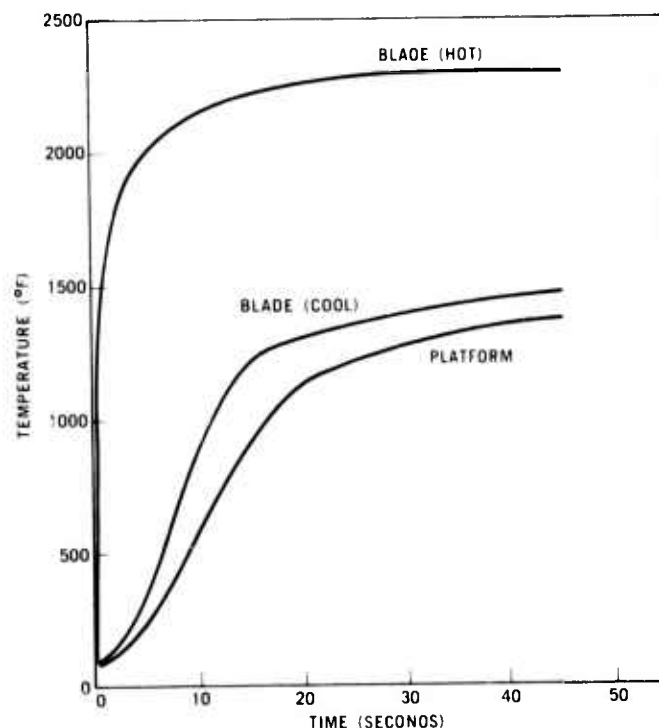


Figure 3.38 Rotor Thermal Response as Measured on Hot Side of Blade During 2300°F Thermal Shock Testing

3.2 CERAMIC STATORS, ROTOR SHROUDS, NOSE CONES, AND COMBUSTORS

SUMMARY

Significant progress has been made toward developing complete stress analysis codes for use on ceramic components. Emphasis is being placed on the first and second stage statots. Heat transfer coefficients for the first stage stator have been determined and three dimensional grid networks have been generated for second stage statots.

A ceramic combustor can made from "Refel" reaction sintered silicon carbide was tested for 50 hours over a cyclic test sequence which is representative of the 200 hour cycle to be used in meeting program objectives. This combustor survived the test, which included six hours at a turbine inlet temperature of 2500°F.

Work continues toward the improvement of the quality of statots by closely controlling the temperature of the molding tool during fabrication. This is particularly critical in using the first stage stator one piece tooling which was received during this reporting period. A number of Design C one piece first stage statots have been successfully molded.

The stability problem previously encountered with slip cast Si_3N_4 rotor shrouds appears to have been solved. As previously reported, the use of Fe_2O_3 as a nitriding aid improves the dimensional stability, and further improvements have now been achieved. Systematic control of the fabrication process using various heat treatments results in a high yield of rotor shrouds.

The successful completion of a fifty hour engine durability test for the hot flow path ceramic components was accomplished during this reporting period. The ceramic components consisted of a nose cone, first and second stage statots, and first and second stage turbine rotor shrouds. The test consisted of ten cold starts, three hot starts and fifty one-hour cycles during which the speed was automatically varied to follow the test cycle with a flat steady-state temperature schedule of 1930°F. Inspection of the ceramic components revealed that the nose cone was crack free with no apparent signs of deterioration. Both first and second stage rotor shrouds were crack free with no dimensional changes. Each of the twenty five injection molded Si_3N_4 first stage stator vanes were crack free. Eight of the thirty three injection molded Si_3N_4 second stage stator vanes exhibited fine trailing edge cracks, though no pieces came off, and the remaining twenty five vanes were crack free.

As an overall assessment, the development of ceramic statots, rotor shrouds, and nose cones has achieved a major milestone - fifty hours of demonstrated engine durability. Continued improvements in the materials, processing and fabrication areas have enhanced the confidence in meeting the two hundred hour durability objective.

3.2.1 DESIGN AND ANALYSIS

Introduction

Work is in progress on the development and application of an advanced three dimensional mechanical and thermal stress analytical design code. This code will have application for all ceramic turbine components, and this section is concerned with its development for stator analysis. Thus far, convection coefficients for the first stage stator have been determined, and three dimensional grid networks have been generated for second stage stators. These are the initial steps toward developing complete 3-D stress analyses for subsequent correlation with test results.

Computation Programs and Methods

A further refinement in the design process ⁽²⁾ is being devised to provide accurate three dimensional analyses of mechanical and thermal loading on the ceramic stators. A schematic diagram of the analytical approach is shown in Figure 3.39 and features utilization of existing automatic computation procedures at Ford.

The primary units of this plan consist of major computer programs including TSONIC, ⁽¹²⁾ BLAYER, ⁽¹³⁾ TAP, ^(14,15) SAP, ^(16,17,18) ADFORCE, ⁽¹⁹⁾ and WEIBULL ⁽²⁰⁾ These programs function and communicate through use of various buffer, geometry generation, storage, data handling and plotting routines.

These programs will provide a flexible set of analytical tools for development effort and to guide and support future ceramic component designs. Besides stators, these tools will be applicable to rotor analysis, and portions were used in the rotor blade stress analysis discussed in Section 3.1.1 of this report. With slight modifications, they will be also applicable to nose cone and combustor analyses. A general discussion of each program follows:

TSONIC ⁽¹²⁾ - Blade suction and pressure surface velocity profiles are computed by this program which was developed primarily for calculating transonic velocities on a blade-to-blade stream surface of a turbomachine airfoil. The transonic solution is computed by a numerical velocity gradient method, using information obtained from a finite-difference stream function solution at a reduced mass flow. The flow must be essentially subsonic, but may have local supersonic areas. This is representative of the type of flow field produced in the vehicular ceramic turbine.

BLAYER ⁽¹³⁾ - This program computes two-dimensional compressible laminar and turbulent boundary layers in arbitrary pressure gradients on airfoils. The program utilizes velocity distribution from TSONIC adjacent to the boundary layer, as well as wall temperatures and total free-stream conditions. The output of BLAYER comprises all of the principal boundary layer information including the Nusselt number. Film coefficients are obtained directly from the Nusselt number by utilizing real gas conductivity for air at the film temperatures under consideration.

SAP & TAP ^(14,15,16,17,18) have been discussed in detail in Section 3.1.1 of this report.

ADFORCE ⁽¹⁹⁾ - This program computes aerodynamic forces on turbine blade sections from the distribution of pressure or velocity along the surfaces.

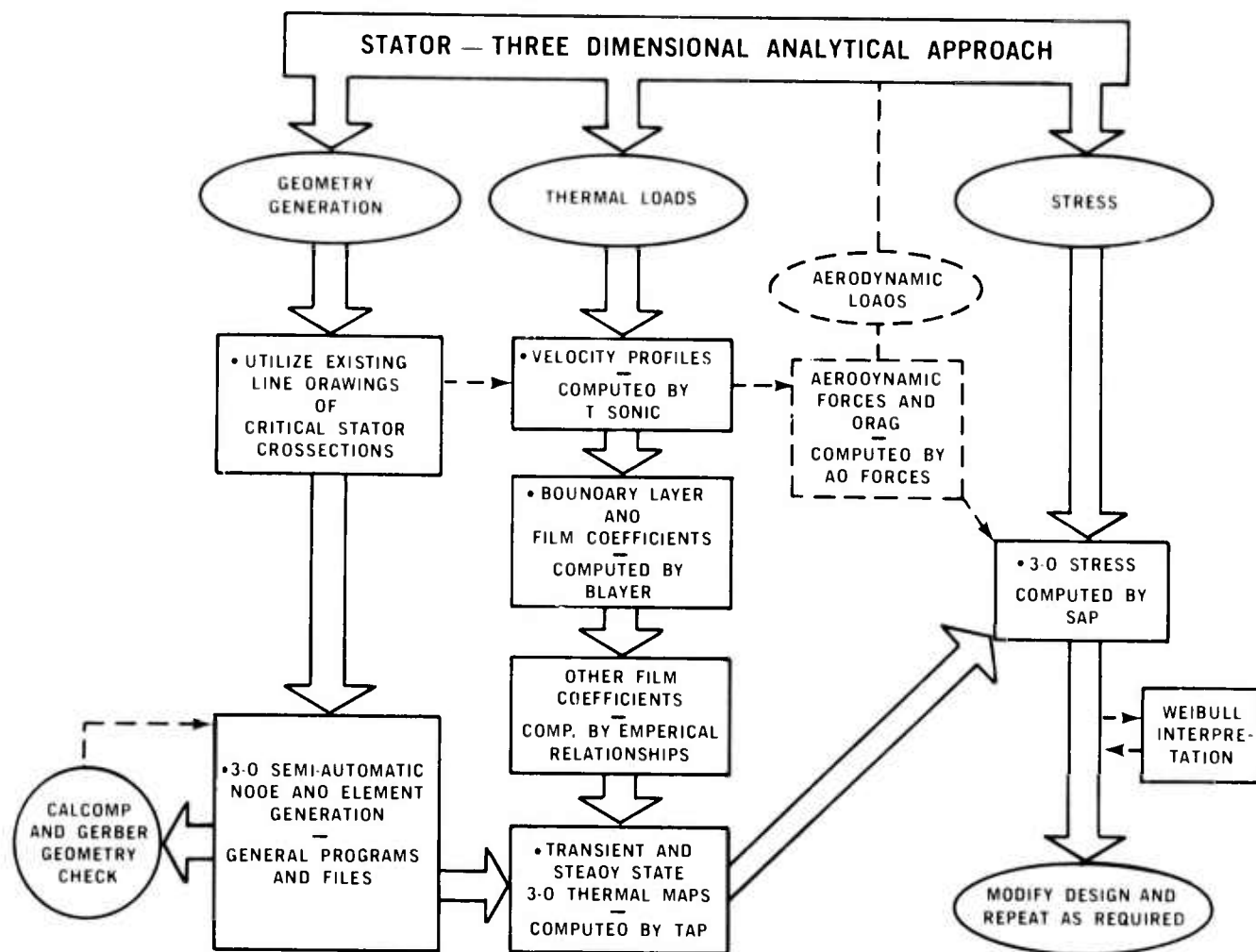


Figure 3.39 Schematic of the Three Dimensional Stress Analysis Process

WEIBULL (20) - The Weibull statistical analyses assess the strength and the probability of failure of the investigated structure for given loading conditions. Application of the Weibull statistical model for brittle materials was discussed in the last report (5).

The preceding computer programs constitute an efficient and technologically advanced package for three dimensional analysis. The programs for thermal boundary computations were selected particularly with regard to their sensitivity to geometric or design changes. This is also true with regard to the sequencing as shown in Figure 3.39.

Film Coefficient Determinations

Film coefficients were computed by programs TSONIC and BLAYER. These data include convective film coefficients computed for the first stage stator vane at radii of $R=1.7$, 1.95 and 2.2 inches respectively from the center axis of the stator. Estimates of the convective film coefficients for the inter blade land or channel by an empirical method are also included.

The purpose of this data is to provide spatially varying film coefficients which will be used for boundary conditions to compute temperatures and thermal loads on the first stage stator vane from zero to the 55% speed condition. This

condition was selected for initial evaluation of the stator because it simulates cold start transients from room temperature to idle speed (55%) at 1930° F turbine inlet temperature. A different set of film coefficients representing the transient from the 55% idle speed condition to 100% speed (T inlet = 2500° F) will be computed.

Film coefficients were calculated by first computing two-dimensional velocity profiles on the first stage stator airfoils by TSONIC. This program yielded complete two-dimensional velocity gradient solutions tangential to pressure and suction surfaces of the airfoil. These data were used for direct input to BLAYER for computation of the two-dimensional airfoil boundary layer and hence the associated convective heat transfer film coefficients. All vane airfoil boundary film coefficients except the stagnation point were computed by BLAYER.

The stagnation point film coefficient was computed by an empirical method of Cohen and Reshotko ⁽²¹⁾. This method is applicable to stagnation point heating of the leading edge of cylinders. It was used here as an approximation for leading edge heating on vanes. The method is as follows:

The stagnation film coefficient: (1)

$$h_s = \frac{k_w}{\sqrt{v_w}} \frac{N_{NU}}{N_{Re_w}} \sqrt{C}$$

where:

N_{Re_w} = wall Reynolds number

N_{NU} = Nusselt number

v_w = kinematic viscosity at the wall

k_w = conductivity of the gas at the wall

and for a cylinder:

$$C = \frac{2U_1}{r} (1 - 0.01416 (M_1^2) - 0.01164 (M_1^4)) \quad (2)$$

where:

M_1 = free stream Mach number

U_1 = free stream velocity

r = radius of vane leading edge

Film coefficients for the inter blade land or channel inner and outer shrouds were computed by an empirical method given by Zysina - Moloshen and Uskov ⁽²²⁾.

This method is:

$$N_{NU_c} = (0.032 + 0.014 \frac{\beta}{100}) N_{Re_c}^{0.8} \left(\frac{t}{b}\right)^{-0.175} \quad (3)$$

$$\text{and } h_c = \frac{N_{NU_c} k_g}{b} \quad (4)$$

β = the deflection angle of the fluid (degrees)

N_{NU_c} = Nusselt number referenced to the chord line

N_{Re_c} = Reynolds number referenced to the chord line

k_g = conductivity for air as a real gas

t = pitch (inches)

b = length of chord line (inches)

This approach provided a good representation of the boundary conditions at mid-span of the vane and provided a quasi-3 dimensionability to vane boundary conditions that is sensitive to geometry changes as well as changes in the free stream.

Figures 3.40, 3.41, and 3.42 present film coefficient h as a function of dimensionless surface distances s/s_{\max} for radii of 1.7, 1.95, and 2.2 respectively. Two-dimensional values of h are shown for both suction and pressure surfaces of the first stage stator vane at 55% speed. Pressure surfaces exhibited all-laminar flow during these conditions. From the stagnation point ($s/s_{\max}=0$) to the dotted curve, the suction surface also exhibited laminar flow. Transition from laminar to turbulent airflow is shown by the dotted curve. From the end of the transition regime to s_{\max} , turbulent flow was predicted on the suction surface of the vane. The preceding were characteristic of all radial cross-sections which were examined.

The stagnation point coefficients computed by the method of Reshetko and Cohen ⁽²¹⁾ are plotted at $s/s_{\max}=0$. Film coefficients for top and bottom inter-blade lands are shown in Figure 3.43. These coefficients are employed with appropriate adiabatic wall (or recovery) film temperatures.

The finite element, three-dimensional model to be used for thermal and stress analyses differs somewhat from that used for turbine rotors. A semi-automatic method was used in which the larger burden of mode generation is placed on the existing 2-dimensional electronic digitizer equipment. The nodes in the essential x-y planes were digitized in a flat curvilinear coordinate system. Z or R elevations were added by a series of computer routines for inner shrouds, outer shrouds, and vanes. These sub-programs generated fillet elevations which approximate the desired radii. They transformed the curvilinear coordinates to an appropriate Cartesian coordinate system and provided generation of any unusual geometric features such as the junction line between slipcast and injection molded portions in the second stage stator. Vane generation is very similar to that discussed in Section 3.1.1 of this report.

Element files for use in finite element computer programs are also semi-automatically generated by separate computer routines. This approach allows a great deal of flexibility early in the evaluation phase of various design changes.

A typical three dimensional model for the second stage stator is shown in Figure 3.44.

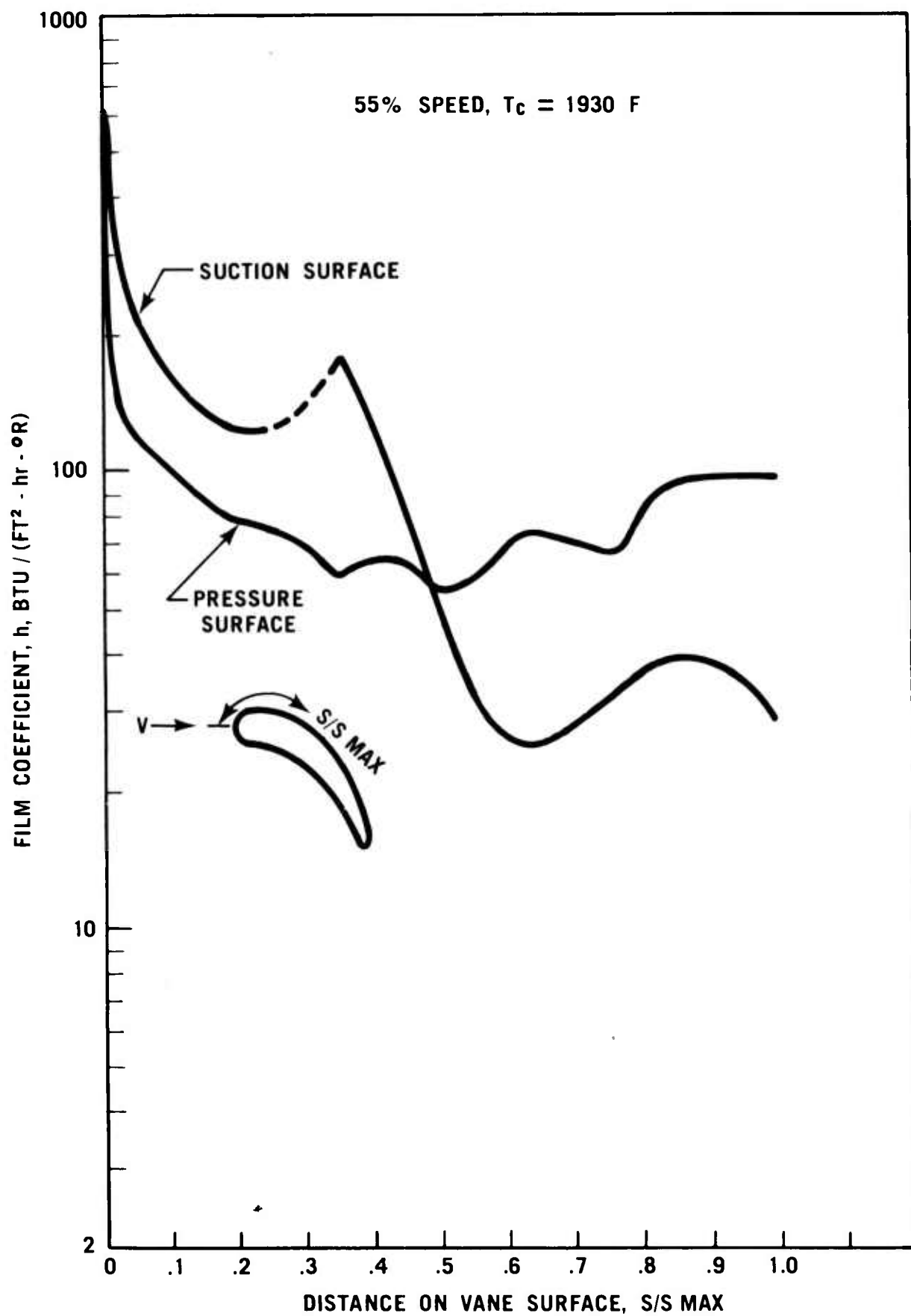


Figure 3.40 Film Coefficients For the First Stage Stator Vane at Radius of 1.7 Inches

TSonic and BLAYER programs will be used to complete the calculations of critical boundary conditions for input to the heat transfer program. Thermal maps of the stators will be generated, and thermal stresses will be computed by the use of the three dimensional general purpose stress programs.

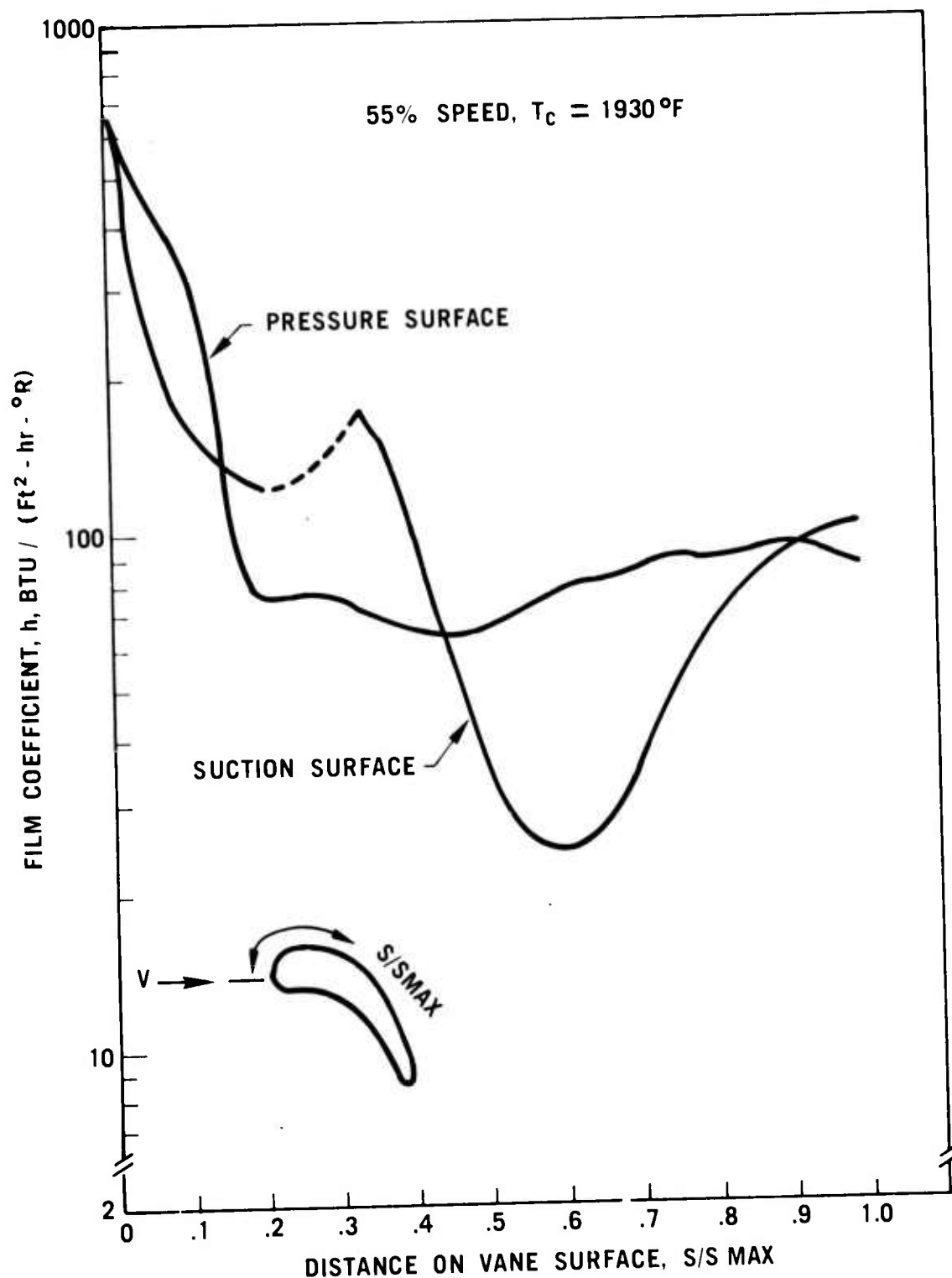


Figure 3.41 Film Coefficients For the First Stage Stator Vane at Radius of 1.95 Inches

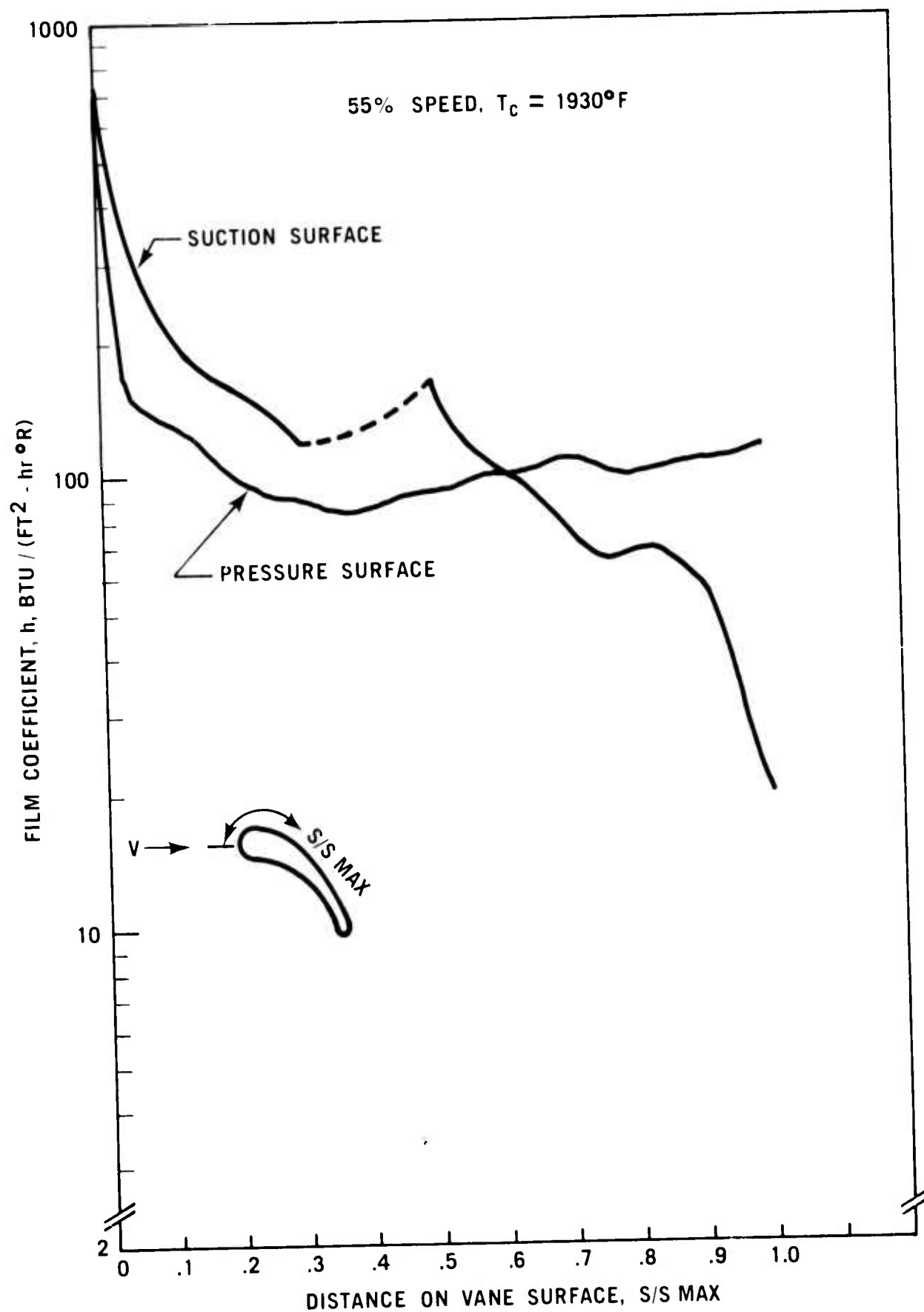


Figure 3.42 Film Coefficients For the First Stage Stator Vane at Radius of 2.2 Inches

CONDITIONS
SPEED = 55%
 $T_7 = 1930^\circ\text{F}$

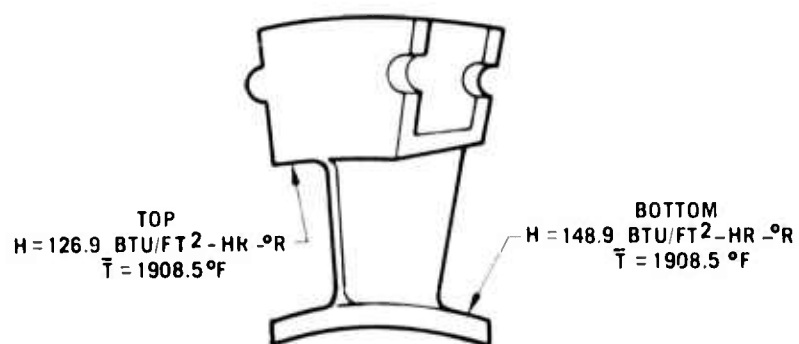


Figure 3.43 Average Film Coefficients For the Surfaces of the Inner and Outer Shrouds of the First Stage Stator

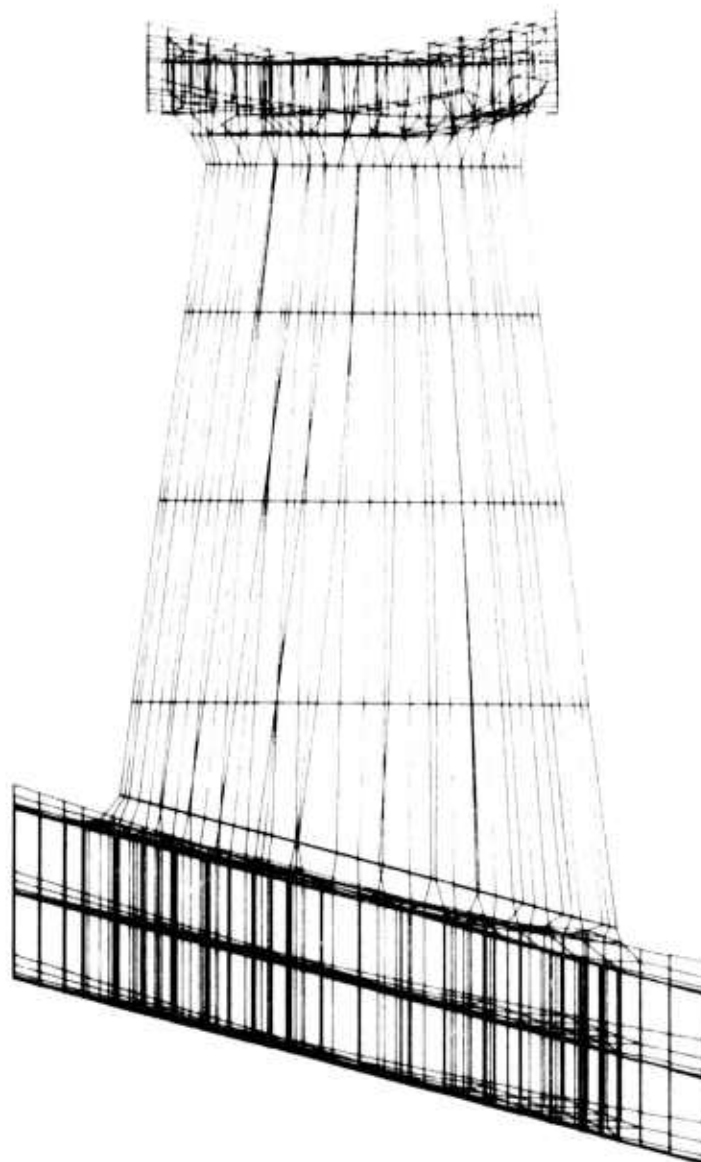


Figure 3.44 Three Dimensional Computer Model of the Second Stage Stator

3.2.2 MATERIALS AND FABRICATION

Introduction

A common type of failure associated with first stage stator assemblies has been outer shroud cracking. Analysis of this type of failure indicates it is caused by a stress concentration effect of the joint between individual stator segments. This part was redesigned as one piece rather than an assembly and tooling was ordered. During this reporting period, the injection molding tooling was received and a number of Design C integral first stage stators were molded.

Earlier work ⁽⁵⁾ resulted in the use of Fe_2O_3 as a nitriding aid to improve the dimensional stability of Si_3N_4 rotor shrouds. Further improvements have now been achieved by a systematic control of the fabrication process using various heat treatments, resulting in a high yield of stable shroud rings.

Stator Fabrication

During this reporting period, tooling was developed to fabricate the Design C first stage stator as a one piece injection molded part. Each half of the tool contains the cavity to form one half of the airfoil. The stationary tool section forms the outer shroud and the moveable section forms the inner shroud. Formation of the inner shroud requires a gap between each tip shroud segment. A collapsible core with wedge shaped inserts at the midpoint between each vane provides the molded-in gap. As the moveable section retracts from the stationary section, the collapsible core moves inward as the tool goes into the eject mode.

To date silicon nitride components have been successfully molded using the conventional organic system as well as an experimental higher density system.

Temperature control is critical in using the one shot tooling. Correct temperature balance minimizes molding flaws such as entrapped gas, shrinkage cracks, and fold and knit lines. Temperature balance is also required to hold the component on the moveable portion of the tool during ejection of the molded component. A slight differential shrinkage retains the component on the desired tool section until it is removed by the ejector system.

A one-piece first stage Si_3N_4 stator is shown in Figure 3.45. All vanes have a free gap at the tip shroud. Tip shroud gaps and concentricity of the part do not change during the binder burnout or nitriding process.

As described in Section 5.3.3 of this report, x-ray radiography has been used to evaluate the molded stator quality with respect to molding flaws. Optimization of molding parameters is planned in the future, as is engine and rig testing of these one piece stators.

Rotor Shroud Development

During this reporting period, emphasis was placed on the control and the refinement of heat treating schedules utilized for screening and stabilizing slip cast Si_3N_4 rotor shroud rings. Testing ⁽⁴⁾ has indicated that the manner and sequence in which the rotor shroud rings are heat treated determine component behavior in an engine environment.

Rotor shroud rings are fabricated by drain casting six inch high cylinders using silicon slips whose rheological properties are controlled to yield final Si_3N_4 densities of 2.65 - 2.72 gm/cc ⁽⁵⁾. The cylinders are argon heat treated,



Figure 3.45 One Piece First Stage Stator Made From Molded Reaction Sintered Silicon Nitride

sliced, and machined into individual rings prior to nitridation. Approximately 0.020 inch stock is left on all surfaces. After nitridation the ring is slotted and the resulting gap is measured. This initial gap measurement serves as the reference point for all subsequent gap measurements.

Experimentation has shown that the following heat treat process yields the best results:

- a) The slotted rings are placed in an air-atmosphere furnace, heated to 1900°F , and held for 100 hours. Care is taken to position the rings so that all surfaces are exposed to the furnace atmosphere and oxidized uniformly.
- b) The rings are diamond ground to final dimension.
- c) All rings, with surfaces uniformly exposed, are again heated to 1900°F in air and held for 100 hours.
- d) The rings are then evaluated in a test rig which closely simulates engine loading conditions, and constrains the rings. They are measured after 70 hours at 1900°F in air and again after 165 hours in air at 1900°F .

After each step in the above process the gap is measured and the data recorded as shown in Figure 3.46. This shows the variability as measured for

four second stage rotor shroud rings. All four rings were machined from the same slip cast blank and processed simultaneously. Note that the maximum final gap change shown in this figure is 0.004 inches, which corresponds to approximately a 0.001 inch diameter change on the shroud ring. This 0.001 inch change is well within design requirements.

This heat treatment process has been incorporated in the manufacture of all slip cast rotor shrouds. The results of this work have raised questions about the affect of oxidation on the properties of reaction sintered silicon nitride. An intensive investigation was started near the end of this reporting period and will be discussed in subsequent reports.

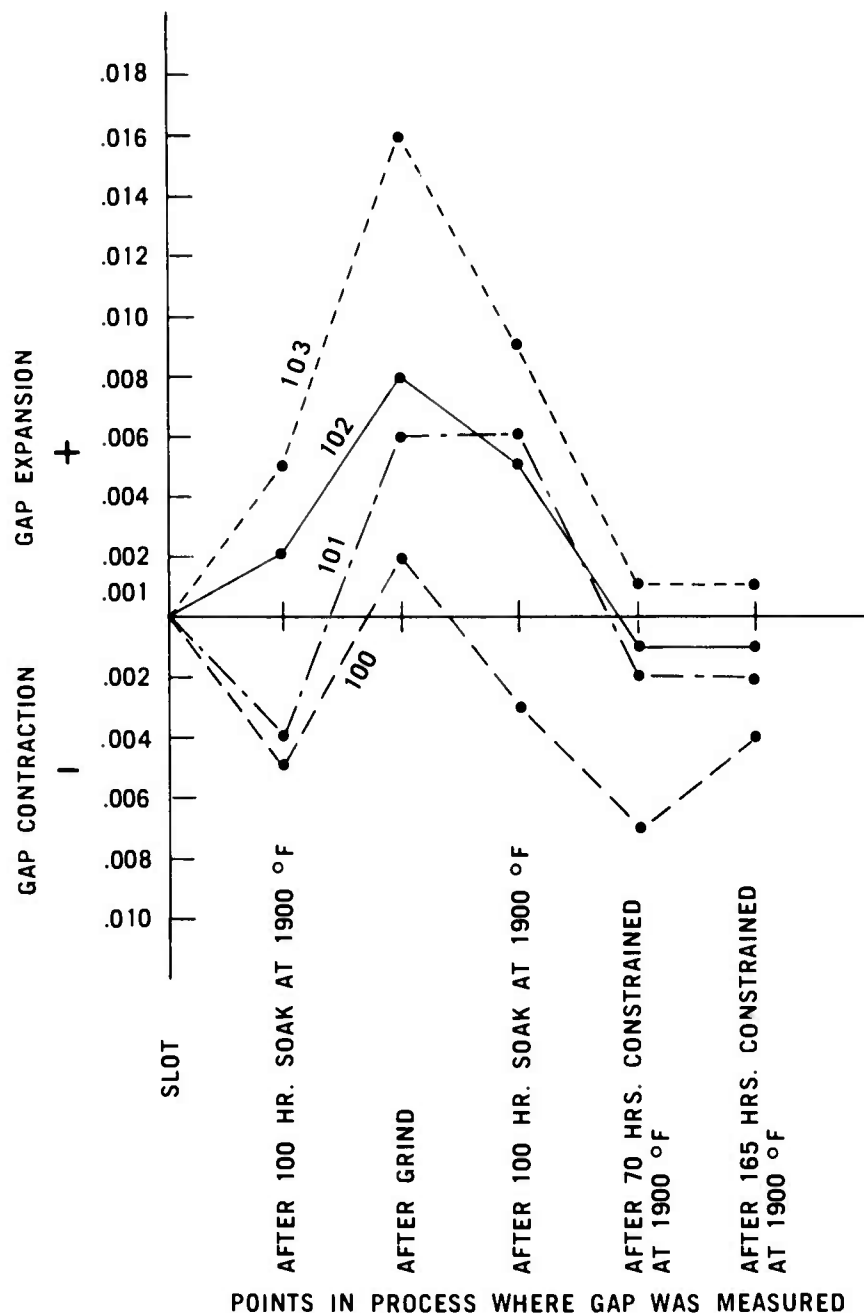


Figure 3.46 Gap Changes in Second Stage Slip Cast Silicon Nitride Rotor Shrouds at Various Stages in the Heat Treatment Cycle

3.2.3 TESTING

Introduction

The stationary hot flow path components include the combustor, turbine inlet nose cone, first and second stage stators, and first and second stage rotor shrouds. In order to develop these components, three different types of test rigs were used. The Combustor Test Rig was used to develop the combustor. The Thermal Shock Test Rig was used for initial tests of stator vane designs and materials, and the Ceramic Stator Test Rig was used to evaluate the nose cone, stators, and shrouds under actual engine conditions.

The Thermal Shock Rig was modified to include a method for determining when a crack was initiated. Initial thermal shock testing of one piece first stage stators was completed. A combustor can of "Refel" SiC was tested for fifty hours, including six hours at 2500°F, without failure. A major program milestone was reached when a fifty hour engine test of stationary ceramic components was completed using metal rotors.

Thermal Shock Testing

During this reporting period the Thermal Shock Test Rig was utilized for additional stator vane testing, and was modified for rotor blade testing. A failure detection system was also incorporated to allow the exact number of cycles to failure to be determined.

In order to detect stator vane and rotor blade failures on the Thermal Shock Test Rig, a strip chart recorder was added to the system as diagramed in the last report (5). The output signal of the Ircon pyrometer was plotted as a function of time for each vane segment tested. By focusing the pyrometer on the vane tip, a plot of temperature on the strip chart recorder will reflect failures in which vane cracking occurs or vane tips fall off. During operation of this system it was noted that sensitivity was sufficient to detect major vane cracks severe enough to alter vane temperature distribution without total vane failure. Examination of temperature plots also facilitates detection of over temperature conditions which occasionally occur due to burner system fluctuations.

Preliminary studies were run on the Design C one piece first stage stator. Segments were subjected to a 45 second cycle to 1900°F part temperature followed by a quench to room temperature with ambient air at 130 cfh. There were no apparent failures after 1000 cycles on eight test segments. Additional testing to 2300°F part temperature resulted in one vane failure at 800 additional cycles and one additional vane failure at 1400 additional cycles. Further testing with complete vane temperature mapping is presently in progress.

Modification to the clamping mechanism of the Thermal Shock Rig facilitated testing of ceramic rotor blades. Temperature profile data, test parameters, and test results are discussed in Section 3.1.3 of this report.

Combustor Testing

Evaluation of ceramic combustors has been conducted by subjecting prototype components to a series of tests simulating engine conditions. The results of these tests were reported previously (4), and showed that dense, high strength silicon carbide was the best candidate. During this reporting period, a combustor can made of "Refel" SiC was successfully evaluated over a cyclic durability

test designed to serve as an abbreviated version of the 200 hour duty cycle to be utilized for demonstrating final program goals.

A "Refel" SiC combustor was tested in the Combustor Test Rig shown in Figure 3.47. This rig provides a simulation of the operating conditions that a combustor will experience in an engine. Combustors can be tested in this rig at airflow rates up to 2 lb/sec, inlet air temperatures up to at least 1800°F, outlet temperatures of up to 2500°F, and inlet pressures of up to 65 psia. The air supply is provided by an air compressor. The inlet air is heated by a gas fired heat exchanger, which can provide air heated to 1100°F, followed by a preheat combustion system which can provide the required additional preheat.

As shown in Figure 3.47, the preheated air enters a 24 inch diameter test section plenum from the side. The test combustor is located centrally within this plenum, and its location is indicated by the fuel nozzle and combustor cover shown in the figure. The combustor exhaust gas discharges into the rig exhaust duct composed of several sections made from either in-house slip cast Si_3N_4 or Norton Crystar SiC. These linings are insulated from the outer metal housing. After leaving the rig exhaust duct, the combustion products are cooled with a water spray prior to entering the exhaust back pressure value.

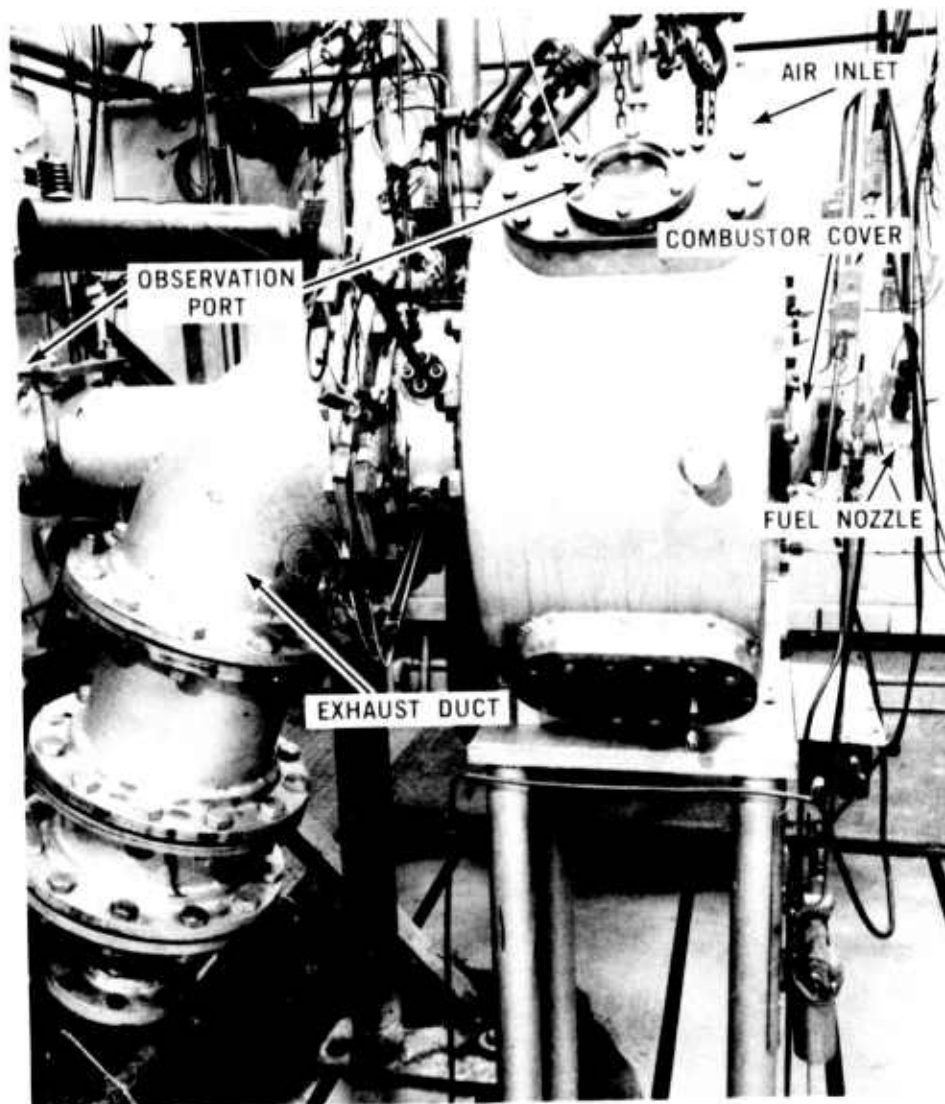


Figure 3.47 Combustor Test Rig

A particularly unique feature of this rig is the observation port shown in Figure 3.47. A quartz window provides a direct line of sight along the axis of the combustor directly into the forward end of the combustor dome. This provides visual observation of both the combustion process and the condition of the interior of the combustor wall. Viewing ports are also provided around the inlet air plenum to allow visual inspection of the exterior of the combustor.

In order to obtain a reasonable evaluation of candidate ceramic combustors, a test cycle was designed consisting of 40 cold starts plus 50 hours of operation at various simulated engine speeds. The amount of time at each speed over the 50 hour cycle and the corresponding combustor outlet temperatures are shown in Table 3.3.

TABLE 3.3

OPERATING CONDITIONS DURING 50 HOUR COMBUSTOR TEST

<u>% Speed</u>	<u>Time</u>	<u>Combustor Outlet Temperature, °F</u>
55.0	23 Hours	1930
59.0	12 Hours, 30 Minutes	1930
69.0	3 Hours, 30 Minutes	1930
77.5	2 Hours, 30 Minutes	1930
86.5	2 Hours, 30 Minutes	1930
100.00	6 Hours	2500
Total 50 Hours		

A photograph of the "Refel" silicon carbide combustor taken after completion of the 40 cold starts and 50 hours of testing is shown in Figure 3.48. Careful visual observation and a check using fluorescent dye penetrant confirmed that there was no cracking. The combustor showed no sign of any visual change, such as oxidation, as compared to its appearance before testing. The temperature

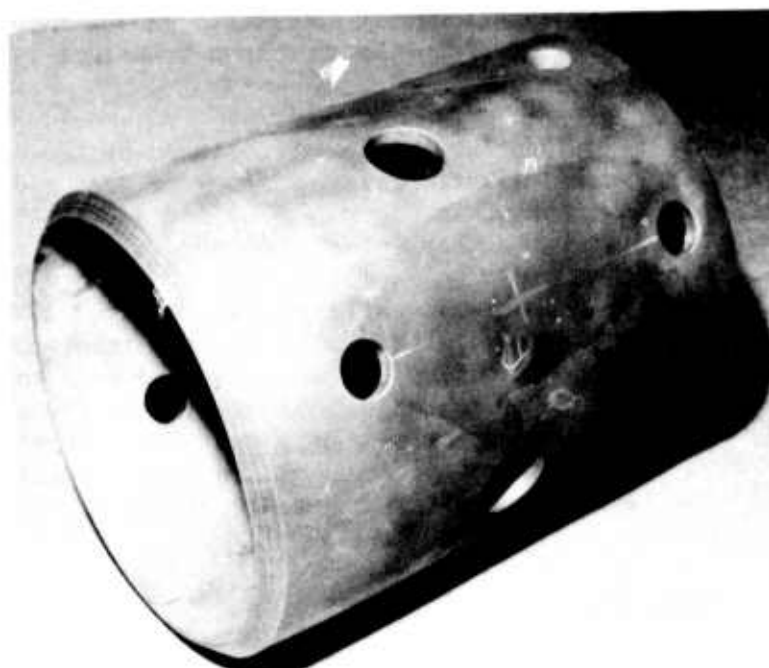


Figure 3.48 "Refel" Silicon Carbide Combustor Tube After Testing

of the outer wall was measured during the test by means of two platinum-platinum 13% rhodium thermocouples which were cemented to the combustor. During operation at 1930°F outlet temperature, the outer wall temperature varied between 1700 and 1800°F. During operation at 2500°F the outer wall surface reached 2160°F.

Because of this successful test, the "Refel" type of silicon carbide is now considered to be the leading candidate for use in ceramic combustors. Additional testing will be performed in order to ascertain the reliability of the material in this design.

Hot Static and Dynamic Testing of Stators, Shrouds, and Nose Cones

During the first portion of this reporting period, the engine and rig test facilities were relocated. While this move consolidated the test facilities into one area, it did result in limiting available test time.

During the move an automatic control system was developed and installed in a turbine engine for ceramic durability testing. The engine was connected directly to a driving or absorbing dynamometer, and a program controller was added to control the dynamometer speed over a predetermined cycle. In addition, an electronic fuel control was developed which directly controlled the turbine inlet temperature to any constant preset value. An automatic shutdown package was also incorporated to protect against system or engine malfunctions. Thus, once the operator started this engine, the test sequence was carried out automatically. The automation provided the degree of precise and reproducible cycle control necessary to assure that ceramic components are tested in a uniform manner which will yield meaningful test data.

The duty cycle selected for durability testing in this engine is shown in Figure 3.49, with the engine speed varying from 55% to 87%, and the steady state turbine inlet temperature controlled at a constant 1930°F. This durability cycle was run in 15 hour segments. At the beginning of each segment there was one cold light with transient conditions as shown in Figure 3.50.

Before ceramic components were subjected to durability testing, they were proof tested by 10 cold lights followed by immediate shutdown. The lightoff transient is shown in Figure 3.50, and the shutdown transient is shown in Figure 3.53.

Future testing will include two shutdowns followed by two hot lights during each 15 hour segment. Typical transient responses were measured for these hot lights and shutdowns and are shown in Figures 3.51 and 3.52. At the end of the 15 hour run there will also be another hot shutdown.

Figure 3.54 shows the complete durability cycle as it will be run with ceramic rotors to 100% engine speed with 2500°F turbine inlet temperature. The 2500°F portion of this cycle can not be run at present due to the temperature limitations imposed by the use of the metal rotors. Until the ceramic rotors are developed and are ready for engine testing, the 2500°F portion of this durability cycle will be carried out without rotors in a special rig. This rig will be called the Flow Path Qualification Rig and is presently being constructed.

Component Durability Testing

During this reporting period, a major milestone was accomplished, the completion of a 50 hour component durability engine test run of the hot flow

path ceramic parts. These components consisted of a nose cone, first and second stage stators, and first and second stage turbine rotor shrouds. The engine was operated over the durability cycle shown in Figure 3.49 using metal rotors. The entire test consisted of 10 cold starts, 3 hot starts, and 50 one-hour cycles during which the speed was automatically varied to follow the test cycle.

Inspection of the ceramic components after the 50 hour test revealed that the nose cone (Figure 3.55) was crack free with no apparent signs of deterioration. Both first and second stage turbine rotor shrouds (Figure 3.56) were crack free and in excellent condition. The first stage shroud did have a chip out of the surface but this had occurred during a previous run. Each of the 25 injection molded silicon nitride stator vanes in the first stage stator (Figure 3.57) were crack free with the only sign of deterioration being a small chip (approximately 0.050 inches wide) from the trailing edge of one vane. This chip appeared to have been caused by a foreign object impacting the vane. Eight of the 33 injection molded silicon nitride stator vanes in the second stage stator exhibited fine trailing edge cracks, though no pieces came off, and the remaining 25 vanes were crack free. This stator is shown in Figure 3.58. Several pieces of the cracked vane had been removed for examination by the time this photograph was made.

The results of this test were generally encouraging. This was the first attempt to conduct a prolonged durability engine test on all of the stationary ceramic components. Except for the second stage stator, all of the ceramic components came through the 50 hour test run in good condition. The type of failure experienced on the eight second stage stator vanes was not at all typical of any previous failures. An analysis of this part is in progress in an attempt to gain an understanding of its behavior.

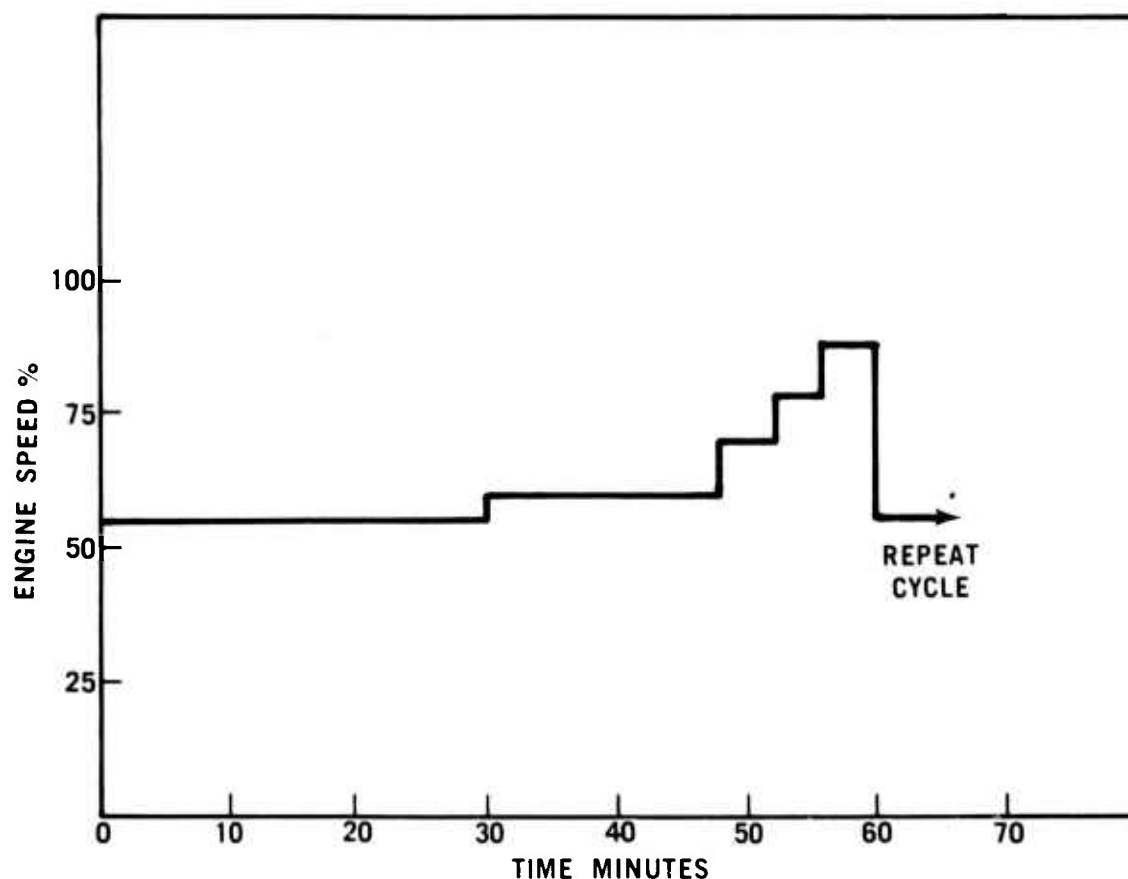


Figure 3.49 Durability Duty Cycle For Ceramic Components Using Metal Turbine Rotors

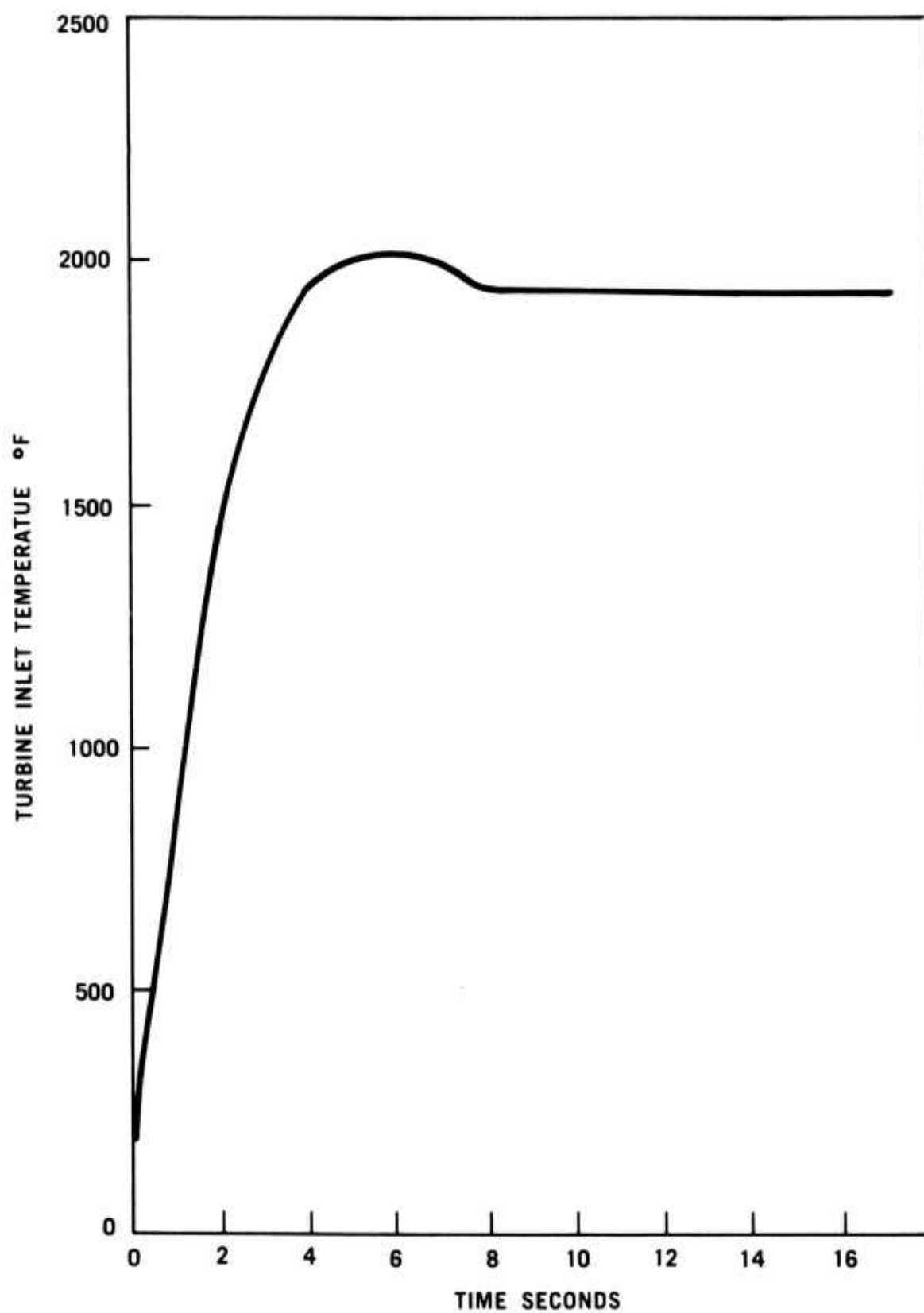


Figure 3.50 Turbine Inlet Temperature vs Time For a Cold Light Transient

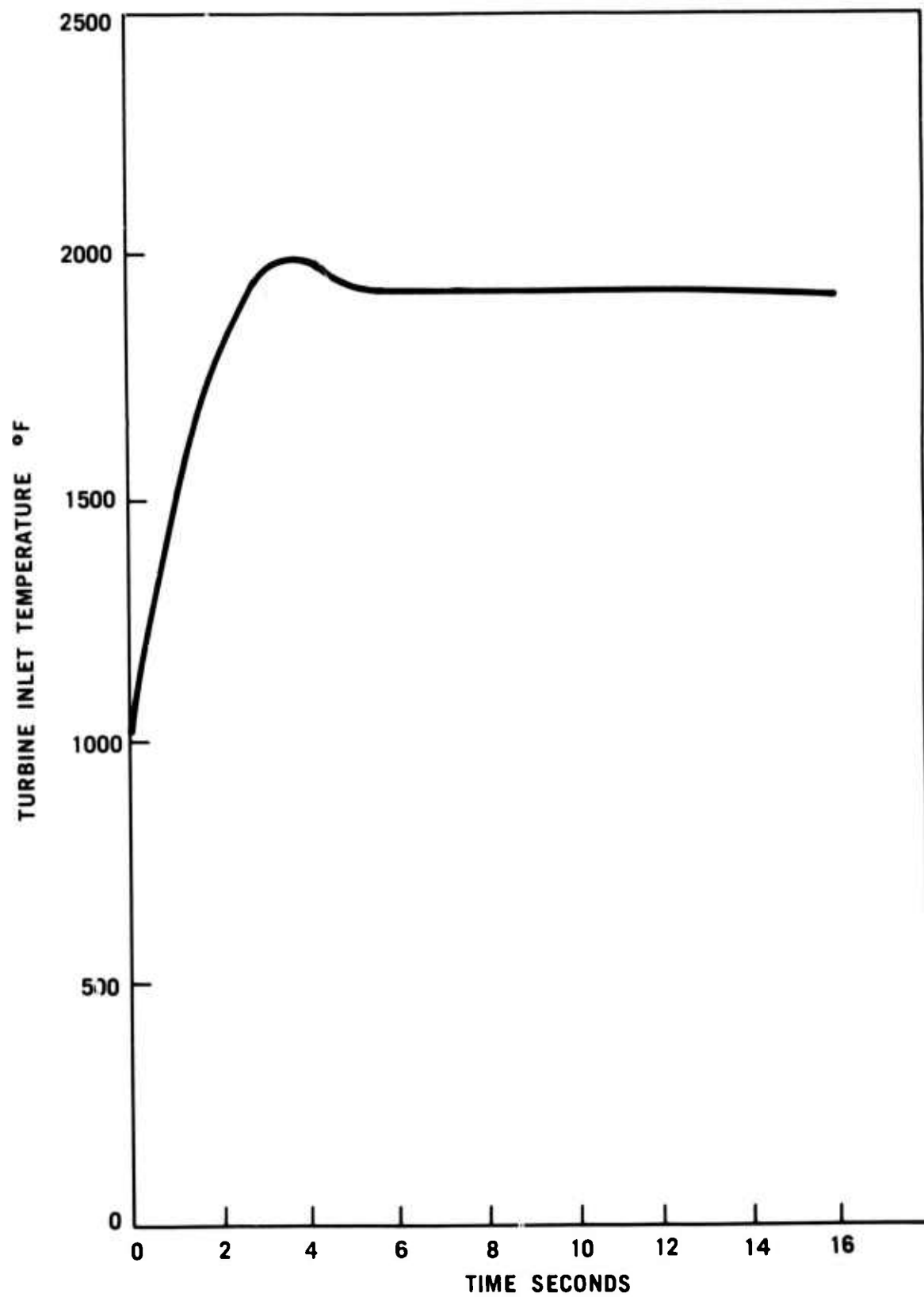


Figure 3.51 Turbine Inlet Temperature vs Time For a Hot Light Transient

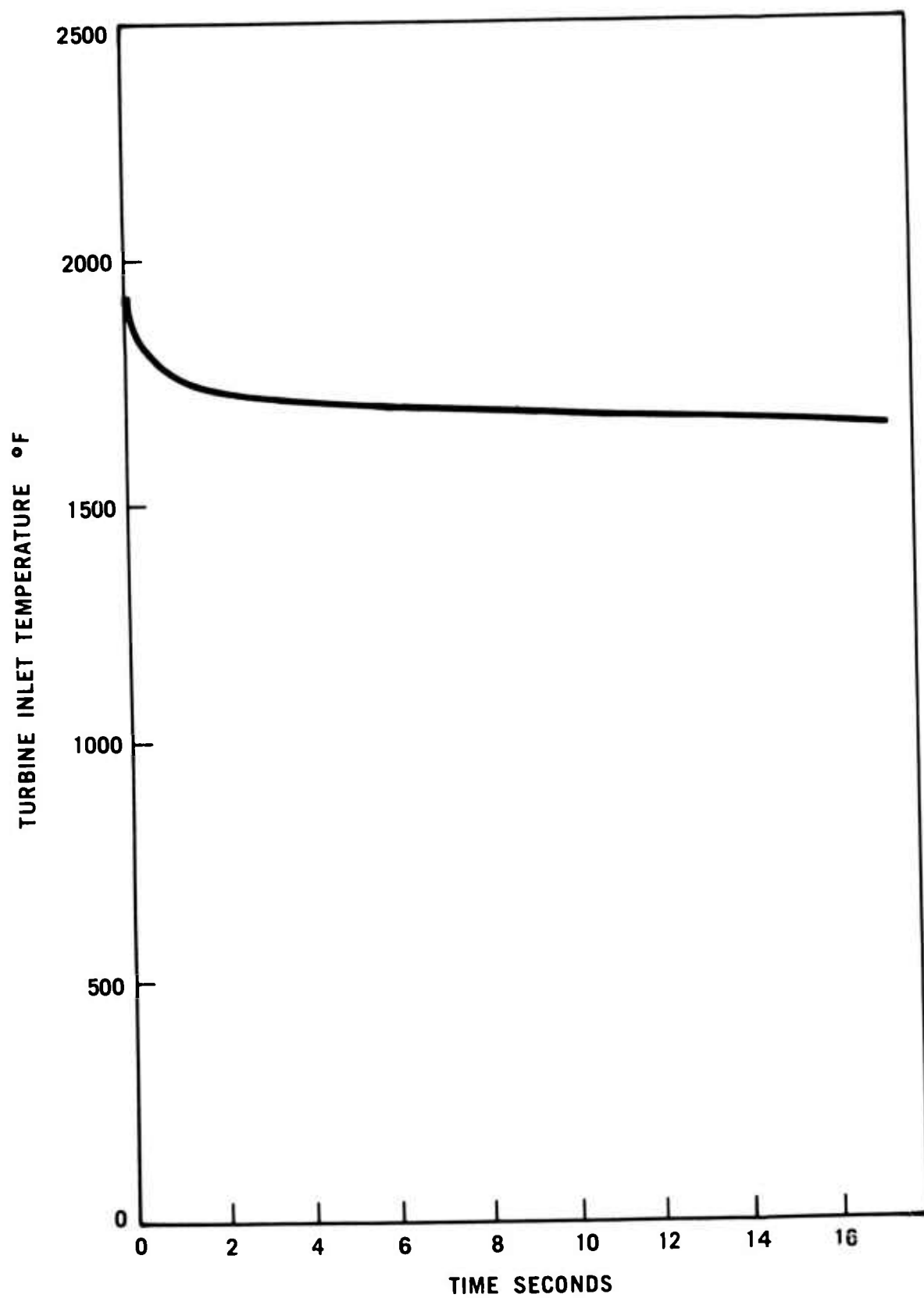


Figure 3.52 Turbine Inlet Temperature vs Time For a Hot Shutdown Transient

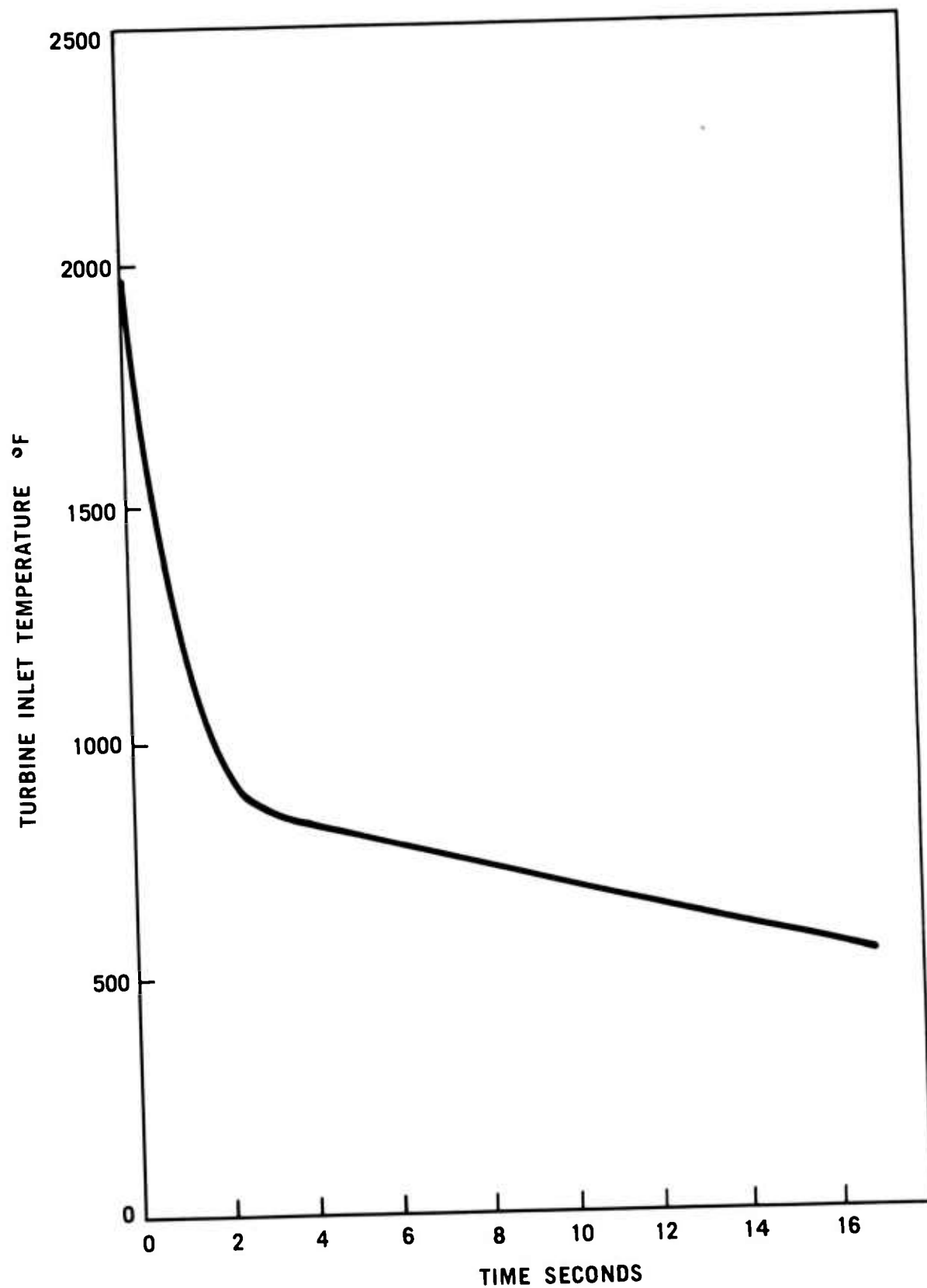


Figure 3.53 Turbine Inlet Temperature vs Time For a Cold Shutdown Transient

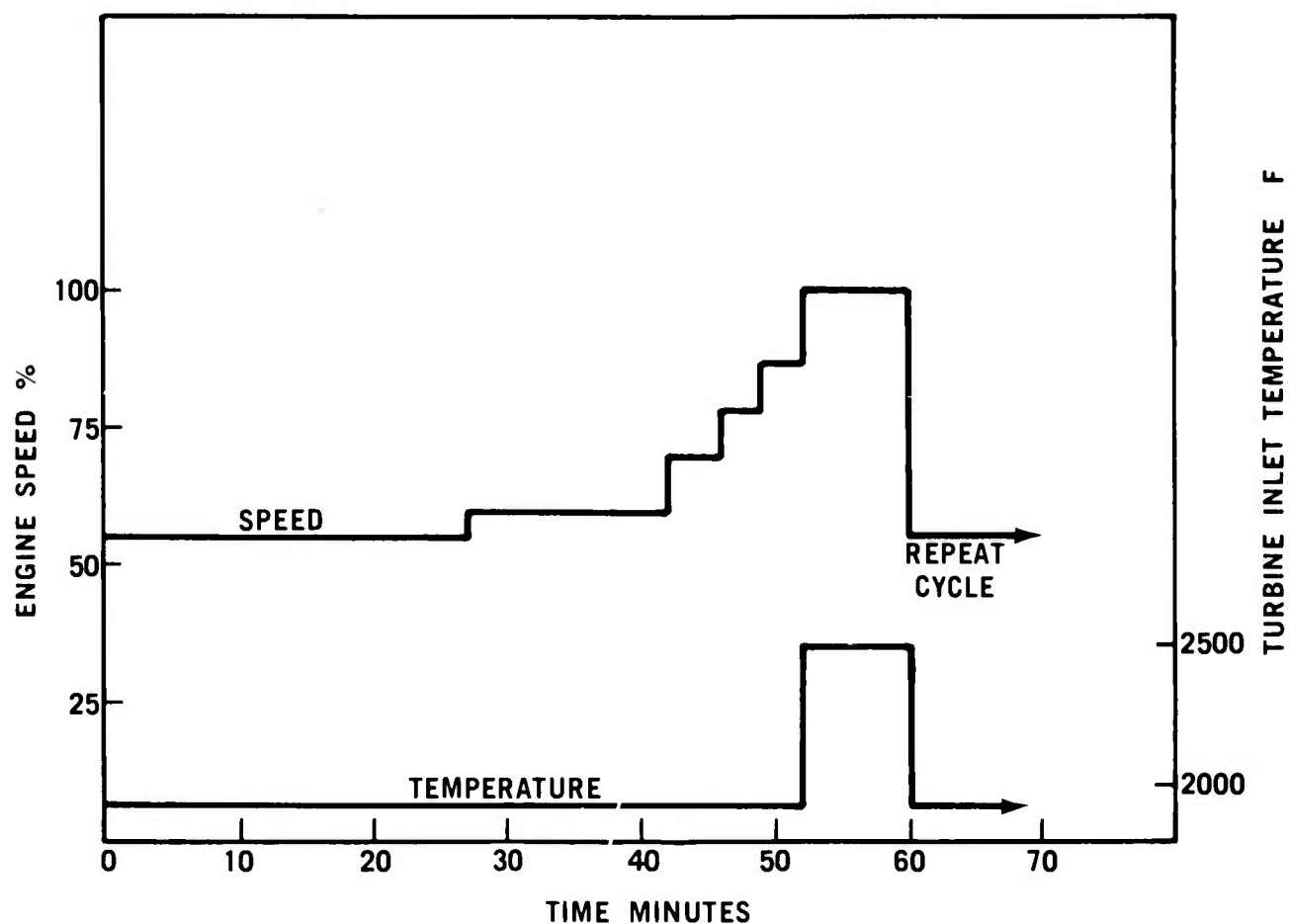


Figure 3.54 Durability Duty Cycle For Ceramic Components Using Ceramic Turbine Rotors



Figure 3.55 Molded Reaction Sintered Silicon Nitride Nose Cone After 50 Hour Durability Test



Figure 3.56 Slip Cast Reaction Sintered Silicon Nitride Turbine Rotor Shrouds After 50 Hour Durability Test

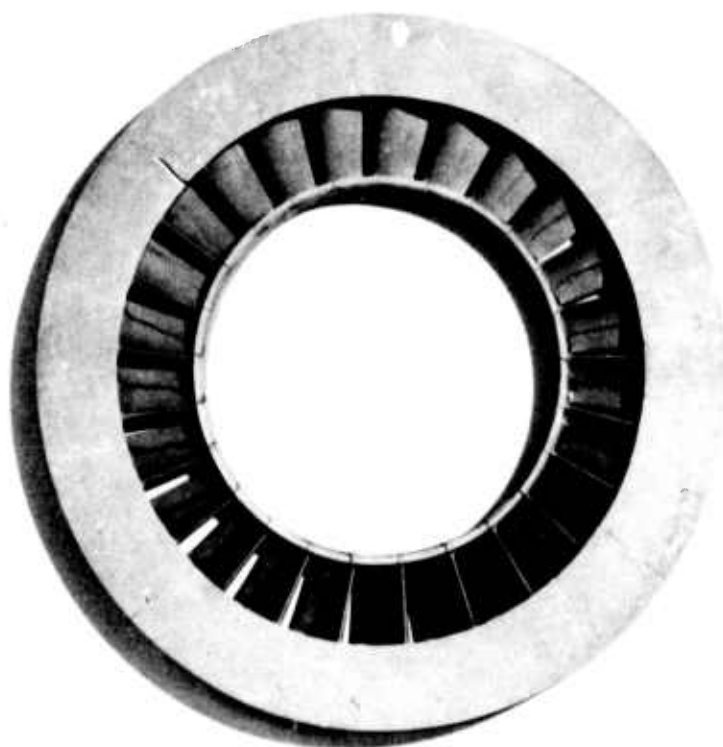


Figure 3.57 Molded Reaction Sintered Silicon Nitride First Stage Stator After 50 Hour Durability Test



Figure 3.58 Inverted Channel Reaction Sintered Silicon Nitride Second Stage Stator After 50 Hour Durability Test

Statistical Analysis of Test Data

Previous reports have tabulated the results of all engine and rig testing by component. This tabulation was becoming very bulky and difficult to interpret since changes were continually being made in materials and designs. A better way to collect and analyze this test data is through the use of Weibull statistics.

A computer program was established to test a given set of data and determine if the best fit is represented by either a two or a three parameter Weibull model. Any component which failed either as the result of another component failure or by any means when out of the engine was considered as a suspended item.

An example of the use of this technique is shown in Figure 3.59, showing the amount of testing time to produce the first crack in ceramic nose cones. Engine durability data for the Design C scalloped and slotted nose cone discussed in the last report ⁽⁵⁾ is compared to data obtained previously on the Design B nose cone. The details of this design were discussed in an earlier report ⁽⁵⁾. Four of the 5 Design C nose cones tested are designated as suspended items. Three of these have not yet failed while one was damaged by the failure of another component. Data presented in this manner enables the improved performance of the Design C nose cone to be readily observed. Similar comparisons have been made for the other ceramic components, but changes in methods of testing render comparisons difficult. It is expected that this technique will be used in subsequent reports, which should result in ready and accurate interpretation of the results of future design and material changes.

Another tabulation of durability data is shown in Table 3.4, which indicates the best life obtained to date on each component in terms of lights, static hours, dynamic hours, and a total of both static and dynamic durability. The best life data point for each of these conditions is underlined, and the resulting condition of each part is noted. This tabulation will be updated in future reports as durability increases.

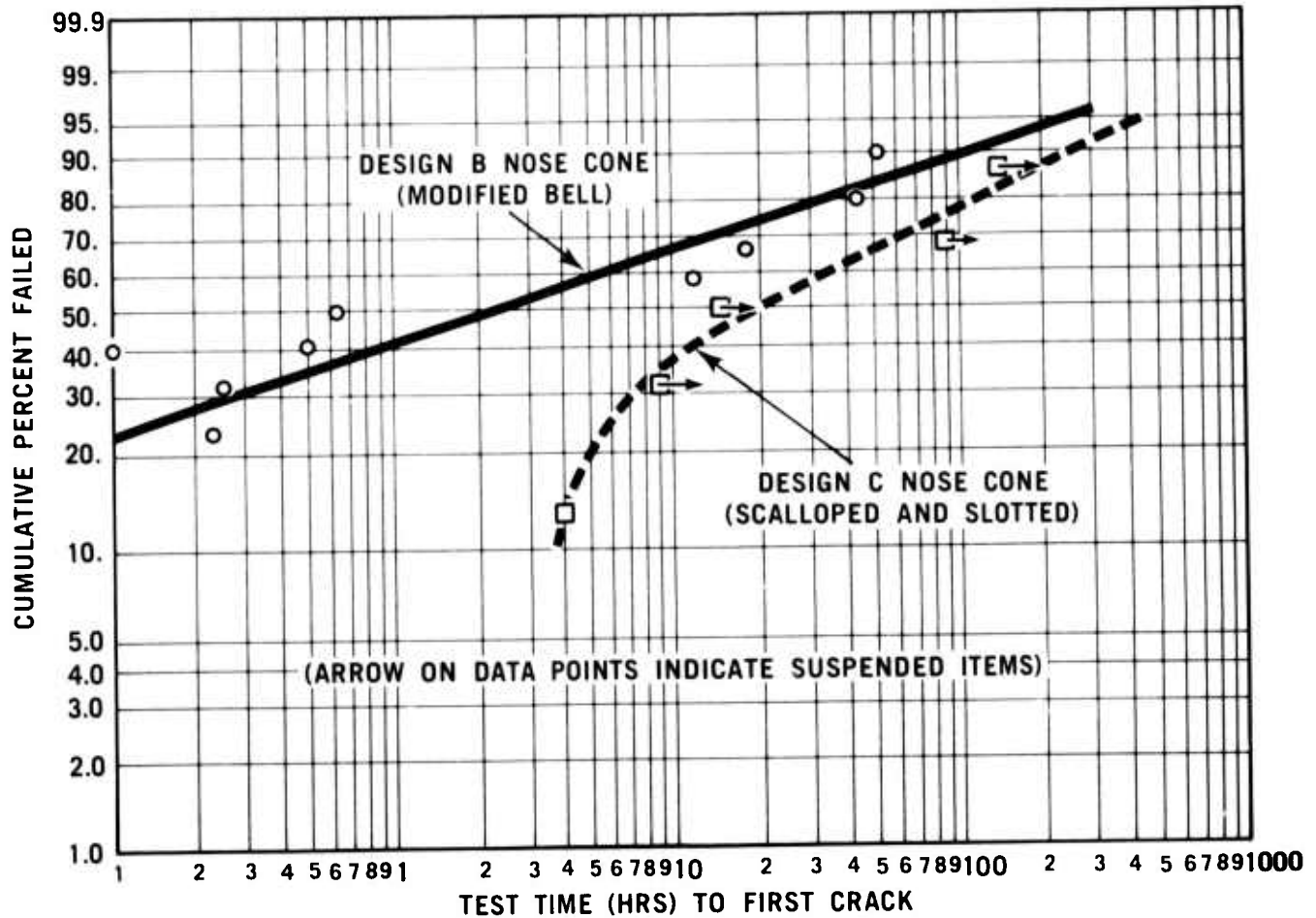


Figure 3.59 Statistical Interpretation of the Results of Ceramic Nose Cone Testing

TABLE 3.4

BEST LIFE ON CERAMIC COMPONENTS

<u>Component & Serial Number</u>	<u>Lights</u>	<u>Static Hours</u>	<u>Dynamic Hours</u>	<u>Total Hours</u>	<u>Status</u>
Nose Cone					
20	61	139.5	0	139.5	S
35	264	<u>159</u>	4	<u>163</u>	S,C
71	422	9	0	9	S
103	<u>74</u>	37	<u>51</u>	88	S
First Stator					
363	78	<u>111</u>	0	<u>111</u>	F,C
366	403	3.5	27.5	31	F,X
367	<u>289</u>	45.5	0	45.5	F,V
372	13	0	<u>50.5</u>	50.5	S
First Shroud					
4	308	<u>134.5</u>	31	<u>165.5</u>	F,K
9	498	42.5	28.5	71	F,K
24	<u>81</u>	78	<u>74.5</u>	152.5	S
Second Stator					
5	19	35.5	<u>54</u>	<u>89.5</u>	F,V
6	47	<u>75.5</u>	0	<u>75.5</u>	F,C
7	<u>163</u>	.5	5.0	5.5	S
Second Shroud					
10	759	<u>16</u>	37	53	F,K
12	<u>85</u>	9	<u>86</u>	<u>95</u>	S
38	22	0	<u>50.5</u>	<u>50.5</u>	S

S - Serviceable

C - Cracked Shroud

F - Failed

X - Result of Other Component Failure

V - Cracked or Broken Vanes

K - Part Failed Due to Creep

3.3 GAS BEARINGS

SUMMARY

A gas bearing system has been selected for the high temperature vehicular gas turbine to eliminate the presence of oil cooling and lubrication required with conventional oil lubricated bearings. The system features HYDRESIL⁽²³⁾ foil type gas bearings developed for Ford by Mechanical Technology Inc. The first generation of these bearings, featuring a single-leaf foil, has been tested successfully in a dynamic simulator test rig up to 95% of engine speed. The second generation, featuring 3-leaf bearings, is being prepared for testing. The 3-leaf bearing is expected to improve performance and alleviate some of the assembly problems associated with the current single-leaf version. Immediate plans call for construction of a single journal test rig to be used in the evaluation and development of high temperature ceramic coatings and journals.

3.3.1 GAS BEARING DESIGN AND DEVELOPMENT

Introduction

Use of the engine working medium (air) as the lubricant for the rotating components in the hot section of the engine offers an ideal solution to cost and thermal problems experienced with conventional organic or mineral lubricants. In addition, it alleviates problems of emissions associated with oil leakages and subsequent mixing with the engine air flow. Since performance of gas bearings improves with increased lubricant temperature, thermal gradients in turbine rotors and stators can be reduced. The soak-back problem, which is so troublesome at engine shutdown with conventional lubricants, will also be eliminated.

Application of ceramics to gas bearings alleviates several serious design problems commonly encountered with this type of bearing in gas turbine applications:

- (a) The lower thermal expansion of ceramic materials, as compared to metals, provides dimensional stability over the complete operating range. This is one of the most critical parameters in gas bearing design and application.
- (b) Certain ceramics or ceramic coatings exhibit excellent wear resistance and lubricity and can tolerate dry starts and occasional rubs experienced during dynamic overloads.
- (c) Extreme surface hardness of a ceramic bearing system will greatly enhance bearing resistance to scuffing.

The HYDRESIL foil bearing developed for Ford by Mechanical Technology Inc., Latham, NY, was selected as having potential for satisfactory bearing performance and low cost.

Gas Bearing Design

The HYDRESIL foil bearing as shown in Figure 3.60 is comprised of a thin foil tape which forms the bearing surface and is supported by a series of raised resilient corrugations. The corrugated bumps provide resilience in the radial direction as well as coulomb and viscous damping. As a result the bearing appears stable for high speed rotating systems and acts as a damping device for control of shaft vibrations. The bearing also exhibits simplicity of construction and excellent self alignment characteristics.

The design of the gas bearings and the analysis of the necessary dynamic response of the rotor-bearing system was performed by Mechanical Technology Inc. The analysis included; modeling of the rotor, calculations of bearing reaction loads and shaft deflections, determination of the static and dynamic characteristics of all supporting bearings, calculation of rotor critical speeds versus various gas bearing stiffnesses, and rotor amplitudes in response to mass unbalances, plus determining the degree of instability of the rotor-bearing system over the range of operating speeds.

The selected rotor bearing system configuration consists of one oil-lubricated journal bearing, one oil-lubricated spiral grooved thrust bearing and two air lubricated HYDRESIL foil bearings (2 in. dia. x 2 in. length) located at the ceramic turbine end of the shaft. Analysis indicates that the rotor-bearing system should perform well. The critical speeds have been removed from the operating range (idle to full speed) and the shaft displacements have been contained within design limits.

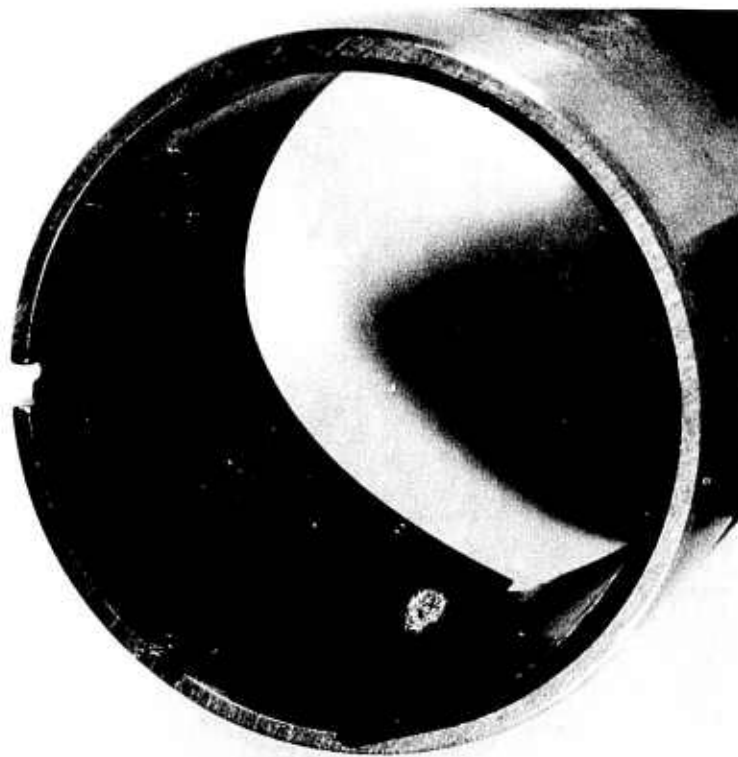


Figure 3.60 Single Leaf HYDRESIL Foil Bearing

A single gas bearing configuration has been investigated but was found inadequate to support the heavy metal shaft. Future plans, which include investigation of ceramic journals, call for a more detailed study of this configuration.

Gas Bearing Dynamic Simulator Test Rig

To properly integrate a gas bearing supported rotor system into the high temperature ceramic gas turbine engine, development work must be carried out in a Rotor-Bearing Dynamics Simulator Rig. Such a rig (Figure 3.61) was designed and constructed to simulate the actual dynamic conditions of the engine. This rig allows a major portion of the development work to be carried out under closely controlled conditions not always possible with the actual engine.

The Rotor-Bearing Dynamics Simulator Rig consists of a high speed shaft and components assembly (Figure 3.62) mounted in two air-lubricated HYDRESIL foil bearings (2 in. dia. x 2 in. length) at the turbine end plus a spherical seated oil-lubricated journal bearing, and an oil-lubricated spiral grooved thrust bearing at the compressor end. The rig uses engine housings and internal parts wherever possible. It is driven by an electric motor through the engine gear train and is capable of operating over the entire engine speed range (0-65000 rpm). A special bearing loading system has been incorporated so that intentional unbalance forces can be introduced at various locations to carry out bearing unbalance response studies. Bearing temperatures and cooling air flow are monitored, and bearing deflections and rotor shaft center line orbits can be monitored at various axial stations; each station consists of a horizontally and vertically placed capacitance probe providing signals which can be combined and shown as x-y displays on oscilloscopes. These signals accurately define the rotor shaft behavior at all times.

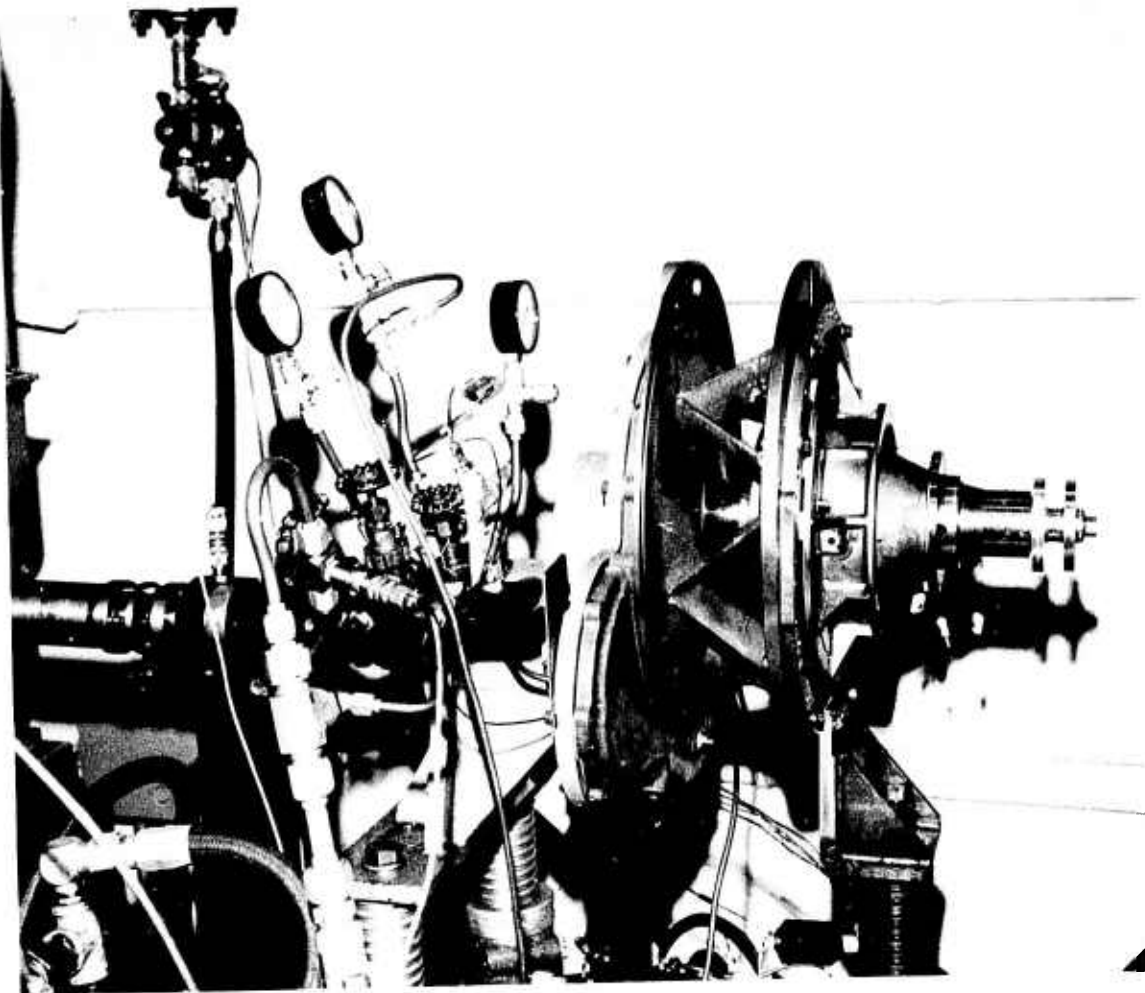


Figure 3.61 Rotor-Bearing Dynamics Simulator Rig

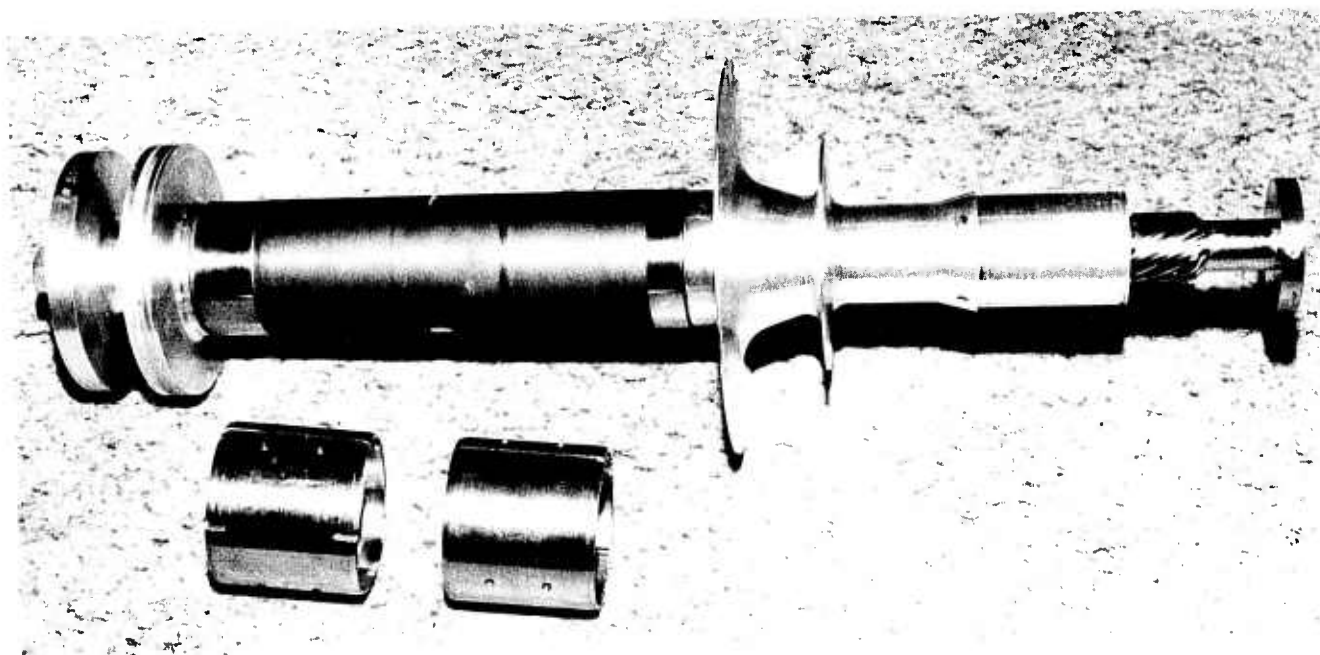


Figure 3.62 High Speed Rotor Simulator

Base Line Tests

The first generation HYDRESIL foil bearings (Figure 3.60) consisted of a single 360° foil leaf. The foil leaf is coated with molybdenum disulfide while the mating steel journals are coated with flame-sprayed chrome oxide. Initial tests indicated that the compressor and turbine components which comprise the high speed rotor assembly were shifting relative to the shaft center line at various rig speeds. As a consequence the rig could only be operated to 32,000 rpm (50% engine speed) at which time the rotor shaft center line orbits began to exceed allowable limits. The turbine and compressor simulator mountings were redesigned to correct this situation. Testing with redesigned mountings was successful to 60,000 rpm (92% engine speed). The rotor shaft center line orbits indicated a stable well-behaved system throughout the operating speed range. Recorded bearing temperatures were low (170 F at 60,000 rpm) indicating that the bearings were lightly loaded.

Future Plans

A second generation HYDRESIL foil bearing (Figure 3.63) consisting of three 120° foil leaves is currently under design and fabrication. These bearings will provide improved load carrying capacity, improved damping properties, and will make rotor shaft installation easier. The rotor shaft system mounted on these three-leaf gas bearings will be tested in the near future.



Figure 3.63 Three Leaf HYDRESIL Foil Bearing

4. PROGRESS ON THE STATIONARY TURBINE PROJECT

4.1 STATOR VANE DEVELOPMENT

SUMMARY

Most of the design effort has been directed toward the modification of the rotating test turbine for 2300°F average turbine inlet temperature, the temperature required to produce peak temperatures of 2500°F locally on the first-stage ceramic stator vanes. A preliminary design specification has been completed for the first-stage stator row and support structure including modification of the inner and outer support rings. Piping and passage requirements have been determined to accommodate the cooling air for the first stage rotor and all subsequent downstream stages of the turbine. A first stage air-cooled rotor blade design has been submitted for bid and fabrication.

As it now stands, both silicon nitride and silicon carbide stator vanes will be evaluated in the test turbine. Two stator vane design configurations are being considered. The second generation design which features tapered-twisted airfoils with tenons enlarged to fill the end cap cavities completely will be installed in limited numbers if static rig results are favorable. A modification of the first generation design featuring tapered-twisted airfoils with tenons representing a torroidal shape superimposed upon the airfoil cross-sectional geometry will be used to fill most first row stator vane positions. The final selection of materials and design can only be made at the conclusion of static rig tests, however, since catastrophic failure must be avoided at all cost when a multi-million dollar machine is involved.

Analysis indicates that maximum principal stresses would approach 100,000 psi if the loading area at the airfoil end cap interface of the first generation design stator vane assembly was reduced to 0.002 in² as it was in the silicon nitride components which failed during static rig testing at 2200°F. A preliminary stress analysis was also performed on the second generation design. The maximum principal stress may reach 125,000 psi under emergency shut down conditions where an average vane surface temperature of 2500°F is reduced to 350°F in 80 seconds. If this result is confirmed by component failure in the static rig at 2500°F, the second generation design will be excluded from further evaluation in the rotating turbine.

The static rig was rebuilt for 2500°F peak temperature service. Five cycles were run to 2300°F to establish heat up and cool down control parameters for the full 2500°F cyclic test sequence. Damage to the ceramic duct and mixer terminated testing. Silicon nitride and silicon carbide stator vane assemblies suffered no apparent damage.

Norton shipped eight sets each of NC-132 silicon nitride and NC-203 silicon carbide stator vane assemblies fabricated to the second generation design specification. These have been qualified by NDT methods of inspection and are now undergoing dimensional checks at GTSD prior to static rig testing at 2500°F.

4.1.1 DESIGN

Introduction

The large size of the Westinghouse stationary power turbine permits a ceramic stator vane design which is particularly well suited to brittle materials. A three-piece vane assembly has been selected to replace the more conventional geometry in which the airfoil is integral with the shrouds in order to minimize stress and simplify fabrication. The use of silicon nitride or silicon carbide stator vanes is intended to increase the service temperature of the resultant machine from 1955°F, average turbine inlet temperature at reserve power to a peak of 2500°F without a need to cool the first stage stator row.

Now that silicon nitride stator vane assemblies have been tested in the static rig under cyclic conditions to a peak temperature of 2200°F,⁽⁵⁾ most of the design effort is directed toward the actual modification of the test turbine for the final evaluation and demonstration of ceramic stator vanes.

The Rotating Test Turbine

Layout drawings and design specifications have been prepared for the modification of the W251 test turbine rotating rig. An average turbine inlet temperature of 2300°F was selected for the design to meet the 2500°F peak temperature requirement on the first stage stator vanes. Since only the first stage vanes will be made from ceramic materials, considerable attention has been given to the cooling of metal components downstream and the cooling air supply.

To begin with, the turbine cylinder or blade ring (Fig. 4.1), which is represented normally as horizontally joined half cylinders enclosing all three stages of the power turbine, has been split and flanged to form upstream and downstream segments. Silicon nitride and/or silicon carbide stator vanes and support structure, including insulator blocks and spring loaded metal shoes, are contained within inner and outer support rings, which are bolted to the static seal housing and the upstream portion of the segmented turbine cylinder, respectively. The first stage rotor and all subsequent downstream stages remain within the downstream segment of the blade ring, remembering that the test rig differs from an actual power generating turbine in that the entire third stage is removed. Work in excess of that required to drive the compressor is expended against an eddy current brake and there is no generator coupled to the shaft of the test turbine.

The ceramic vane assemblies, insulators, seals, and support structure which constitute the first stage stator vane row of the turbine test rig will be the same design as those used for static rig tests.⁽²⁾ A full complement of 80 vanes will be tested in the turbine, however, rather than the cascade of 8 vanes which comprises the test configuration in the static rig.⁽⁴⁾ The performance of two airfoil geometries will be compared. Eight to ten airfoils will be of second generation design, i.e., tapered, twisted airfoils with dog-bone torroidal ends shaped to completely fill the cavities in mating end caps. The alternative airfoil is also tapered and twisted for proper flow orientation to the first rotating stage. However, the torroidal tenon ends are machined to shape the airfoil cross-section in a fashion similar to that of the

first generation design.(2) Trailing edge relief is provided as shown in Fig. 4.2. Hot-pressed silicon nitride (Norton Noralide NC-132) and hot-pressed silicon carbide (Norton Noralide NC-203) will be represented in the turbine tests by alternating the materials as stator vane assembly pairs in the circumferential array which forms the first stage vane row (the nozzle guide vanes). The second generation design vanes, if employed, will appear in pairs (both Si_3N_4 or SiC) uniformly spaced throughout the full 360° with the actual number used determining the interval. They will not be isolated in a single sector.

This discussion is the first inference of a test plan for the operation of a stationary power turbine containing ceramic vanes in the first stage stator row. The costs involved in the manufacture and operation of a 30 Mw frame size machine dictate the adoption of an extremely conservative test philosophy. While the cracking of vane components can be tolerated, every precaution must be taken to preclude any possibility of large fragments of failed ceramic vanes being

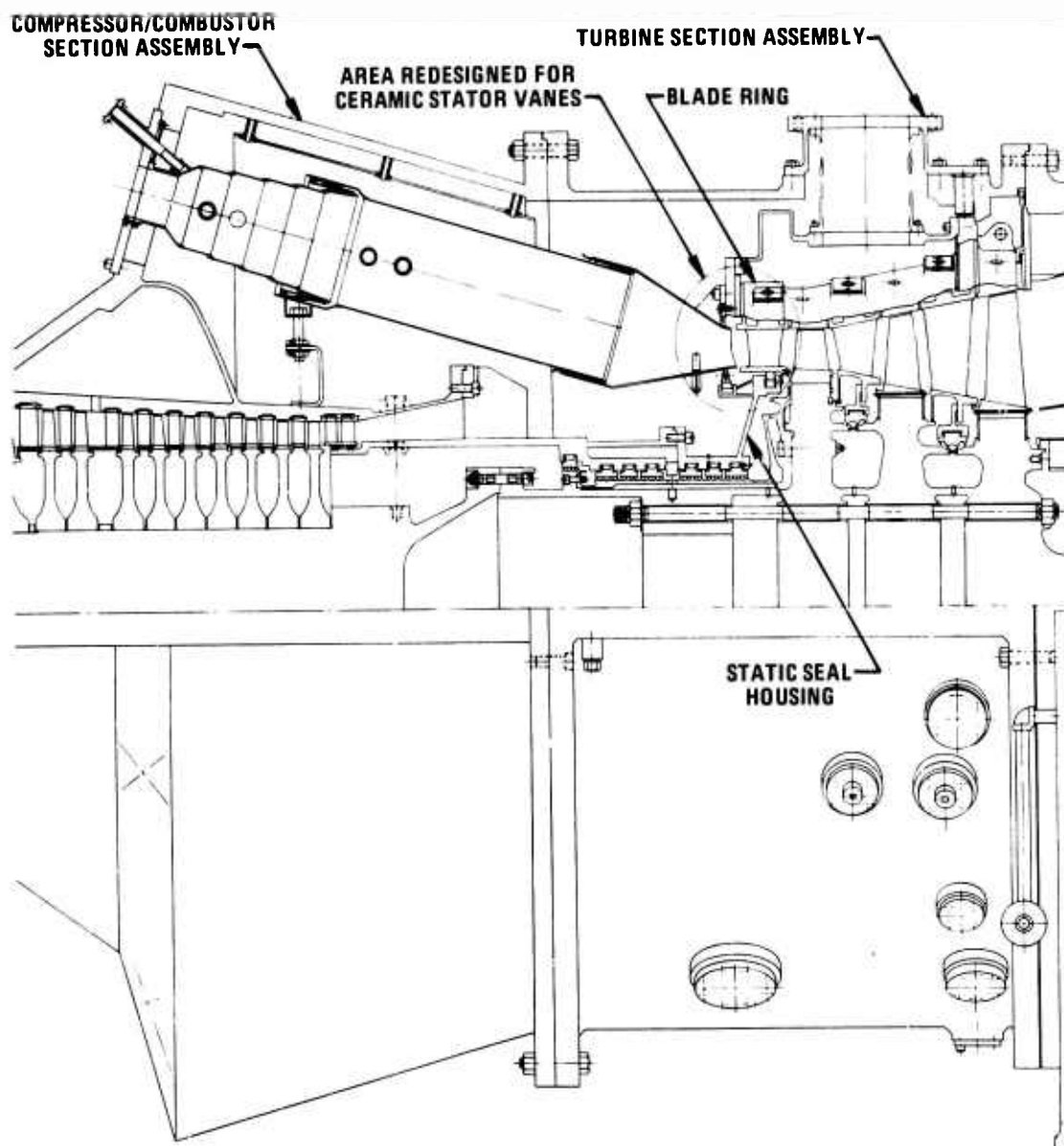


Figure 4.1 -- W-251 Rotating Test Turbine

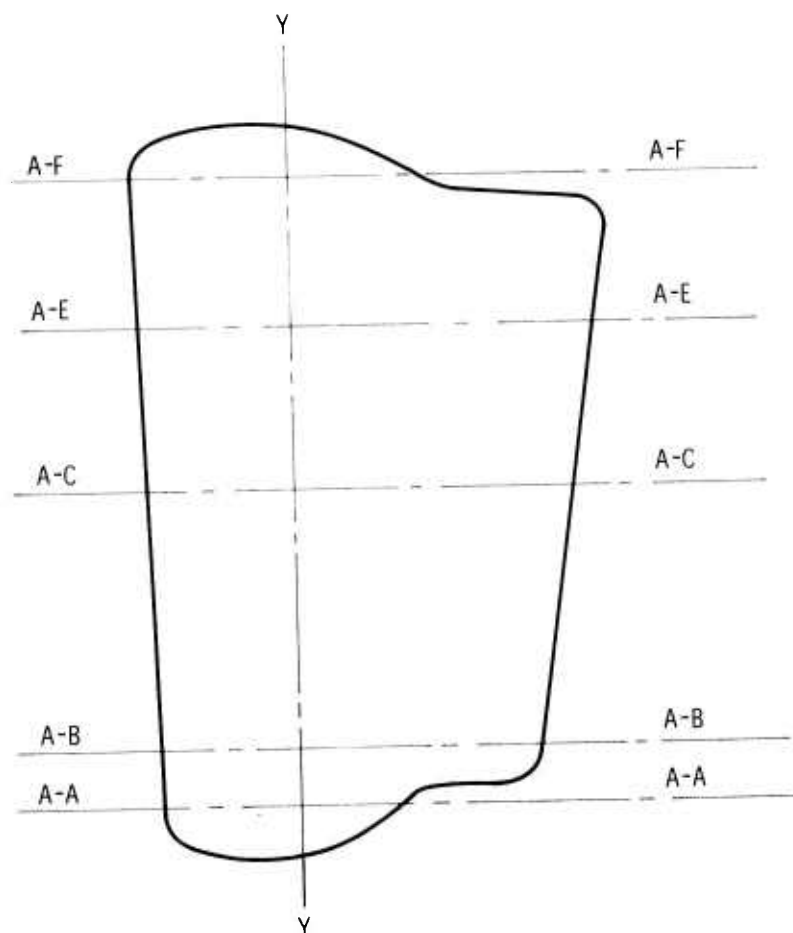


Figure 4.2 -- Tapered-Twisted Airfoil Section - Stator Vane Assembly for Rotating Turbine Test

discharged downstream to impact rotating parts leading to catastrophic failure of the power section. Therefore, no design or material which has not been fully qualified by extensive static rig testing will be evaluated in the turbine. The subjective probability of failure for the second generation design is high and static rig tests are expected to disqualify it from further testing. There is little experience with hot-pressed silicon carbide at this time although it is more sensitive to surface defects, is susceptible to static fatigue from a fracture toughness standpoint, and appears to be less thermal shock resistant than hot-pressed silicon nitride. The fact that hot-pressed silicon carbide is stronger and more creep resistant than hot-pressed silicon nitride at temperatures above 2100°F may be very significant because a degree of plastic response may be required to reduce thermal stress transients in vane applications.

The general cooling flow requirements for the turbine and the design concept for an impingement, convection cooled first stage rotor blade were presented in the last report.⁽⁵⁾ First stage rotor blading has been ordered from a casting vendor for delivery in approximately one year. Although the existing castings can be used, the second stage vane segments require redesigned cooling inserts and an extensive modification of the inner shroud region to supply additional cooling air to the second row rotating blades and the faces of the first and second turbine rotor discs.

The second row rotating blades will be cooled by air passing radially outward through a series of round holes extending from the root of the blade to the tip of the airfoil. These holes will be electro-chemically machined into existing blades which are now solid forgings. Cooling air is supplied to the blade roots through a series of holes drilled in the second row disc. Most of the cooling air holes have been enlarged. Minor modification of the stationary ring segments over the two rotor blade rows is also required.

Since the metal components of the first stage stator vane support structure are cooled by air from the compressor shell, the air box which supplies the required auxiliary cooling air has been made smaller and two pipes have been added to feed the air box system. These lines make two additional penetrations through the turbine cylinder mandatory.

Additional design effort is required for the modification of the exhaust cylinder, the exhaust manifold and mixer, and the exhaust ducting systems. The supervisory instrumentation to ensure safe operation of the rig and to determine the environment must also be defined.

4.1.2 THE STRESS ANALYSIS OF STATOR VANES

Introduction

Finite element stress analysis was used to describe the state of stress in the silicon nitride stator vanes which failed in the static rig at 2200°F, an apparent result of out-of-tolerance machining. The preliminary stress analysis of the second generation vane assembly design is also discussed.

Stress Analysis Motivated by Static Rig Test Results

Additional stress analyses were performed to help explain vane failures from the 2200°F static rig tests. These failures were attributed to edge loading or a contact stress problem resulting from out-of-tolerance machining of both the airfoil tenon and end cap cavity.⁽⁵⁾ Contact scars and the differential accumulation of combustion by-products and/or corrosion presented direct evidence of the point loading condition.

The existing finite element model was modified to consider the effects of a constant radial load applied over three small areas of contact between the airfoil and the end cap in any desired combination. Moreover, the area of contact, for the case of a single load uniformly applied near the leading edge of the airfoil, was reduced four times. Contact area versus the greatest maximum principal stress was plotted for the five conditions analyzed to permit an estimate of the contribution to failure by the non-contact stress as a function of contact area. The results are presented in Fig. 4.3. Certainly the maximum principal stresses contribute significantly to failure if the loading area is

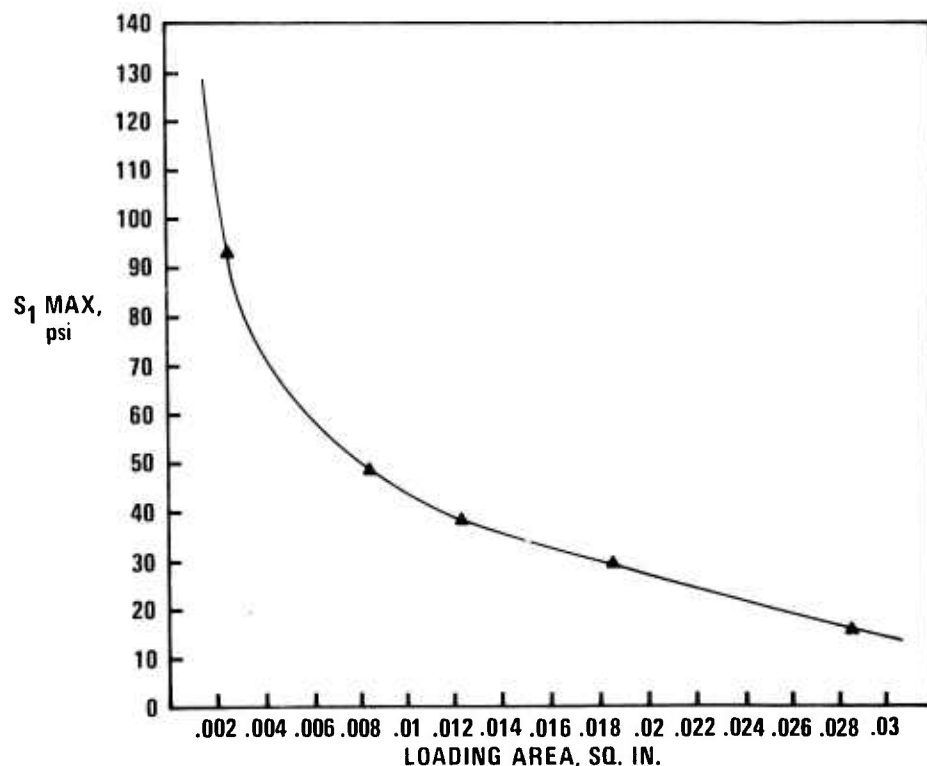


Figure 4.3 -- Effect of Loading Area on the Maximum Principal Stress

reduced in magnitude to point or line contact as observed at the airfoil tenon-end cap cavity interface.

The shape of the fracture surfaces of the failed airfoils suggest the possibility of torque applied on planes normal to the radial direction. Boundary value problems have been solved but the magnitude of the unit couple (applied at two of the same contact areas already chosen) can only be estimated roughly at this time. The mechanical boundary load results can be superimposed on the thermal stress results to approximate the effect of the operating conditions better. However, since the magnitude of stresses obtained from the thermal analysis is very dependent on the temperature distribution obtained from the heat conduction analysis which, in turn, depends upon the film heat transfer coefficients over the boundary surface, more reliable data are required. Instrumented metal vanes and end caps will be tested to yield low temperature heat transfer coefficients from which extrapolation of higher temperature results is justified. Strain gauges will be used to check the final results of the analysis.

4.1.3 STATIC RIG TESTS

Introduction

The static rig was initially designed and built to meet the 2200°F requirements for testing ceramic stator vane assemblies and all of the support structure, including insulators, in a cascade of eight vanes. Chromel-Alumel thermocouples, the metal duct, and mixer sections performed well in the 100 cycle sequence operating from 1200 to 2200°F. These rig components have been replaced with Platinum-Platinum-10 Rhodium thermocouples and a silicon nitride bonded silicon carbide duct and mixer, respectively, for 2500°F testing. Pertinent features of the static rig modification, certain delays in the resumption of testing, and the cursory results of cyclic tests to establish control parameters for 2500°F operation are discussed.

The 2500°F Static Rig Modification

The static rig modification for 2500°F service was completed in early June with the installation of the ceramic mixer section. A series of silicon nitride bonded silicon carbide tubes are arranged or angled in what is essentially a large ceramic cylinder to form the gas mixer which receives hot combustion gases from the ceramic duct. These tubes mix the hot central portion of the profiled gas stream with cooler gases from the periphery to level thermal gradients and produce uniform exhaust gases entering the spool piece where the rig control thermocouples are located. Other changes, including instrumentation, the wide angle boroscope, 3 radiation pyrometers, the silicon nitride bonded silicon carbide duct, and the rapid data acquisition and processing system, were described in detail in the last report.⁽⁵⁾

Platinum-Platinum 10% Rhodium thermocouples were installed at control locations in the static rig. Chromel-Alumel thermocouples will continue to be used in the rake locations to establish profiles in the gas path temperatures, to establish control parameters and to calibrate the rig. However, these activities will be accomplished at 2200°F peak temperature as measured in the vane inlet area because thermocouple rakes with 2500°F capability are not available. The control temperature and temperature profiles for actual 2500°F peak temperature tests will represent a 300°F extrapolation of the 2200°F calibration conditions. Three radiation pyrometers will monitor temperatures at the vane leading edge position. The upstream thermocouple rakes at vane inlet and exit will be withdrawn during 2500°F testing.

2500°F Test Components

The cascade test fixture⁽⁵⁾ has been reassembled with new ceramic vane assemblies and insulators. First generation design silicon carbide airfoil and end caps were used to fill test positions 5-8. Untested silicon nitride components of the same design tested at 2200°F occupy positions 1-4. Second generation design silicon nitride and silicon carbide vane assemblies together with four silicon nitride vane assemblies tested previously⁽⁵⁾ are also available. These components will be substituted periodically during the 100 cycle test program to insure the broadest possible evaluation. Vanes must survive a full 100 cycles at 2500°F, however, to qualify a material or design for turbine test.

New insulators were developed because the lithium aluminum silicate (LAS) used originally cracked badly at the leading edge. Insulator materials to be tested in the static rig now include:

- 1) Si_3N_4 (Reaction Sintered - AME, England)
- 2) Si_3N_4 (Hot-Pressed - Norton Co.)
- 3) BN (Combat Type A - Carborundum)
- 4) BN- SiO_2 (Combat Type M - Carborundum)
- 5) Fiber-frax-filled, Mast. X Honeycomb (Fab. by Precision Tool)
- 6) LAS (Cervit-140 Owens Illinois) shape changed to provide better load distribution
- 7) SiAlON (Hot-pressed grade - Mfd. by W R&D)

The design has been changed to crown or radius the circumferential edges of the insulator to eliminate edge loading and wedging at this location. The honeycomb seals in the test assembly were replaced with 70% dense fiber felt to maintain the proper temperature at the leading edge of the insulator.

LAS, reaction bonded Si_3N_4 , and hot-pressed Si_3N_4 insulators are represented in the initial assembly of the test fixture for 2500°F testing. One LAS insulator of the design used in the 2200°F tests has been included for control and comparative purposes.

2500°F Static Rig Tests

Static rig testing was resumed in June after a 6 month delay caused by the late delivery of the ceramic mixer section. The modified version of the static rig was baked out for 16 hours at 1800°F. Following this, the rig was cycled between 1200 and 2200°F at 0.5 simulation (5 atmosphere pressure) to establish the effect of a 10°F/sec ramp rate at the control position. The ramp rate had been reduced from 25°F/sec to anticipate the effects of thermal lag resulting from the ceramic duct and mixer. After 2 cycles, the pressure ratio was increased to 8:1. Testing was terminated at the end of the 5th cycle when pieces dislodged from the ceramic duct were heard striking the metal exhaust manifold and hot spots developed on the shell wall. A peak temperature of 2300°F was recorded on the fifth cycle.

Preliminary Stress Analysis of Second Generation Vane Assembly

A preliminary thermal transient stress analysis of the second generation airfoil was performed for conditions of parabolic surface temperature decay from a constant 2500°F to 350°F in 80 seconds. The airfoil cross section at its end cap cavity entrance location is illustrated in Fig. 4.4. The finite element model with typical values of maximum principal stress resulting from thermal deformations at the nodal points appear in Fig. 4.5. The greatest maximum principal stress (166000 psi) occurs 8 seconds after shutdown in the region where the geometric approximation of the finite element model is the poorest; i.e. the transition region between the airfoil and tenon at the leading edge.

Since one of the standard checks incorporated into WISEC (Westinghouse Three Dimensional Isparametric Finite Element Code) confirmed the

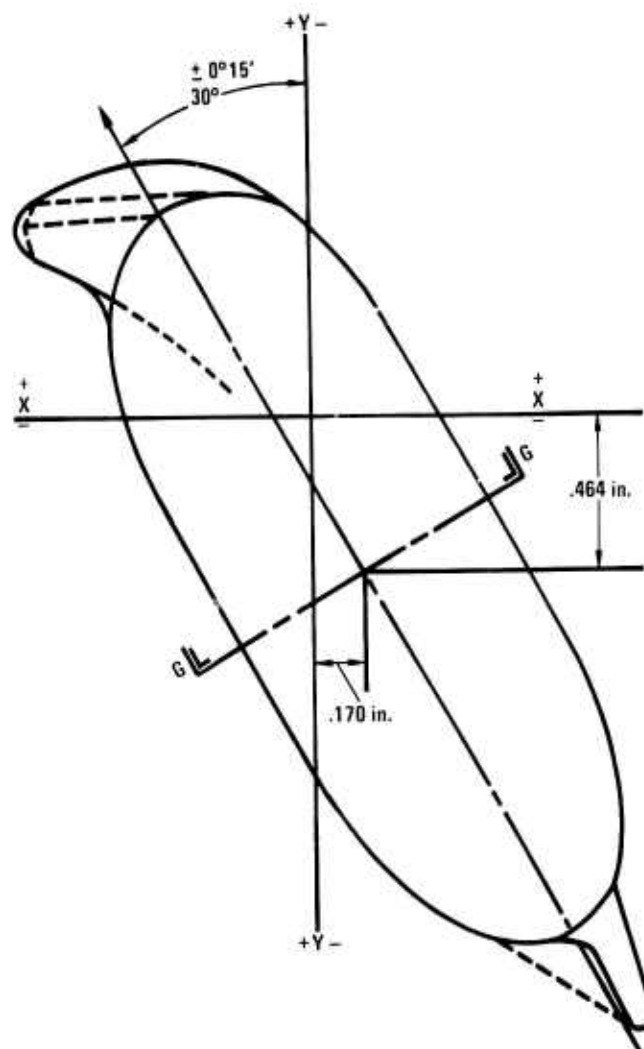


Figure 4.4 -- Second Generation Airfoil Cross Section at the End Cap Surface

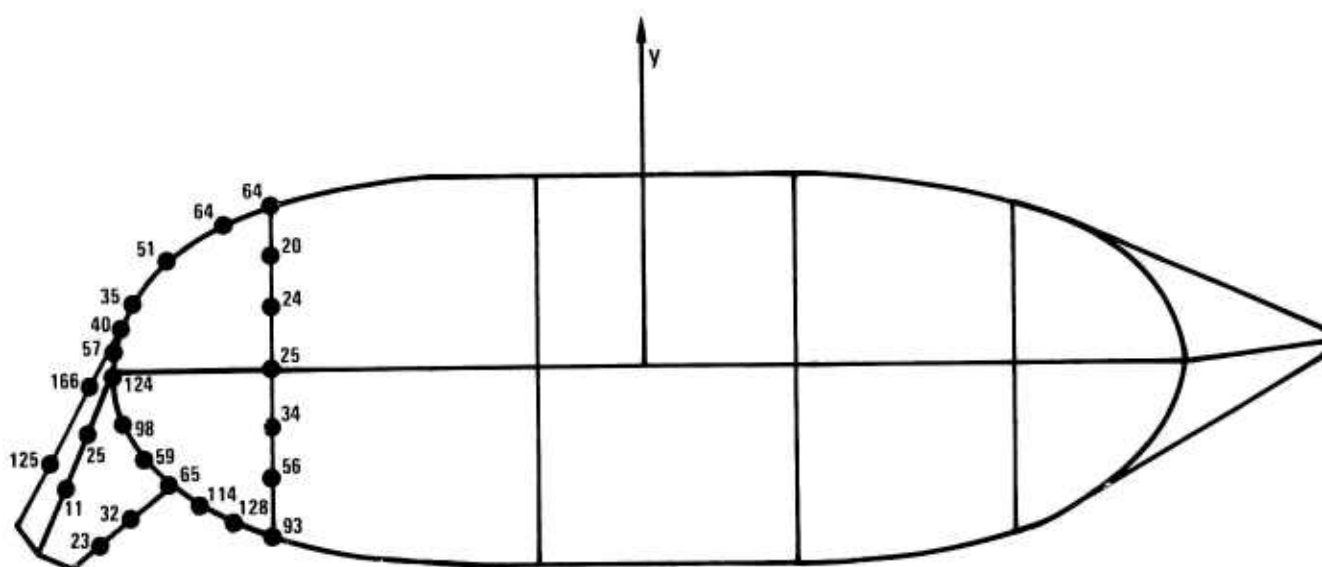
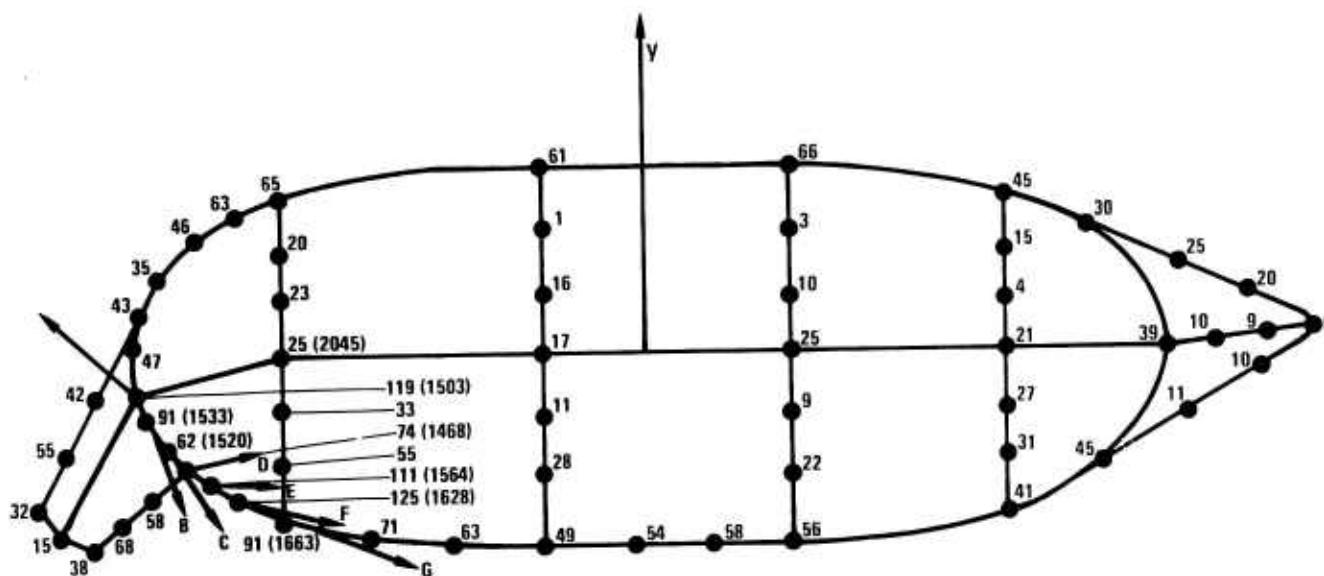


Figure 4.5 -- Finite Element Model of Airfoil Section (Selected Stress Values in KSI)

These results are considered preliminary in that only half the airfoil was represented based on the assumption of symmetry about any line perpendicular to the radial direction. The model should include the entire airfoil because taper makes it asymmetric with respect to lines perpendicular to the radial direction. Since the end cap models will be developed simultaneously, elements in the airfoil and end caps will be made to coincide so that displacements in the surface of the airfoil tenon can be compared easily with those of the corresponding end cap cavities.

The airfoil-end cap interface must be designed to prevent edge loading which could cause catastrophic failure of both vane and end cap. A shift of the contact area to achieve kinematic equilibrium has been discussed.(3) Edge loading occurs when the displacement of the contact center is large enough to reduce the actual contact area; i.e., where the nominal contact surface is moved beyond the extent of the pieces in contact. This creates a much higher stress field or region of contact singularity.(4) In order to preclude any such singularities, the center of contact under conditions of zero load must be located on the airfoil cross section in such a way as to provide adequate vane area for the contact area to be displaced from the zero load position without edge loading the vane. The contact conditions most likely to cause the edge loading effect for any interface geometry are the two extremes of the coefficient of sliding friction; i.e., $\mu_{su} = 0.45$ and $\mu_{su} = .05$. If the friction coefficient is high, which occurs particularly when the interface is hot, the center of contact tends to remain at the



97

zero load position. The contact area approaches the concave side of the airfoil under these conditions. At low friction coefficient, more of the gas load is reacted by normal forces across the interface, and larger shifts of the center of contact from the zero load position are required. In this case, the contact area approaches the convex side of the airfoil.

Two elliptical contact areas are projected onto the vane cross section of the inner interface in Fig. 4.7. These contact areas represent $\Delta R = .002''$, the minimum design difference in the vane and end cap torroidal radii. Here, the center of contact at zero load is located in the wider section of the airfoil near the leading edge where there is enough vane area to prevent edge loading of the vane on either the concave or convex side. At higher values of ΔR , the contact area is smaller. This allows for more clearance between the contact area and the airfoil perimeter. The tensile stress due to contact increases directly with the radial difference, however, and values of ΔR which may be used have an upper bound based on the contact stresses.

The effect of varying the coefficient of sliding friction and the radial difference on the maximum tensile stress due to contact is shown in Figs. 4.8 and 4.9. The maximum and minimum stress conditions appear at points A and B, respectively. There is a large range of stress

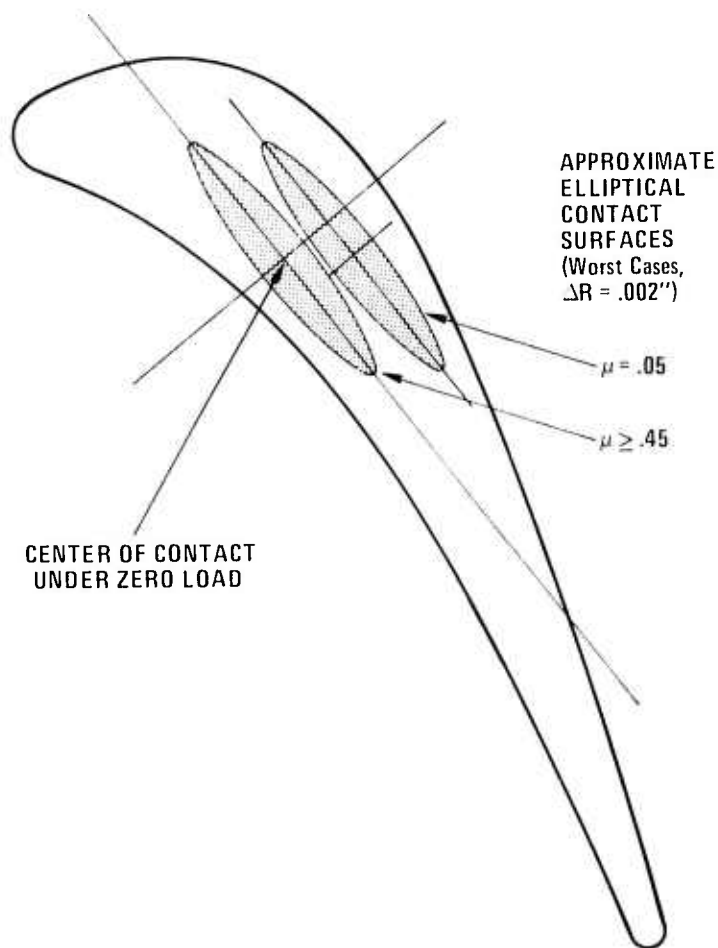


Figure 4.7 -- Vane Cross Section Showing Elliptical Contact Surface Projections for the Worst Contact Conditions at the Inner Vane-End Cap Interface

values possible as a function of friction and radial difference. The maximum value of contact tensile stress under start-up conditions is 16,500 psi for $\mu_{SU} = .25$ and $\Delta R = .008$. At shutdown, the maximum anticipated value of contact tensile stress is 17,000 psi where $\Delta R = .008$ and $\mu_{SU} = .05$. A design incorporating high contact stresses was selected to preclude any possibility of edge loading in the vane.

The temperature change recorded at the vane inlet position during startup and shutdown followed that at the control position. A desired ramp of 25°F/sec at the vane inlet was not achieved by controlling temperature increases and decreases at 10°F/sec.

All of the vane hardware survived without damage. Xyglo dye penetrant failed to disclose any evidence of cracking in either silicon nitride or silicon carbide airfoils or end cap elements. The control insulator, lithium aluminum silicate without edge relief, chipped at the leading edge location reminiscent of the 2200°F static rig tests.⁽⁵⁾ All other insulators, even those made from LAS survived indicating that the design change had been partially successful. The seal change apparently helped also.

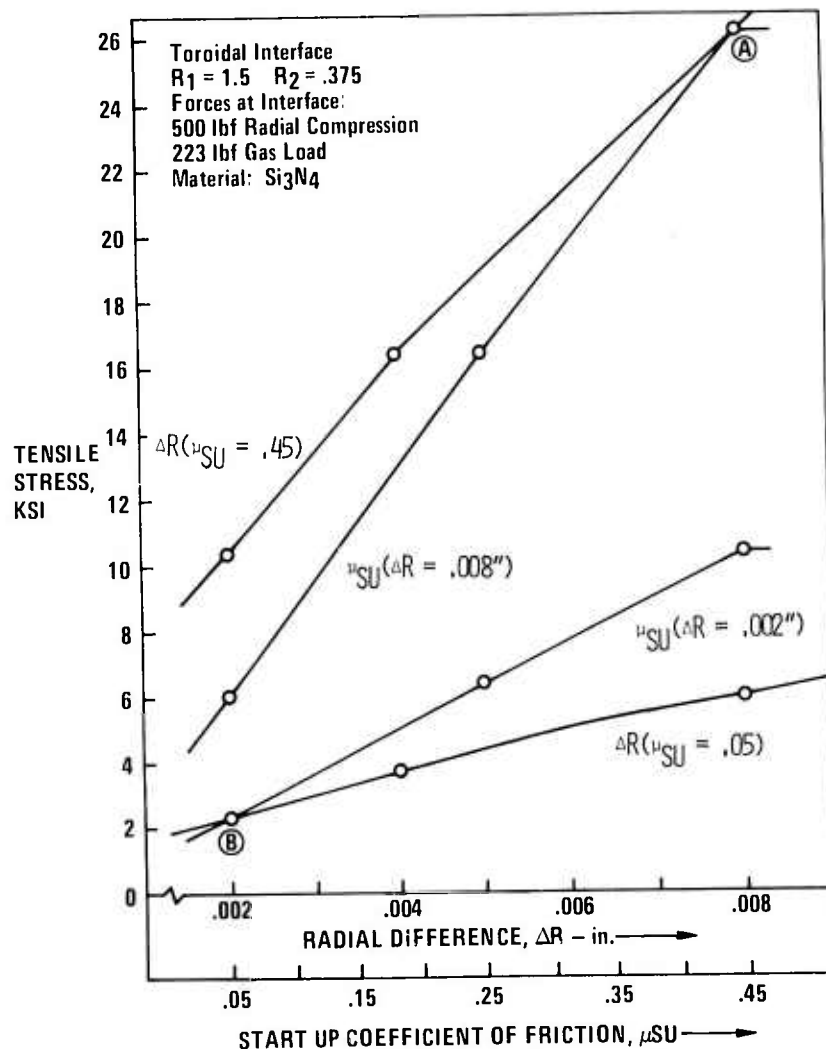


Figure 4.8 -- The Effects of Parameter Variation on Contact Tensile Stress at the Airfoil-End Cap Interface Under Start Up Conditions

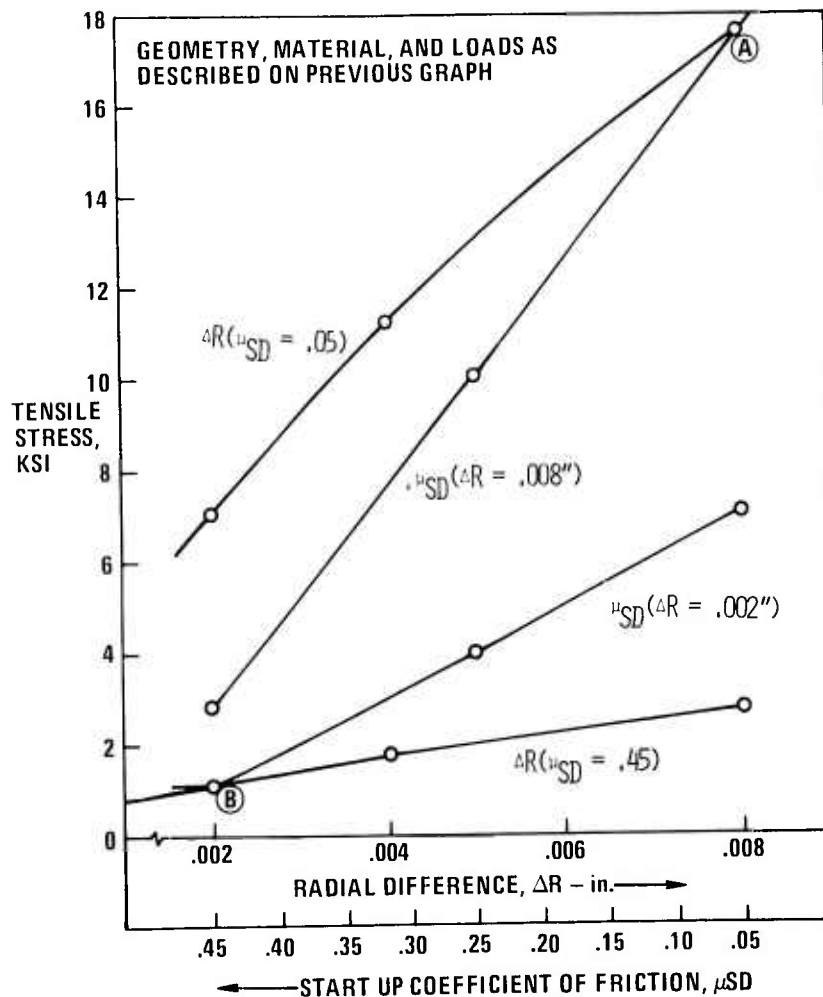


Figure 4.9 -- The Effects of Parameter Variation on Contact Tensile Stress at the Airfoil-End Cap Interface Under Shut Down Conditions

Examination of the ceramic duct after test revealed severe cracking and the loss of large pieces from the section. The metal substructure which encapsulates the duct and insulation was distorted badly. Thermal shock apparently cracked the duct allowing hot gas to penetrate to the metal support locally. Non-uniform thermal stress gradients warped the metal causing shifts to occur in the cracked duct which then permitted high velocity gas to dislodge failed sections and propel them downstream through the mixer and spool out into the exhaust manifold.

The mixer section was not damaged excessively. A few holes were observed in the Refrax tubing but these apparently resulted from erosion by the high velocity gas stream rather than by impact. Cavitation appeared to remove insulating material from behind the tubes where the holes broke through the tube walls. Instrumentation downstream remained unaffected.

The Westinghouse P-2500 computerized data acquisition system which accepts and stores data on tape at 40 increments/sec worked extremely well. Results are produced directly in engineering units at 20 increments/sec.

Unfortunately, the static rig testing of silicon nitride and silicon carbide stator vanes must be delayed until the aft end of the static rig is rebuilt. A spare Refrax duct is available and the ceramic mixer, which, incidently, performed its function very well, can be used again with minor repair. In any event, repairs are expected to take six to eight weeks. The 2500°F static rig tests should be resumed by September 1, 1974 and run through October barring further difficulty.

A water cooled metal duct has been ordered to replace the ceramic duct in the event of future failures. Should installation of this component be required, testing could be delayed until December to make provisions for an adequate water supply. Alternatives for the ceramic mixer are being considered.

X-ray radiography and ultrasonic scanning indicated that the silicon nitride and silicon carbide were remarkably free of high and low density inclusions, respectively. The X-ray radiography disclosed density variations in silicon nitride which were not observed before.

Gas Turbine System Division personnel are performing the dimensional inspection now. These components will be represented in the 2500°F static rig tests on a substituted basis. They do not constitute part of the test configuration as presently assembled.

Eight to ten of these second generation design stator vanes will be installed in the rotating turbine for test and evaluation if performance in the static rig justifies such action.

Stator Vane Assemblies for the Rotating Test Turbine

Quotes have been received for the fabrication of 100 stator vane assemblies required to complete the first stage vane row of the rotating test turbine. The end caps are comparable to the second generation design. The airfoil design was discussed in Section 4.1 of this report. At the present time, NC-132 silicon nitride and NC-203 silicon carbide have been designated suitable vane materials. Both types will be manufactured in equal quantities unless or until one or the other is disqualified by static rig testing at 2500°F. Norton has begun to hot-press silicon nitride billets for the fabrication of airfoils and end caps and has made arrangements with a new vendor for the machining of airfoils in large quantities. Tooling has been ordered to meet the design specification. Norton and Westinghouse have discussed qualification specifications for acceptance of the components. Inspection and certification will be performed as part of the airfoil machining process to specifications agreed to mutually by Norton, Westinghouse and Ex Cello, the airfoil machining vendor. Ex Cello will make all the gillotine guage tooling required to qualify the airfoils.

4.1.4 VANE FABRICATION

Introduction

The Norton Company continues as the sole source of hot-pressed silicon nitride and silicon carbide for the fabrication of stator vane assemblies. Sixteen sets of second generation design silicon nitride and silicon carbide hardware were delivered. The silicon carbide end caps of first generation design were reworked to meet modified design tolerances. Silicon nitride billets are being produced for the fabrication of 100 stator vane assemblies to be tested in the rotating test turbine.

First Generation Silicon Carbide Vane Assemblies

Fourteen silicon carbide end caps were returned to Norton for rework when dimensional checks indicated discrepancies serious enough to cause edge loading along the airfoil-end cap interfaces. Norton corrected the problem by mechanical lapping which removed surface irregularities and increased the nominal major and minor torroidal radii by 0.005 in. An asymmetric condition in the cavity cross section was also eliminated in the process.

A bluing technique was used to confirm an acceptable fit between airfoils and end caps. Every possible combination was evaluated to assign elements of the vane assemblies on a best fit basis to minimize edge loading in subsequent static rig tests.

Second Generation Stator Vane Assemblies

The Norton Company delivered 16 stator vane assemblies conforming to the second generation design specification.⁽⁴⁾ Eight sets each were machined from Norton NC-132 silicon nitride and NC-203 silicon carbide. The components are illustrated in Fig. 4.10. Changes in the end cap are relatively minor. The major radius at the end cap-insulator interface has been reduced and the depth of the end cap cavity (not shown) has been reduced also. The airfoil was machined to reflect the proper taper and twist. The airfoil tenon now fills the entire end cap cavity.

Fluorescent dye penetrant failed to reveal any characteristic surface defects although chips were observed occasionally along the periphery of end cap cavities and on the trailing edges of the airfoils. These are considered serious because they represent probable sites for crack initiation. Prominent grinding marks and the random pattern of surface scratches observed previously⁽³⁾ were not identified. However, the airfoil surfaces were severely undercut at the fillet radius in all cases. In one instance, the end cap cavity broke through to the side surface of an outer end cap.

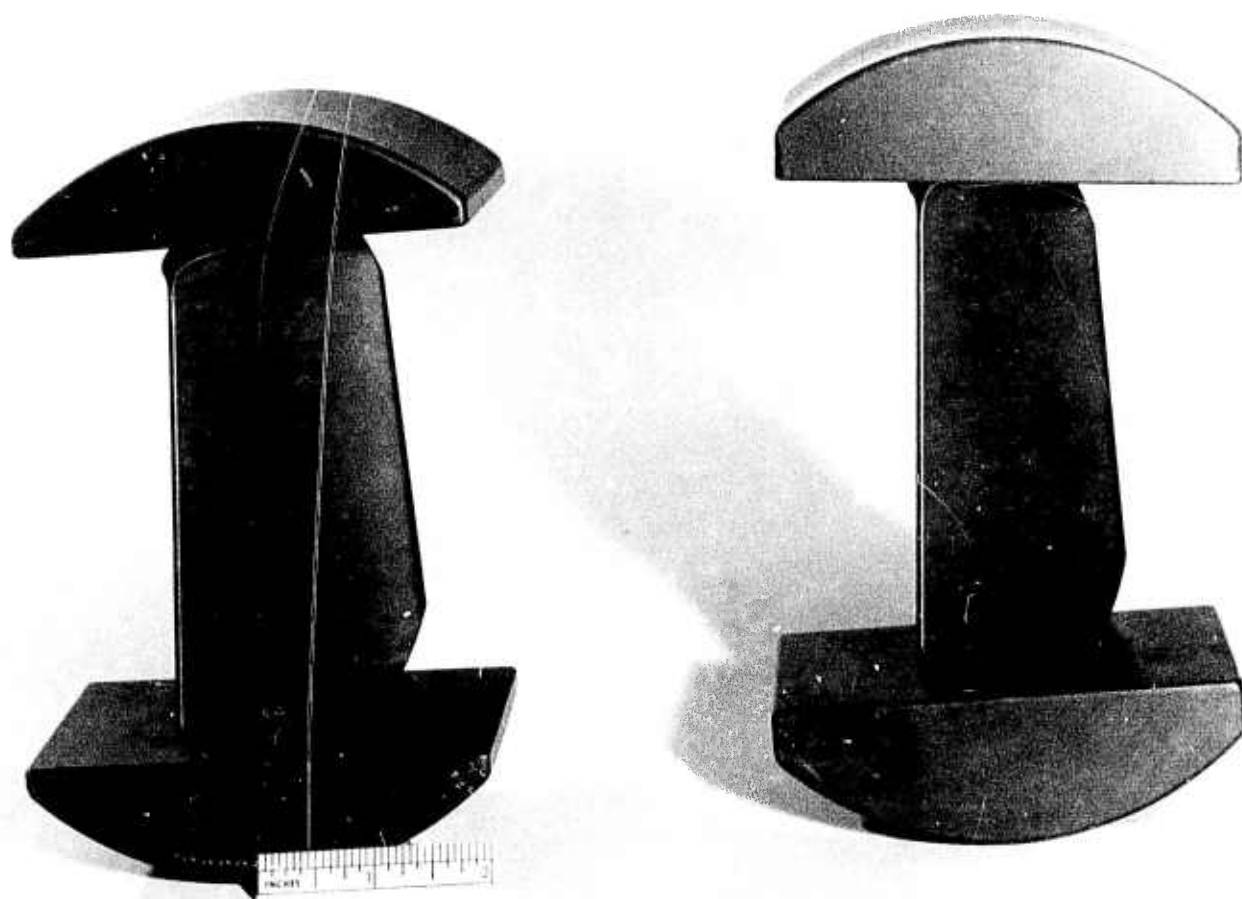


Figure 4.10 -- Second Generation Silicon Carbide (Left) and Silicon Nitride (Right) Stator Vane Assemblies

4.2 ROTOR BLADE DEVELOPMENT

SUMMARY

A rotor blade configuration is used to demonstrate the applicability of the WISEC computer code for analyzing three dimensional problems involving complicated geometries under high temperature loading conditions. Results indicate that a maximum tensile stress of 18,686 psi occurs in the root and that high stresses are confined to a small area near the neck of the root. However, the nature of several assumptions, namely that the blade is supported along a small contact area and that the frictional force is the maximum obtainable, requires that the stresses obtained from this analysis be interpreted as upper bounds to the actual state of stress. The maximum tensile stresses may be reduced by (1) altering the root geometry, (2) increasing the contact area, and (3) reducing the coefficient of friction through the use of a low friction material at the contact interface. Natural frequencies are reported for the stationary blade. The theory for finite element stress and heat conduction analyses are presented also. Additional work is underway to determine the vibratory and transient thermal stresses imposed on the blade during a full operating cycle.

4.2.1 WISEC ROTOR BLADE ANALYSIS

Introduction

The latest version of a ceramic rotor blade analysis is presented to demonstrate the current state of development of WISEC, the Westinghouse Three Dimensional Isoparametric Finite Element Stress Analysis Code. A steady state heat conduction analysis was performed to obtain the temperature distribution within the blade due to gas flow from the combustor. Stresses were then determined using the thermal distribution and the centrifugal force field induced at a rotational speed of 3600 rpm. (The results are not meant to represent the state of stress in an actual rotor blade because the W-251 test turbine is designed to operate at 4800 rpm with a blade of equivalent size.) WISEC utilizes the same collection of finite elements or mesh for both the heat transfer and stress analyses to simplify data preparation and to facilitate data transfer between both computer programs. Since linear elastic behavior is assumed, the stresses may be summed to yield the combined effects of steady state thermal and centrifugal loading.

The Analysis

The finite element model of the ceramic blade (Fig. 4.11) has been presented previously.⁽³⁾ This model may be viewed in five sections;

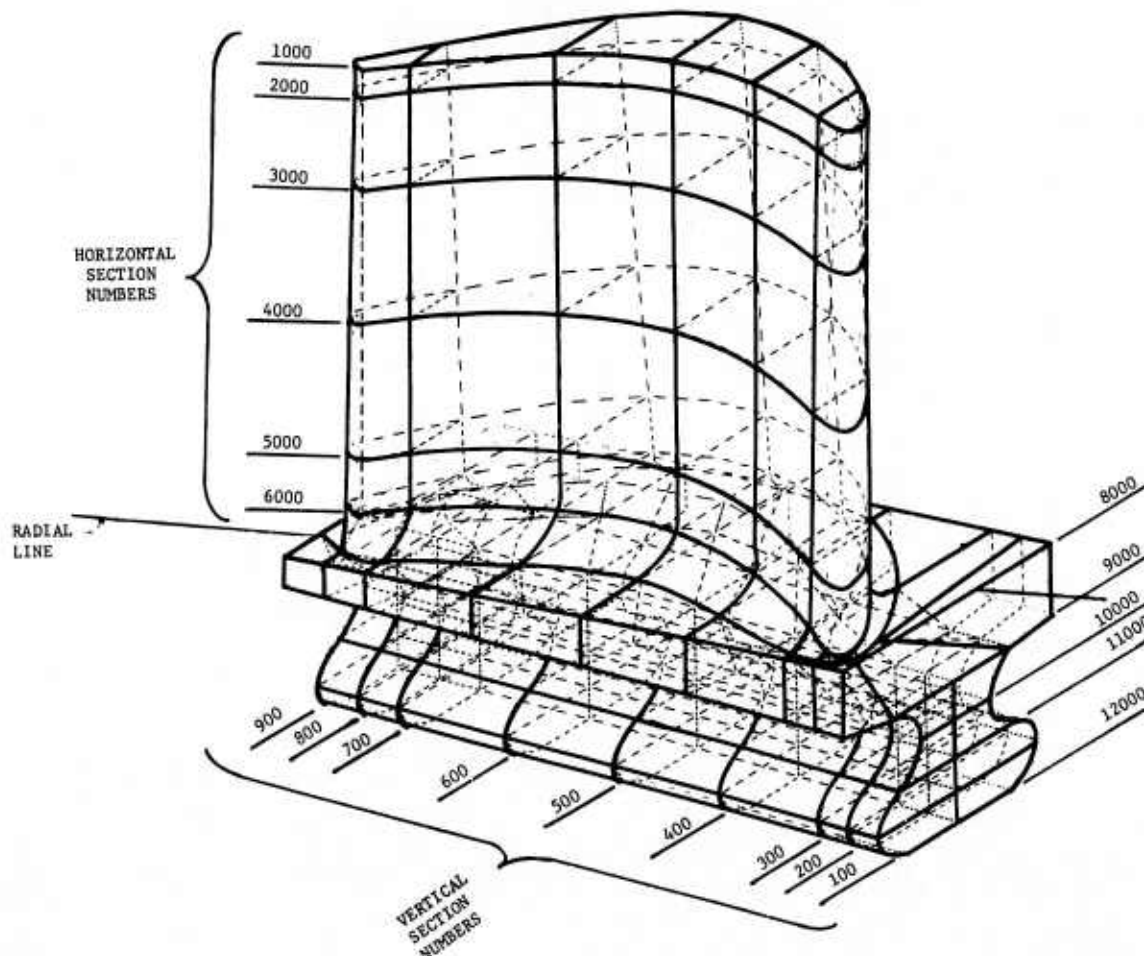


Figure 4.11 -- Computer Plot of Ceramic Rotor Blade

the airfoil, the airfoil-platform fillet, the platform, the platform-root transition, and the root base with cubic elements⁽¹⁾ used to describe the fillet and part of the root and quadratic elements elsewhere. The airfoil and platform geometries are similar to metal blade designs currently in use. The dovetail root was selected to compliment ceramic material properties specifically.

The blade is supported by the rotor disc (assumed to be rigid) along a strip near the intersection of Section 11000 and the root boundary surface (Fig. 4.11), an area of 0.52 in² on each side of the root. The effect of friction is simulated by a shearing traction of 8791 psi acting tangentially on the contact area. This magnitude is estimated by consideration of the friction coefficient and the angle of the root. A parametric study of the effect of varying contact area on the maximum tensile stress in the root was reported previously.⁽³⁾

Since a blade would be machined from billet material as shown in Fig. 4.12, it would reflect the orthotropic material properties of hot-pressed silicon nitride⁽³⁾ with the radial direction of the blade (the 2 axis in Fig. 4.12) corresponding to the strong direction of the material. Orthotropic material properties as well as temperature dependent materials properties are considered by the stress analysis code.

For the thermal loading, a boundary condition of forced convection is assumed. The inlet temperature profile is shown in Fig. 4.13. The surface film convection coefficient varies from point to point on the blade because of changes in Reynolds' number. The film coefficient (h) is considered constant on the platform and root area except in the contact area. Typical values of film coefficient with respect to airfoil location are given in Fig. 4.14.

Temperature distributions are represented in Figs. 4.15 and 4.16. These distributions remain essentially uniform through the thickness of the airfoil and follow variations in the inlet temperature profile closely (Fig. 4.13). The corresponding radial stress contours resulting from these temperature fields appear in Figs. 4.17 and 4.18. Other components of stress, not indicated here, are, in general smaller than the radial stress. Representative radial stress contours for centrifugal loading appear in Figs. 4.19 and 4.20, while Figs. 4.21 and 4.22 illustrate the corresponding stress contours for the combination of thermal and centrifugal loading.

A maximum tensile stress of 18,686 psi for the centrifugal loading occurs in the neck of the root near the middle of the airfoil, at Section 500. For the combined thermal and centrifugal loading, the maximum tensile stress of 18,509 psi also occurs in the root neck, but at Section 400. A two dimensional generalized plane strain study⁽⁵⁾ of the root area has shown that the maximum tensile stress in the root can be decreased by reducing the coefficient of friction, by increasing the contact area, and by choosing a 30° root angle instead of a 60° angle as was done in the present analysis. Only a moderate amount of bending occurs in the airfoil.

The natural frequencies were obtained for the airfoil section of the blade only, that is, the portion of the blade between the horizontal sections 1000 and 8000. The finite element model for the eigenvalue analysis consists of 40 quadratic elements with 345 nodal points.

The 43 nodal points at section 8000 were completely constrained so that the model has 906 degrees of freedom.

The material properties used in the natural frequency analysis are the same as used for the stress analysis. (2,3) The three lowest natural frequencies for the stationary blade computed by the program are:

Mode	Frequency in Hz
1	4770
2	6890
3	11000

These frequencies are considerably higher than for a metal blade of the same dimensions because the density of silicon nitride is lower than that of the metals used for blades and the modulus of elasticity is higher.

The tensile stresses in the airfoil of the ceramic blade caused by the centrifugal forces vary between 0 and 8000 psi. These stresses are too low to have a significant effect on the stiffness of the airfoil. The frequencies of the rotating blade obtained with the program are within the range of accuracy of the computer the same as those shown for the stationary blade.

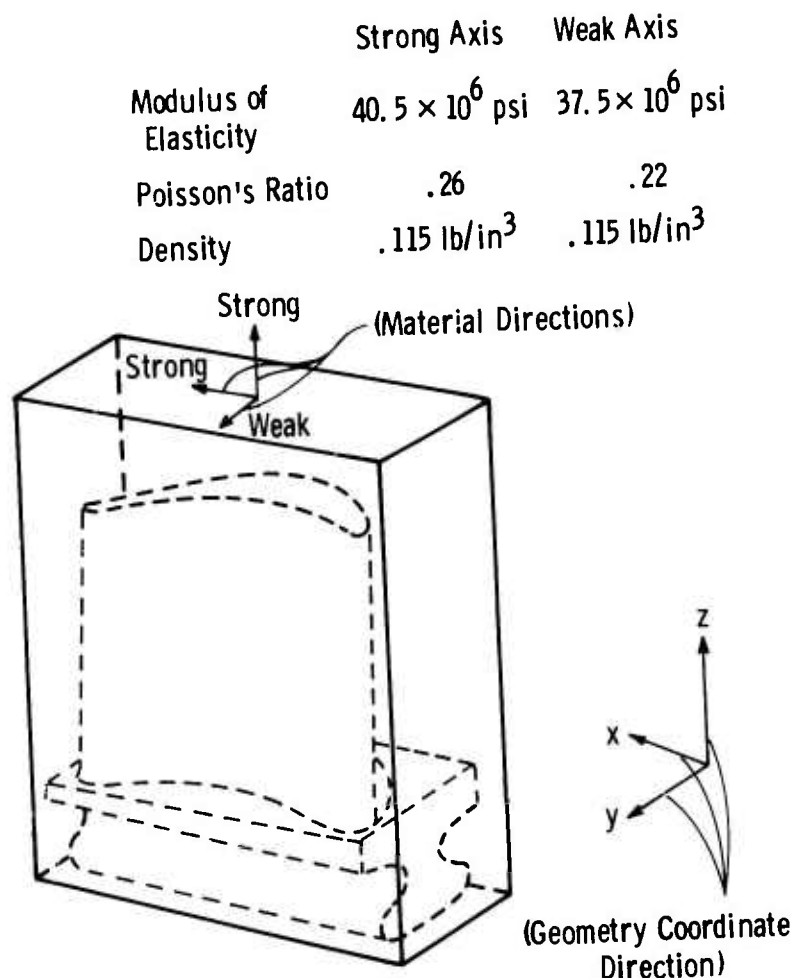


Figure 4.12 -- Material Orientation for Orthotropic Analysis

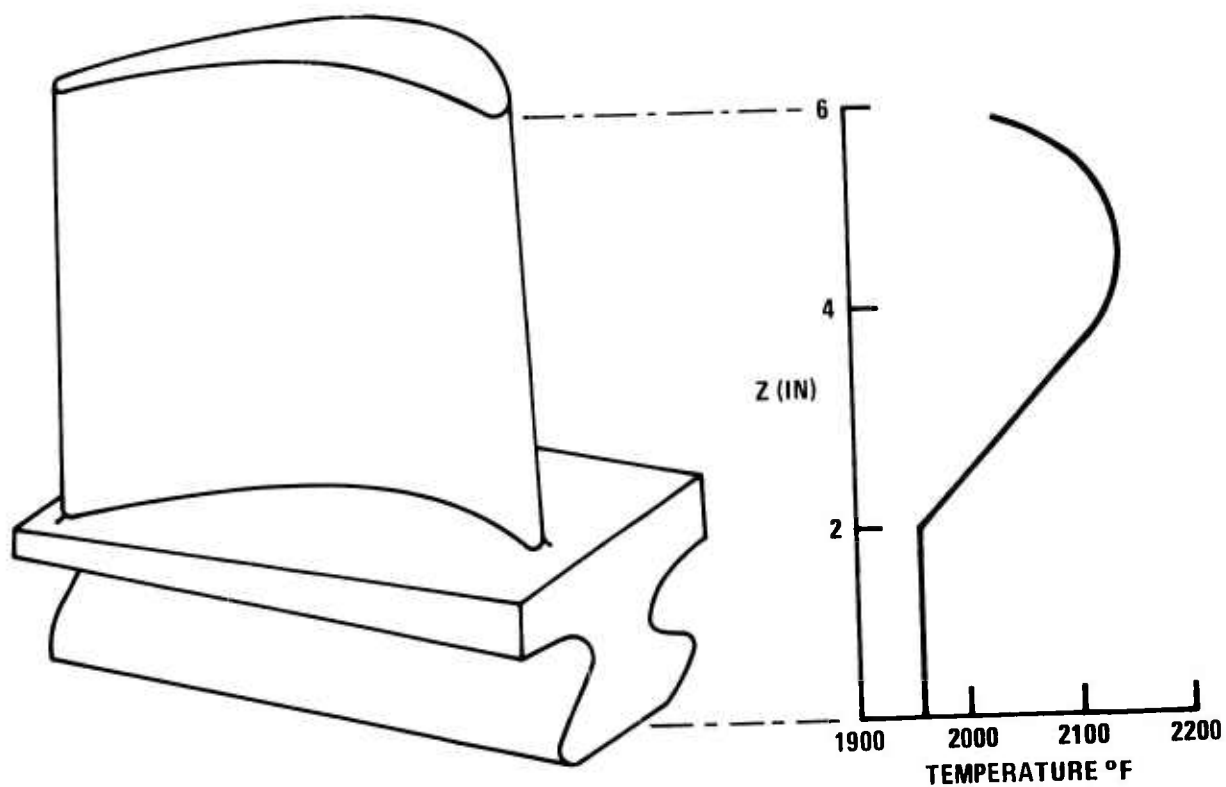


Figure 4.13 -- Inlet Temperature Profile

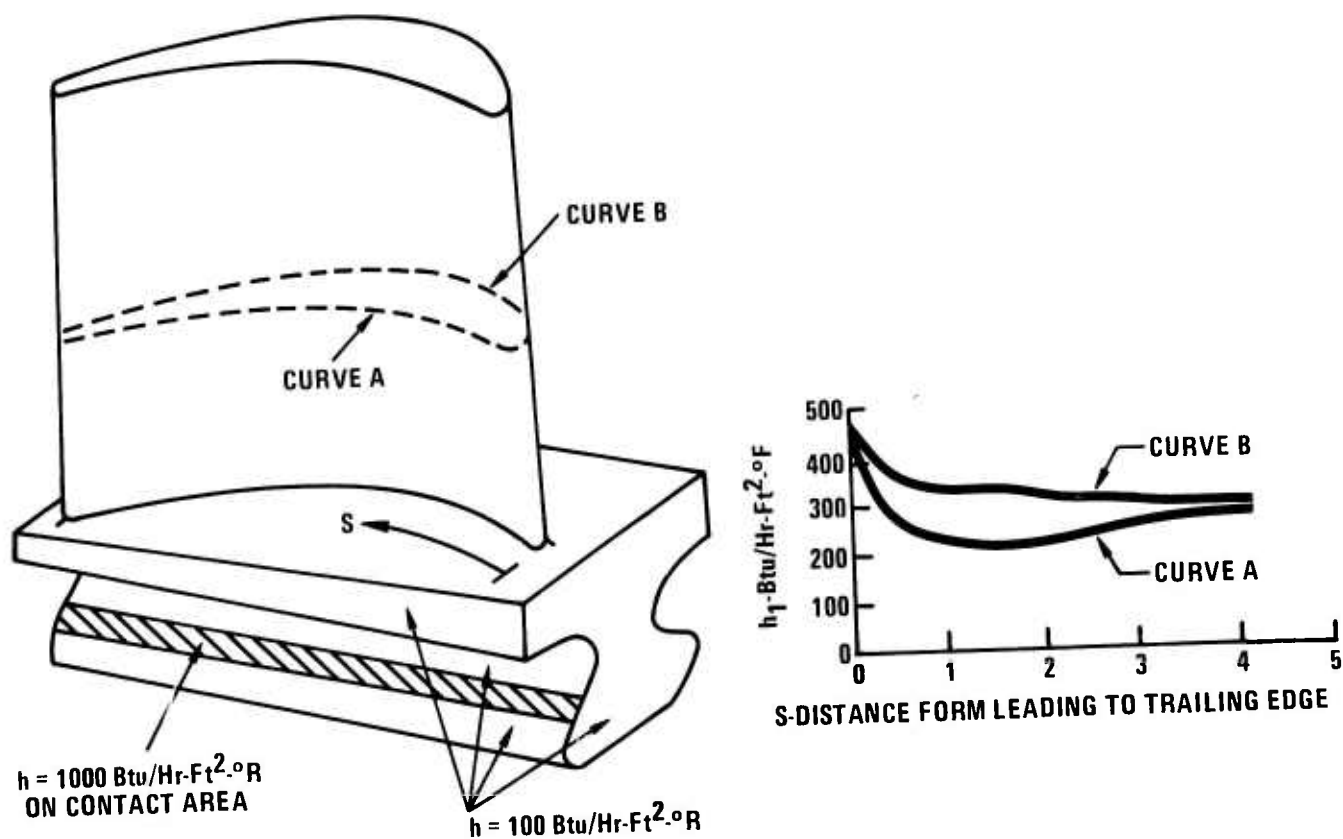


Figure 4.14 -- Film Convection Coefficients for the Ceramic Rotor Blade

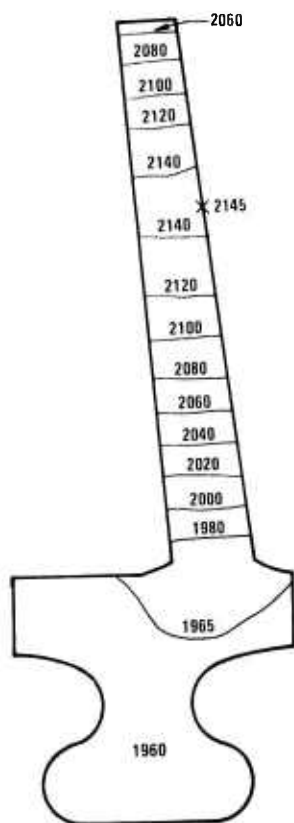


Figure 4.15 -- Temperature Distribution for Ceramic Rotor Blade at Section 300 (Contours-°F)

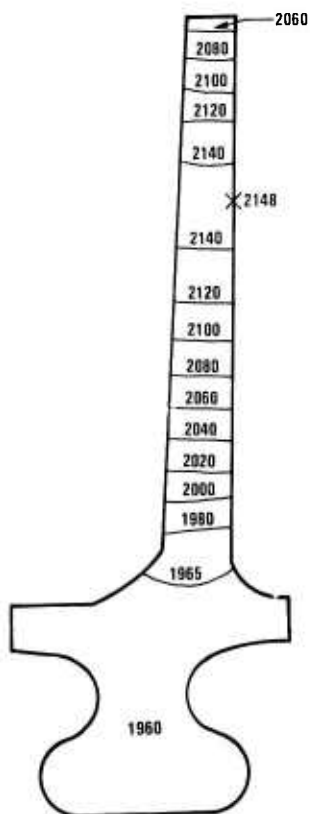


Figure 4.16 -- Temperature Distribution for Ceramic Rotor Blade at Section 700 (Contours-°F)

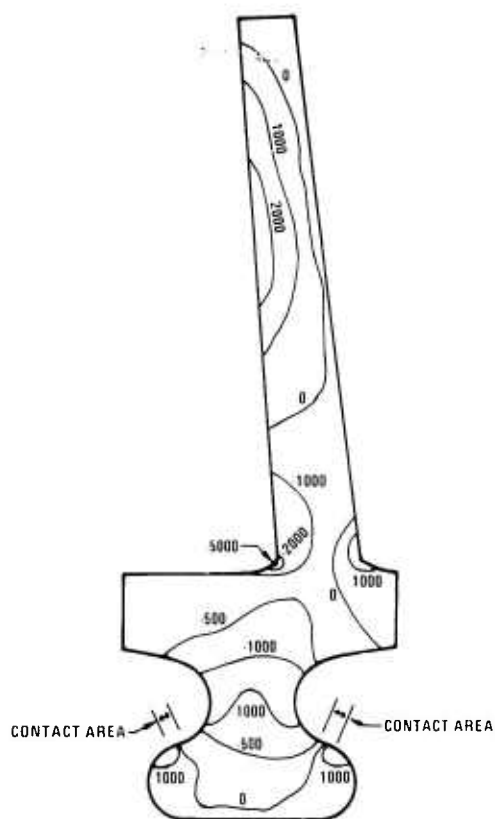


Figure 4.17 -- Steady State Radial Thermal Stress Distribution for Ceramic Rotor Blade at Section 300 (Contours-psi)

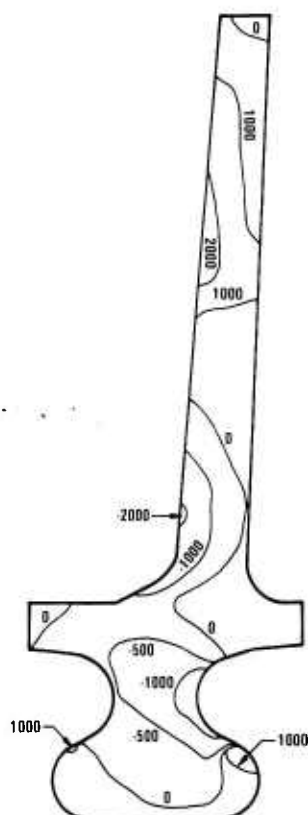


Figure 4.18 -- Steady State Radial Thermal Stress Distribution for Ceramic Rotor Blade at Section 700 (Contours-psi)

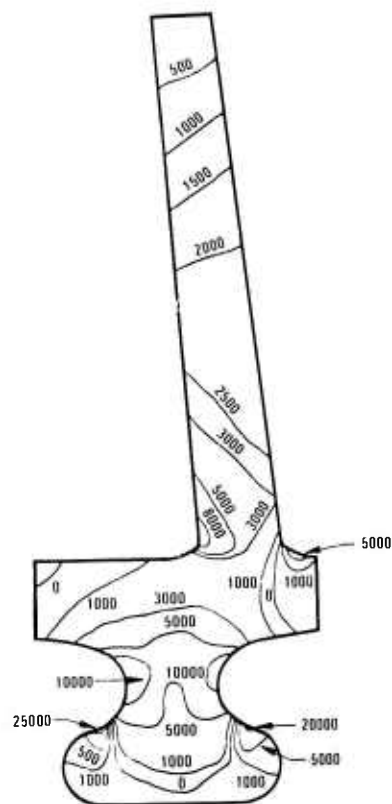


Figure 4.19 -- Radial Stress Distribution for Ceramic Rotor Blade Under Centrifugal Loading at Section 300 (Contours-psi)

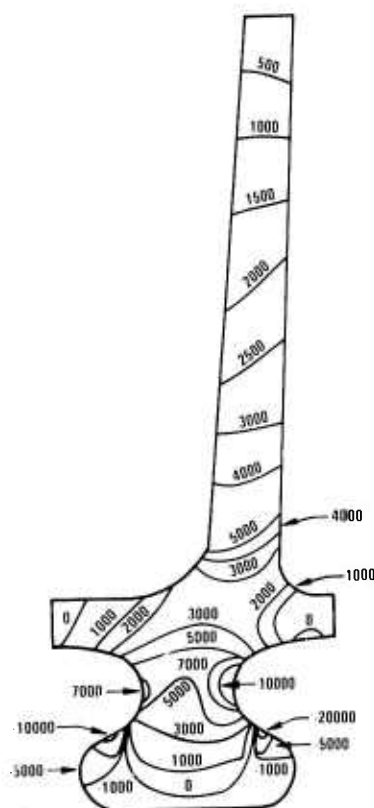


Figure 4.20 -- Radial Stress Distribution for Ceramic Rotor Blade Under Centrifugal Loading at Section 700 (Contours-psi)

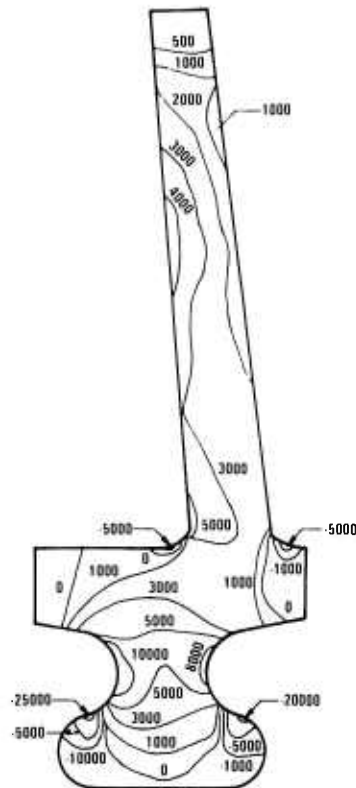


Figure 4.21 -- Combined Steady State Thermal and Centrifugal Stress Distribution for Ceramic Rotor Blade at Section 300 (Contours-psi)

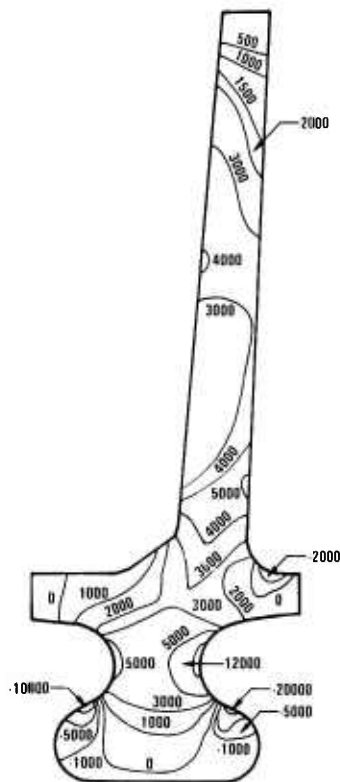


Figure 4.22 -- Combined Steady State Thermal and Centrifugal Stress Distribution for Ceramic Rotor Blade at Section 700 (Contours-psi)

5. PROGRESS ON MATERIALS TECHNOLOGY - VEHICULAR
 AND STATIONARY TURBINE PROJECTS

5.1 MATERIALS ENGINEERING DATA

SUMMARY

Design technology is highly dependent upon mechanical, chemical, and physical properties of the materials being used. This section deals with work performed during this reporting period on the acquisition of such property information. Many of the materials being investigated are in the development stage and improvements in properties are anticipated; this will require that some, if not all, of the properties must from time to time be redetermined. Therefore, property characterization of the ceramic materials for turbine engine use is a task which will continue throughout the life span of the contract.

Additional tensile strength testing of Norton hot pressed Si_3N_4 and SiC yielded data consistent with that previously reported. The Si_3N_4 material is stronger at intermediate temperatures, with the SiC material being stronger above 2300°F . Work on tensile creep measurement on hot pressed SiC has shown the existence of a corrosion problem between the test samples and the metal grips which produced premature failure. Because of this phenomenon, previous suggestions that hot pressed silicon carbide is stress-rupture limited appear premature.

Further corrosion-erosion testing of Norton hot pressed Si_3N_4 and SiC indicate some weight loss and loss of strength as measured at 2000°F . Initial reversible low cycle fatigue testing of HS-130 silicon nitride indicated relatively low life when hold times were imposed at maximum tensile and compressive stress levels.

Continued creep testing of injection molded reaction sintered Si_3N_4 has shown that material nitrided with small amounts of hydrogen added to the nitrogen has improved creep resistance. Initial stress rupture testing in 4 point bending of molded Si_3N_4 indicates good life at temperatures ranging from 2300 to 2500°F . One sample tested at 2300°F and 10 ksi load had not failed after 800 hours.

Elastic constants of silicon nitride at four density levels as measured from room temperature to 1830°F have been determined and are presented.

5.1.1 PROPERTIES OF HOT-PRESSED MATERIALS

Introduction

The comprehensive program to evaluate the mechanical and thermal properties of many varieties of silicon nitride, silicon carbide, and lithium aluminum silicate in gas turbine applications is continuing. These data not only contribute valuable fundamental information about the materials but also are considered essential to an optimum design with brittle materials in order to provide the maximum safety factor. All of the candidate materials have been improved significantly. Since the potential for greater improvement exists, the Material Engineering task is expected to continue for the full term of the turbine project.

Tensile Properties of Hot-Pressed Silicon Nitride and Silicon Carbide

Additional tensile data have been acquired to complete the minimum statistical test plan for the characterization of Norton HS-130 silicon nitride and NC-203 silicon carbide. Ultimate strength versus temperature for Si_3N_4 is reported in Fig. 5.1. The results, tabulated in Table 5.1, indicate that new data are consistent with those reported previously⁽⁴⁾ and that little change is apparent in the standard deviation.

The tensile strength of Norton NC-203 silicon carbide is summarized in Fig. 5.2 and Table 5.2 where room temperature properties are reported for the first time. These data are consistent with earlier tests at elevated temperatures⁽⁴⁾ but the room temperature values are clearly lower than the extrapolation used previously.⁽⁴⁾

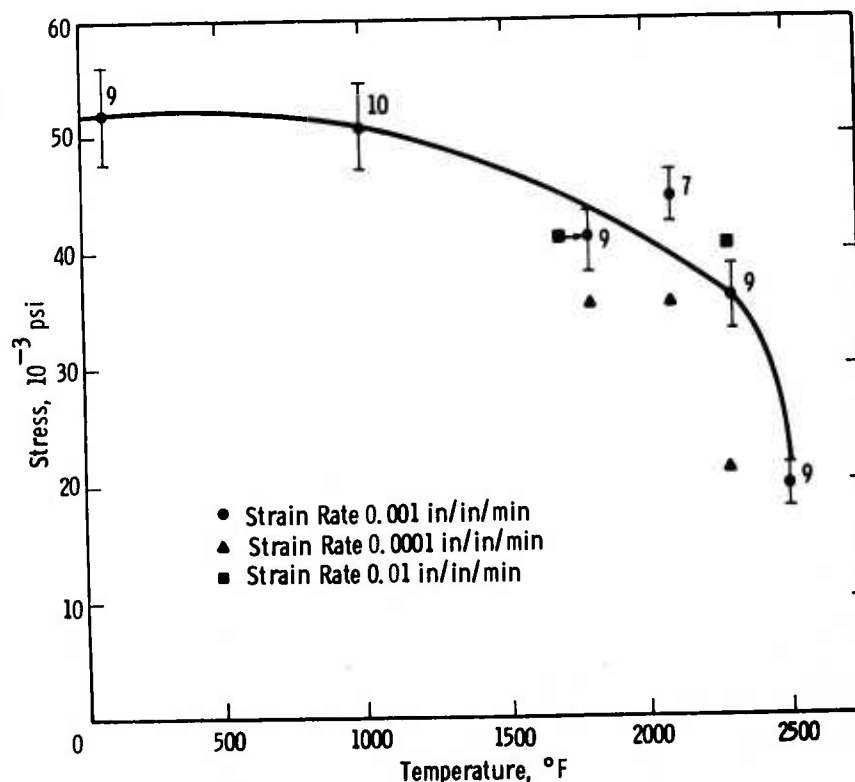


Figure 5.1 -- Tensile Strength of Norton HS-130 Silicon Nitride

The elastic modulus in tension for both the silicon nitride and the silicon carbide are plotted in Fig. 5.3. New data failed to alter the results significantly. It is interesting to note that these values were confirmed by 4 point flexural tests at room temperature, 1000, 1800, 2300 and 2500°F using specimens 0.125" x 0.250" x 1.125" (outer span 1 in., inner span 0.5 in. at 0.01 in/in/min).

Tensile and compressive outer fiber strain was measured with strain gauges at room temperature.

Comparing the two materials with respect to tensile properties, HS-130 silicon nitride is clearly superior at intermediate temperatures where the maximum transient tensile stress is likely to occur as a result

TABLE 5.1

TENSILE PROPERTIES OF NORTON HS-130 SILICON NITRIDE

Source of Test Data	Strain Rate in/in/min	Tensile Strength, psi					
		RT	1000°F	1800°F	2100°F	2300°F	2500°F
Westinghouse R&D	0.001	59,650	72,050	36,550	31,450	36,250	13,450
		54,650	56,100	48,000	32,750	42,100	20,200
		69,800	64,300	42,250	38,900	45,400	20,000
		40,300	60,000	40,800	35,350	46,400	20,100
		46,300	36,850	36,850	34,900	30,250	25,250
		<u>42,600</u>	<u>40,450</u>	<u>37,400</u>	<u>36,000</u>	<u>38,200</u>	<u>22,300</u>
		52,200	54,950	40,300	34,900	39,800	20,200
Westinghouse Astro	0.001		41,500	49,200	35,800	31,400	16,200
			42,600	48,800		33,400	17,400
			52,400	30,900		26,200	19,800
			<u>43,200</u>				
			44,925	42,967	35,800	30,333	17,800
Westinghouse R&D	0.0001			29,800	39,100	22,950	
				42,600	24,950		
					41,800		
					37,350		
					<u>37,800</u>		
				36,200	36,200	22,950	
Westinghouse Astro	0.0001			41,000		25,500	
				<u>48,600</u>		<u>26,600</u>	
				44,800		27,550	
Westinghouse R&D	0.01			<u>42,550</u>		<u>46,650</u>	
Westinghouse Astro	0.01					35,700	
				<u>49,000</u>		<u>42,900</u>	
						39,300	

of shutdown in any turbine application. The lower tensile modulus would also appear to favor silicon nitride but this advantage is completely off set by lower thermal conductivity as demonstrated by finite element stress analysis. The high temperature strength of NC-203 silicon carbide clearly favors it at temperatures above 2300°F.

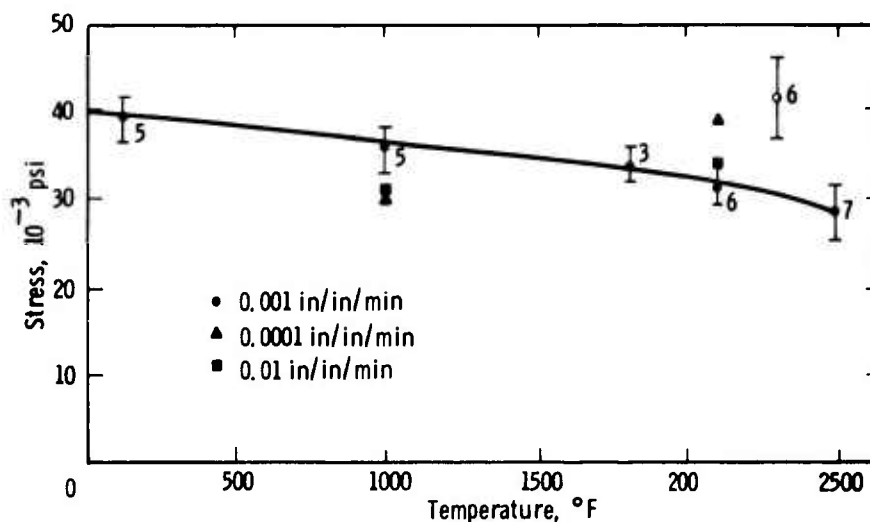


Figure 5.2 -- The Tensile Strength of Norton Hot-Pressed Silicon Carbide

TABLE 5.2

TENSILE PROPERTIES OF NORTON HOT-PRESSED SILICON CARBIDE

Strain Rate in/in/min	Tensile Strength, psi					
	RT (72°F)	1000°F	1800°F	2100°F	2300°F	2500°F
.001	32,200	47,100	35,950	25,450	35,150	28,950
	28,700	43,000	31,750	30,400	52,700	33,150
	45,150	30,100	36,400	28,950	37,800	18,900
	33,600	37,000		36,100	42,700	*
	35,900	*		32,500	37,600	37,200
		26,250		35,000	41,450	23,900
						24,000
						29,800
	29,100	36,700	34,700	31,400	41,200	28,000
0.0001		29,400		39,150		
		31,250		41,300		
				36,600		
		30,325 ± 1,000		39,017 ± 1,900		
0.01		30,900		30,100		
				32,650		
				38,300		
* Broke during alignment or reaction				33,683 ± 3,500		

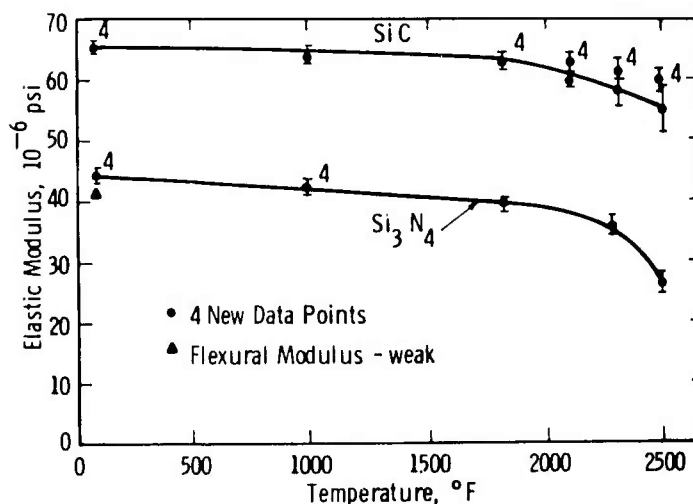


Figure 5.3 -- The Effect of Temperature on the Elastic Modulus of Norton Hot-Pressed Silicon Nitride and Silicon Carbide

Flexural Strength of Silicon Nitride and Silicon Carbide

A large number of flexural strength and flexural modulus measurements on both hot-pressed silicon nitride and silicon carbide have been made at room temperature and 2300°F in an effort to determine the true meaning and implication of the test. Specimens an 1/8" x 1/4" in cross section in lengths of 5.5 in., 3.0 in., and 1.5 in., lengths were broken (4 pt. 1/4 pt. loading at 0.01 in/in/min) in addition to the standard specimen 0.125 in. x 0.250 in. x 1.125 in. Plate and beam orientations were employed.

The data are deleted because of the results which are summarized as follows:

(1) The flexural strength and flexural modulus in the beam orientation exceeds that of the plate orientation by 15% in all directions of the materials where the specimen length is 1.5 in. or less.

(2) Orientation does not affect the results in 3 in. or 5.5 in. specimens.

(3) The modulus of rupture results are consistent for room temperature and 2300°F leading to the conclusion that specimens should be at least 2 in. long to yield acceptable strength values.

While these experiments failed to add desirable credibility to the flexural test method, they did disclose a third directional property in silicon nitride. If the specimen is broken in the strong direction of the material at right angles to the normal orientation a third value which lies between the conventional strong and weak values of the materials is identified. This observation was confirmed by Norton. The phenomenon is not expected to influence vane performance, however.

Since Westinghouse would like to use flexural data as a criterion for screening new materials and for assessing billet to billet variations in standard materials, the analysis of the flexural test⁽⁵⁾ was extended to reflect the effects of time dependence.

Time dependent deformation can be represented by the surface OANBCDE shown schematically in Fig. 5.4. A plane of constant strain intersecting this surface produces a stress-relaxation curve. A partial stress-relaxation curve (FC) in plane FJKCI is also shown. The constant strain rate curve (OFB) is obtained by intersection with a plane such as OGBH, in which strain is linearly proportional to time. The creep curve ANB results from an intersecting plane of constant stress (GMBL).

For the flexural test, an additional curve must be considered. The instantaneous stress-strain curve within the specimen (from the neutral axis to the outer fiber) is described by the intersection of the stress-strain-time surface with a plane of constant time. The curve DCB is one such curve in the DLBH plane. Point B represents the stress and strain condition at the outer fiber, point D the condition at the neutral axis, and point C the condition at a fiber halfway between. The line EF was similarly generated by a previous constant time plane.

The differences between the instantaneous stress-strain behavior and the behavior of the outside fiber is illustrated in Fig. 5.5, which is a projection of these curves in the stress-strain plane. It is the instantaneous stress-strain curve that controls the instantaneous force and moment balances. The fact that they differ from the outer fiber curve disallows the time independent treatment from being used.

The analysis of the time-dependent flexure test assumes: (a) the bar has a constant cross-section (rectangular, for simplicity); (b) it is loaded by forces directed perpendicular to its longitudinal axis; (c) the cross-sectional dimensions are small relative to the length in order to neglect shear stresses; (d) the rate of deflection is constant; and, finally, (e) the cross-sections remain plane during

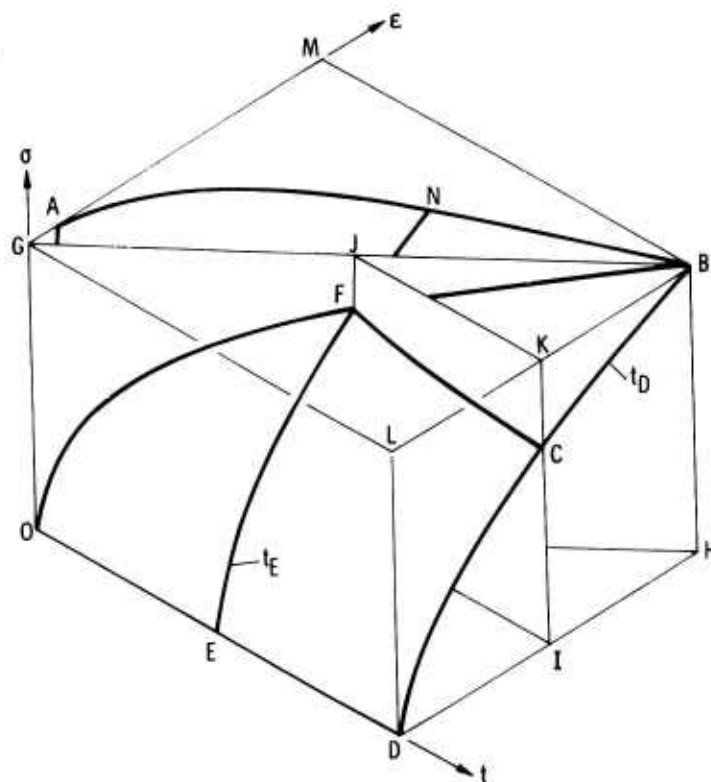


Figure 5.4 Schematic Diagram of Time Dependent Deformation

bending. The last assumption implies that the strains, ϵ , are linearly proportional to the distance, y , from the neutral axis:

$$\epsilon = \frac{y}{R} \quad (1)$$

where R is the radius of curvature due to bending. The total strain, ϵ^* , across the height, h , of the specimen is therefore

$$\epsilon^* = \frac{h}{R} = \epsilon_t + \epsilon_c \quad (2)$$

where ϵ_t is the maximum tensile strain at the outer tensile fiber and ϵ_c is the maximum compressive strain at the outer compressive fiber.

The equilibrium force equation is:

$$F = \int_{-h/2}^{h/2} \sigma(\epsilon, t) dA_R = \frac{bh}{\epsilon^*} \int_{\epsilon_c}^{\epsilon_t} \sigma(\epsilon, t) d\epsilon = 0 \quad (3)$$

where $\sigma(\epsilon, t)$ is the stress, A_R is the area, and b is the specimen width. The applied moment, M , must be resisted by the specimen resulting in the equilibrium:

$$M = \int_{-h/2}^{h/2} \sigma(\epsilon, t) y dA_R = \frac{bh^2}{\epsilon^{*2}} \int_{\epsilon_c}^{\epsilon_t} \sigma(\epsilon, t) \epsilon d\epsilon \quad (4)$$

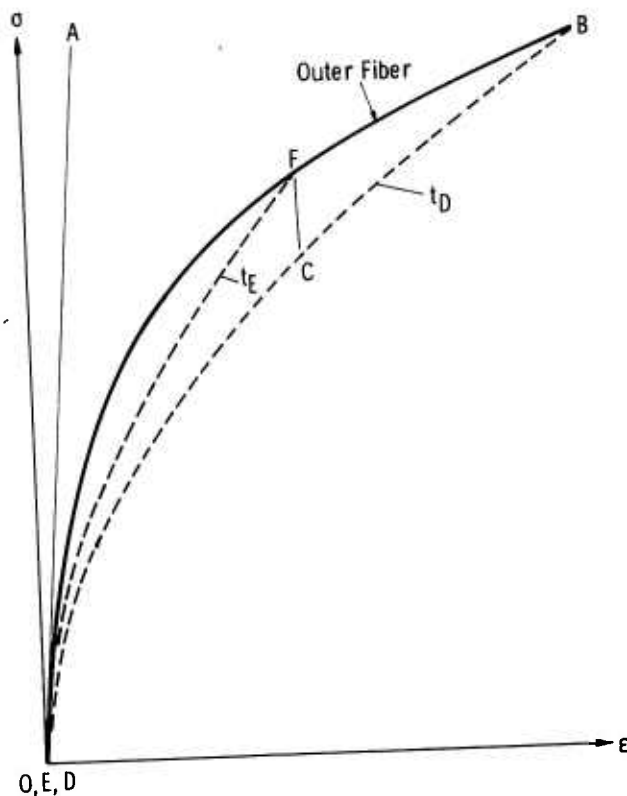


Figure 5.5 -- Schematic Diagram of the Stress-Strain Behavior Showing the Time Dependent Outer Fiber Curve OFB, and Two Instantaneous Curves, EF and DCB

For the four point flexure test in Fig. 5.6,

$$M = \frac{Pa}{2} \quad (5)$$

for all points within the inner span; P is the applied load, and a is the moment arm. Also, the strain, ϵ^* , is proportional to the applied deflection, D:

$$\epsilon^* = cD = \frac{6h}{3al - 4a^2} D \quad (6)$$

Since the test is being conducted at a constant deflection rate, the strain rate is also constant, and

$$\epsilon^* = kt \quad (7)$$

Differentiating Eq. (3) with respect to time, t, results in:

$$\frac{1}{bh} \frac{d(F\epsilon^*)}{dt} = 0 = \gamma + \sigma_t \frac{d\epsilon_t}{dt} - \sigma_c \frac{d\epsilon_c}{dt} \quad (8)$$

where σ_t is the stress at the outer tensile fiber, σ_c is the stress at the outer compressive fiber, and

$$\gamma = \int_{\epsilon_c}^{\epsilon_t} \frac{d\sigma(\epsilon, t)}{dt} d\epsilon \quad (9)$$

Similarly, differentiating Eq. (4) with respect to time results in:

$$\frac{1}{bh^2} \frac{d(M\epsilon^{*2})}{dt} = \lambda + \sigma_t \epsilon_t \frac{d\epsilon_t}{dt} + \sigma_c \epsilon_c \frac{d\epsilon_c}{dt} \quad (10)$$

where:

$$\lambda = \int_{\epsilon_c}^{\epsilon_t} \frac{d\sigma(\epsilon, t)\epsilon}{dt} d\epsilon \quad (11)$$

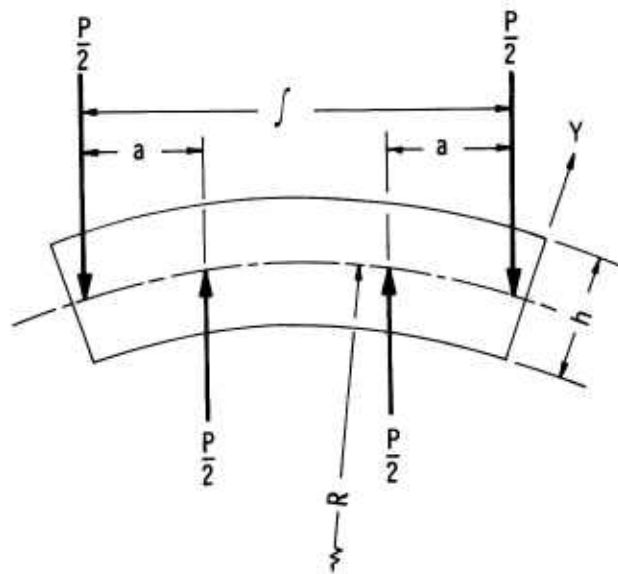


Figure 5.6 -- Bending of a Bar in Four Point Flexure

Also the differential of Eq. (2) is

$$\frac{d\epsilon_t}{dt} + \frac{d\epsilon_c}{dt} = \frac{d\epsilon^*}{dt} = K \quad (12)$$

By substitution, Eq. (10) can be written as:

$$\frac{1}{bh^2} \frac{d(M\epsilon^{*2})}{dt} = \lambda + \frac{\sigma_t \sigma_c}{(\sigma_c + \sigma_t)} \epsilon^* \frac{d\epsilon^*}{dt} + \frac{(\sigma_c \epsilon_c - \sigma_t \epsilon_t)}{\sigma_c + \sigma_t} \gamma \quad (13)$$

For the constant deflection rate test, the total strain rate $d\epsilon^*/dt$ is also constant and Eq. (13) may be written as:

$$\frac{1}{bh^2} (2K\epsilon^* M + \epsilon^{*2} \frac{dM}{dt}) = \lambda + \frac{\sigma_t \sigma_c}{(\sigma_t + \sigma_c)} K\epsilon^* + \left(\frac{\sigma_c \epsilon_c - \sigma_t \epsilon_t}{\sigma_t + \sigma_c} \right) \gamma \quad (14)$$

If deflection and therefore the total strain, ϵ^* , is held constant, then the stress relaxation version of Eq. (13) becomes

$$\frac{1}{bh^2} \left(\epsilon^{*2} \frac{dM}{dt} \right)_{\epsilon^*} = \lambda + \left(\frac{\sigma_c \epsilon_c - \sigma_t \epsilon_t}{\sigma_t + \sigma_c} \right) \gamma \quad (15)$$

where $dM/dt \big|_{\epsilon^*}$ is the rate of moment change due to stress relaxation. Subtracting Eq. (15) from Eq. (14) results in

$$\frac{\sigma_t \sigma_c}{\sigma_t + \sigma_c} = \frac{1}{bh^2} \left[2M + \frac{\epsilon^*}{K} \left(\frac{dM}{dt} - \frac{dM}{dt} \bigg|_{\epsilon^*} \right) \right] \quad (16)$$

This is the general equation relating the outer fiber stresses to the moment and time. In the time independent treatment dM/dt at constant strain is zero.

It is necessary to have another function relating σ_t and σ_c in order to obtain exact values. Without knowledge of this function, it is possible to establish boundaries within which most materials will fall. It can also be argued that material properties will usually fall closer to one or the other boundaries, and furthermore, it is easy to establish which. For materials which undergo true plastic deformation, the tensile and compressive stress-strain curves will be equivalent, i.e., σ_t will equal σ_c . Therefore, the first boundary is easily established. A large class of materials are highly resistant to deformation in the compressive mode. The second boundary occurs by letting the compressive stress be time-independent linear elastic. A simple compression test establishes which of the two conditions hold and in the elastic case establishes the compressive strain function, i.e., the modulus of elasticity.

In order to obtain the additional moment-time relationships in Eq. (16), either additional stress-relaxation tests must be performed or the usual constant deflection rate test must be altered. The specimen is initially deflected at the chosen rate, k_d , to some small deflection (point A on Fig. 5.7). The test machine is stopped and the deflection is held constant for some time increment, Δt (to point B). Deflection is then continued for the same time increment, Δt (to

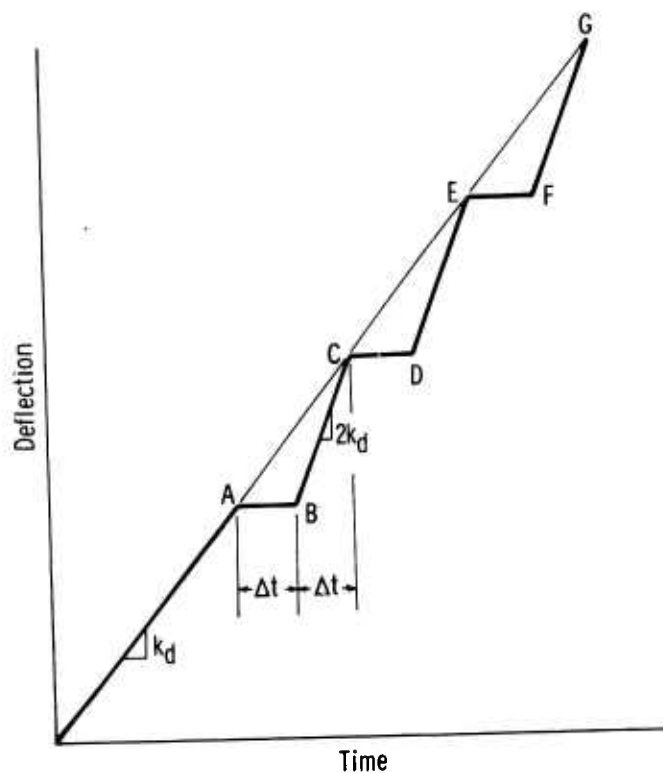


Figure 5.7 -- Deflection-Time Relationship for Proposed Time Dependent Flexural Test

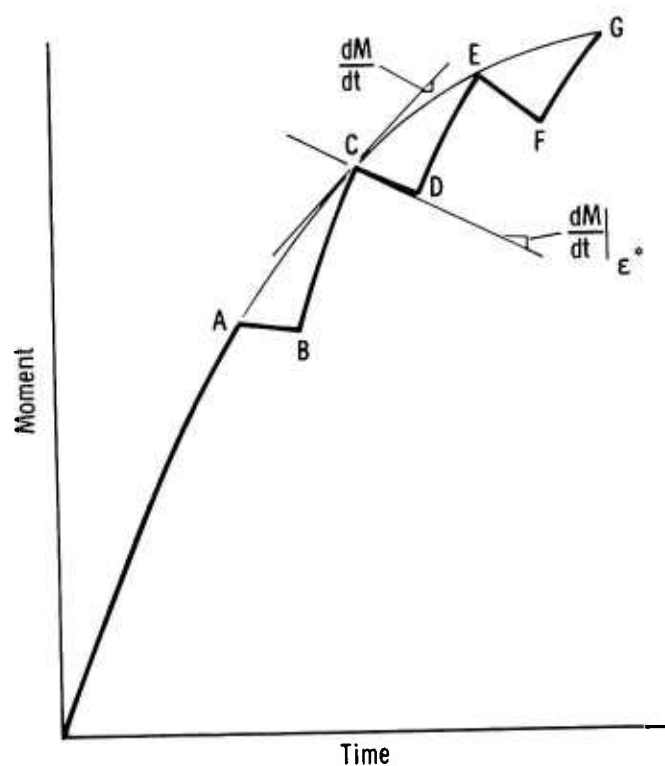


Figure 5.8 -- Moment-Time Relationship for the Proposed Time Dependent Flexural Test

point C), but at double the initial rate, $2 k_d$. Repeating this cycle to failure results in the moment-time curve in Fig. 5.8, the points A, B and C being equivalent to those of Fig. 5.5. The slope, dM/dt , is then the tangent to the moment-time curve which would have been generated if the test were not interrupted (curve OACEG). The slope $dM/dt|_{\epsilon^*}$ is the tangent to the constant deflection curve where it intersects with the above curve.

When tensile and compressive stress-strain relationships are the same, then Eq. (16) becomes:

$$\sigma_t = \sigma_c = 2\phi = \frac{2}{bh^2} [2M + t \left(\frac{dM}{dt} - \frac{dM}{dt} \Big|_{\epsilon^*} \right)] . \quad (17)$$

Also

$$\epsilon_t = \epsilon_c = \frac{\epsilon^*}{2} = \frac{k}{2} t \quad (18)$$

where k is proportional to the original deflection rate.

The corresponding stress-strain curves are shown in Fig. 5.9. The dashed curves are the time-independent stress-strain curves which represent the instantaneous condition within the specimen. Had the specimen, initially at point A, been allowed to relax to point X and then had it been instantaneously loaded, it would have followed curve OXC.

The interrupted deflection-time test outlined in Fig. 5.7 results in a moment-time curve similar to Fig. 5.8 for the non-linear tensile and linear compressive case. The corresponding stress-strain curves are shown in Fig. 5.10. During the relaxation process the compressive strain, ϵ_c , decreases slightly while the tensile strain, ϵ_t , increases.

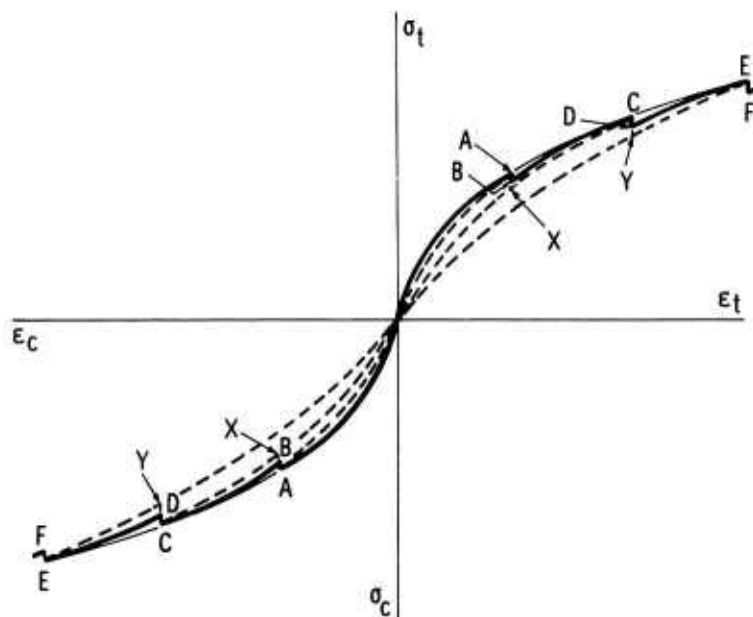


Figure 5.9 -- The Stress-Strain Relationship for the Proposed Flexural Test (Both Tension and Compression Have the Same Time Dependent Deformation Behavior)

This is necessary to maintain both the force balance and the constant total strain, ϵ^* . Once again, the dashed lines represent the instantaneous stress-strain relationships within the specimen.

The analysis of the present case is dependent on knowledge of the rate of change of momentum with total strain at constant time. The moment-strain curve equivalent to the moment-time curve of Fig. 5.8 is shown in Fig. 5.11. The dashed lines represent the instantaneous behavior.

The differential of force with respect to total strain is:

$$\left. \frac{1}{bh} \frac{d(F\epsilon^*)}{d\epsilon^*} \right|_t = 0 = \int_{\epsilon_c}^{\epsilon_t} \frac{d\sigma(\epsilon, t)}{d\epsilon^*} d\epsilon + \sigma_t \frac{d\epsilon_t'}{d\epsilon^*} - \sigma_c \frac{d\epsilon_c'}{d\epsilon^*} \quad (19)$$

where

$$\int_{\epsilon_c}^{\epsilon_t} \frac{d\sigma(\epsilon, t)}{d\epsilon^*} d\epsilon = 0 \quad (20)$$

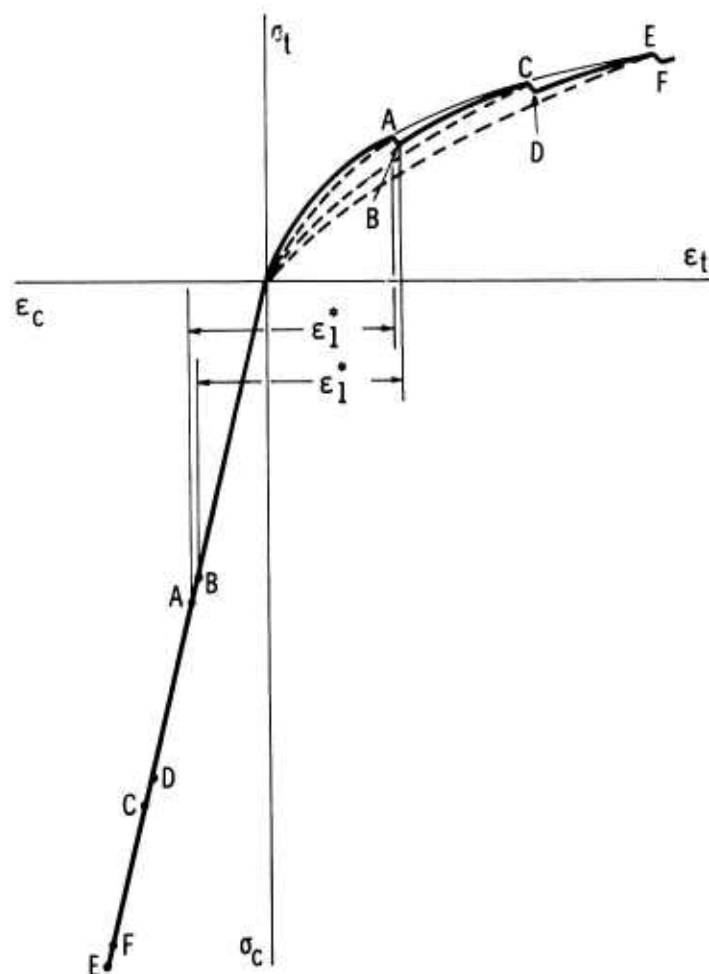


Figure 5.10 -- The Stress-Strain Relationships for the Proposed Flexural Test for Time Dependent Tensile and Elastic Compressive Deformation

since σ is not a function of ϵ^* . The differential of the moment at constant time with total strain is

$$\left. \frac{1}{bh^2} \frac{d(M\epsilon^{*2})}{d\epsilon^*} \right|_t = \int_{\epsilon_c}^{\epsilon_t} \frac{d(\sigma(\epsilon, t)\epsilon)}{d\epsilon^*} d\epsilon + \sigma_t \epsilon_t \frac{d\epsilon_t'}{d\epsilon^*} + \sigma_c \epsilon_c \frac{d\epsilon_c'}{d\epsilon^*} \quad (21)$$

where

$$\int_{\epsilon_c}^{\epsilon_t} \frac{d(\sigma(\epsilon, t)\epsilon)}{d\epsilon^*} d\epsilon = 0 .$$

Solving as before

$$\frac{\sigma_t \sigma_c}{\sigma_t + \sigma_c} = \frac{1}{bh^2 \epsilon^*} \left. \frac{d(M\epsilon^{*2})}{d\epsilon^*} \right|_t = \phi \quad (22)$$

This is the same ϕ which was previously determined in Eq. (16).

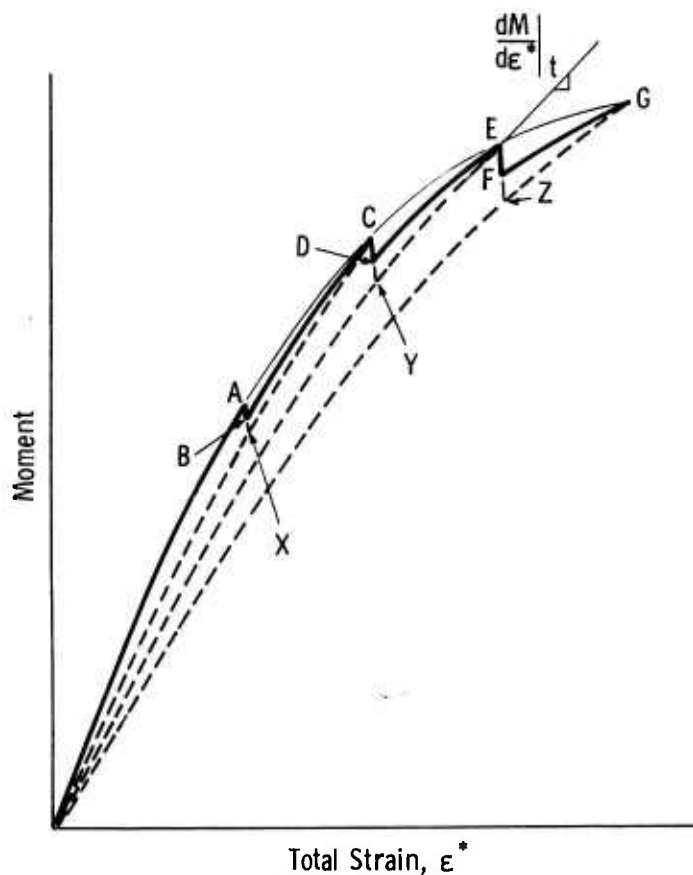


Figure 5.11 -- The Moment-Strain Relationship for the Time Dependent Flexural Test

The moment-deflection data can now be incrementally analyzed under conditions of constant time by noting that for small changes:

$$\sigma_{t_i} \Delta \epsilon_{t_i} = \sigma_{c_i} \Delta \epsilon_{c_i} \quad (23)$$

where

$$\Delta \epsilon_{t_i} = \epsilon_{t_i} - \epsilon_{t_{i-1}} \quad (24)$$

$$\Delta \epsilon_{c_i} = \epsilon_{c_i} - \epsilon_{c_{i-1}} = \epsilon_i^* - \epsilon_{t_i} - \epsilon_{c_{i-1}} \quad (25)$$

and

$$\sigma_{c_i} = \frac{\epsilon_{c_i}}{A} \quad (26)$$

where A is the elastic compliance (the reciprocal of the elastic modulus). By proper substitution into Eq. (22):

$$\begin{aligned} \epsilon_{t_i}^2 + (\epsilon_{c_{i-1}} - 2 \epsilon_i^*) \epsilon_{t_i} + [A \phi \epsilon_{t_{i-1}} + (\epsilon_i^* - A \phi) \\ (\epsilon_i^* - \epsilon_{c_{i-1}})] = 0 \end{aligned} \quad (27)$$

The quadratic equation can be solved for ϵ_{t_i} . By substitution, ϵ_{c_i} , σ_{c_i} and σ_{t_i} can in turn be determined.

To demonstrate the differences in results from the three types of analyses (elastic, time-independent arbitrary deformation law, and time-dependent arbitrary deformation law), moment-time values were generated, and the outer fiber stress-strain relationships determined from these. The stress-strain-time surface used in the synthesis was determined from an equation of the form:

$$\epsilon = A\sigma + B \sigma^n t^m \quad (28)$$

and the following parameters were chosen:

$$A = 2 \times 10^{-7}$$

$$B = 2.2 \times 10^{-16}$$

$$n = 3$$

$$m = 1/2$$

$$\text{strain rate} = .01$$

Results of the tensile analyses for equivalent tensile and compressive deformation (experimental curve A in Fig. 5.12) are shown in Fig. 5.13. For the given deformation equation and parameters, the elastic beam

analysis results in a maximum stress that is 25 percent too high. The time independent analysis underestimates the stress by 7 percent.

Results of the tensile analyses for time dependent tensile and elastic compressive deformation (experimental curve B in Fig. 5.12) are shown in Fig. 5.14. In this case, the elastic beam theory not only produces a higher maximum stress, 78 percent, but the maximum strain is diminished by 26 percent. The time independent analysis reduces the maximum stress by 7 percent.

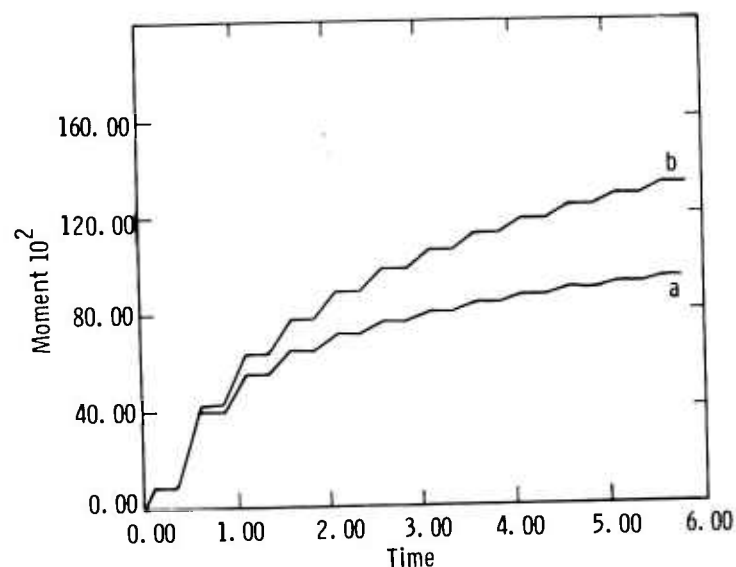


Figure 5.12 -- Moment-Time Curves for Equivalent Time Dependent Tensile and Compressive Deformation (a) and Time-Dependent Tensile and Elastic Compressive Deformation (b)

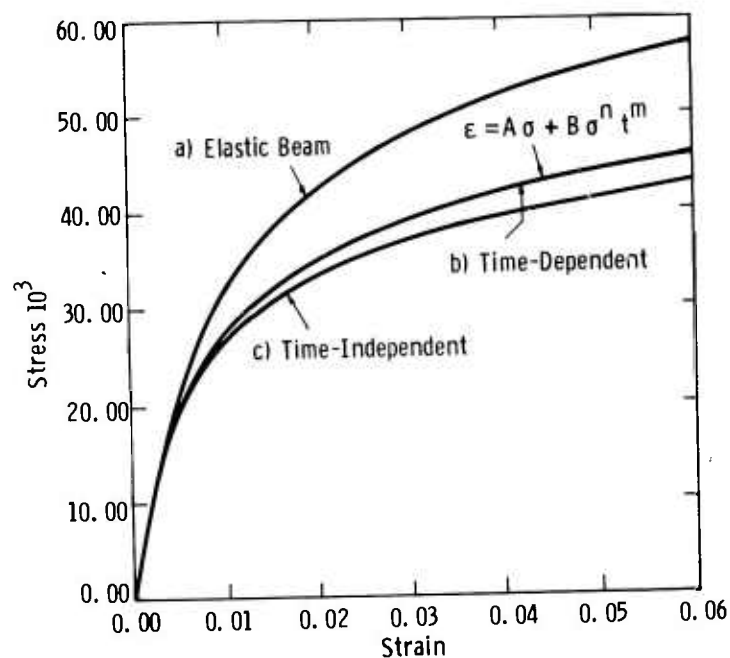


Figure 5.13 -- Outer Fiber Tensile Stress-Strain Relationships for Equivalent Tensile and Compressive Deformation as Determined from Elastic Beam Theory (a), Time-Dependent Deformation Theory (b) and Time-Independent Deformation Theory (c)

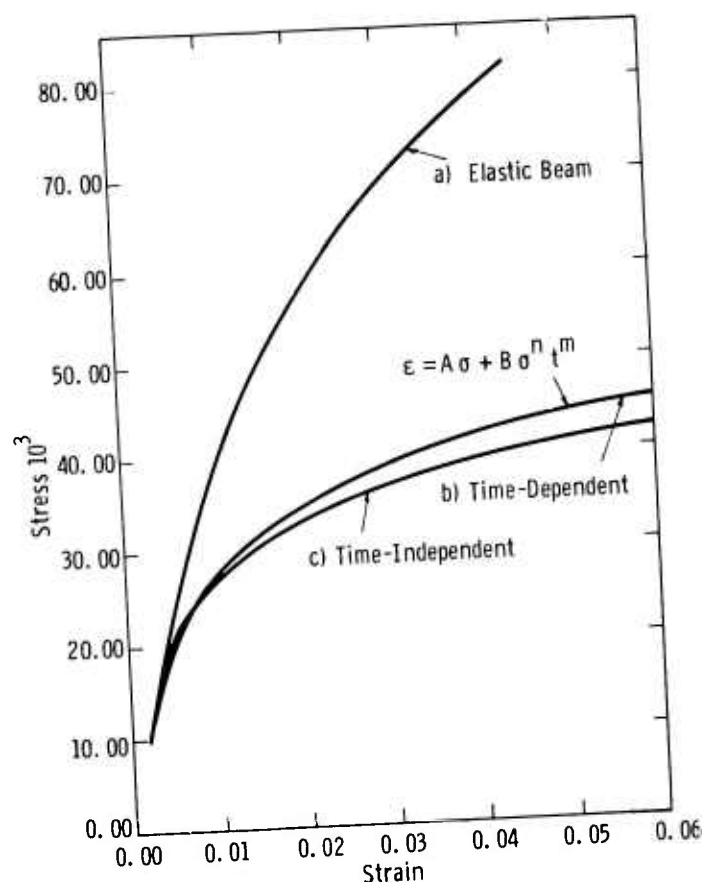


Figure 5.14 -- Outer Fiber Stress-Strain Relationships for Non-Linear Tensile and Linear Compressive Deformation as Determined from Elastic Beam Theory (a), Time-Dependent Deformation Theory (b), and Time-Independent Deformation Theory (c)

Creep Properties of Hot-Pressed Silicon Nitride and Silicon Carbide

Additional tensile creep results for silicon nitride and silicon carbide are reported in Table 5.3. The silicon nitride data were generated in air by the Westinghouse Astronuclear Laboratory using silicon carbide grips. These data extend the creep results⁽⁵⁾ to 2400°F and confirm points at lower temperatures. Rupture strain and stress rupture life is consistent with all measurements made previously.⁽⁵⁾ Strain rate sensitivity in silicon nitride is stress dependent.

Considerable problems have been encountered in the creep measurements on silicon carbide. Creep strain is consistently small at 0.2-0.3%. The stress rupture life is extremely erratic, varying from a few minutes to > 2000 hours at stress levels of 10,000 and 15,000 psi. Recent observations indicate, however, that the scatter may not be characteristic of the material but rather the result of corrosion as illustrated in Fig. 5.15. In this particular example the specimen did not fail (2000 hours at 10,000 psi stress) but similar reaction zones were found as failure origins in other tests. In some cases reactions between TD Ni-Cr grips and the specimens may have caused a redistribution of load and subsequent premature failure due to bending. Hot-pressed SiC is very susceptible to liquid metal corrosion probably due to reactions

at the grain boundary. Therefore, any conclusion suggesting that silicon carbide is stress rupture limited must be considered premature at this time.

Table 5.3

CREEP PROPERTIES OF HOT-PRESSED SILICON NITRIDE AND SILICON CARBIDE

Material	Temperature °F	Stress 1000 psi	Atmosphere	Grips	Rupture Life hrs	Rupture Strain %,	Comments
SiC	2300	15	air	SiC	619	ND	
SiC	2300	10	air	TD-NiCr	< 2100	0.3	test interr. reaction with liquid metals
SiC	2300	15	air	TD-NiCr	2 min.		
SiC	2300	10	air	TD-NiCr	650	0.3	
Si ₃ N ₄ (NC-132)	2200	16	air	SiC	7.5	5.2	suspected grip defor.
Si ₃ N ₄ (NC-132)	2200	14	air	SiC	0.5	0.15	
Si ₃ N ₄ (NC-132)	2200	12	air	SiC	---	---	broke upon loading
Si ₃ N ₄ (NC-132)	2200	10	air	SiC	2.9	2899	failed due to temperature cycle
Si ₃ N ₄ (HS-130)	2400	6	air	SiC	450	6.7	
Si ₃ N ₄ (HS-130)	2400	8	air	SiC	52	4.3	
Si ₃ N ₄ (HS-130)	2400	8	air	SiC	20.1	1.9	
Si ₃ N ₄ (HS-130)	2400	4	air	SiC	1065	5.5	
Si ₃ N ₄ (HS-130)	2400	8	air	SiC	19	2.5	
Si ₃ N ₄ (HS-130)	2200	16	air	SiC	21	0.41	
Si ₃ N ₄ (HS-130)	2200	15	air	SiC	14	0.2	

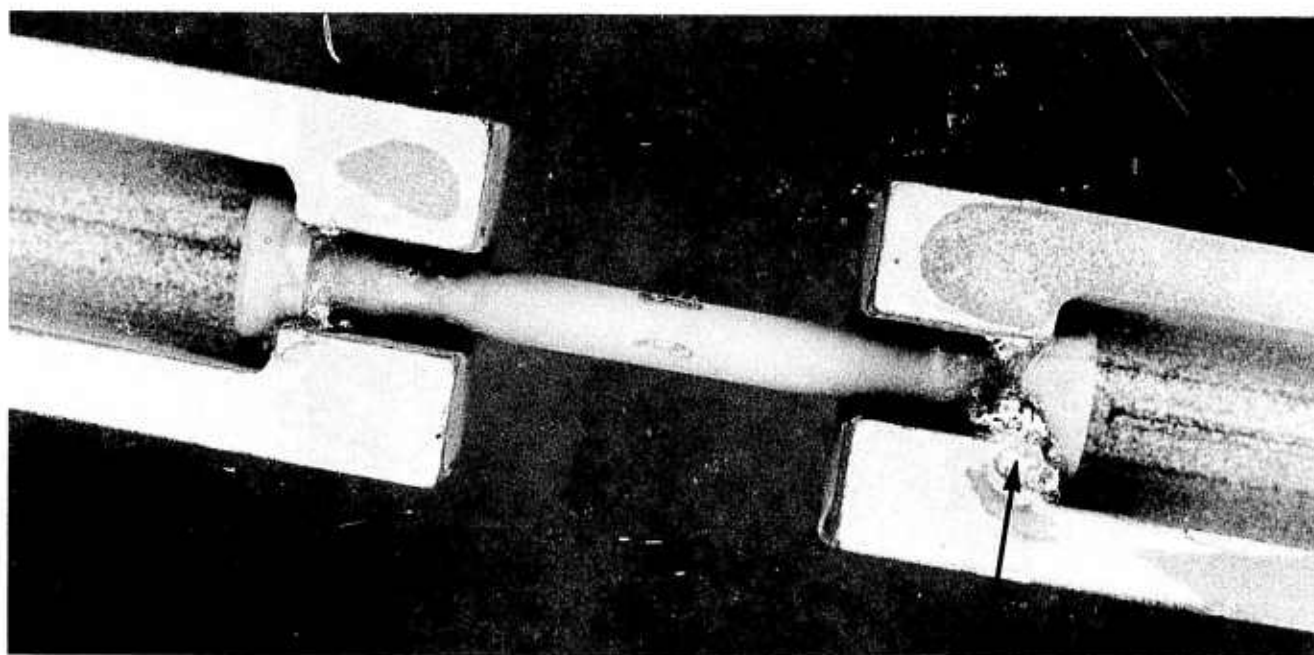


Figure 5.15 -- Molten Metal-Metal Oxide Silicon Carbide Reaction in High Temperature Stress Rupture Test (2300°F in Air)

A number of 4 point flexural creep measurements were made on silicon nitride at 2300°F for comparison with tensile creep results. Representative creep curves are plotted in Fig. 5.16. Steady state creep rates in the flexural mode are typically less than half that observed in pure tension.

Corrosion-Erosion Tests at 2500°F

Since the alumina liner in the pressurized turbine test passage was found to contaminate the surfaces of Si_3N_4 and SiC specimens, it was removed from the pressurized turbine test passage. The passage was modified for 2500°F operation as follows.

(1) The combustor was shortened to approximately 12 in. and made to butt up directly against a hot-pressed silicon nitride plate 6 in. in diameter with a 2 in. x 4 in. rectangular hole in the center.

(2) The specimen section was installed directly behind the silicon nitride plate.

(3) A single-platinum-platinum-10% rhodium thermocouple was installed directly downstream of the samples.

(4) An alumina-lined duct was used to connect the passage and gas stream to the barrier plate and exhaust muffle.

Four specimens each of hot-pressed Si_3N_4 and SiC were exposed to hot combustion gases at 2500°F, 3 atm pressure and 500 fps gas velocity

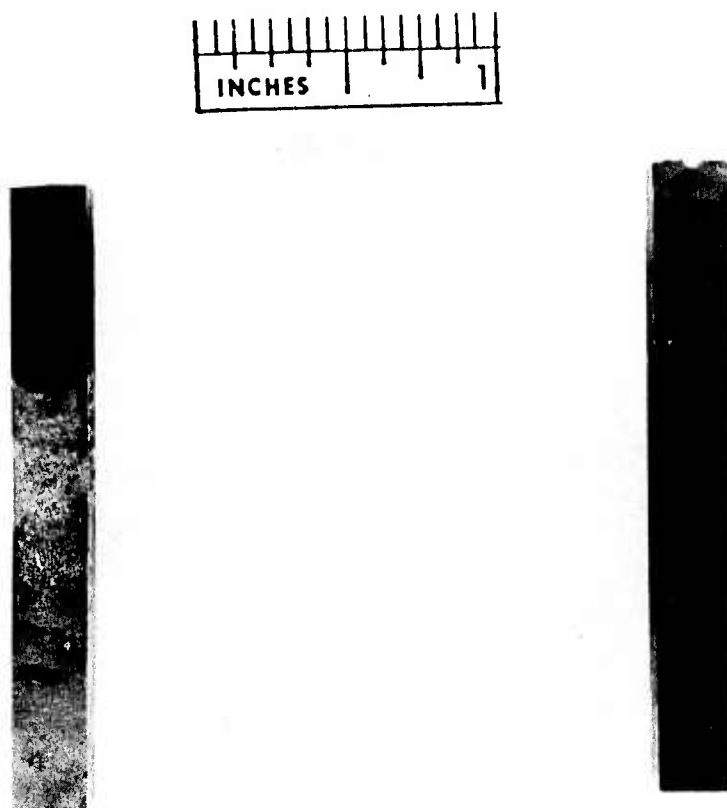


Figure 5.16 -- Creep of Norton HS-130 Silicon Nitride at 2300°F in Air

obtained by burning # GT-2 clean Exxon fuel. After a total exposure of 42 hours, the specimen surfaces, shown in Fig. 5.17, were found to be covered with white cristobalite in addition to MgSiO_3 on Si_3N_4 and Al_2SiO_5 on SiC . After removing these surface oxides and other deposits by light sandblasting, some degradation of the specimen surfaces was noticed as shown in Fig. 5.18. Weight loss (after removing the surface deposits) and flexural strength appear as functions of exposure time in Table 5.4. The flex strength of the corroded specimens was measured under conditions 4-point loading at a strain rate of 0.001/min at 2000°F.

It is evident that an appreciable degradation in the strength of both Si_3N_4 and SiC , up to 20%, was caused by exposure to hot combustion gases at 2500°F. These tests are continuing to accumulate longer exposure time. An additional test sequence will be run to verify a highly oxidizing condition at temperature since carbon deposits were observed on cooled samples. Some effort will be made to assess effects of reducing conditions since carbon is known to deposit on turbine components downstream of the combustors.

Friction for Hot-Pressed Silicon Nitride

The coefficient of static friction with respect to temperature was determined for silicon carbide versus itself using the apparatus and method described.⁽²⁾ The data appear in Table 5.5. When compared with silicon nitride,⁽²⁻³⁾ silicon carbide exhibits much higher values at elevated temperature. The bonding observed at 2500°F could cause problems in the three piece stator vane assembly at high temperature.

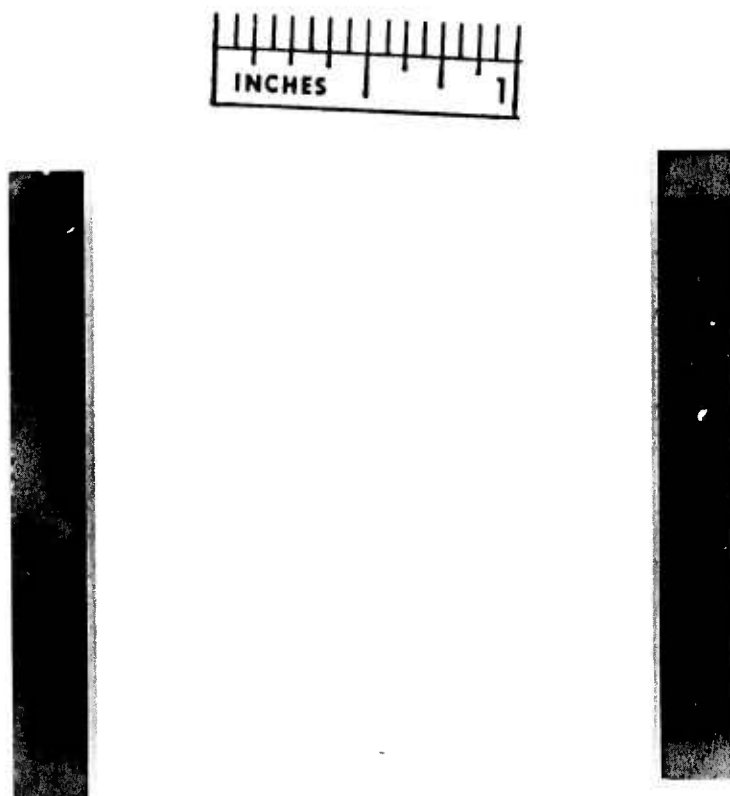


Figure 5.17 -- Silicon Nitride (Left) and Silicon Carbide (Right) Specimen as Tested in Turbine Passage at 2500°F

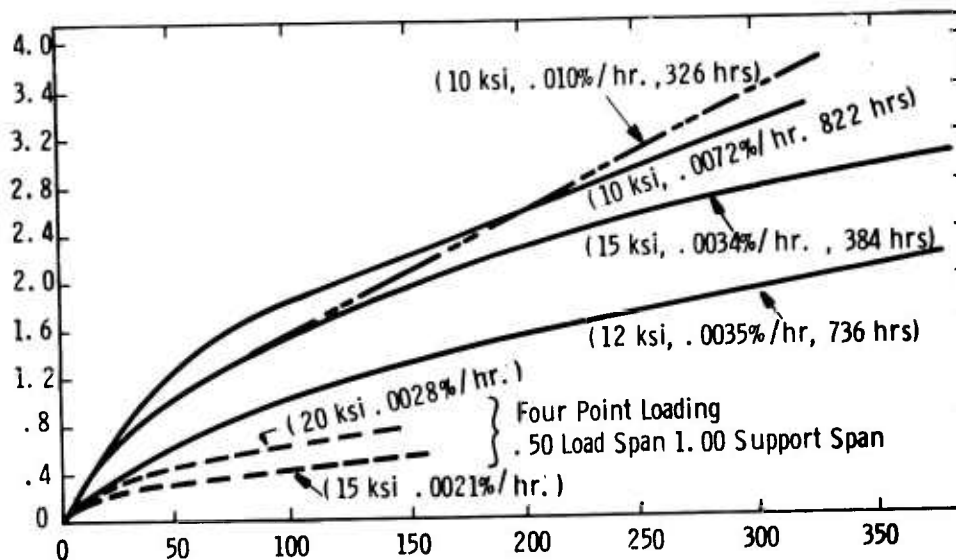


Figure 5.18 -- Silicon Nitride (Right) and Silicon Carbide (Left) Specimens from Turbine Passage Test at 2500°F After Sandblast

TABLE 5.4
EFFECT OF CORROSION-EROSION AT 2500°F

Hrs.	Si_3N_4		SiC	
	Wt Loss mg/cm^2	Flex Strength at 2000°F ksi	Wt Loss mg/cm^2	Flex Strength at 2000°F ksi
0	--	80	--	65
10	2.5	65	1.0	55
20	3.0	65	1.5	56
30	4.0	63	2.0	52
40	6.5	63	2.5	57
43	7.0	60	2.5	55

Table 5.5
STATIC COEFFICIENT OF FRICTION FOR HOT-PRESSED SILICON CARBIDE
SiC vs SiC Load-1700 psi
Test speed-.01"/min

Temp.	Static	Dynamic
RT	.35	.25
1000	0.60	Stick-Slip
1800°F	1.25	Stick-Slip
1800°F	1.40	Stick-Slip
2000°F	1.46	Stick-Slip
2000°F	1.68	Stick-Slip
2100°F	1.82	Stick-Slip
2100°F	2.00	Stick-Slip
2200°F	1.85	Stick-Slip
2300°F	2.50	Stick-Slip
2400°F	2.85	Stick-Slip
2500°F	Samples would not break loose with a force of > 15 lbs. static	

Low Cycle Fatigue

A fully reversible low cycle fatigue test was implemented in the 4 point flexural mode using the 0.125 in. x 0.250 in. x 1.125 in. rectangular specimen. When the load was applied, reduced, and reapplied in the fashion of a sine wave no failures were recorded after 1500 cycles. Life ranged from 14 to 1640 cycles, however, when a hold time at maximum stress was imposed. The fatigue characteristic of silicon nitride are compared in Fig. 5.19. While high cycle fatigue is not expected to be a problem, the low cycle fatigue properties are of concern, since thermal cycling is a critical mode in an operating turbine.

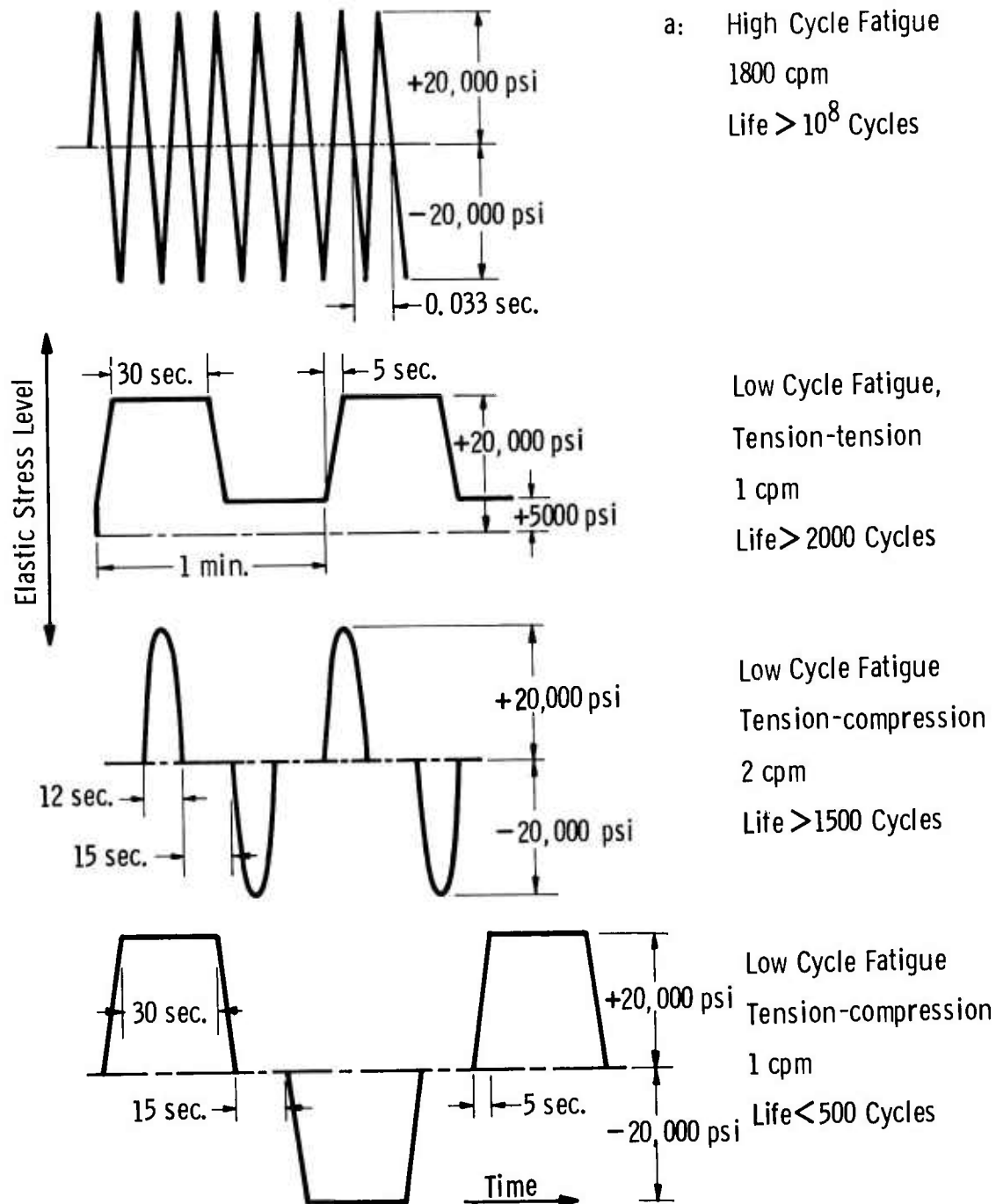


Figure 5.19 -- Schematic of Fatigue Response in HS-130 Si_3N_4 at 2300°F in Air

5.1.2 PHYSICAL PROPERTIES OF REACTION SINTERED SILICON NITRIDE

Introduction

During this reporting period measurements were made of high temperature flexural strength, elastic constants, flexural creep, and flexural stress rupture of reaction sintered Si_3N_4 .

The flexural strength of Norton reaction sintered NC-350 Si_3N_4 was measured up to 1500°F , and comparisons made with the strength of hot pressed Norton HS-130 materials.

Additional flexural creep properties of both Ford reaction sintered and slip cast Si_3N_4 were determined along with preliminary stress rupture data. Data is also presented to supplement the proposed model for the creep behavior of the injection molded Si_3N_4 previously reported ⁽⁵⁾. Comparisons are made between reaction sintered Si_3N_4 and Norton HS-130 hot pressed Si_3N_4 .

Shear and elastic moduli were measured on silicon nitride with densities between 2.37 and 3.18 gm/cm^3 in the temperature range 0 - 1000°C . The density dependence of both moduli compared favorably with theoretical calculations.

Strength of NC-350 Silicon Nitride

Bars of reaction sintered Si_3N_4 designated NC-350 by the manufacturer (Norton Company) were fractured as a function of temperature in four-point flexure. Specimens, approximately $1/8" \times 1/8" \times 1-1/4"$ were received in the as-fired condition. The tensile and compression sides were ground (220 grit diamond) to remove the oxidized surface; the other surfaces were left in the as-received condition. The loading fixture had an outer span of 0.875 in. and an inner span of 0.375 in. , and the crosshead speed was 0.005 in/min.

The temperature dependence of fracture stress is seen in Figure 5.20. Fracture stress is essentially invariant to about 1300°C , peaks slightly at 1400°C and then decreases significantly thereafter. The invariance is consistent with the predominance of a single fracture mechanism. The peak likely indicates the onset of significant plastic response, presumably manifest as a local and not particularly effective crack blunting mechanism, judging by the incremental stress advantage conferred. As in the hot pressed material, the fracture paths at all temperatures appear to follow the grain boundaries. A comparison with the high temperature fracture resistance of hot pressed Si_3N_4 (HS-130), portrayed as a dashed line in Figure 5.20 (1300 - 1400°C), indicates that the strength of NC-350 appears to fall within the envelope of that extrapolated curve. Refinement of processing technique could well confer to the reaction sintered product a strength advantage at high temperatures over the hot pressed product. While slow crack growth is clearly a factor in hot pressed material at temperatures above about 1200°C , no such evidence of slow crack growth was detected in NC-350 up to 1500°C . While this observation requires further confirmation and may be simply a stress level effect (the reaction sintered product being unable to support the stress necessary to cause a viscous response along the grain boundary path), it may also indicate the advantage of reducing the glass-forming impurity levels.

Creep and Stress-Rupture Injection Molded Si_3N_4

Figure 5.21 is an updated curve of steady state strain rate ($\dot{\epsilon}$) vs stress for four types of injection molded Si_3N_4 . Please refer to the last^s report ⁽⁵⁾ for processing, property, and impurity data. Note that the Type D material at 2500°F

exhibits lower creep rates than the Type C material at 2300°F and the Type B at 2200°F. It should also be noted that the stress exponent, n , is the same for all grades of material, indicating the same mechanism is operating in all cases.

Figure 5.22 is a plot of $\dot{\epsilon}$ vs reciprocal temperature, giving the apparent activation energy of 50-55 Kcal/mole. Again it should be noted that the activation energies are similar, indicating the same creep mechanism is active.

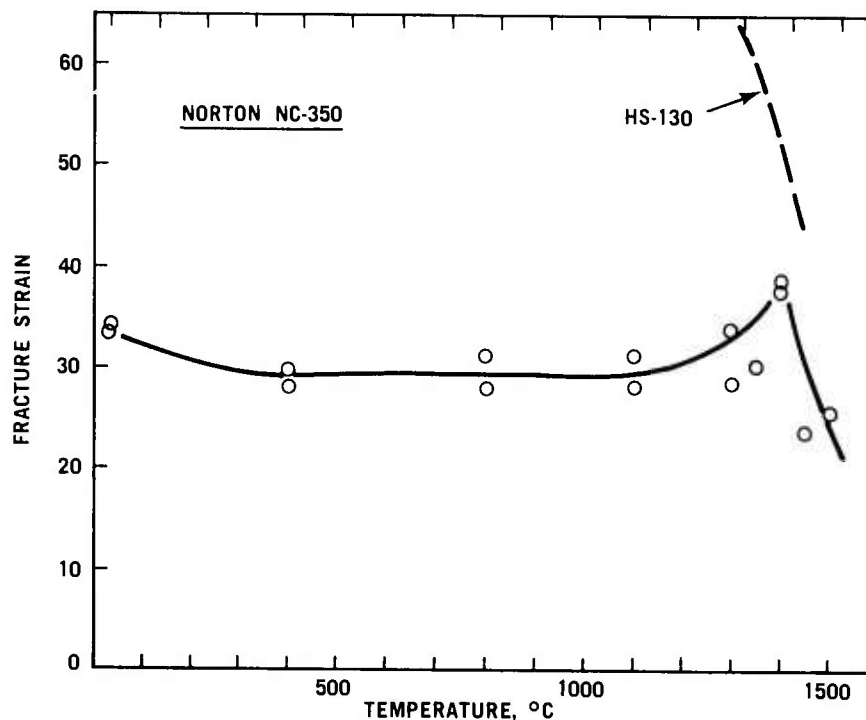


Figure 5.20 Bend Strength vs Temperature of Norton NC-350 Reaction Sintered Silicon Nitride

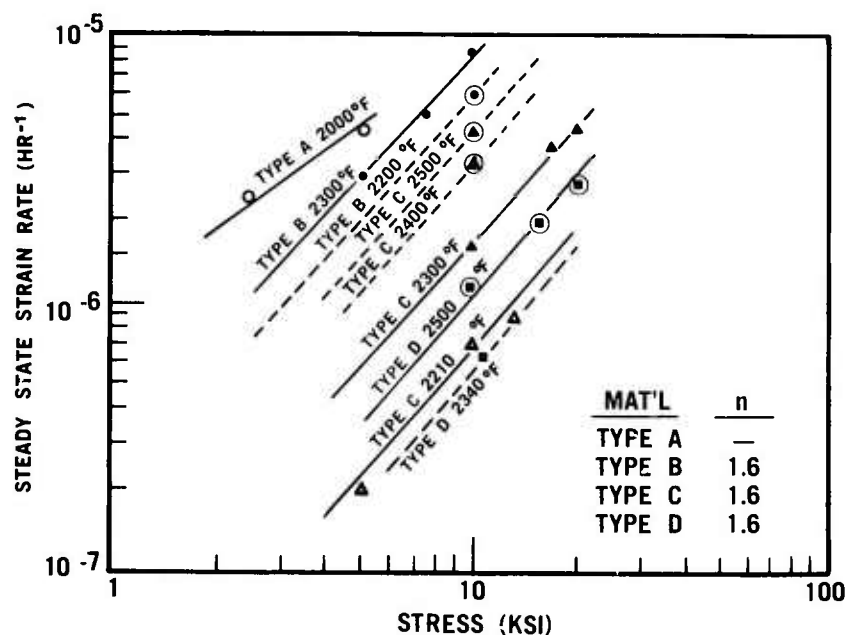


Figure 5.21 Steady State Strain Rate vs Applied Stress For Reaction Sintered Silicon Nitride

Table 5.6 gives a current summary of the stress-rupture properties of the Types C and D Si_3N_4 . As can be observed, the only evidence of premature failure occurred with the Type C material at 2300°F and 20 ksi. However, this result is reasonable considering the stress level which is equivalent to 80-87% of the high temperature bend strength of this material.

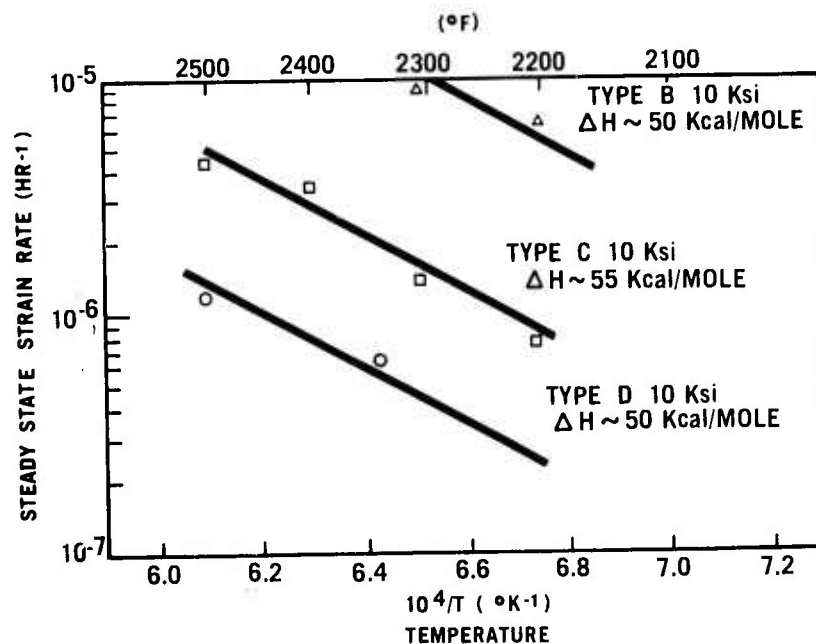


Figure 5.22 Steady State Strain Rate vs Temperature For Reaction Sintered Silicon Nitride

TABLE 5.6

STRESS-RUPTURE PROPERTIES OF REACTION SINTERED SILICON NITRIDE

Material	Temp.	ATM	Stress*	Rupture Life
Type C Si_3N_4	2300°F	Air	10 ksi	> 200 hours
	2300°F	Air	10 ksi	> 800 hours
	2300°F	Air	20 ksi	19 hours
	2300°F	Air	20 ksi	256 hours
	2300°F	Air	20 ksi	> 200 hours
	2400°F	Air	10 ksi	> 150 hours
	2500°F	Air	10 ksi	> 160 hours
Type D Si_3N_4	2300°F	Air	15 ksi	> 160 hours
	2500°F	Air	10 ksi	> 150 hours
	2500°F	Air	15 ksi	> 120 hours
	2500°F	Air	20 ksi	> 50 hours

*Modulus of rupture

Type C	RT	23-25 ksi
	2300°F	23-25 ksi
	2500°F	23-25 ksi
Type D	RT	23-25 ksi
	2300°F	23-25 ksi

Figure 5.23 shows that the creep resistance of injection molded Si_3N_4 is a function of the calcium impurity level and of the nitriding atmosphere. This can be seen by comparing Type A with Type B material fired in nitrogen, and comparing Type B with Type C material fired in different atmospheres. It is obvious that the creep resistance is improved an order of magnitude by adding hydrogen to the nitriding atmosphere.

In the previous report (5), the concept was introduced that related creep in injection molded Si_3N_4 to a glassy grain boundary phase. The composition of this grain boundary phase was determined by Auger electron spectroscopy (Table 5.7). These compositions were then used to calculate the glassy grain boundary in oxide form, and the viscosity of the grain boundary glassy phase (24) was plotted as a function of creep rate (Figure 5.24) where it can be seen that $\dot{\epsilon}_s$ is a function of $1/\eta$.

Creep of Slip Cast Si_3N_4

In the last reporting period, the composition of the slip cast Si_3N_4 was finalized with respect to nitriding additions. This composition contained 3% Fe_2O_3 additive, and is identified as NE-12.

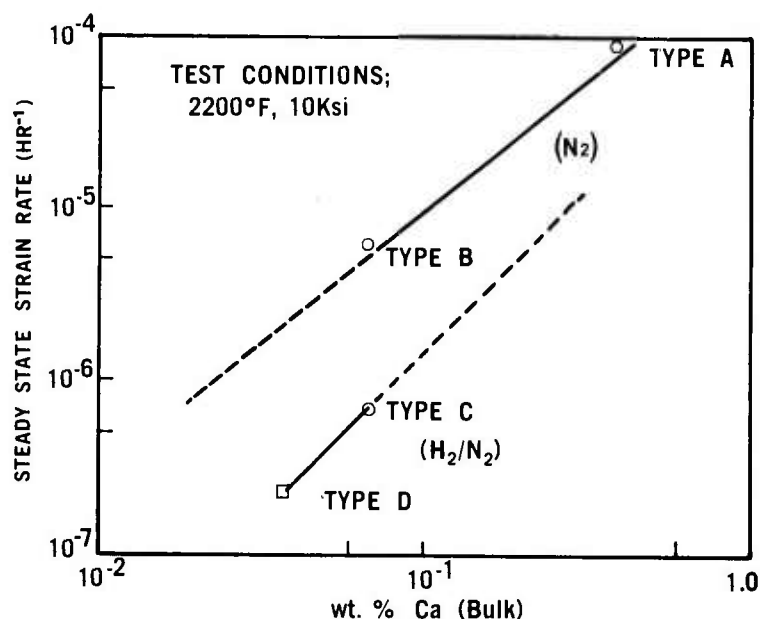


Figure 5.23 Steady State Strain Rate vs Calcium Content of Reaction Sintered Silicon Nitride

TABLE 5.7

AUGER ANALYSIS OF FRACTURE SURFACES (wt %)

Material	Ca	Al	Fe	O ₂	N ₂	Si
Type A	4-5	16	N.D.	20-25	16-25	Bal.
Type B	0-1	16	N.D.	15-20	26-30	Bal.
Type C	N.D.	N.D.	N.D.	20-25	35-40	Bal.
Type D	N.D.	N.D.	N.D.	22-27	30-35	Bal.

N.D. = not detected

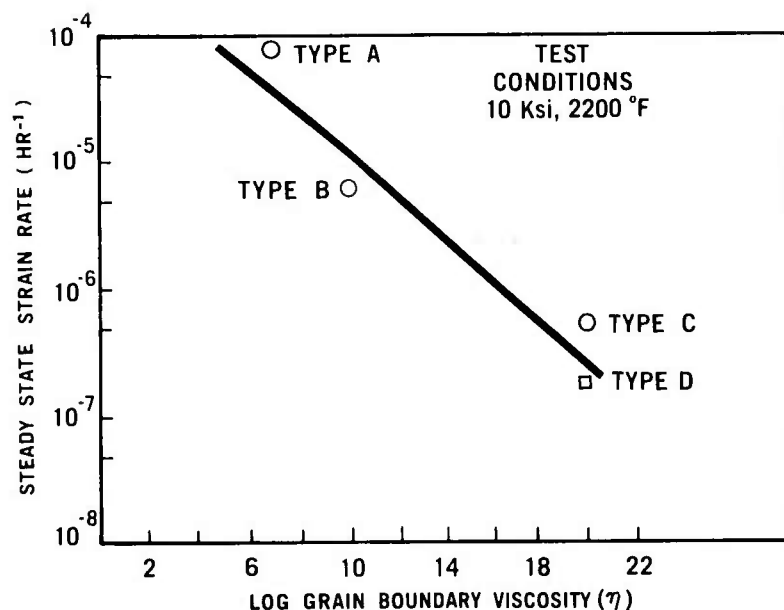


Figure 5.24 Steady State Strain Rate vs Grain Boundary Viscosity of Reaction Sintered Silicon Nitride

Preliminary creep testing of the NE-12 composition has been performed and the results are illustrated in Table 5.8. These results reveal no apparent creep; however, a stress rupture problem is evident. The density of slip cast Si_3N_4 is 2.72 gm/cc with a room temperature modulus of rupture of 41,000 psi. When tested at 17,000 psi (41% of R.T. MOR) short time failures occur. When this data is compared to the Type C and D injection molded Si_3N_4 , the slip cast Si_3N_4 is shown to be inferior, even though it has higher density and room temperature strength. Work is continuing in an effort to understand the reasons for this difference in stress rupture.

Comparison With Hot Pressed Silicon Nitride

In addition to testing the creep of reaction sintered silicon nitride, a limited number of bend creep tests were performed on the Norton HS-130 hot pressed silicon nitride. The purpose of these tests was to correlate the bend creep results with the tensile creep results obtained on HS-130.

Table 5.9 shows selected creep results of the various reaction sintered silicon nitrides compared to the bend and tensile creep results of HS-130. Comparison of the creep of reaction sintered Si_3N_4 of two purity levels (A and B) with that of HS-130 in bending shows the strain rates to be of the same order of magnitude, regardless of purity. The total strains obtained from bend tests were about 1/2 those from the tensile test. The results of the tests with injection molded silicon nitride show about 1-1/2 to 2 orders of magnitude less creep than the bending creep of the HS-130, while the slip cast silicon nitride shows no creep.

It can therefore be assumed that the general creep properties of the reaction sintered silicon nitride are superior to the hot pressed silicon nitride. Because of the costs of conducting tensile creep tests and because material development is on a steep learning curve, tensile creep testing of reaction sintered Si_3N_4 is being deferred until later in the program.

TABLE 5.8

CREEP OF SLIP CAST SILICON NITRIDE

<u>Material</u>	<u>Test Temp (°F)</u>	<u>Stress</u>	<u>Duration of Test (hrs.)</u>	<u>$\dot{\epsilon}$ (in/in/hr)</u>
NE12	2300	10 ksi	65	No detectable creep
NE12	2300	17 ksi	45	No detectable creep- then rupture
NE12	2300	20 ksi	5	No detectable creep- then rupture

TABLE 5.9

COMPARISON OF CREEP DATA
BENDING CREEP RESULTS

<u>Material</u>	<u>Temp</u>	<u>Stress</u>	<u>Test ATM</u>	<u>$\dot{\epsilon}_s$</u>	<u>Creep Strain 100 Hour</u>
Type B Inj. Molded Si_3N_4	2210°F	10 ksi	Air	$7 \times 10^{-6}/\text{hr}$	0.15%
Type C Inj. Molded Si_3N_4	2300°F	10 ksi	Air	$1.5 \times 10^{-6}/\text{hr}$	0.02%
Type D Inj. Molded Si_3N_4	2500°F	15 ksi	Air	$2 \times 10^{-6}/\text{hr}$	0.05%
NE-12 Slip Cast Si_3N_4	2300°F	10 ksi	Air	No Detectable Creep	No Creep Strain
Hot Pressed Si_3N_4 (HS-130)	2300°F	10 ksi	Air	$4-6 \times 10^{-5}/\text{hr}$	0.8-1.0%
	2500°F	15 ksi	Air	$4 \times 10^{-4}/\text{hr}$	> 2.5%

TENSILE CREEP RESULTS

Hot Pressed HS-130A Si_3N_4	2300°F	10 ksi	Air	$7-10 \times 10^{-5}/\text{hr}$	20%
HS-130B	2300°F	10 ksi	Air	$2 \times 10^{-5}/\text{hr}$	-

Elastic Constants of Si_3N_4

The speed of 10 MHz longitudinal sound waves has been measured in four silicon nitride samples with densities between 2.37 and 3.18 gm/cm^3 in the temperature range 0 to 1000°C. These data, together with shear wave data, some of which were reported earlier (2,3) allow a complete tabulation of the elastic constants of the samples studied in the stated temperature interval. Both longitudinal and shear moduli increase systematically with sample density. They appear to be determined by sample density rather than the details of material processing.

The longitudinal modulus $C = \lambda + 2G$ and shear modulus G , shown as functions of temperature in Figures 5.25 and 5.26, were calculated point by point from the measured longitudinal and shear wave sound speeds, V_L and V_S , using the formulas

$$C = \rho V_L^2 \quad (1)$$

$$G = \rho V_S^2$$

ρ being the sample density. Young's modulus E and Poisson's ratio ν (Figures 5.27 and 5.28) were calculated from C and G using the elasticity formulas

$$E = \frac{3C - 4G}{C - G} G \quad (2) \quad \text{and} \quad \nu = \frac{1}{2} \frac{C - 2G}{C - G} \quad (3)$$

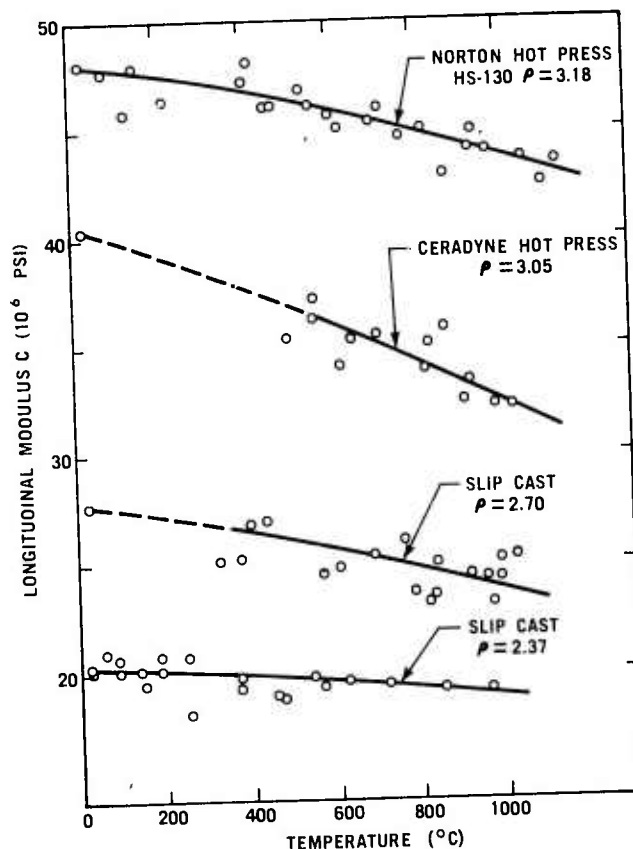


Figure 5.25 Longitudinal Modulus vs Temperature For Various Silicon Nitrides

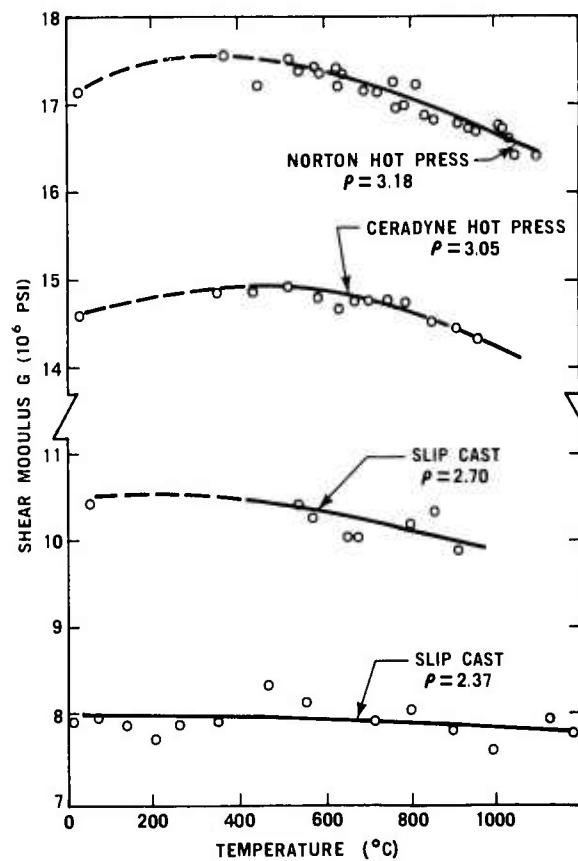


Figure 5.26 Shear Modulus vs Temperature For Various Silicon Nitrides

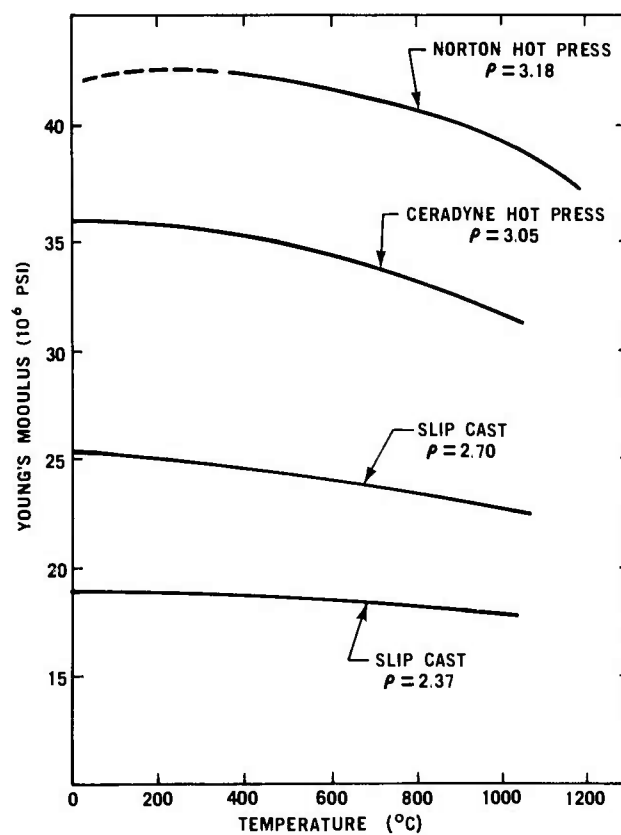


Figure 5.27 Young's Modulus vs Temperature for Various Silicon Nitrides

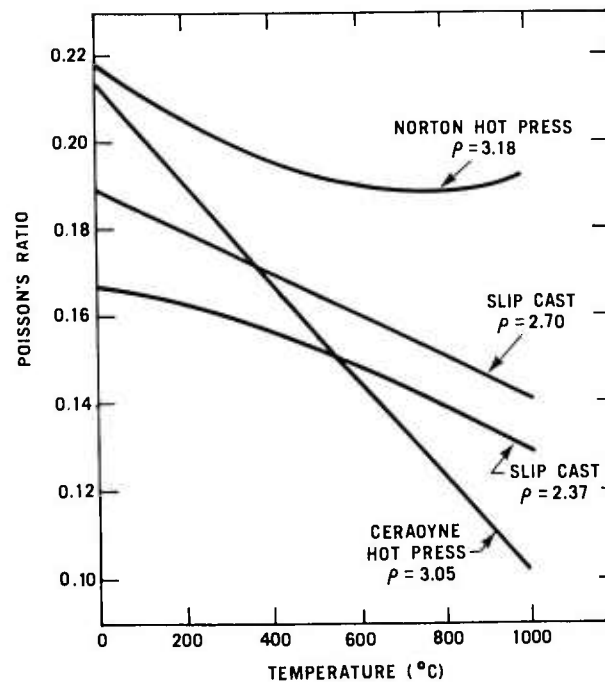


Figure 5.28 Poisson's Ratio vs Temperature For Various Silicon Nitrides

The density dependence of both moduli at room temperature (where data on more than four samples are available) can be shown to be in reasonable agreement with a theory of elastic constants of composite materials due to Budiansky ⁽²⁵⁾. For an n-component composite system Budiansky shows that:

$$\sum_{i=1}^n f_i \left\{ 1 - a + a (K_i/K) \right\}^{-1} = 1 \quad (4)$$

$$\sum_{i=1}^n f_i \left\{ 1 - b + b (G_i/G) \right\}^{-1} = 1 \quad (5)$$

where K and G are the bulk and shear moduli of the composite, K_i and G_i are the bulk and shear moduli of the i 'th component, f_i is the volume fraction of the i 'th component,

$$a = \frac{1}{3} \frac{1+\nu}{1-\nu} \quad (6) \text{ and } b = \frac{2}{15} \frac{4-5\nu}{1-\nu} \quad (7)$$

ν being the Poisson's ratio of the composite. In the present case there are two phases, pure Si_3N_4 and pores. For the pore phase (say $i=1$) we have $G_1 = K_1 = 0$ and for $f_1 = f_p$ the pore volume fraction. For the silicon nitride phase ($i=2$) $G_2 = G_0$, the shear modulus of fully dense Si_3N_4 , $K_2 = K_0$ the bulk modulus of fully dense Si_3N_4 , and $f_2 = 1 - f_p$. Thus, from equations (4) and (5)

$$\frac{K}{K_0} = 1 - \frac{f_p}{1-a} = \frac{\rho/\rho_0 - a}{1-a} \quad (8)$$

$$\frac{G}{G_0} = 1 - \frac{f_p}{1-b} = \frac{\rho/\rho_0 - b}{1-b} \quad (9)$$

where ρ is the density of the composite, ρ_0 is the density of fully dense material and we used $f = 1 - \rho/\rho_0$. Over the density range studied $0.17 \leq v \leq 0.22$ (see Figure 5.28). Thus from equation (4) $0.470 \leq a \leq 0.521$ and $0.496 \leq b \leq 0.507$. The assumption that $a \approx b \approx \frac{1}{2}$ is sufficiently accurate for the density range considered. From equation (5) and the elasticity formula $C = K + \frac{4}{3}G$ these results

$$\frac{K}{K_0} = \frac{C}{C_0} = \frac{G}{G_0} = 2 \frac{\rho}{\rho_0} - 1 \quad (6)$$

The experimental data are compared with equation (6) in Figure 5.29. The values of C_0 , G_0 and ρ_0 appropriate to the high density Norton HS-130 sample, $C = 48.0$ MPsi, $G = 17.15$ MPsi, and $\rho = 3.18$ gm/cm³ were used to normalize the data. Both moduli seem to have nearly the same variation with density which is slightly stronger than theory predicts. At higher temperatures, but below 1000°C, (where data on only four samples are available) the normalized elastic moduli show a density variation almost identical to the experimental data of Figure 5.29 while the theoretical curve predicted by the Poisson's ratios of Figure 5.28 and equation (5) is changed only slightly from the theoretical curve of Figure 5.29.

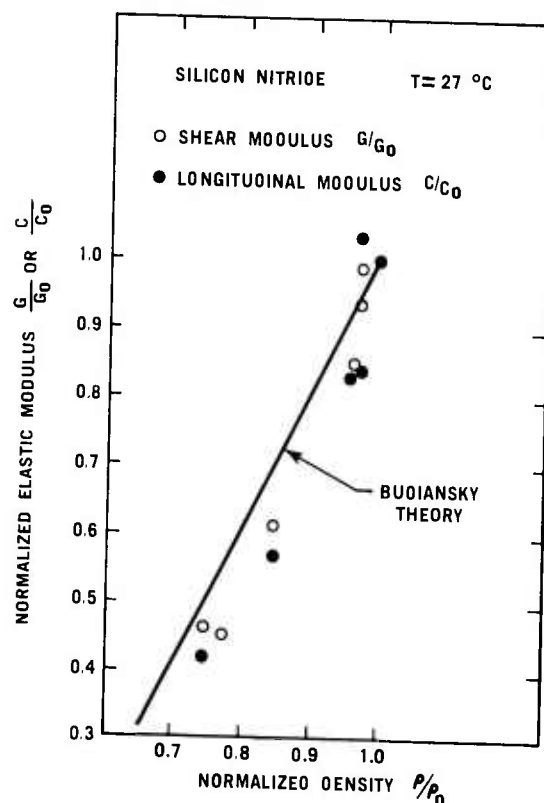


Figure 5.29

Room Temperature Elastic Constant Data For Silicon Nitride Compared With Budiansky Theory

5.2 MATERIAL SCIENCES

SUMMARY

The purpose of detailed investigations into material sciences is to develop an understanding of material behavior which will lead to improved material through better control of composition, processing, and fabrication. This is of particular importance since the ceramic materials being utilized in turbine engines are relatively new and appear capable of considerable improvement. Various phases of the material sciences investigation will be continued throughout the life of the program.

The impurities in 15 billets of Norton HS-130 hot pressed Si_3N_4 have been determined and are reported. The most significant impurity, calcium, is maintained at the relatively low level of 0.029 ± 0.005 w/o.

Simultaneous oxidation-sulfidation testing of Norton hot pressed SiC was conducted at temperatures ranging from 1800 to 2500 F. Weight changes were found to be equivalent to those obtained when testing was performed in pure oxygen, indicating that sulfidation does not occur in this material.

A study of fracture in HS-130 hot pressed Si_3N_4 was performed using a Vickers diamond pyramid indenter to precrack the sample. The cracks were then propagated by 4 point bending. A low fracture energy value, typical of a sharp crack, was measured. A critical flaw size of 20μ was calculated, and the temperature dependence of fracture strength on flawed and unflawed material was determined. Subcritical crack growth was observed under modest loading.

5.2.1 MICROSTRUCTURE OF HOT-PRESS SILICON NITRIDE AND SILICON CARBIDE

Introduction

The microstructural characterization of Norton HS-130 silicon nitride and Norton hot-pressed silicon carbide, now identified as NC-203, is essentially complete as reported.⁽¹⁻⁵⁾ Remnant material from the fabrication of vane assemblies has been examined and found to be consistent generally with the established aspects of microstructure. Norton NC-132 silicon contains far fewer low density inclusions, however, which apparently accounts for its superior low temperature strength.⁽⁴⁻⁵⁾ New data include additional chemical analysis of silicon nitride.

TABLE 5.10
SPECTROGRAPHIC ANALYSIS OF NORTON HS-130 SILICON NITRIDE

Sample/Billet		Al	Na	B	Ni	Ca	Cr	Fe	K	Li	Mg	Mn
Billet #2	- 1	> 0.1	.02	< .003	< .001	.11	.014	> 0.1	.006	.001	> 0.1	.014
	- 2	> 0.1	.02	< .003	< .001	.11	.010	> 0.1	.006	.002	> 0.1	.015
Billet #10	- 1	> 0.1	.009	.004	< .001	.033	.039	> 0.1	.005	< .001	> 0.1	.050
	- 2	> 0.1	.009	.004	< .001	.028	.040	> 0.1	.005	< .001	> 0.1	.051
Billet #9	- 1	> 0.1	.009	< .003	< .001	.017	.036	> 0.1	.006	.001	> 0.1	.047
	- 2	> 0.1	.009	< .003	< .001	.018	.037	> 0.1	.006	.001	> 0.1	.044
002172A	- 1	> 0.1	.008	< .003	< .001	.022	.034	> 0.1	.005	< .001	> 0.1	.052
	- 2	> 0.1	.008	< .003	< .001	.024	.037	> 0.1	.005	< .001	> 0.1	.057
062072A	- 1	> 0.1	.009	< .003	< .001	.024	.034	> 0.1	.005	< .001	> 0.1	.051
	- 2	> 0.1	.009	< .003	< .001	.025	.036	> 0.1	.005	< .001	> 0.1	.066
060672A	- 1	> 0.1	.005	< .003	< .001	.023	.037	> 0.1	.005	< .001	> 0.1	.059
	- 2	> 0.1	.005	< .003	< .001	.023	.037	> 0.1	.005	< .001	> 0.1	.059
060272A	- 1	> 0.1	.005	< .003	< .001	.024	.034	> 0.1	.005	< .001	> 0.1	.056
	- 2	> 0.1	.005	< .003	< .001	.023	.036	> 0.1	.005	< .001	> 0.1	.063
060972A	- 1	> 0.1	.005	< .003	< .001	.023	.038	> 0.1	.005	< .001	> 0.1	.057
	- 2	> 0.1	.005	< .003	< .001	.025	.036	> 0.1	.005	< .001	> 0.1	.057
060872B	- 1	> 0.1	.005	< .003	< .001	.023	.033	> 0.1	.005	< .001	> 0.1	.051
	- 2	> 0.1	.005	< .003	< .001	.023	.033	> 0.1	.005	< .001	> 0.1	.049
061472	- 1	> 0.1	.005	< .003	< .001	.028	.033	> 0.1	.005	< .001	> 0.1	.063
	- 2	> 0.1	.006	< .003	< .001	.025	.035	> 0.1	.005	< .001	> 0.1	.060
061272	- 1	> 0.1	.006	< .003	< .001	.026	.031	> 0.1	.005	< .001	> 0.1	.049
	- 2	> 0.1	.006	< .003	< .001	.028	.032	> 0.1	.005	< .001	> 0.1	.053
060172A	- 1	> 0.1	.006	< .003	< .001	.023	.032	> 0.1	.005	< .001	> 0.1	.056
	- 2	> 0.1	.006	< .003	< .001	.034	.033	> 0.1	.005	< .001	> 0.1	.051
060572A	- 1	> 0.1	.006	< .003	< .001	.023	.033	> 0.1	.005	< .001	> 0.1	.053
	- 2	> 0.1	.006	< .003	< .001	.025	.036	> 0.1	.005	< .001	> 0.1	.058
062872A	- 1	> 0.1	.006	< .003	< .001	.041	.039	> 0.1	.005	< .001	> 0.1	.058
	- 2	> 0.1	.006	< .003	< .001	.024	.038	> 0.1	.005	< .001	> 0.1	.058
051872A	- 1	> 0.1	.006	< .003	< .001	.025	.036	> 0.1	.005	< .001	> 0.1	.052
	- 2	> 0.1	.006	< .003	< .001	.041	.034	> 0.1	.005	< .001	> 0.1	.054
053172A	- 1	> 0.1	.003	.003	< .001	.047	.040	> 0.1	.003	< .001	> 0.1	.053
	- 2	> 0.1	.002	.003	< .001	.028	.039	> 0.1	.003	< .001	> 0.1	.056
061972A	- 1	> 0.1	.002	< .003	< .001	.028	.038	> 0.1	.004	< .001	> 0.1	.066
	- 2	> 0.1	.002	< .003	< .001	.043	.038	> 0.1	.002	< .001	> 0.1	.054
051572A	- 1		.003	< .003	< .001	.025	.034	> 0.1	.005	< .001	> 0.1	.051
	- 2		.003	< .003	< .001	.042	.036	> 0.1	.005	< .001	> 0.1	.051
052472A	- 1		.002	.004	< .001	.024	.042	> 0.1	.003	< .001	> 0.1	.063
	- 2		.002	.005	< .001	.029	.040	> 0.1	.003	< .001	> 0.1	.056

The Chemical Composition of Norton HS-130 Silicon Nitride

Quantitative spectrographic analyses have been obtained on the last 15 billets of Norton HS-130 silicon nitride in duplicate. The results appear in Table 5.10. Tungsten content is typically < 0.3 w/o and, therefore, is not shown. The carbon analysis was deleted because it is associated stoichiometrically with tungsten at < 0.04 w/o in the form of WC which as a high density inclusion does not affect the strength or performance of the material.

The Ca concentration appears to be the most significant part of the analysis in that it is maintained at respectively low levels in these latter billets. Billet to billet variation is small, average 0.029 ± 0.005 w/o, where the accuracy of the analysis is considered to be 50%.

Billets #2, 9-10, and 002172A appear in Table 5.10 as control samples to verify the reproducibility of the results. When these data are compared with previous analyses,⁽³⁾ the agreement is certainly within experimental error. Values of 0.07, 0.03, and 0.04 w/o Ca were reported for billets 2, 9 and 10, respectively.

An analysis of all remaining silicon carbide billets is in progress. These results will be summarized and reported later when the work is completed.

5.2.2 GAS-SOLID REACTIONS

Introduction

The kinetic processes involved in the static oxidation and sulfidation of silicon nitride and silicon carbide have been discussed.⁽¹⁻⁵⁾ This work has progressed to the point where simultaneous oxidation-sulfidation kinetics can be reported for Norton hot-pressed SiC.

Static Oxidation-Sulfidation of Silicon Carbide

The simultaneous oxidation-sulfidation kinetics for Norton's hot-pressed SiC were studied by continuous thermogravimetry using an automatic Cahn electrobalance. The procedure was the same as that used for the study of the oxidation-sulfidation behavior of Si₃N₄.⁽⁵⁾ In short, SiC specimens, 1/2" x 1/2" x 0.070", were suspended from the balance with a sapphire fiber and held at temperature in a flowing atmosphere of N₂/O₂/SO₂. All experiments were carried out at 1 atm total pressure using the following gas mixture:

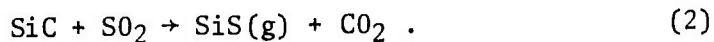
N ₂	89.9073%
O ₂	10.0%
SO ₂	0.0927%

This gas mixture corresponds to an equilibrium SO₂/SO₃ ratio of about 25.7 at 1300°K. A platinum wire gauze was placed in the hot zone of the reaction tube to catalyze the conversion of SO₂ to SO₃ according to the reaction:



The SO₂/SO₃ ratio employed is several times higher than that expected in a gas turbine, even with very high sulfur-containing heavy residual fuels; 6.70 for 0.5 wt % S fuel at 1300°K, for example.

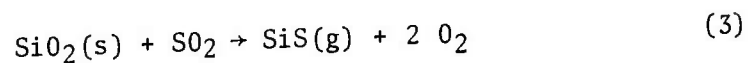
A small weight loss was observed during the initial oxidation period of a few minutes at all temperatures in the range 1800 to 2500°F. This loss in weight may be caused by the volatilization of tungsten oxide formed from the tungsten carbide (WC) present in hot-pressed SiC, or it may be due to the formation of some SiS(g) according to reaction



However, after this short period of weight loss, the magnitude of weight gain was found to be equivalent to that observed in pure oxygen within the limits of experimental uncertainty. X-ray diffraction analysis of the surface oxide showed that no SiS₂ was present. This observation confirms the results of the thermodynamic calculations presented previously.

Therefore, the oxidation behavior of hot-pressed SiC in very high sulfur fuels is expected to be similar to that in clean fuels.

Once a $\text{SiO}_2(\text{s})$ layer is formed on the surface of SiC, the formation of SiS(g) according to reaction (2) is greatly suppressed. However, one could expect the formation of SiS(g) by the reaction:



Under turbine conditions burning 0.5 wt % sulfur diesel oil at a compression ratio of 10:1, the partial pressure of SiS(g) by reaction (3) is calculated to be of the order of 10^{-32} atm at 1300°K (1880°F) and 10^{-24} atm at 1600°K (2420°F). These pressures are extremely small and therefore the formation of SiS(g) is of no consequence in the oxidation-sulfidation behavior of hot-pressed SiC.

5.2.3 SUBCRITICAL CRACK GROWTH STUDIES

Introduction

The physical and mechanical processes at a static or advancing crack tip can be influenced by local stress levels and temperature such that the crack advances relatively slowly until it attains a critical size such that catastrophic failure occurs according to the Griffith criteria. Further, subcritical crack growth can, depending on the circumstances, occur at small fractions of the normal fracture stress when time is provided for the deleterious processes to develop. It is this possibility that is of concern to the designer.

One approach to the study of brittle structural materials is to purposely introduce flaws of a controlled or at least measurable size and shape, and monitor the influence on fracture stress and mechanism through fractographic analysis. In this way one can control the initiation of fracture and tailor ancillary experiments accordingly. This approach to the study of fracture in Si_3N_4 leads to a demonstration of subcritical crack growth in this material.

Crack Studies

Bend test specimens of a previously described design ⁽⁴⁾ of Norton HS-130 Si_3N_4 were prepared by polishing the tensile surface with 3μ diamond. A single operational crack was introduced into the center of the polished surface of the specimen by an indentation technique using a Vickers diamond pyramid

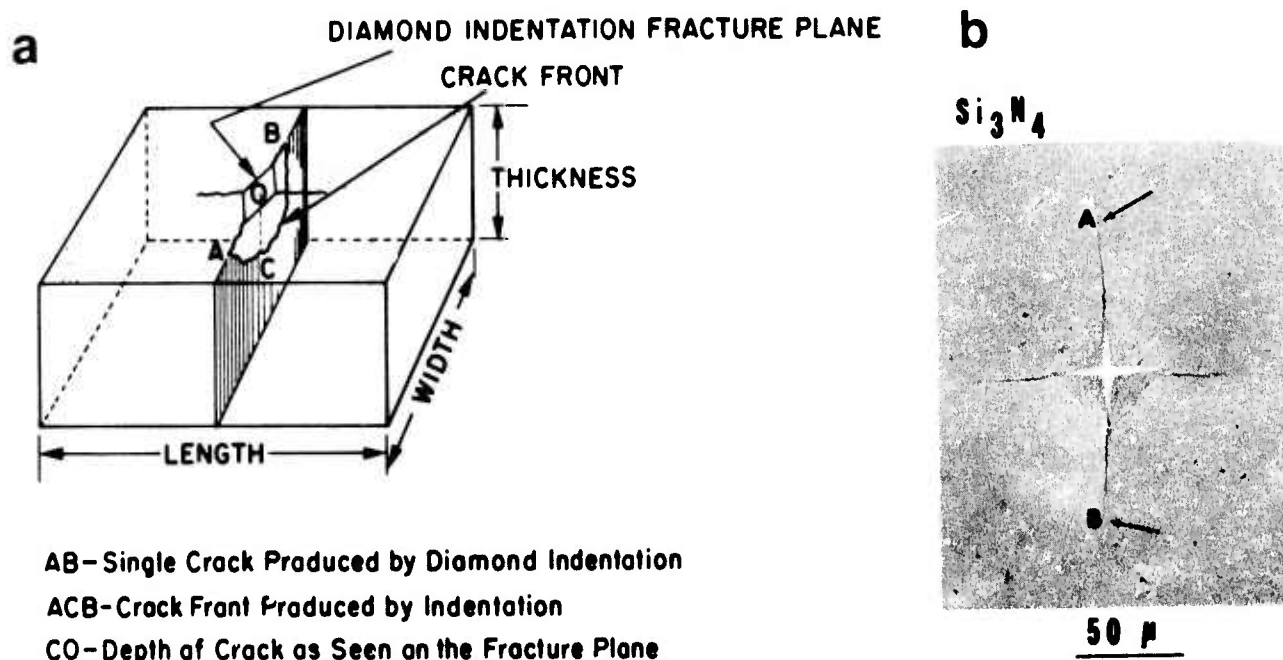


Figure 5.30 (a) Sample Pre-cracking Schematic of Crack Configuration Enplaced by Hardness Indenter

(b) Appearance of Typical Surface Crack in Norton HS-130 Hot Pressed Si_3N_4

indenter. This technique has been described elsewhere (26) and is shown schematically in Figure 5.30a, while a typical surface crack (s) configuration is shown in Figure 5.30b. Materials were evaluated nominally in the as-received condition. Tests were performed by 4 point bending in air in a Centorr furnace affixed to an Instron testing machine operated at a cross-head rate of 0.005 in/min.

Preliminary studies directed to establish the relationship between indentation load and crack depth indicated a reproducible correspondence (Figure 5.31). The influence of crack depth, OC, on fracture stress at room temperature follows the expected linear relation of σ_f to $C^{-1/2}$, where C is the depth OC measured on the fracture surface. The effective fracture energy, γ_i , taken from the Griffith relationship is about 18,000 ergs/cm², a low value typical of a sharp crack. Extrapolation of critical flaw size (size at σ_f) to the strength of the nominally unflawed material indicates an operational flaw size in the neighborhood of 20 μ by this technique. It is noteworthy that the γ_i value determined is lower than that typically obtained using relatively larger fracture initiating flaws in conventional fracture mechanics tests. The root of this less conservative variation on the part of "fracture mechanics" tests is as yet not clear and is an area of some concern.

Comparison of the temperature dependence of fracture strength in unflawed versus flawed (4000 gm indenter load, OC approximately 90 μ) material is shown in Figure 5.32. The σ_f of the unflawed material begins to decrease at about 1100°C, and the decreasing viscosity of the grain boundary glassy phase becomes less able to support the grain boundary cracks. A smooth decrease follows. The 90 μ flaws cannot support a load above 3000 Kg/cm², and since the fracture process is invariant so also is the σ_f level, the elastic modulus decrease being insignificant in this range. At about 1200-1250°C the stress level in the vicinity of the crack tip is sufficient to induce some modest plastic response in the viscous grain boundary layer thereby blunting the crack and producing an "anomalous" rise in fracture resistance. At 1250°C and above plasticity leads to a weakening in the fracture path with concomitant decrease in fracture strength.

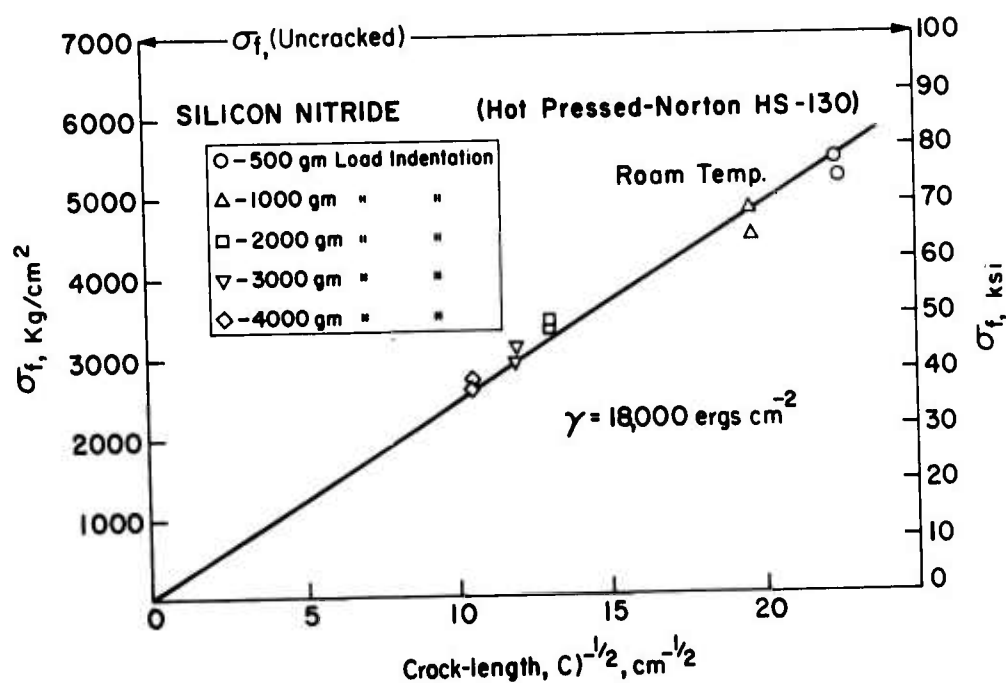


Figure 5.31 Plot of Fracture Stress As a Function of Crack Size

In this range also subcritical crack growth is observed to occur as the viscous grain boundary phase gives way under modest stresses in the range of loading rates used. Subcritical crack growth in HS-130 has been demonstrated to exist first by incrementally loading a precracked specimen and observing the resultant crack growth as in Figure 5.33. Specimens such as that in Figure 5.33 were then loaded to failure at room temperature and the relation between cracking on the tensile surface and that on the fracture surface was established. In Figure 5.34b we find that the relationship, previously inferred, is that the slow crack growth region has a higher amplitude path, and consequent different reflectivity in optical illumination, than the path of catastrophic failure. Figure 5.34 illustrates the proportionally increasing degree of subcritical crack growth at higher temperatures prior to catastrophic failure consistent with the sharply decreasing viscosity of the boundary phase and empirically with the decreasing stress level at failure.

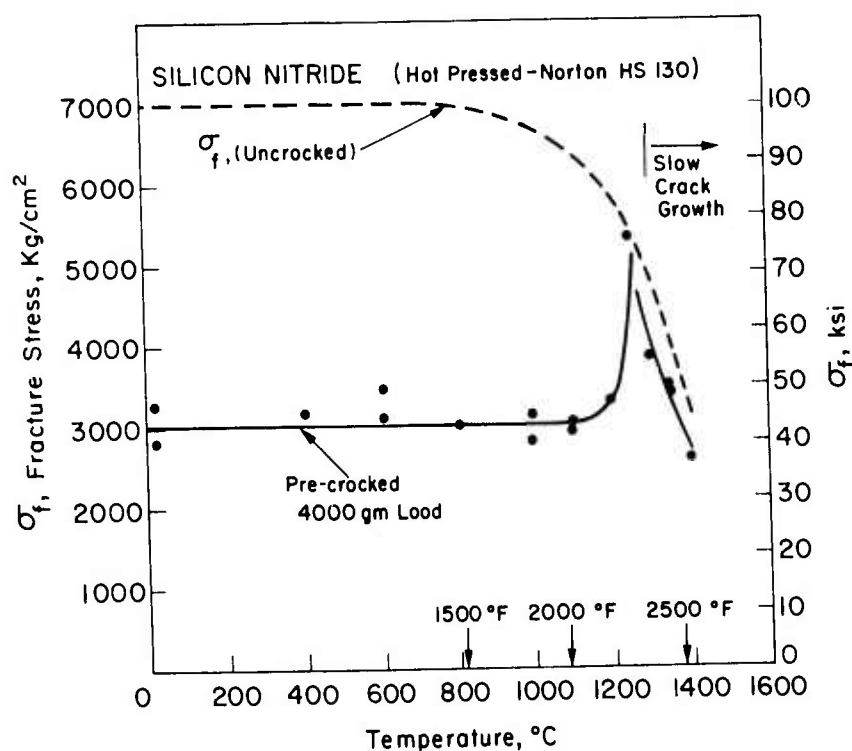
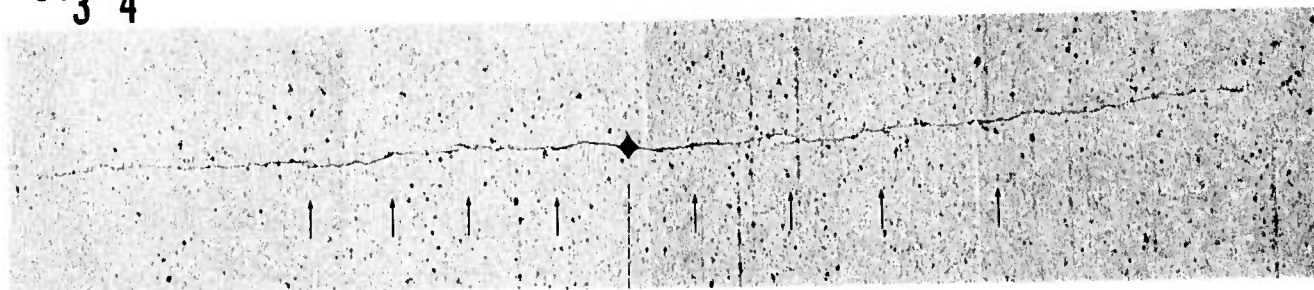


Figure 5.32 Comparison of Temperature Dependence of Fracture Stress in Nominally Unflawed Material to that Containing 90 μ Flaws



1350 °C

0.5 mm

Figure 5.33 Appearance of Surface Crack After Subcritical Crack Growth

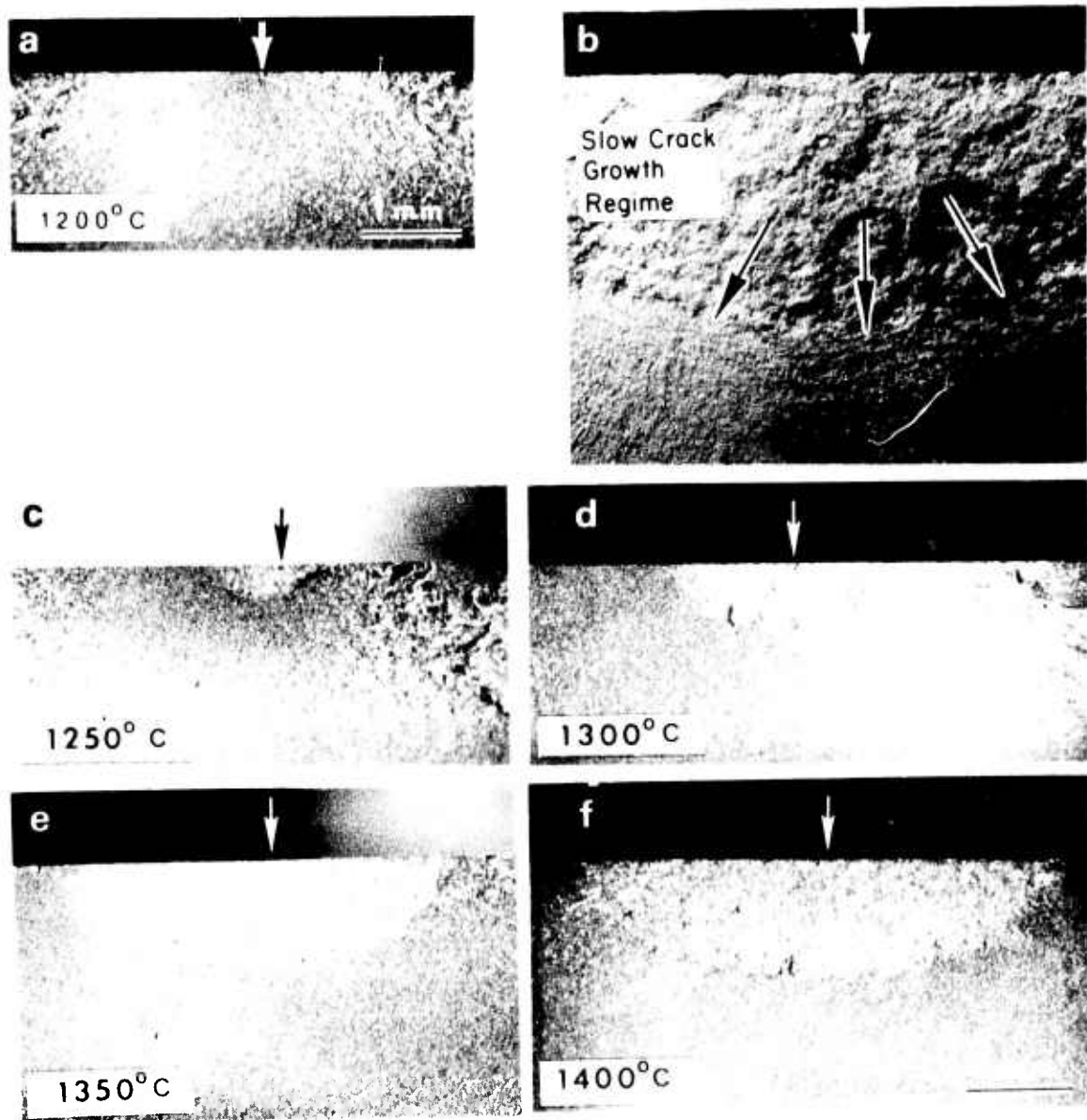


Figure 5.34 Temperature Dependence of the Extent of Subcritical Crack Growth Shown by Optical Microscopy. (b) is a Higher Magnification View by SEM of (c)

5.2.4 SIALON DEVELOPMENT

Ceramics of the Sialon ($\text{Si}_3\text{N}_4\text{-Al}_2\text{O}_3$) type are being investigated as possible materials for the fabrication of high temperature turbine parts by pressureless sintering. Relevant properties are being evaluated as a function of composition, preparation conditions and additives. In addition, the physical chemistry of the composition region of greatest interest is being studied. This preliminary study will be discussed in next report.

5.3 NON-DESTRUCTIVE EVALUATION OF MATERIALS

SUMMARY

A very important aspect of the development of ceramic gas turbine engines is the need to meaningfully inspect and test ceramic components before installation in the engine. The objectives of the NDE work are to identify and classify defects and to gain much information as possible on the properties of the material from which the component is manufactured. Both property and defect information are being related to performance of the component, leading eventually to routine inspection and acceptance/rejection based upon established actual performance. All available nondestructive means must be used to accomplish this goal and new methods must constantly be evaluated to determine their usefulness. Procedures utilizing ultrasonics, x-ray radiography, and acoustic emission are currently being applied to ceramic systems for evaluation purposes.

Flow detection in dense ceramics was enhanced by the use of the computer-aided ultrasonic technique. Resolution was improved by a factor of five and an increase in sensitivity was obtained. This system also demonstrated the ability to reject mode converted signals which could be erroneously interpreted as sub-surface flaws.

A block of hot pressed silicon nitride with a series of laser drilled holes was used as a standard in order to determine commercial ultrasonic equipment limitations with respect to flaw depth in the material. Defects approximately 60 microns in size can be detected provided they lie between 5 to 60 mm below the surface. Using a scan ultrasonics, additional work was done on detecting defects in hot pressed silicon nitride.

Acoustic emission (AE) testing of stator assemblies resulted in good correlation between AE response and observed cracks. Furnace testing to determine the AE response at temperature would be beneficial in selecting design/material combinations to eliminate outer shroud cracking.

X-ray radiography was used as the principle evaluation tool in a molding study of ceramic turbine rotor blade rings which resulted in a significant decrease in molding flaws. Analysis was accomplished in the as-molded condition, eliminating additional processing of flawed components. Optimum molding parameters were determined by selecting various molding conditions and comparing the resulting quality of the components by radiographic analysis. Similar results were obtained by radiographing individual as-molded stator vanes.

The need for increased radiographic sensitivity, to detect flaws on the order of 10-25 microns in dense ceramics, is apparent in order for this method to approach the usefulness of ultrasonic NDE.

Various NDE techniques are summarized with respect to specific advantages and limitations established through experience in application to ceramic turbine components and materials. Resolution and sensitivity limits of x-ray radiography and ultrasonic pulse echo testing for various materials and flaw types are presented.

5.3.1 ULTRASONIC NDE

Introduction

Progress in the development of a computer-aided ultrasonic test system for the detection of discontinuities in ceramic materials was reported earlier ⁽⁴⁾. Using this system, discontinuities undetected by conventional ultrasonic techniques were located in hot pressed Si_3N_4 . A test performed on a disk of Norton HS-110 material demonstrated increased resolution. The tests on a radiographic step block of hot pressed Si_3N_4 also showed the increased resolution of the computer aided system.

Additional work was done to establish the sensitivity and detection limits and to develop reliable standards for use in A scan ultrasonic defect detection in hot pressed Si_3N_4 .

Ultrasonic System

Since the detection and accurate location of discontinuities in ceramic materials involves large amounts of data, a computer-aided ultrasonic system was designed to collect, process, and display the data. The usefulness of such a computer-aided system is enhanced if it is sufficiently automated so that the data can be collected by relatively unskilled personnel.

The ultrasonic system designed and constructed for this purpose embodies this "automated system" concept. Since most of the ultrasonic and computer hardware had been assembled and tested earlier ⁽⁴⁾, only a few modifications were necessary to fit this hardware into the complete system. Most of this effort was devoted to the design of a software operating system which would perform the necessary data processing. This software has been in operation for four months and has fulfilled most of its design goals. While the software system is not yet totally integrated, it does constitute the framework for the automated system.

Resolution and Detectability Experiments

The computer-aided ultrasonic system is superior to conventional systems primarily in its ability to detect small discontinuities and to determine whether or not the detected signal is due to one or more sources. The former property is referred to as detectability or sensitivity and the latter as resolution. The detectability of the ultrasonic system is determined by the noise from the transducer and amplifiers and the noise from random reflections in the ceramic material. All the data presented was collected using a sensitivity enhancement technique designed to reduce the transducer and amplifier noise. Figure 5.35 shows a discontinuity map of a section of a HS-110 ceramic disk. The computer-aided contact scanning system located more discontinuities than the conventional C-scan system even when the threshold was set at a value about five times greater than the noise generated by the random ultrasonic reflections. With a lower threshold, discontinuities were detected in virtually every numbered area. Quantitative data on the size of the minimum detectable discontinuity awaits the results of sectioning the HS-110 disk.

Data collected from a variety of ceramic samples indicates that, with the use of this sensitivity enhancement technique, the detectability of the ultrasonic system is not limited by the transducer and amplifier noise but by the random reflections the ultra-sound wave undergoes in the ceramic material.

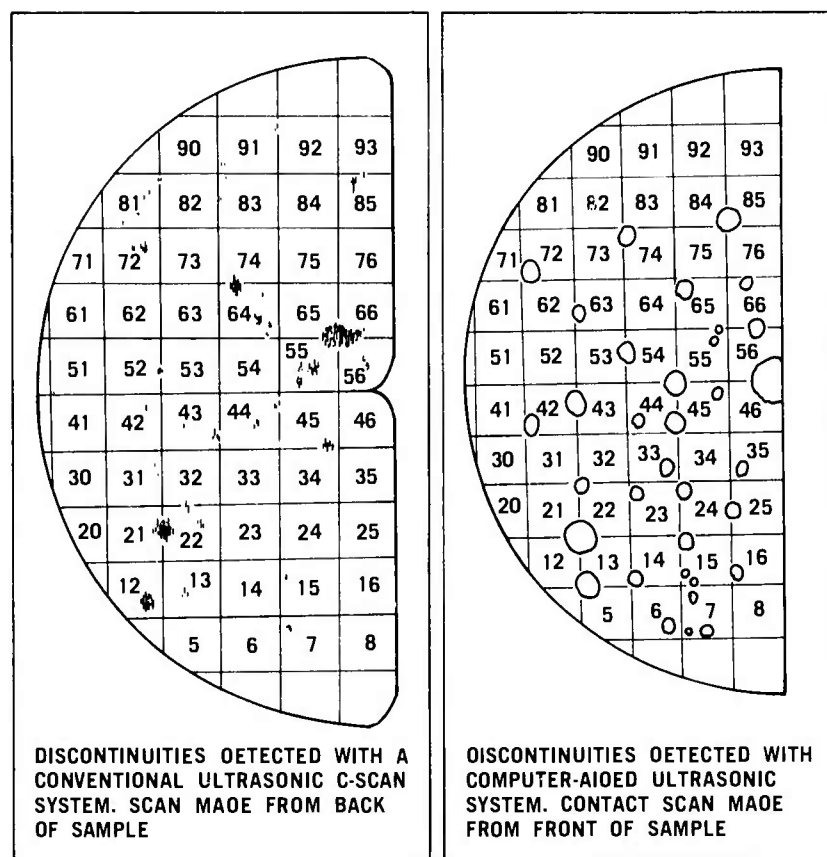


Figure 5.35 Sensitivity Comparison of the Conventional and the Computer Aided System on a Disk of HS-110 Hot Pressed Silicon Nitride

Resolution tests were performed, as shown in Figure 5.36, on the HS-130 hot pressed Si_3N_4 radiographic step block standard illustrated in a previous report (3). Only the first three steps of 0.031 inch, 0.026 inch, and 0.021 inch were resolved with the computer aided system, as shown in Figure 5.37. None of these steps were resolved with the conventional system, as shown in Figure 5.38. The first two ultrasonic measurements are within 10% of the measured values. The large error in the third step appears to be due to its relatively small amplitude and to the fact that the system is operating at its resolution limit. The estimated resolution of a conventional system is 0.134 inch, a factor of five larger than the computer-aided 0.026 inch resolution. The resolution figures for the computer-aided system could be extended by another factor of two or three with hardware improvements.

Figure 5.39 demonstrates another feature of the computer-aided system. The unprocessed data in Figure 5.39a shows the multiple reflections of the ultrasonic pulse between the front and back surfaces of a disk of HS-130 hot-pressed Si_3N_4 . This data was processed, as shown in Figure 5.39b, to provide ultrasonic velocity data for use in the resolution experiments. In addition to providing more accurate velocity data, the processed data also shows that the mode converted signals often interfere with the interpretation of the ultrasonic data, and therefore, their attenuation should aid in data evaluation.

While data from the computer-aided system has improved resolution and accuracy, the improvements are restricted to one dimension only - the radial distance from the transducer. The system cannot distinguish the angular

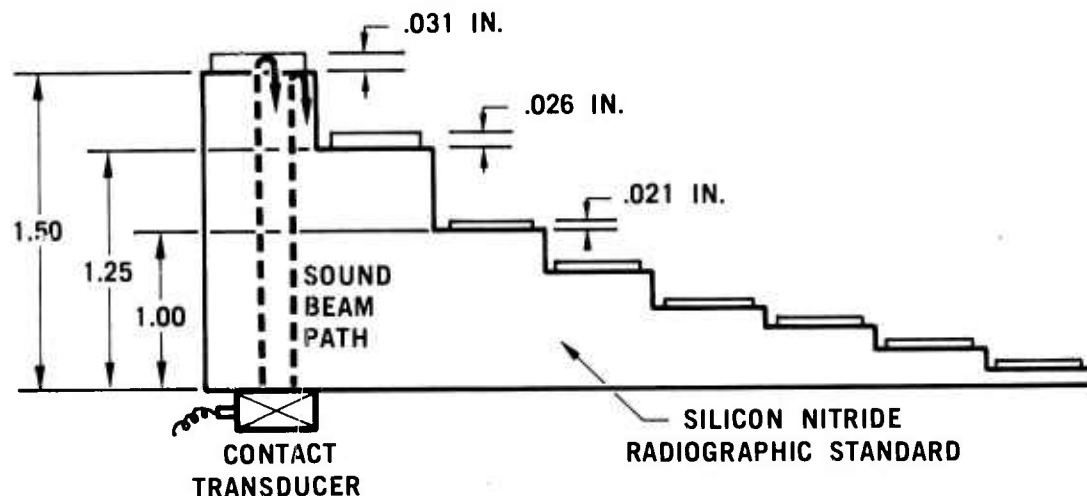


Figure 5.36 Method of Testing Radiographic Test Block, Where Each Large Step Contains a Smaller Step Which is 2% of the Thickness of the Large Step

position of the discontinuity. To achieve angular resolution, the transducer must scan the target and process the data received at each position. This is the next logical step in the development of an ultrasonic system to detect and locate discontinuities in ceramic materials.

Once the ultrasonic system has sufficient radial and angular resolution, the discontinuity can be located and characterized by the exact location of each ultrasonic reflector. These reflectors will trace an outline of the discontinuity surface, and the final result will appear as a "picture" of the discontinuity.

A Scan Ultrasonic Development

The development and use of A and C scan ultrasonics has been discussed in previous reports ^(3,4). Commercial techniques have been particularly sensitive to low density inclusions (poorly consolidated Si_3N_4 or BN) or voids in hot-pressed silicon nitride and silicon carbide greater than 150 microns. Cracks are resolved with difficulty and high density inclusions remain unresolved presumably because the reaction of Fe and W, for example, with the matrix material provides a low acoustic impedance particle-matrix interface which does not constitute a discontinuity for sound waves.

Additional work has been done to establish the sensitivity and detection limits of A scan ultrasonics using a 10 MHz Branson transducer at a 200 mm focal length. These results appear in Table 5.11.

This activity continually demonstrates the critical need for reliable standards. To this end, a series of holes about 400 μm in diameter were laser drilled to regularly increasing depths in a Si_3N_4 block. The block was scanned from all possible orientations again using the Branson transducer (10 MHz, 200 mm focal length). Peak height of the reflected signals is plotted as a function of hole location with respect to the incident surface in Figure 5.40. Disregarding the fact that defects less than 5 mm below the surface may be obscured by the frontal reflection signal, the intensity increases with hole depth because the position of the defect relative to the fixed focal point of the beam changes. Defects $\sim 60 \mu\text{m}$ can be detected provided they lie 5 to 60 mm below the surface.

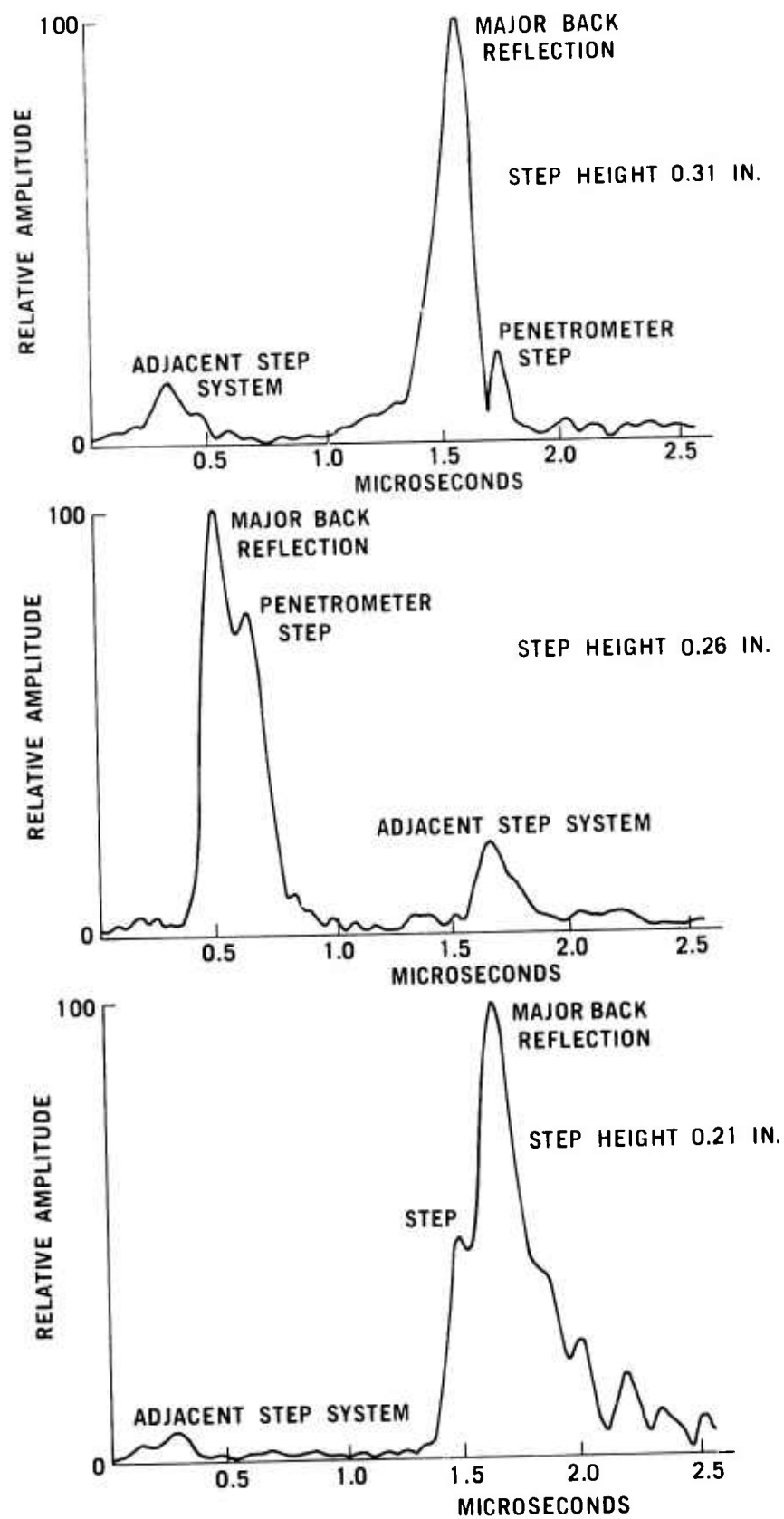


Figure 5.37 Step-Block Resolution of the Computer-Aided Ultrasonic System

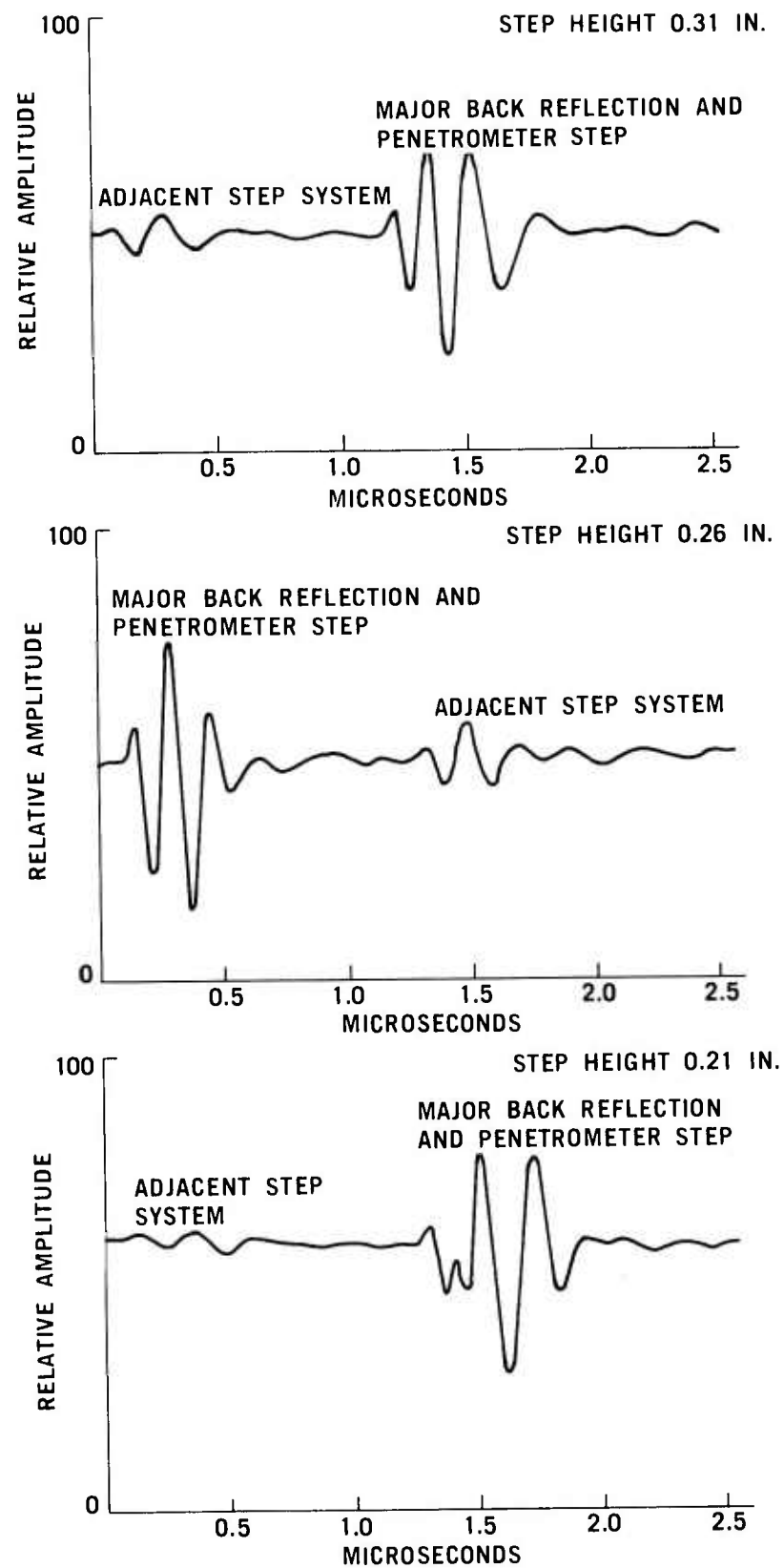


Figure 5.38 Step-Block Resolution of the Conventional Ultrasonic System

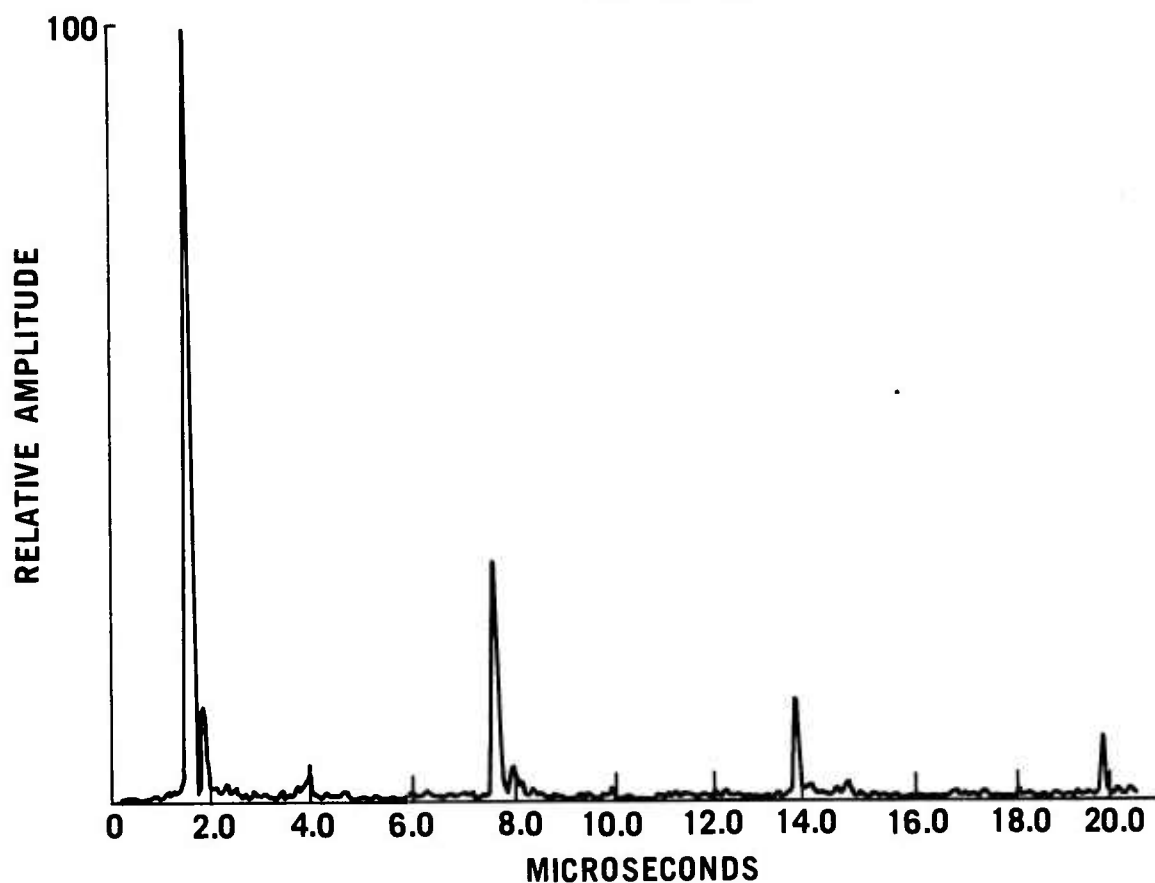
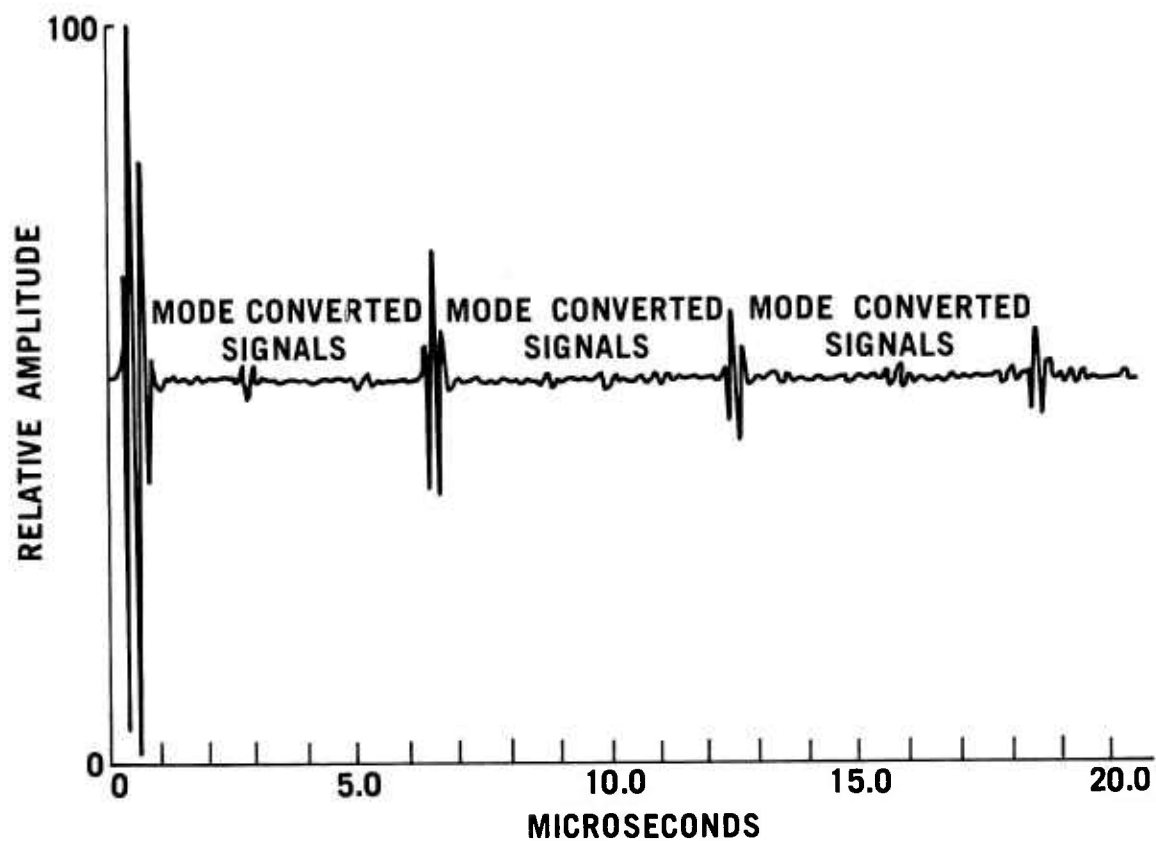


Figure 5.39 Reflections From the Back Surface of a HS-130 Silicon Nitride Disk, Showing the Differences Between (a) The Conventional System and (b) The Computer-Aided System

TABLE 5.11

DETECTION OF DEFECTS BY A-SCAN ULTRASONICS
(10 MHz Branson Transducer, 200 mm Focal Length)

	<u>Sensitivity</u>	<u>Detection Limit in 20 mm Piece</u>
BN Filled Cavity	--	Not Detected
Crack or Void	< 0.05	< 100 μm
Steel Particle	--	Not Detected
WC Particle	--	Not Detected

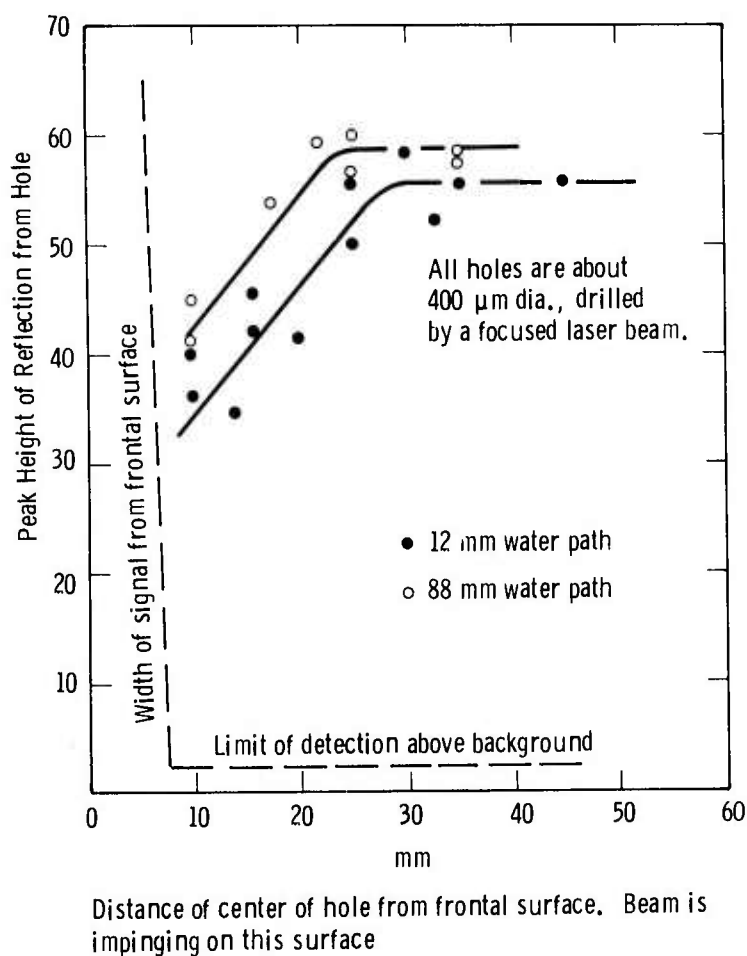


Figure 5.40 Strength of A Scan Ultrasonic Reflection vs Depth of Hole

5.3.2 ACOUSTIC EMISSION

Introduction

The acoustic emission (AE) response to elevated temperature on several stator assemblies was established using the technique described in the previous report (5). The data indicates the AE response varies depending on the specific stator design and material composition. A total of 698 hours in a furnace at 1900°F with no visible damage has been accumulated on a specific second stage stator assembly. Conversely, a different second stage stator incurred damage after only 60 hours at 1900°F.

Stator Testing

Test results indicate the ability of AE to detect both low and high energy stress waves over a wide range of occurrences. This covers the range from microcrack initiation/propagation to intermittent macrocrack extension. The curve shown in Figure 5.41 is the AE response of a spalling or shivering type of material failure. Many discrete bursts of released energy were detected which, for the duration of testing, resulted in a linear increase in AE with time at temperature. However, axial and circumferential cracks were noted in another assembly, after testing at 1900°F, although the AE curve, shown in Figure 5.42, had similar characteristics. Both curves were generated using digital envelope processing instrumentation (DEP) and indicate the need for additional means of displaying AE data since more than one failure mechanism may be active.

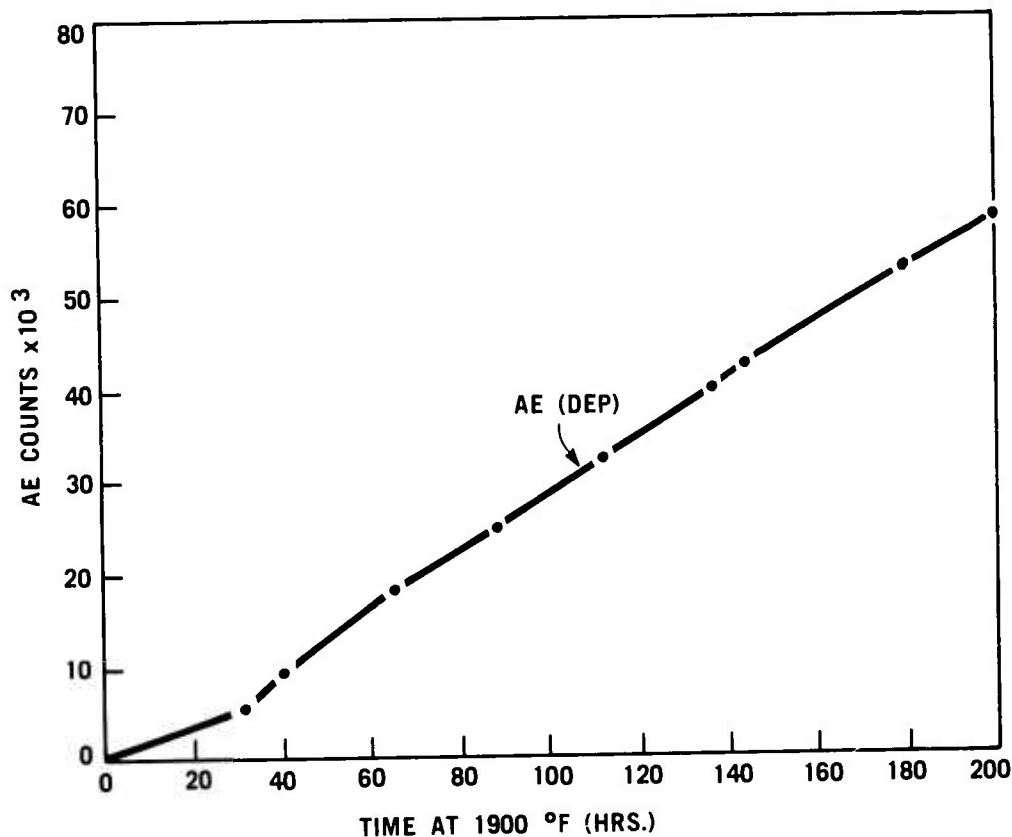


Figure 5.41 Acoustic Emission vs Time For a Second Stage Stator Assembly

The curve shown in Figure 5.43 indicates very little AE with high occurrence frequency (DEP data) but a high rate of AE was noted after 160 hours. This stator assembly had one tight axial crack in the outer shroud which probably occurred between 160 and 188 hours at 1900°F. The presence of these cracks supports the contention that AE data must be processed and displayed in various ways in order to fully understand the manner in which the AE is being emitted.

The curve in Figure 5.44 implies macrocrack propagation between 13 and 91 hours at which time testing was discontinued. Examination of the stator assembly revealed one large axial crack and several other small axial cracks in the outer shroud. These stators varied in terms of silicon nitride composition and design and the AE response varied accordingly.

The data demonstrates the usefulness of AE techniques in evaluating material and design variations. AE processing instrumentation, measuring the summation of all detected events and DEP processed events, has shown a capability to differentiate types of failure mechanisms. The information is not absolute, but on a relative basis is considered to be a valuable aid in analyzing the effects of material and design modifications in a complex shape such as a stator assembly.

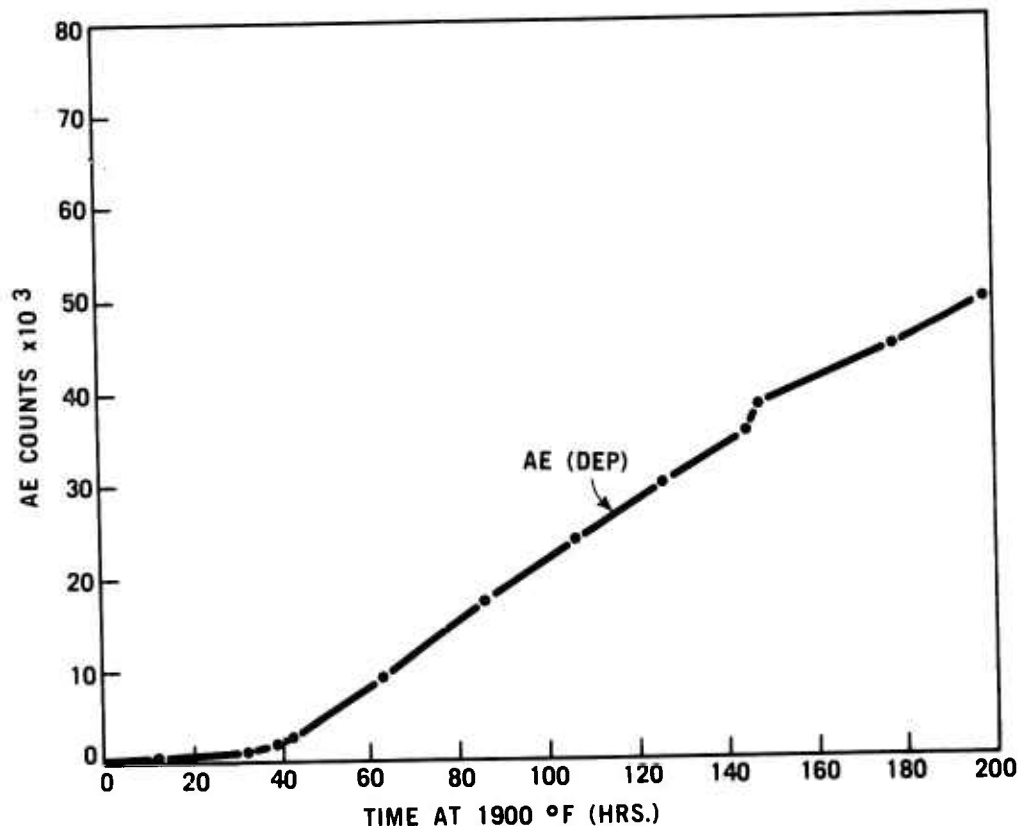


Figure 5.42 Acoustic Emission vs Time For a Second Stage Stator Assembly

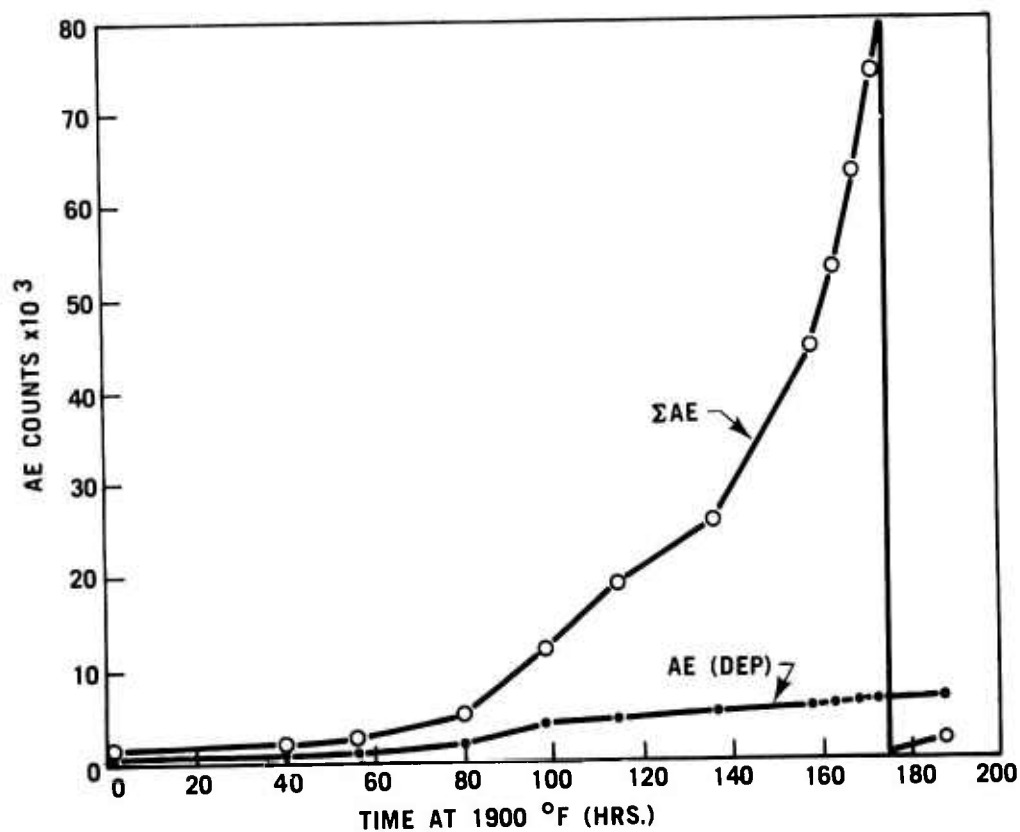


Figure 5.43 Acoustic Emission vs Time For a Second Stage Stator Assembly

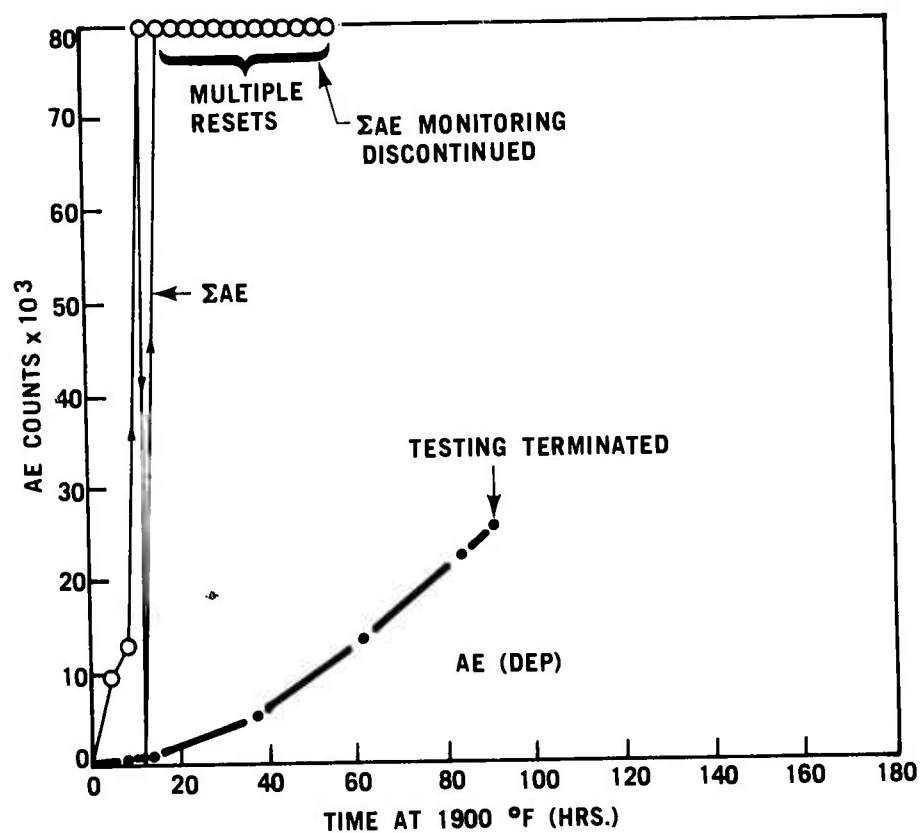


Figure 5.44 Acoustic Emission vs Time For a Second Stage Stator Assembly

5.3.3 X-RAY RADIOGRAPHY

Introduction

The results of comparison documented in the last report (5) indicated the usefulness of conventional x-ray radiography to detect subsurface voids in as-molded rotor blade rings. Radiography was further used to optimize the molding parameters and is being used to continuously monitor the process. These efforts have resulted in a significant increase in quality, as unacceptable rotor blade rings are eliminated without being processed and tested. Similar programs are being conducted on other molded components to quickly and efficiently establish the best molding conditions.

The x-ray detection limits of common defects in both hot pressed silicon nitride and silicon carbide in terms of 20mm thick section were determined.

Rotor Blade Rings

The presence of undesirable flaws in the platform area as well as gross defects in the molded disk region gave the impetus to evaluate all blade rings. Verification of this condition and an analysis of the effects of different molding parameters was accomplished using x-ray radiography. A correlation between a thin disk sprue section and the presence of subsurface flaws was found as shown in Figure 3.27 in Section 3.1.2 of this report. This condition was traced to a floating sprue bushing which, at times, reduced the mold orifice resulting in poor material fill and many subsurface flaws. A significant increase in yield was observed by simply correcting to retain a larger orifice, allowing more uniform material flow into the tool.

The next step was to optimize the entire process using x-ray radiography to ascertain the quality of parts molded under specific conditions as discussed in Section 3.1.2 of this report. Initially, the various molding conditions were evaluated based on the radiographic results of the blade ring disks. A correlation was observed between good disk fill and good platform fill as shown in Figure 3.26 in Section 3.1.2. The molding process will be further optimized by determining, through x-ray radiography, those conditions which result in eliminating small voids detected in the rotor blades.

Other Ceramic Components

X-ray radiography is also used on all other as-molded components. This includes first and second stage stators and nose cones. The second stage stators are fabricated by bonding individually molded vanes to a slip cast outer ring. This necessitates an initial x-ray evaluation of the individual vanes to assure none with flaws are used to fabricate the stator assembly. A comparison of good and flawed vanes is shown in Figure 5.45.

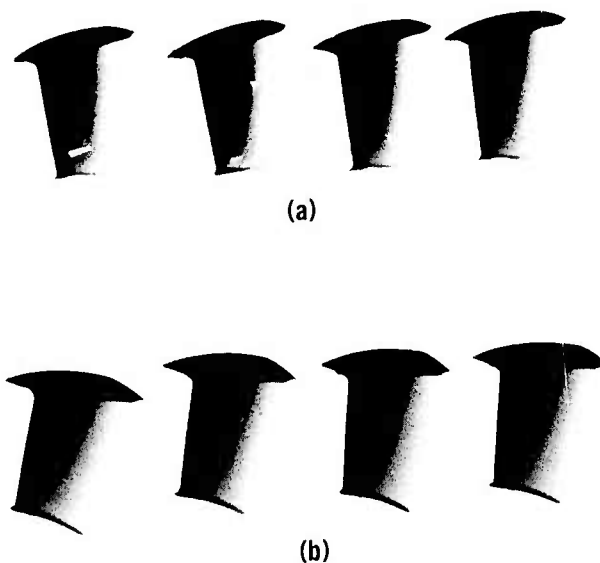
Nose cones and one piece first stage stators are similarly evaluated. An initial molding optimization study is followed by process monitoring to assure the quality of as-molded parts.

Hot Pressed Materials

The bulk of x-ray radiography on the stationary turbine project was performed to qualify second generation design silicon nitride and silicon carbide stator vane hardware for static rig testing at 2500°F. The detection limits for commonly recognized defects in Si_3N_4 and SiC are reported in terms

of 20 mm thick pieces in Table 5.12. Sensitivity, formerly referred to as Resolution Limit, ⁽⁵⁾ for a 60-100 kV, 10 mA source at a 60 in. distance is also summarized in this table.

If the detection limit and sensitivity could be reduced to 10-25 μm and 0.0005-0.0025 in., respectively, x-ray radiography would be an extremely valuable final inspection method for hot pressed ceramic turbine components.



RADIOGRAPHIC REVERSAL PRINT OF INJECTION MOLDED
SECOND STAGE STATOR VANES.

- (a) FLAWED VANES
- (b) UNFLAWED VANES AS A RESULT OF THE
OPTIMIZED MOLDING PROCESS

Figure 5.45 Radiographic Reversal Print of Injection Molded Second
Stage Stator Vanes, Showing (a) Flawed Vanes and (b)
Good Vanes

TABLE 5.12

DETECTION OF DEFECTS BY X-RADIOGRAPHY
(60-100 kV, 10 mA, 60 in. Source Distance)

	<u>Sensitivity</u>	<u>Detection Limit in 20 mm Piece</u>
BN Filled Cavity	0.04	800 μm
Crack, Hole	0.03	600 μm
Steel Particle	0.007	140 μm
WC Particle	0.005	100 μm

5.3.4 NDE AND CERAMIC COMPONENT FABRICATION

Introduction

NDE methods are being employed as integral steps in the fabrication of ceramic components to assure only quality hardware is processed. Utilizing NDE as early as possible is the ultimate objective, as this leads directly to more efficient use of time and manpower. Available NDE methods such as x-ray radiography and ultrasonics can provide meaningful data with respect optimizing and monitoring a specific fabrication procedure.

NDE and Its Relation to Ceramic Component Fabrication

The fabrication sequence for ceramic turbine components made of slip cast and injection molded Si_3N_4 is shown schematically in Figure 5.46. The small cross-hatched boxes indicate those points in the process where NDE is applied. Available NDE methods are used to initially eliminate flawed components and then to monitor the effects of specific fabrication steps.

X-ray radiography is extensively used on as-molded components but is not used on slip cast components prior to the sintering/prenitriding step because of their low strength at this point in the process. Radiography is also used to check for unreacted silicon metal after the nitridation process and to evaluate the duo-density rotor bond between the injection molded blade ring and the hot pressed disk section.

Sonic velocity measurements, in both longitudinal and transverse modes, are taken to determine properties such as modulus of elasticity, shear modulus and Poisson's ratio. This data is also intended to aid in future work to measure, as early as possible, the effects of process and material changes.

Acoustic emission (AE) monitoring of ceramic components subjected to mechanical or thermal stresses are primarily in the developmental stage, although trends have been observed between AE and component quality.

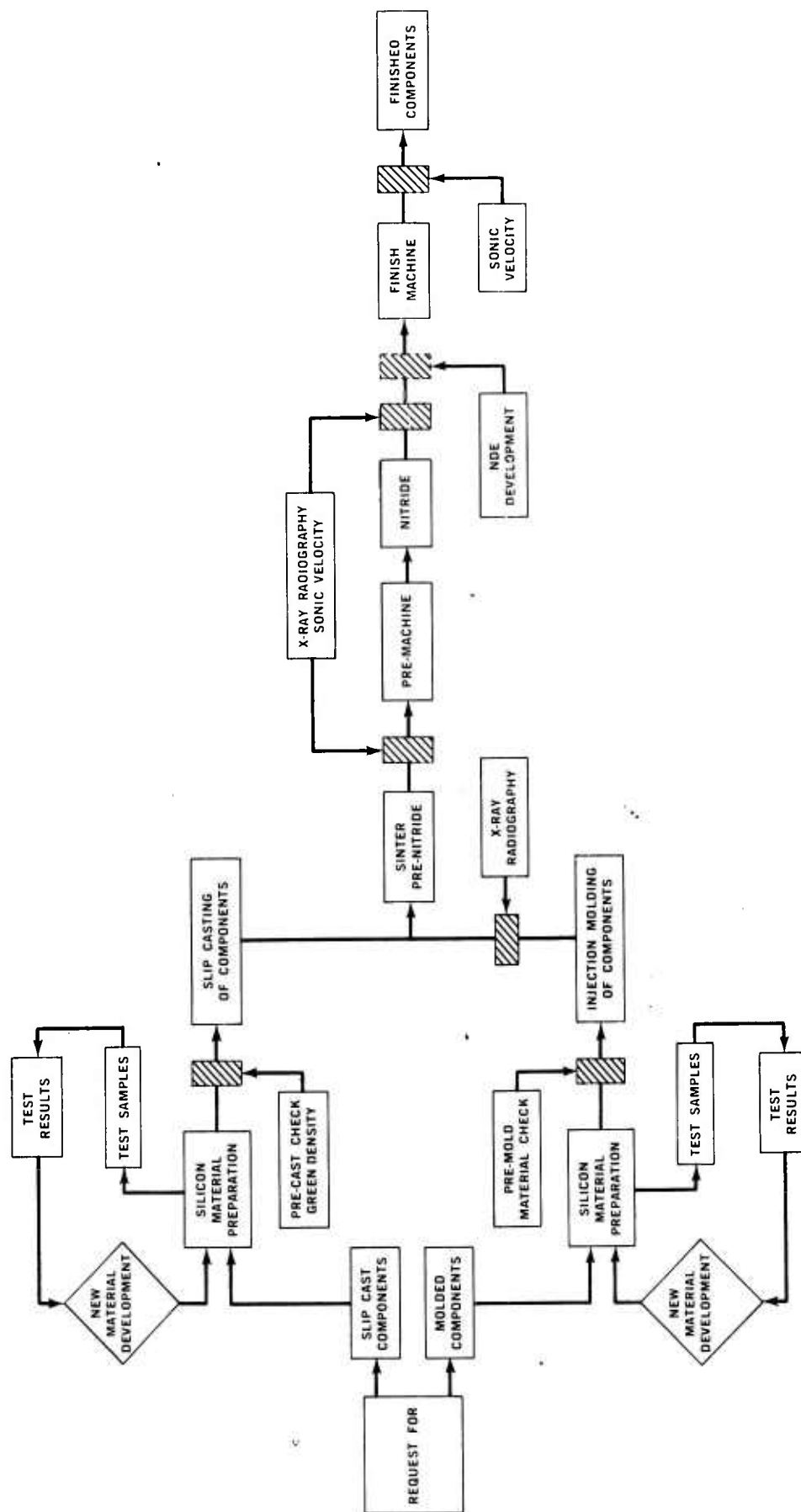


Figure 5.46 Schematic of Ceramic Component Fabrication Sequence Indicating Points in The Process Where NDE is Utilized

5.3.5 SUMMARY OF NDE METHODS

At this point in the program, it was felt useful to summarize specific NDE methods used to evaluate ceramic engine components and materials. The summary lists the NDE method, materials investigated, types of detectable flaws (or the intended application) and the advantages or limitations of each method as determined through actual application.

Table 5.13 lists the established sensitivity and/or resolution limitations for NDE methods used on specific materials. Sensitivity levels are given in terms of the smallest flaw which can be detected at a given depth in the materials. Resolution limits, that is, how close two separate flaws may be to each other and still be resolved, are given for dense silicon nitride.

The balance of this section consists of tabulations of the applications, advantages, and limitations of various non-destructive evaluation methods as determined to date through application to various turbine ceramic materials.

TABLE 5.13

SENSITIVITY/RESOLUTION LIMITS

<u>NDE METHOD</u>	<u>MATERIAL SYSTEM</u>	<u>SENSITIVITY- FLAW SIZE</u>		<u>FLAW TYPE</u>	<u>FLAW DEPTH (in.)</u>
Ultrasonics:		<u>In.</u>	<u>μm</u>		
.Immersion	Si ₃ N ₄ -R.B.	1/64	400	F.B.H.	0.38
	Si ₃ N ₄ -R.B.	1/32	800	F.B.H.	0.50
	Si ₃ N ₄ -H.P.	1/64	400	S.H.	2.10
	LAS	1/32	800	F.B.H.	1.00
X-ray Radiography					
	Si ₃ N ₄ -H.P.	0.040	1000	BN	1.00
		0.030	750	Hole	1.00
		0.007	175	Steel	1.00
		0.005	125	WC	1.00
	LAS	0.030	750	Hole	0.94
		<u>RESOLUTION LIMIT</u>			

Ultrasonics:

.Contact Si₃N₄ -H.P. 0.026 660 Back Reflection 1.50

Key: R.B. - Reaction Bonded, H.P. - Hot Pressed, F.B.H. - Flat Bottom Hole,
S. H. - Side Hole

NDE Method: Dye Penetrants (Fluorescent Particle and Filtered Particle)

Materials Investigated: H.P. Si_3N_4 , R.B. Si_3N_4 , LAS

Areas/Applications Investigated:

- .Surface cracks
- .Segregated porosity

Advantages:

- .Easily applied
- .Flourescent characteristic increases flaw visibility
- .Complex geometries are easily inspected

Limitations:

- .Limited sensitivity
- .Surface porosity may mask flaw indications
- .Part must be thoroughly cleaned prior to inspections
- .Permanent records not easily obtained

NDE Method: Ultrasonic Pulse Echo

Materials Investigated: Si_3N_4 (All Densities), LAS

Areas/Applications Investigated:

- .Subsurface flaws
- .Velocity measurements; mechanical properties (MOE, μ)

Advantages:

- .High sensitivity
- .Permanent record obtained (C-scan)
- .Access to only one surface required

Limitations:

- .Reference standards required
- .Complex shapes limit applicability
- .High density inclusions with low acoustic impedance may not be detected
- .Cracks parallel to sonic beam cannot be detected
- .Trained operators required

NDE Method: Radiography, X-ray (Conventional Film Imaging)

Materials Investigated: Silicon metal/organic composites, Si_3N_4 (all densities),
LAS, SiC

Areas/Applications Investigated:

.Subsurface defects; voids, low density areas, laminations, shrinkage,
etc.

Advantages:

.Can evaluate complex shapes
.Detects small inclusions when density is higher than matrix material
.Permanent record obtained

Limitations:

.Detectable flaw size depends on material thickness, geometry, film
response
.Flaw orientation may not be favorable
.Reference standards necessary

NDE Method: Xeroradiography (Conventional x-ray source)

Materials Investigated: Silicon metal/organic composites, sintered silicon metal, Si_3N_4

Areas/Applications Investigated:

.Subsurface defects; voids, low density areas, laminations, shrinkage, etc.

Advantages:

- .Can evaluate complex shapes
- .Detects small inclusions when density is higher than matrix material
- .Permanent record obtained - paper copy
- .More sensitive to density variations than conventional film imaging techniques
- .Can obtain a given x-ray quality level over a greater range of material thicknesses in a single exposure

Limitations:

- .Detectable flaw size depends on material thickness, geometry and powder imaging process
- .Flaw orientation may not be favorable
- .Reference standards necessary

NDE Method: Acoustic Emission

Materials Investigated: H.P. Si₃N₄, R.B. Si₃N₄, LAS, SiC

Areas/Applications Investigated:

Material response to mechanical and thermal stresses including

- .Thermal shock
- .Residual stress
- .Crack initiation/growth
- .Critical crack growth
- .Detection of surface flaws (using CO₂ laser to thermally stress the surface material)

Advantages:

- .Dynamic detection of cracks at room or elevated temperatures
- .Ability to indicate precursor to catastrophic failure
- .Continuous surveillance in laboratory or actual operation environments
- .Permanent record

Limitations:

- .Part must be stressed
- .A surface of the part must be accessible
- .Extraneous noise must be eliminated or suppressed
- .Baseline or reference noise levels must be established
- .Trained operators required

NDE Method: Sonic Testing - Mechanical Impact (Resonant frequency shift)

Materials Investigated: R.B. Si_3N_4

Areas/Applications Investigated:

- .Material degradation
- .Bonded joint evaluation

Advantages:

- .Elaborate fixturing not necessary
- .Simple to operate - minimum training
- .Permanent record obtained

Limitations:

- .Geometry and mass affect results
- .Data is not absolute, requiring references for comparison
- .Insensitive to small cracks unless there is sufficient crack surface interaction

6. REFERENCES

1. McLean, A. F., Fisher, E. A., Harrison, D. E., "Brittle Materials Design, High Temperature Gas Turbine". AMMRC-CTR-72-3, Interim Report, March, 1972.
2. McLean, A. F., Fisher, E. A., Bratton, R. J., "Brittle Materials Design, High Temperature Gas Turbine". AMMRC-CTR-72-19, Interim Report, September, 1972.
3. McLean, A. F., Fisher, E. A., Bratton, R. J., "Brittle Materials Design, High Temperature Gas Turbine". AMMRC-CTR-73-9, Interim Report, March, 1973.
4. McLean, A. F., Fisher, E. A., Bratton, R. J., "Brittle Materials Design, High Temperature Gas Turbine". AMMRC-CTR-73-32, Interim Report, September, 1973.
5. McLean, A. F., Fisher, E. A., Bratton, R. J., "Brittle Materials Design, High Temperature Gas Turbine". AMMRC-CTR-74-26, Interim Report, April, 1974.
6. Zienkiewicz, O. C., "On the Principle of Repeatability and Its Application in Analysis of Turbine and Pump Impellers", International Journal for Numerical Methods in Engineering, Volume 4, p 445-452 (1972).
7. Wilson, E. L., "Incompatible Displacement Models", International Symposium on Numerical and Computer Methods in Structure Mechanics, Office of Naval Research, Section I-3 (September 8-10, 1971).
8. Johnson, L. G., "Theory and Technique of Variation Research", 1964, Elsevier Publishing Co., p 69-82.
9. Heller, R. A. and Heller, S. A., "Analysis of Early Failures in Unequal Size Samples", Annals of Assurance Sciences, 1973, p 198-202.
10. Johnson, L. G., "The Median Ranks of Sample Values in Their Population with an Application to Certain Fatigue Studies", Industrial Mathematics, 2, 1951, p 1-9.
11. Acquaviva, S. J., Bortz, S. A., "Structural Ceramics and Testing of Brittle Materials", 1968, Gordon and Breach, Science Publisher, p 179.
12. Katsanis, T., "Fortran Program for Calculating Transonic Velocities on a Blade-to-Blade Turbomachine Stream Surface", NASA TND-5427, Lewis Research Center, Cleveland, Ohio, Sept. 1969.
13. McNally, W. D., "Fortran Program for Calculating Compressible Laminar and Turbulent Boundary Layers in Arbitrary Pressure Gradients", NASA TND-5681, Lewis Research Center, Cleveland, Ohio, May 1970.
14. Peterson, F. E., "Three-Dimensional Transient Heat Transfer Analysis Using Finite Element Procedure, User Information and Programming Details", Engineering/Analysis Corporation, Redondo Beach, California, August 1971.

15. Peterson, F. E. and Hui, H., "Three-Dimensional Transient Heat Transfer Analysis Using a Finite Element Procedure, Theoretical Basis and Sample Solutions", Engineering/Analysis Corporation, Redondo Beach, California, August, 1971.
16. Wilson, E. L., "Solid SAP, A Static Analysis Program for Three-Dimensional Solid Structures", Structural Engineering Laboratory, University of California, Berkley, California, September, 1971, Revised March, 1972.
17. Sidhu, H. S., "Training and Reference Manual for Solid SAP", Analytical & Technical Services, Inc., Barrington, Ill., 1973.
18. Wilson, E. L., and Doherty, W. P. "Finite Element Analysis of Mine Structures, Final Report", PB-220 141, Denver Mining Research Center, U.S. Department of the Interior, Bureau of Mines, Contract No. H0110231, September, 1972.
19. McNally, W. D., "Fortran Program for Calculating Aerodynamic Forces from Pressure or Velocity Distributions on Blade Section", NASA TMX-2123, Lewis Research Center, Cleveland, Ohio 44135, November, 1970.
20. Weibull, W., "A Statistical Theory of the Strength of Materials". The Royal Swedish Institute for Engineering Research, Stockholm, 1939.
21. Reshotko, E. & Cohen, C. B., "Heat Transfer at the Forward Stagnation Point of Blunt Bodies", NACA TN-3513, Lewis Flight Propulsion Laboratory, Cleveland, Ohio, July 1955.
22. Zysina-Molozhen, L. M. & Uskov, I. B., "Experimental Investigation of the Heat Transfer on the End Wall of a Blade Channel (in turbines)", Translated from Russian for NASA by the Israel Program for Scientific Translations
23. Hydrodynamic Foil Bearings, U.S. Patent No. 3,809,443.
24. Rossin, R., et. al., Rev. Hautes Tempe'r et Re'fract, I, 1964, p 159-170.
25. Budiansky, B., "Thermal and Thermoelastic Properties of Isotropic Composites", J. Composite Materials, 4, p 286-295 (1970).
26. K. R. Kinsmen, R. K. Govila & Beardmore, P., "The Varied Role of Plasticity in the Fracture of Inductile Ceramics", Deformation of Ceramics, Penn. State Univ., July, 1974, in press.

ARMY MATERIALS AND MECHANICS RESEARCH CENTER
WATERTOWN, MASSACHUSETTS 02172

TECHNICAL REPORT DISTRIBUTION

No. of Copies	To
1	Office of the Director, Defense Research and Engineering, The Pentagon, Washington, D.C. 20301
12	Commander, Defense Documentation Center, Cameron Station, Building 5, 5010 Duke Street, Alexandria, Virginia 22314
1	Metals & Ceramics Information Center, Battelle Memorial Institute, 505 King Avenue, Columbus, Ohio 43201
2	Dr. James I. Bryant, Office of the Chief of Research, Development and Acquisition, ATTN: DAMA-CSS, The Pentagon, Washington, D.C. 20310
1	Commanding Officer, Army Research Office (Durham), Bx CM, Duke Station Durham, North Carolina 27706 ATTN: Dr. H. M. Davis
1	Commanding General, U.S. Army Material Command, Washington D.C. 20315 ATTN: AMCRD-TC (Dr. El-Bisi)
1	ATTN: ANCDL (Dr. Dillaway)
1	Commanding General, U.S. Army Missile Command, Redstone Arsenal, Alabama 35809 ATTN: Technical Library
4	Commanding General, U.S. Army Tank-Automotive Command, Warren, Michigan 48090, ATTN: AMSTA-BSL, Research Library Br, ATTN: AMSTA-RKM (Mr. C. Green), ATTN: AMSTA-RGR (Mr. Engel), ATTN: AMSTA (Dr. Banks)
1	Commanding General, U.S. Army Weapons Command, Research and Development Directorate, Rock Island, Illinois 61201, ATTN: AMSWE-RDR
1	Commanding Officer, Aberdeen Proving Ground, Maryland 21005, ATTN: Technical Library, Building 313
1	Commanding Officer, U.S. Army Aviation Material Laboratories, Fort Eustis, Virginia 23604
1	Librarian, U.S. Army Aviation School Library, Fort Rucker, Alabama 36360 ATTN: Bldg. 5907
1	Commanding Officer, USACDC Ordnance Agency, Aberdeen Proving Ground, Maryland 21005 ATTN: Library, Building 350

ARMY MATERIALS AND MECHANICS RESEARCH CENTER
WATERTOWN, MASSACHUSETTS 02172

TECHNICAL REPORT DISTRIBUTION

No. of Copies	To
1	U.S. Army Air Mobility Research and Development Laboratory ATTN: J. White, Assistant Technical Director, Eustis Directorate, Ft. Eustis, Virginia 23604
1	U.S. Army Air Mobility Research and Development Laboratory ATTN: R. Berrisford, Chief, Structures Division, Eustis Directorate, Ft. Eustis, Virginia 23604
1	U.S. Army Air Mobility Research and Development Laboratory ATTN: T. Coleman, Director, Langley Directorate, Langley Research Center, Langley Field, VA 23365
2	U.S. Army Air Mobility Research and Development Laboratory ATTN: J. Accurio, Director, Lewis Directorate, NASA, Lewis Research Center, 21000 Brookpark Road, Cleveland, Ohio 44135
1	Commanding General, U.S. Army Aviation Systems Command, ATTN: R. Long, Deputy Director RD&E, P.O. Box 209, St. Louis, MO 63166
1	Office Chief Research & Development, Department of Army, ATTN: Col. J. Barnett, Physical & Engineering Sciences Division, Washington, D.C. 20315
1	Commanding General, Army Missile Command, ATTN: AMCDL, Webb Taylor, 5001 Eisenhower Avenue, Alexandria, VA 22304
1	Commanding General, Army Missile Command, ATTN: AMCRD-F, J. Beebe, Washington, D.C. 20315
1	Office, Chief Research & Development, Department of the Army, ATTN: R. Ballard, Physical & Engineering Sciences Division, Washington, D.C. 20315
1	Commander, USA Foreign Science & Technology Center, ATTN: AMXST-SD3, Mr. C. Petschke, 220 7th Street NE, Charlottesville, VA 22901
1	Mr. Irving Machlin, High Temperature Materials Div., Materials and Processes Branch, (NAIR-52031D), Naval Air Systems Command, Department of the Navy, Washington, D.C. 20360

ARMY MATERIALS AND MECHANICS RESEARCH CENTER
WATERTOWN, MASSACHUSETTS 02172

TECHNICAL REPORT DISTRIBUTION

No. of Copies	To
1	Commanding Officer, U.S. Army Engineer Waterways Experiment Station, Vicksburg, Mississippi 39180 ATTN: Research Center Library
	Commanding Officer, U.S. Army MERDEC, Fort Belvoir, Virginia 22060
2	ATTN: STSFB-EP (Mr. James Horton)
1	ATTN: STSFB-EP (Mr. W. McGovern)
1	ATTN: AMCPM-FM (Mr. Allen Elkins)
	Director, Army Materials and Mechanics Research Center, Watertown, Massachusetts 02172
2	ATTN: AMXMR-PL
1	AMXMR-PR
1	AMXMR-CT
1	AMXMR-AP
1	AMXMR-X (Dr. Gorum)
1	AMXMR-EO (Dr. Katz)
2	AMXMR-TM (Dr. Lenoe)
2	AMXMR-D (Dr. Priest)
1	AMXMR-EO (Dr. Messier)
2	AMXMR-P (Dr. Burke)
1	AMXMR-MS (Mr. MacDonald)
1	AMXMR-E (Dr. Larson)
	Advanced Research Projects Agency, 1400 Wilson Blvd., Arlington, Virginia 22209
2	ATTN: Director
1	Dep Director
1	Director of Materials Sciences - Dr. Stickley
1	Dep. Director Materials Sciences - Dr. van Reuth
1	Tech. Information Office - Mr. F. A. Koether
1	Mr. R. M. Standahar, Office of the Director of Defense, Research and Engineering, Room 3D1085, Pentagon, Washington, D.C. 20301
1	Mr. Charles F. Bersch, Department of the Navy, Naval Air Systems Command, Washington, D.C. 20360
1	Dr. A. M. Diness, Metallurgy Branch, Code 471, Office of Naval Research, 800 N. Quincy Street, Arlington, Virginia 22217
2	U.S. Army Air Mobility Research and Development Laboratory, Advanced Systems Research Office, Ames Research Center, Moffett Field, California 94035 ATTN: F. Immen, J. Wheatly

ARMY MATERIALS AND MECHANICS RESEARCH CENTER
WATERTOWN, MASSACHUSETTS 02172

TECHNICAL REPORT DISTRIBUTION

No. of Copies	To
1	Mr. Keith Ellingsworth, Office of Naval Research, Power Program, Arlington, VA 22217
1	Mr. John Fairbanks, Naval Ships Engineering, Prince George Center, Hyattsville, Maryland 20782
1	Capt. D. Zabierek, Air Force Aeropropulsion Lab, Wright- Patterson Air Force Base, Ohio 45433
1	Capt. Smyth, Air Force Materials Laboratory, Wright-Patterson Air Force Base, Ohio 45433
1	Mr. S. Lyons, Wright-Patterson Air Force Base, Ohio 45433
4	Aerospace Research Laboratory, ATTN: ARL-LL, Wright- Patterson Air Force Base, Ohio 45433 ATTN: Dr. Henry Graham ATTN: Dr. James Wimmer ATTN: Maj. L. Jacobson ATTN: Mr. Larry Hjelm
4	NASA Lewis Research Center, 21000 Brookpark Road, Cleveland, Ohio 44135 ATTN: Mr. W. Sanders Dr. Hubert Probst Dr. Robert C. Bill Mr. Donald Guentert
1	Dr. G. C. Deutsch, Ass't Director of Research (Materials), Code RR-1 NASA, Washington, D.C. 20546
1	Mr. George Staber, Office of Coal Research, U.S. Department of the Interior, Washington, D.C. 20240
1	Dr. S. Wiederhorn, Physical Properties Section, Institute for Materials Research, National Bureau of Standards, Washington, D.C. 20234
1	Mr. R. Reynik, Director, Div. of Materials Research, National Science Foundation, 1800 G. Street, N.W., Washington, D.C. 20550
1	Dr. Robb Thomson, Senior Research Scientist, Rm B109, Bld. 225, National Bureau of Standards, Washington, D.C. 20234
1	Mr. H. Morrow, Eustis Directorate, AMRDL, Fort Eustis, VA 23604
1	Dr. R. Warren, Contact Officer, Defense Research & Development Staff, British Embassy, 3100 Massachusetts Avenue N.W., Washington, D.C. 20008

ARMY MATERIALS AND MECHANICS RESEARCH CENTER
WATERTOWN, MASSACHUSETTS 02172

TECHNICAL REPORT DISTRIBUTION

No. of Copies	To
3	Environmental Protection Agency, Division of Advanced Automotive Systems, 2565 Plymouth Road, Ann Arbor, Mi 48105 ATTN: Mr. George Thur Mr. Robert Schultz Mr. Thomas Sebestyen
1	Dean Daniel C. Drucker, Engineering College, University of Illinois, Urbana, Illinois 61801
1	Professor Merton Flemings, Massachusetts Institute of Technology, Cambridge, Massachusetts 02139
1	Professor Edward E. Hucke, Materials and Metallurgical Engineering, The University of Michigan, Ann Arbor, MI 48104
1	Professor Frank A. McClintock, Department of Mechanical Engineering, Massachusetts Institute of Technology, Cambridge, Massachusetts 02139
1	Dr. R. M. Spriggs, Assistant to the President, Lehigh University, Bethlehem, Pennsylvania 18015
1	Mr. J. D. Walton, Jr., EES, Georgia Tech., Atlanta, Georgia 30332
1	Mr. Y. Baskin, Manager Inorganic Chemical Research, Technical Center, Ferro Corporation, 7500 East Pleasant Valley Road, Independence, Ohio 44131
3	Mr. Robert Beck, Dept. Head, Development Materials, Teledyne CAE, 1330 Laskey Road, Toledo, Ohio 43601 Dr. Eli Benstien, Director of Engineering Mrs. Marlene S. Dowdell, Librarian
1	Dr. J. E. Burke, General Electric Company, Corporate Research & Development, P.O. Box 8, Schenectady, New York 12301
1	Dr. C. A. Bruch, Manager, Advanced Studies, General Electric Company, Aircraft Engine Group, Cincinnati, Ohio 45215
1	Mr. A. R. Canady, Caterpillar Tractor Company, Technical Center Building F, Peoria, Illinois 61602
1	Mr. Seymour Bortz, IIT Research Institute, 10 West 35th Street, Chicago, Illinois 43601

ARMY MATERIALS AND MECHANICS RESEARCH CENTER
WATERTOWN, MASSACHUSETTS 02172

TECHNICAL REPORT DISTRIBUTION

No. of Copies	To
1	Mr. L. M. Donley, Owens Illinois Glass, 1900 North Westwood Avenue, Toledo, Ohio 43601
1	Mr. E. J. Dulis, President, Colt Industries, Materials Research Center, Box 88, Pittsburgh, PA 15230
1	Mr. O. Prachar, Passenger Car Turbine Department, Engineering Staff, General Motors Technical Center, Warren, MI 48090
1	Mr. Winston Duckworth and Mr. Lewis E. Hulbert, Battelle Columbus Laboratories, 505 King Avenue, Columbus, Ohio 43201
1	Energy Research Corporation, Bethel, Connecticut 06801
1	Dr. Peter L. Fleischner, National Beryllia Corp., Haskell, New Jersey 07420
1	Mr. O. I. Ford, Technical Manager, Combustor Systems, Aerojet Liquid Rocket Company, P.O. Box 18222, Sacramento, Calif. 95813
1	Mr. Chester T. Sims, Manager, Advanced Materials General, Electric Company, Gas Turbine Products Div., Schenectady, N.Y. 12301
1	Mr. E. W. Hauck, Market Manager, Engine Components, Norton Company, 1 New Bond Street, Worcester, Massachusetts 01606
1	Mr. M. Herman, Detroit Diesel Allison Division, General Motors Corporation, Indianapolis Operations, P.O. Box 894, Indianapolis, Indiana 46206
1	Mr. J. B. Mann, Director of Research, Chrysler Corporation, P.O. Box 1118, Detroit, MI 48231
1	Mr. James F. Holloway, Materials Project Engineer, Pratt & Whitney Corporation, 400 Main Street, E. Hartford, Connecticut 06108
1	Dr. Paul Jorgensen, Associate Director, Materials Laboratory, Stanford Research Institute, Menlo Park, California 94025
1	Dr. A. V. Illyn, Technical Director, Refractories Division, Babcock & Wilcox, Old Savannah Road, Augusta, Georgia 30903
1	Mr. Paul F. Jahn, Vice President, Fiber Materials, Inc., Broadway and Main Streets, Graniteville, Massachusetts 01829

ARMY MATERIALS AND MECHANICS RESEARCH CENTER
WATERTOWN, MASSACHUSETTS 02172

TECHNICAL REPORT DISTRIBUTION

No. of Copies	To
1	Dr. Robert F. Kirby, Materials Engineering Dept. 93-393M, AiResearch Manufacturing Company, Div. of the Garrett Corporation, Sky Harbor Airport, 402 South 36th Street, Phoenix, Arizona 85034
1	Mr. John G. Lanning, Corning Glass Works, Corning, NY 14830
1	Mr. William D. Long, Manager, Product Development, K-Ramics, Kaman Sciences Corporation, Garden of the Gods Road, Colorado Springs, Colorado 80907
1	Mr. James Lynch, Metals & Ceramics Information Center, Battelle Columbus Laboratories, 505 King Avenue, Columbus Ohio 43201
1	Mr. C. H. McMurtry, Project Manager, Research and Development Div., The Carborundum Company, Niagara Falls, New York 14302
1	Mr. Deo Mattoon, Sing Sing Road, Horseheads, New York 14845
1	Mr. G. Kookootsedes, Market Development, Resins and Chemicals, Dow Corning, Midland, Michigan 48640
1	Professor Burton Paul, Dept. of Mechanical Engineering, University of Pennsylvania, Philadelphia, Pennsylvania 19104
1	Mr. Y. K. Pei, Owens Illinois Glass, 1020 North Westwood Avenue, Toledo, Ohio 43607
1	Dr. Jerry D. Plunkett, President, Materials Consultants, Inc., 2150 South Josephine Street, Denver, Colorado 80210
1	Mr. J. A. Rubin, President, Ceradyne Incorporated, 8948 Fullbright Avenue, Chatsworth, California 91311
1	Mr. P. Hansen, Director of Corporate Dev., Kawecki-Berylco Industries, Inc., P.O. Box 1462, Reading, Pennsylvania 19603
1	Mr. Jack W. Sawyer, Gas Turbine International, 4519 Eighteen Street North, Arlington, VA 22207
1	Mr. D. W. McLaughlin, Research & Development Div., Mechanical Technology, Inc., 968 Albany-Shaker Road, Latham, New York 12110

ARMY MATERIALS AND MECHANICS RESEARCH CENTER
WATERTOWN, MASSACHUSETTS 02172

TECHNICAL REPORT DISTRIBUTION

No. of Copies	To
1	Mr. A. R. Stetson, Chief, Process Research Laboratories, Mail Zone R-1, Solar Div. of Int. Harvester Company, 2200 Pacific Highway, San Diego, California 92112
1	Dr. M. L. Torti, Norton Company, 1 New Bond Street, Worcester Massachusetts 01606
1	Dr. T. Vasilos, Applied Technology Division, Avco Corp., Lowell Industrial Park, Lowell, Massachusetts 01851
1	Mr. Francis L. VerSnyder, Manager, Materials Engineering and Research Lab, Pratt & Whitney Corporation, 400 Main Street, E. Hartford, Connecticut 06108
1	Mr. McCoy, Materials Engineering, Garrett-AiResearch Dept. 93-393M, 412 South 36th Street, Phoenix, Arizona 85034
1	Mr. Donald E. Weyer, Dow Corning Corporation, Midland, MI 48640
1	Dr. Michael Guinan, B. Div./L-24, P.O. Box 808, Lawrence Livermore Laboratory, Livermore, California 94550
1	Dr. Mark Wilkins, B Div./L-24, P.O. Box 808, Lawrence Livermore Laboratory, Livermore, California 94550
1	Dr. Charles J. McMahon, Jr., Assoc. Prof. Materials Science, School of Metallurgy & Materials Science, University of Pennsylvania, 3231 Walnut Street, Philadelphia, Pennsylvania
1	Mr. Gaylord D. Smith, The International Nickel Co., Inc., 1 New York Plaza, New York, New York 10004
1	Mr. H. R. Schelp, Garrett Corporation, 9851 Sepulveda Blvd., Los Angeles, California 90009
1	Dr. Robert Widmer, President, Industrial Materials Technology 19 Wheeling Avenue, Woburn, Massachusetts
1	Dr. William Wells, Lawrence Livermore Lab, Livermore, California 94550
1	Prof. R. P. Kroon, University of Pennsylvania, Philadelphia, Pennsylvania
1	Dr. Paul G. Shewmon, D212, Argonne National Laboratory, 9700 South Cass Avenue, Argonne, Illinois 60439

ARMY MATERIALS AND MECHANICS RESEARCH CENTER
WATERTOWN, MASSACHUSETTS 02172

TECHNICAL REPORT DISTRIBUTION

No. of Copies	To
1	Dr. Thomas D. McGee, Professor of Ceramic Engineering, Iowa State University, Ames, Iowa 50010
1	Mr. Joe Glotz, Department of the Navy, Naval Air Propulsion Test Center, Trenton, New Jersey 08628
1	Mr. John Miguel, Naval Underwater System Center, Newport, Rhode Island
1	Mr. Robert Benham, AEP-22, U.S. Naval Air Propulsion Test Center (AE), Philadelphia, PA 19112
1	Mr. R. Barry Strachan, Williams Research Corp., Walled Lake, Michigan 48088
1	Mr. S. Walosin, Curtis-Wright Corp. One Passaic Street, Woodridge, N.J. 07075
1	Prof. Marc Richman, Engineering Division, Brown University, Providence, Rhode Island 02912
1	Mr. R. Rice, Naval Research Laboratory, Washington, D.C. 20390
1	Mr. George A. Wacker, Head Metal Physics Br., Naval Ships Research & Development Center, Annapolis, Md. 21402, ATTN: Code 2812
1	Dr. R. Charles, Manager Ceramics Branch, General Electric Co., Corporate R & D Center, P.O. Box 8, Schenectady, New York 12301
1	Mr. C. F. Cline, Manager, Strength Physics Department, Allied Chemical Corporation, P.O. Box 1021R, Morristown, New Jersey 07960
1	Dr. J. T. Bailey, American Lava Corp., Chattanooga, Tennessee 37405
1	Mr. S. T. Wlodek, Cabot Corp. Stellite Div., 1020 West Park Avenue, Kokomo, Indiana 46901
2	Cummins Engine Company, Inc., Columbus, Indiana 47201 Mr. R. Kano, Mr. K. J. Mather
1	Mr. J. D. Mote, EF Industries, Inc., 1301 Courtesy Rd. Louisville, Colorado 80027
1	Mr. William E. Gurwell, Eaton Corporation, Research Center 26201 Northwestern Highway, Southfield, MI 48076

ARMY MATERIALS AND MECHANICS RESEARCH CENTER
WATERTOWN, MASSACHUSETTS 02172

TECHNICAL REPORT DISTRIBUTION

No. of Copies	To
1	Mr. Robert W. Gibson, Jr., Head, Library Dept. General Motors Corporation GM Technical Center, Warren, MI 48090
1	Mr. R. L. Lormand, Lawrence Radiation Lab, P.O. Box 508, Livermore, California 94550
2	Ms. Bolick, National Aeronautics and Space Administration Goddard Space Flight Center, Greenbelt, Maryland 20771
1	Mr. Neil T. Saunders, Ch. Mat'ls Appl'n Branch, National Aeronautics and Space Administration, Lewis Research Center, Cleveland, Ohio 44135
1	Ms. Rayna Lee Caplan, Librarian, Northern Research and Engineering Corp., 219 Vassar Street, Cambridge, Mass. 02139
1	Mrs. Jame Bookmyer, Info. Services Div., PPG Industries, Inc., P.O. Box 11472, Pittsburgh, Pennsylvania 15238
1	Mr. P. W. Parsons, Manager, Commercial Research Dept., Stackpole Carbon Company, St. Marys, Pennsylvania 15857
1	Ms. Lucille Steelman, Order Librarian, Stanford Research Institute ATTN: G-037 Library, Menlo Park, Calif. 94025
1	Technical Library, TRW Equipment, TRW Inc., 23555 Euclid Avenue, Cleveland, Ohio 44117
1	Dr. E. P. Flint, U.S. Department of Interior, Bureau of Mines, Room 4513, Interior Bldg., Washington, D.C. 20240
1	Mr. W. Wheatfall, Naval Ship R & D Lab, Code 2812, Annapolis, Maryland 21402
1	Dr. Joseph E. Motherway, University of Bridgeport, Bridgeport, Connecticut 06602
1	Dr. Soloman Musikant, Manager, Metallurgy & Ceramics Lab General Electric Valley Forge, Valley Forge, PA
1	Mr. Louis J. Fiedler, Mat'ls & Process Technology Lab., Avco Corporation, 550 S. Main Street, Stratford, Connecticut 06497
1	Mr. Donald Lapades, The Aerospace Corporation, P.O. Box 92957, Los Angeles, California 90009

ARMY MATERIALS AND MECHANICS RESEARCH CENTER
WATERTOWN, MASSACHUSETTS 02172

TECHNICAL REPORT DISTRIBUTION

No. of Copies	To
1	Mr. Thomas J. Ahrens, Assoc. Prof. of Geophysics, California Institute of Technology, Seismological Laboratory, 295 San Rafael Avenue, P.O. Bin 2, Arroyo Annex, Pasadena, California 91109
1	Mr. Victor de Biasi, Editor, Gas Turbine World, P.O. Box 494, Southport, Connecticut 06490
1	SKF Industries, Inc., Engineering & Research Center, 1100 1st Avenue, King of Prussia, PA 19406, ATTN: Warren E. Jameson & Harish Dalal
1	Dr. Edward Reynolds, General Motors Technical Center, Passenger Car Turbine Division, Warren, MI 48090
1	Dr. Wm. R. Freeman, Jr., V.P. and Technical Director, Howmet Corporation, Superalloy Group, One Misco Drive, Whitehall, Michigan 47461
1	Mr. D. William Lee, Arthur D. Little, Inc. Acorn Park, Cambridge, Massachusetts 02140
1	Dr. L. Kaufman, Project Director, Manlabs, Inc., 21 Erie Street, Cambridge, Massachusetts 02139
1	Prof. Morris E. Fine, Northwestern University, The Technological Institute, Dept. of Materials Science, Evanston, Illinois
1	Prototype Developments Associates, Esplanade I, Suite 204 3001 Red Hill Avenue, Costa Mesa, California 92626, ATTN: Mr. John I. Slaughter, President
1	Raytheon Company, Research Division Library, Foundry Avenue, Waltham, Massachusetts 02154, ATTN: Ms. Madaleine Bennett, Librarian
1	Prof. T. L. Chu, Southern Methodist University, Institute of Technology, Electronic Sciences Center, Dallas, Texas 75222
1	Mr. H. Stuart Starrett, Head, Mechanics Section, Southern Research Institute, 2000 Ninth Avenue South, Birmingham, Alabama 35205

ARMY MATERIALS AND MECHANICS RESEARCH CENTER
WATERTOWN, MASSACHUSETTS 02172

TECHNICAL REPORT DISTRIBUTION

No. of Copies	To
1	Dr. O. Conrad Trulson, Union Carbide Corporation, Carbide Products Division, 270 Park Avenue, New York, New York 10017
1	Prof. Earl R. Parker, University of California, Department of Materials Science and Engineering, 286 Hearst Mining Building, Berkeley, California 94720
1	Mr. Willard H. Sutton Manager, Ceramics Projects, Special Metals Corporation, New Hartford, New York 13413
1	Dr. Maurice J. Sinnott, Department of Chemical & Metallurgical Engineering, The University of Michigan, Ann Arbor, MI 48104
1	Mrs. R. J. Benacquista, R.I.A.S., 9190 Red Branch Road, Columbia, Maryland 21043
1	Prof. M. C. Shaw, Head, Department of Mechanical Engineering, Cornegie-Mellon University, Pittsburgh, Pennsylvania 15213
1	Mr. Gail Eichelman, Manufacturing Processes Div., Air Force Mateials Laboratory, Wright-Patterson AFB, Ohio 45433
1	Dr. J. C. Lewis, Metals & Minerals Economics Div. Battelle Memorial Institute, 505 King Avenue, Columbus, Ohio 43201
1	Massachusetts Institute of Technology, Cambridge, Massachusetts, 02139, ATTN: Prof. D. W. Kingery, Rm. 13-4090
1	Prof. Michael F. Ashby, Gordon McKay Professor of Metallurgy, Pierce Hall, Harvard University, Cambridge, Massachusetts 02138
1	Dr. Richard G. McKaig, Owens-Illinois Development Center, P.O. Box 1035, Toledo, Ohio 43666
1	Prof. I. B. Cutler, University of Utah, College of Engineering Division of Materials Science and Engineering, Salt Lake City, Utah 84112
1	Mr. J. A. Alexander, Manager, Materials Research Department, TRW 23555 Euclid Avenue, Cleveland, Ohio 44117
1	Airesearch Manufacturing Company, Sky Harbor Airport, 402 South 36th Street, Phoenix, Arizona 85034, Attn: Supervisor, Propulsion Engine Advanced Technology Dept., 93-12M
1	Mr. M. Blake, Norton Company, One New Bond Street, Worcester, Mass. 01606

ARMY MATERIALS AND MECHANICS RESEARCH CENTER
WATERTOWN, MASSACHUSETTS 02172

TECHNICAL REPORT DISTRIBUTION

No. of Copies	To
1	Dr. H. P. Kirchner, Ceramic Finishing Company, P.O. Box 498, State College, Pennsylvania 16801
1	Dr. Morris Berg, General Motors Corporation, AC Spark Plug Division Flint, Michigan 48556
1	Dr. Michael J. Noone, General Electric Company, Space Sciences Laboratory, Box 8555, Philadelphia, Pennsylvania 19101
1	Dr. Richard Kliener, GTE Sylvania, Tonawanda, Pennsylvania 18848
1	Mr. F. E. Krainess, Rockwell International Corporation, D/391-204 AB70 12214 Lakewood Boulevard, Downey, California 90241
1	Mr. David Cormier, Nuclear Planning Division, Stone and Webster Engineering Corporation, 99-13 High Street, Boston, Massachusetts 02107
1	Mr. John F. Burst, Technical Director, General Refractories Company, 1520 Locust Street, Philadelphia, Pennsylvania 19102
1	Mr. V. A. Chase, Chief of Development Laboratory, Whittaker Corporation, Research and Development Division, 3540 Aero Court, San Diego, Cal. 92123
1	Dr. Stanley Waugh, Research Division, Raytheon Corporation, Research Division, 28 Seyon Street, Waltham, Massachusetts 02154
1	Coors Porcelain Company, Research Department, 17750 West 32nd Avenue, Golden, Colorado 80401
1	Professor Robert F. Davis, North Carolina State University, Department of Materials Science, Box 5427, Raleigh, North Carolina 27607
1	Dr. H. von E. Doering, Manager, Fuels/Corrosion Unit, General Electric Company, Gas Turbine Products Division, Building 53-311, Schenectady, New York 12345
1	Dr. R. Ruh, AFML/LLS, Air Force Materials Laboratory, Wright-Patterson AFB, Ohio 45433
1	Mr. Michael E. Naylor, General Motors Technical Division, Passenger Car Turbine Division, Warren, Michigan 48090
1	Dr. John V. Milewski, ESSO Research and Engineering Company, Government Research Laboratory, P.O. Box 8, Linden, New Jersey 07036
1	Mr. M. J. Klein, Research Staff Specialist, Mail Zone R-1, Solar, 2200 Pacific Highway, P.O. Box 80966, San Diego, California 92138

ARMY MATERIALS AND MECHANICS RESEARCH CENTER
WATERTOWN, MASSACHUSETTS 02172

TECHNICAL REPORT DISTRIBUTION

No. of Copies	To
1	Dr. Frank Galasso, United Aircraft Research Laboratories, East Hartford Conn. 06108
8	Lt. Col. E. E. Chick, Chief, Materials Branch, European Research Office U. S. Army R&D Group, (EUR), Box 15, FPO New York 09510
1	Dr. Joseph Griffo, U. S. Atomic Energy Commission Space Nuclear Systems Division, Century XXI Building, Mail Station F-309, Washington, D.C. 20545
1	Mr. Joseph Simpson, Rohr Industries, Inc., Technical Library P.O. Box 1516, Chula Vista, California 92012
1	Mr. Philip J. Willson, Chemical Research, Chrysler Corporation, Box 1118, CIMS 418-19-18, Detroit, Michigan 48231
1	Mr. William Combs, Battelle Memorial Institute, 2030 M Street N.W. Washington, D.C. 20036
1	Mr. M. A. Schwartz, U.S. Department of the Interior, Bureau of Mines Tuscaloosa Metallurgy Research Laboratory, P.O. Box 1, University, Alabama 35486
1	Turbo Power and Marine Systems, Inc., ATTN: Mr. Carl Merz, Farmington, Connecticut 06032
1	Mr. R. N. Singh, Argonne National Laboratory, Materials Science Division 9700 South Cass Avenue, Argonne, Illinois 60439
1	Mr. Richard E. Engdahl, Deposits & Composites, Inc., 1821 Michael Faraday Drive, Reston, Virginia 22090
1	Mr. Leonard Topper, Office of Energy Policy, National Science Foundation 1800 G Street N. W., Washington, D.C. 20550
1	Mr. Ron Lowrey, U.S. Bureau of Mines, P.O. Box 70, Albany, Oregon 97321
1	Materials Science Corporation, Technical Library, Blue Bell Office Campus, Merion Towle Building, Blue Bell, Pennsylvania 19422
1	Ms. Sharon Wright, Creare Inc., Technical Library, Hanover, New Hampshire 03755

ARMY MATERIALS AND MECHANICS RESEARCH CENTER
WATERTOWN, MASSACHUSETTS 02172

TECHNICAL REPORT DISTRIBUTION

No. of Copies	To
1	Mr. John Polyansky, Gas Turbine Design Engineering, Turbodyne Corporation, 626 Lincoln Avenue S E, St. Cloud, Minnesota 56301
1	Mr. Donald J. Legacy, Turbodyne Corporation, Wellsville, New York 14895
1	Mr. P. R. Miller, NASA Headquarters, Code RPD, 600 Independence Avenue S. W., Washington, D.C. 20546
1	Dr. Charles Berg, Chief Engineer, Federal Power Commission, Room 2100 825 North Capital Street, N.E., Washington, D.C. 20426
1	Mr. Michael Lauriente, Department of Transportation, 400 Seventh Street, S. W., Washington, D.C. 20590
1	Dr. Donald Vieth, National Bureau of Standards, Administration Bldg., Room A1002, Washington, D.C. 20234
1	Dr. Leonard Topper, National Science Foundation, Office of Energy R & D Policy, Room 537, 1800 G Street NW, Washington, D.C. 20550
2	Electric Power Research Institute, P.O. Box 10412, Palo Alto, California 94304 ATTN: Dr. Richard E. Balzhiser, Dr. Arthur Cohn
1	W. C. Christensen, Assistant for Resources, Directorate for Energy, OASD (I&L), Room 2B341 Pentagon, Washington, D.C. 20301
1	Mr. Tyler Port, Special Assistant, OASA (I&L), Room 3E620 Pentagon, Washington, D.C. 20301
1	Major Jose Baca, Hdqtrs., Air Force Systems Comman/DLFP, Propulsion and Power Branch, Andrews Air Force Base, Washington, D.C. 20034
1	Mrs. Patricia Mooney, Office of Management and Budget, Energy R&D Coordination Branch, Room 8001, New Executive Office Bldg., Washington, D.C. 20503
1	James Johnson, Environmental Protection Agency, Air Technology Branch, RD-681, Room 621 W, 401 M Street, N.W., Washington, D.C. 20490
1	Mr. Thomas Gross, Staff Member, Office of Energy Conservation, Federal Energy Office, Room 4234, Columbia Plaza Bldg., Washington, D.C. 20461

ARMY MATERIALS AND MECHANICS RESEARCH CENTER
WATERTOWN, MASSACHUSETTS 02172

TECHNICAL REPORT DISTRIBUTION

No. of Copies	To
1	Dr. John S. Foster, Jr., Vice President for Energy Research and Development, TRW Incorporated, One Space Park, Redondo Beach, California 90278
1	Dr. Raymond Bisplinghoff, Deputy Administrator, National Science Foundation, 1800 G. Street, N.W., Washington, D.C. 20550
1	Dr. Alan Womack, Assistant Director, Gas Cooled Reactors, Atomic Energy Commission, Washington, D.C. 20545
1	Dr. Donald Weidhuner, Chief, Power Division, Research Development & Engineering Directorate, Army Materials Command Headquarters, 5001 Eisenhower Avenue, Alexandria, Virginia 22304
1	Dr. A. Lovelace, Deputy Assistant Secretary (R&D), Office of Assistant Secretary of the Air Force (Research & Development), Room 4E973, Pentagon, Washington, D.C. 20330
1	Dr. Neal Richardson, TRW Incorporated, One Space Park, Redondo Beach, California 90278
1	Mr. Roy Peterson, Chief, Pollution Abatement & Gas Turbine Research, Ship Research & Technology Division, Naval Ship Systems Command Hqtrs., 2531 Jefferson Davis Highway, Arlington, Virginia 20362
1	Dr. Eugene C. Gritton, The Rand Corporation, Physical Sciences Department, 1700 Main Street, Santa Monica, California 90406
1	Mr. C. A. Vassilakis, Turbo Power & Marine Systems, New Britain Ave., Farmington, Conn. 06032
1	Mr. P. E. McConnell, Owens-Corning Fiberglas Corporation, Technical Center, Granville, Ohio 43023
1	Turbodyne Corporation, 711 Anderson Avenue North, St. Cloud, Minnesota 56301, ATTN: Diane Konsor
1	Mr. N. B. Elsner, General Atomics Corporation, Box 81608, San Diego, California 92037
1	Mr. Eldor R. Herrmann, Ceramic Systems, Inc., 11402 Schaefer Highway, Detroit, Michigan 48227
1	Dr. William H. Rhodes, GTE Laboratories, Waltham Research Center, 40 Sylvan Road, Waltham, Massachusetts 02154

ARMY MATERIALS AND MECHANICS RESEARCH CENTER
WATERTOWN, MASSACHUSETTS 02172

TECHNICAL REPORT DISTRIBUTION

No. of Copies	To
1	Anne M. Theil, Avco Everett Research Laboratory, Inc., 2385 Revere Beach Parkway, Everett, Massachusetts, 02149
1	Mr. William Oldfield, Materials Research and Computer Simulation, 634 Berkeley Place, Westerville, Ohio 43081
1	Dr. Wilfred H. Dukes, Assistant Director Engineering for Development Bell Aerospace, P.O. Box 29307, New Orleans, Louisiana 70189
1	Dr. Keith E. McKee, Director of Research Engineering Mechanics Div., IIT Research Institute, 10 West 35th Street, Chicago, Illinois 60616
1	Dr. Donald R. Uhlmann, Associate Professor of Ceramics, Department of Metallurgy and Materials Science, Massachusetts Institute of Tech., Cambridge, Massachusetts 02139
1	Dr. John B. Wachtman, Jr., Division Chief, Inorganic Materials Div. National Bureau of Standards, Room A359, Materials Building, Washington, D.C. 20234
1	Mr. Donald G. Groves, Staff Engineer, National Materials Advisory Board, National Academy of Sciences, 2101 Constitution Ave., N.W., Washington, D.C. 20418
1	Major Roger Austin, Air Force Materials Laboratory, Wright-Patterson Air Force Base, Ohio 45433
1	Mr. James J. Gangler, Advanced Research & Technology Div., Code RRM, Room B556, National Aeronautics and Space Administration, Headquarters, Washington, D.C. 20546
3	Authors
<hr/> 291	Total Copies Distributed

Army Materials and Mechanic Research Center,
Watertown, Massachusetts 02172

AD

BRITTLE MATERIALS DESIGN
HIGH TEMPERATURE GAS TURBINE

Key Words
Gas turbine engine
Brittle design
Ceramics
High temperature materials
Silicon nitride
Silicon carbide
Non-destructive tests
Mechanical properties

Arthur F. McLean, Eugene A. Fisher, Ford Motor Company, Dearborn, Michigan 48121
Raymond J. Bratton, Westinghouse Electric Corporation, Pittsburgh, Pennsylvania 15235

Technical Report ANMRC CTR 74-59, September, 1974
180 pgs., 135 illus., 17 tables, Contract DAAG 46-71-C-0162, ARPA Order Number 1849, Sixth Interim Report, January 1, 1974 to June 30, 1974

ABSTRACT

The "Brittle Materials Design, High Temperature Gas Turbine" program is to demonstrate successful use of brittle materials in demanding high temperature structural applications. A small vehicular gas turbine and a large stationary gas turbine, each utilizing uncooled ceramic components, will be used in this iterative design and materials development program. Both the contractor, Ford Motor Company, and the subcontractor, Westinghouse Electric Corporation, have had in-house research programs in this area prior to this contract.

In the vehicular turbine project, three dimensional stress analysis programs are being developed and applied to turbine rotors and stator vanes. Improvements have been made in the fabrication of duo density silicon nitride rotors. A major objective was reached with the completion of a 50 hour cyclic engine test of ceramic hot flow path components. A silicon carbide combustor tube was tested in a combustor rig for 50 hours, including 6 hours at an outlet temperature of 2500°F. Non-destructive evaluation techniques have been applied to the fabrication of ceramic components resulting in the elimination of defective parts at an early stage in processing.

In the stationary turbine project, considerable design effort was expended on the modification of the rotating test turbine for the high temperature testing to meet program objectives. The static test rig was rebuilt for 2500°F peak temperature operation, and five cycles were run to 2300°F to establish control parameters. Damage to the new ceramic duct section and to the mixer vane assemblies being tested were apparently undamaged. A rotor blade configuration was analyzed by the three dimensional stress analysis program and the results are presented.

Army Materials and Mechanic Research Center,
Watertown, Massachusetts 02172

AD

BRITTLE MATERIALS DESIGN
HIGH TEMPERATURE GAS TURBINE

Key Words
Gas turbine engine
Brittle design
Ceramics
High temperature materials
Silicon nitride
Silicon carbide
Non-destructive tests
Mechanical properties

Arthur F. McLean, Eugene A. Fisher, Ford Motor Company, Dearborn, Michigan 48121
Raymond J. Bratton, Westinghouse Electric Corporation, Pittsburgh, Pennsylvania 15235

Technical Report ANMRC CTR 74-59, September, 1974
180 pgs., 135 illus., 17 tables, Contract DAAG 46-71-C-0162, ARPA Order Number 1849, Sixth Interim Report, January 1, 1974 to June 30, 1974

ABSTRACT

The "Brittle Materials Design, High Temperature Gas Turbine" program is to demonstrate successful use of brittle materials in demanding high temperature structural applications. A small vehicular gas turbine and a large stationary gas turbine, each utilizing uncooled ceramic components, will be used in this iterative design and materials development program. Both the contractor, Ford Motor Company, and the subcontractor, Westinghouse Electric Corporation, have had in-house research programs in this area prior to this contract.

In the vehicular turbine project, three dimensional stress analysis programs are being developed and applied to turbine rotors and stator vanes. Improvements have been made in the fabrication of duo density silicon nitride rotors. A major objective was reached with the completion of a 50 hour cyclic engine test of ceramic hot flow path components. A silicon carbide combustor tube was tested in a combustor rig for 50 hours, including 6 hours at an outlet temperature of 2500°F. Non-destructive evaluation techniques have been applied to the fabrication of ceramic components resulting in the elimination of defective parts at an early stage in processing.

In the stationary turbine project, considerable design effort was expended on the modification of the rotating test turbine for the high temperature testing to meet program objectives. The static test rig was rebuilt for 2500°F peak temperature operation, and five cycles were run to 2300°F to establish control parameters. Damage to the new ceramic duct section and to the mixer vane assemblies being tested were apparently undamaged. A rotor blade configuration was analyzed by the three dimensional stress analysis program and the results are presented.

Army Materials and Mechanic Research Center,
Watertown, Massachusetts 02172

AD

BRITTLE MATERIALS DESIGN
HIGH TEMPERATURE GAS TURBINE

Key Words
Gas turbine engine
Brittle design
Ceramics
High temperature materials
Silicon nitride
Silicon carbide
Non-destructive tests
Mechanical properties

Arthur F. McLean, Eugene A. Fisher, Ford Motor Company, Dearborn, Michigan 48121
Raymond J. Bratton, Westinghouse Electric Corporation, Pittsburgh, Pennsylvania 15235

Technical Report ANMRC CTR 74-59, September, 1974
180 pgs., 135 illus., 17 tables, Contract DAAG 46-71-C-0162, ARPA Order Number 1849, Sixth Interim Report, January 1, 1974 to June 30, 1974

ABSTRACT

The "Brittle Materials Design, High Temperature Gas Turbine" program is to demonstrate successful use of brittle materials in demanding high temperature structural applications. A small vehicular gas turbine and a large stationary gas turbine, each utilizing uncooled ceramic components, will be used in this iterative design and materials development program. Both the contractor, Ford Motor Company, and the subcontractor, Westinghouse Electric Corporation, have had in-house research programs in this area prior to this contract.

In the vehicular turbine project, three dimensional stress analysis programs are being developed and applied to turbine rotors and stator vanes. Improvements have been made in the fabrication of duo density silicon nitride rotors. A major objective was reached with the completion of a 50 hour cyclic engine test of ceramic hot flow path components. A silicon carbide combustor tube was tested in a combustor rig for 50 hours, including 6 hours at an outlet temperature of 2500°F. Non-destructive evaluation techniques have been applied to the fabrication of ceramic components resulting in the elimination of defective parts at an early stage in processing.

In the stationary turbine project, considerable design effort was expended on the modification of the rotating test turbine for the high temperature testing to meet program objectives. The static test rig was rebuilt for 2500°F peak temperature operation, and five cycles were run to 2300°F to establish control parameters. Damage to the new ceramic duct section and to the mixer vane assemblies being tested were apparently undamaged. A rotor blade configuration was analyzed by the three dimensional stress analysis program and the results are presented.

Army Materials and Mechanic Research Center,
Watertown, Massachusetts 02172

AD

BRITTLE MATERIALS DESIGN
HIGH TEMPERATURE GAS TURBINE

Key Words
Gas turbine engine
Brittle design
Ceramics
High temperature materials
Silicon nitride
Silicon carbide
Non-destructive tests
Mechanical properties

Arthur F. McLean, Eugene A. Fisher, Ford Motor Company, Dearborn, Michigan 48121
Raymond J. Bratton, Westinghouse Electric Corporation, Pittsburgh, Pennsylvania 15235

Technical Report ANMRC CTR 74-59, September, 1974
180 pgs., 135 illus., 17 tables, Contract DAAG 46-71-C-0162, ARPA Order Number 1849, Sixth Interim Report, January 1, 1974 to June 30, 1974

ABSTRACT

The "Brittle Materials Design, High Temperature Gas Turbine" program is to demonstrate successful use of brittle materials in demanding high temperature structural applications. A small vehicular gas turbine and a large stationary gas turbine, each utilizing uncooled ceramic components, will be used in this iterative design and materials development program. Both the contractor, Ford Motor Company, and the subcontractor, Westinghouse Electric Corporation, have had in-house research programs in this area prior to this contract.

In the vehicular turbine project, three dimensional stress analysis programs are being developed and applied to turbine rotors and stator vanes. Improvements have been made in the fabrication of duo density silicon nitride rotors. A major objective was reached with the completion of a 50 hour cyclic engine test of ceramic hot flow path components. A silicon carbide combustor tube was tested in a combustor rig for 50 hours, including 6 hours at an outlet temperature of 2500°F. Non-destructive evaluation techniques have been applied to the fabrication of ceramic components resulting in the elimination of defective parts at an early stage in processing.

In the stationary turbine project, considerable design effort was expended on the modification of the rotating test turbine for the high temperature testing to meet program objectives. The static test rig was rebuilt for 2500°F peak temperature operation, and five cycles were run to 2300°F to establish control parameters. Damage to the new ceramic duct section and to the mixer vane assemblies being tested were apparently undamaged. A rotor blade configuration was analyzed by the three dimensional stress analysis program and the results are presented.

Amy Materials and Mechanic Research Center,
Watertown, Massachusetts 02172

AD

BRITTLE MATERIALS DESIGN
HIGH TEMPERATURE GAS TURBINE

Key Words
Gas turbine engine
Brittle design
Ceramics
High temperature materials
Silicon nitride
Silicon carbide
Non-destructive tests
Mechanical properties

Arthur F. McLean, Eugene A. Fisher, Ford Motor Company, Dearborn, Michigan 48121
Raymond J. Bratton, Westinghouse Electric Corporation, Pittsburgh, Pennsylvania 15235

Technical Report ANMRC CTR 74-59, September, 1974
180 pps, 135 illus, 17 tables, Contract DAAG 46-71-C-0162, ARPA Order Number 1849, Sixth Interim Report, January 1, 1974 to June 30, 1974

ABSTRACT

The "Brittle Materials Design, High Temperature Gas Turbine" program is to demonstrate successful use of brittle materials in demanding high temperature structural applications. A small vehicular gas turbine and a large stationary gas turbine, each utilizing uncooled ceramic components, will be used in this iterative design and materials development program. Both the contractor, Ford Motor Company, and the subcontractor, Westinghouse Electric Corporation, have had in-house research programs in this area prior to this contract.

In the vehicular turbine project, three dimensional stress analysis programs are being developed and applied to turbine rotors and stators. Improvements have been made in the fabrication of low density silicon nitride rotors. A major objective was reached with the completion of a 50 hour cyclic engine test of ceramic hot flow path components. A silicon carbide combustor tube was tested in a combustor rig for 50 hours, including 6 hours at an outlet temperature of 2500°F. Non-destructive evaluation techniques have been applied to the fabrication of ceramic components resulting in the elimination of defective parts at an early stage in processing.

In the stationary turbine project, considerable design effort was expended on the modification of the rotating test turbine for the high temperature testing to meet program objectives. The static test rig was rebuilt for 2500°F peak temperature operation, and five cycles were run to 2300°F to establish control parameters. Damage to the new ceramic duct section and to the mixer vane assemblies being tested were apparently undamaged. A rotor blade configuration was analyzed by the three dimensional stress analysis program and the results are presented.

Amy Materials and Mechanic Research Center,
Watertown, Massachusetts 02172

AD

BRITTLE MATERIALS DESIGN
HIGH TEMPERATURE GAS TURBINE

Key Words
Gas turbine engine
Brittle design
Ceramics
High temperature materials
Silicon nitride
Silicon carbide
Non-destructive tests
Mechanical properties

Arthur F. McLean, Eugene A. Fisher, Ford Motor Company, Dearborn, Michigan 48121
Raymond J. Bratton, Westinghouse Electric Corporation, Pittsburgh, Pennsylvania 15235

Technical Report ANMRC CTR 74-59, September, 1974
180 pps, 135 illus, 17 tables, Contract DAAG 46-71-C-0162, ARPA Order Number 1849, Sixth Interim Report, January 1, 1974 to June 30, 1974

ABSTRACT

The "Brittle Materials Design, High Temperature Gas Turbine" program is to demonstrate successful use of brittle materials in demanding high temperature structural applications. A small vehicular gas turbine and a large stationary gas turbine, each utilizing uncooled ceramic components, will be used in this iterative design and materials development program. Both the contractor, Ford Motor Company, and the subcontractor, Westinghouse Electric Corporation, have had in-house research programs in this area prior to this contract.

In the vehicular turbine project, three dimensional stress analysis programs are being developed and applied to turbine rotors and stators. Improvements have been made in the fabrication of low density silicon nitride rotors. A major objective was reached with the completion of a 50 hour cyclic engine test of ceramic hot flow path components. A silicon carbide combustor tube was tested in a combustor rig for 50 hours, including 6 hours at an outlet temperature of 2500°F. Non-destructive evaluation techniques have been applied to the fabrication of ceramic components resulting in the elimination of defective parts at an early stage in processing.

In the stationary turbine project, considerable design effort was expended on the modification of the rotating test turbine for the high temperature testing to meet program objectives. The static test rig was rebuilt for 2500°F peak temperature operation, and five cycles were run to 2300°F to establish control parameters. Damage to the new ceramic duct section and to the mixer vane assemblies being tested were apparently undamaged. A rotor blade configuration was analyzed by the three dimensional stress analysis program and the results are presented.

Amy Materials and Mechanic Research Center,
Watertown, Massachusetts 02172

AD

BRITTLE MATERIALS DESIGN
HIGH TEMPERATURE GAS TURBINE

Key Words
Gas turbine engine
Brittle design
Ceramics
High temperature materials
Silicon nitride
Silicon carbide
Non-destructive tests
Mechanical properties

Arthur F. McLean, Eugene A. Fisher, Ford Motor Company, Dearborn, Michigan 48121
Raymond J. Bratton, Westinghouse Electric Corporation, Pittsburgh, Pennsylvania 15235

Technical Report ANMRC CTR 74-59, September, 1974
180 pps, 135 illus, 17 tables, Contract DAAG 46-71-C-0162, ARPA Order Number 1849, Sixth Interim Report, January 1, 1974 to June 30, 1974

ABSTRACT

The "Brittle Materials Design, High Temperature Gas Turbine" program is to demonstrate successful use of brittle materials in demanding high temperature structural applications. A small vehicular gas turbine and a large stationary gas turbine, each utilizing uncooled ceramic components, will be used in this iterative design and materials development program. Both the contractor, Ford Motor Company, and the subcontractor, Westinghouse Electric Corporation, have had in-house research programs in this area prior to this contract.

In the vehicular turbine project, three dimensional stress analysis programs are being developed and applied to turbine rotors and stators. Improvements have been made in the fabrication of low density silicon nitride rotors. A major objective was reached with the completion of a 50 hour cyclic engine test of ceramic hot flow path components. A silicon carbide combustor tube was tested in a combustor rig for 50 hours, including 6 hours at an outlet temperature of 2500°F. Non-destructive evaluation techniques have been applied to the fabrication of ceramic components resulting in the elimination of defective parts at an early stage in processing.

In the stationary turbine project, considerable design effort was expended on the modification of the rotating test turbine for the high temperature testing to meet program objectives. The static test rig was rebuilt for 2500°F peak temperature operation, and five cycles were run to 2300°F to establish control parameters. Damage to the new ceramic duct section and to the mixer vane assemblies being tested were apparently undamaged. A rotor blade configuration was analyzed by the three dimensional stress analysis program and the results are presented.

Amy Materials and Mechanic Research Center,
Watertown, Massachusetts 02172

AD

BRITTLE MATERIALS DESIGN
HIGH TEMPERATURE GAS TURBINE

Key Words
Gas turbine engine
Brittle design
Ceramics
High temperature materials
Silicon nitride
Silicon carbide
Non-destructive tests
Mechanical properties

Arthur F. McLean, Eugene A. Fisher, Ford Motor Company, Dearborn, Michigan 48121
Raymond J. Bratton, Westinghouse Electric Corporation, Pittsburgh, Pennsylvania 15235

Technical Report ANMRC CTR 74-59, September, 1974
180 pps, 135 illus, 17 tables, Contract DAAG 46-71-C-0162, ARPA Order Number 1849, Sixth Interim Report, January 1, 1974 to June 30, 1974

ABSTRACT

The "Brittle Materials Design, High Temperature Gas Turbine" program is to demonstrate successful use of brittle materials in demanding high temperature structural applications. A small vehicular gas turbine and a large stationary gas turbine, each utilizing uncooled ceramic components, will be used in this iterative design and materials development program. Both the contractor, Ford Motor Company, and the subcontractor, Westinghouse Electric Corporation, have had in-house research programs in this area prior to this contract.

In the vehicular turbine project, three dimensional stress analysis programs are being developed and applied to turbine rotors and stators. Improvements have been made in the fabrication of low density silicon nitride rotors. A major objective was reached with the completion of a 50 hour cyclic engine test of ceramic hot flow path components. A silicon carbide combustor tube was tested in a combustor rig for 50 hours, including 6 hours at an outlet temperature of 2500°F. Non-destructive evaluation techniques have been applied to the fabrication of ceramic components resulting in the elimination of defective parts at an early stage in processing.

In the stationary turbine project, considerable design effort was expended on the modification of the rotating test turbine for the high temperature testing to meet program objectives. The static test rig was rebuilt for 2500°F peak temperature operation, and five cycles were run to 2300°F to establish control parameters. Damage to the new ceramic duct section and to the mixer vane assemblies being tested were apparently undamaged. A rotor blade configuration was analyzed by the three dimensional stress analysis program and the results are presented.

UNCLASSIFIED

SECURITY CLASSIFICATION OF THIS PAGE (When Data Entered)

REPORT DOCUMENTATION PAGE		READ INSTRUCTIONS BEFORE COMPLETING FORM
1. REPORT NUMBER AMMRC CTR 74-59	2. GOVT ACCESSION NO.	3. RECIPIENT'S CATALOG NUMBER
4. TITLE (and Subtitle) Brittle Materials Design, High Temperature Gas Turbine		5. TYPE OF REPORT & PERIOD COVERED Interim Report Number 6 1/1/74 to 6/30/74
		6. PERFORMING ORG. REPORT NUMBER
7. AUTHOR(s) A. F. McLean, Ford Motor Company E. A. Fisher, Ford Motor Company R. J. Bratton, Westinghouse Electric Corp.		8. CONTRACT OR GRANT NUMBER(s) DAAG 46-71-C-0162
9. PERFORMING ORGANIZATION NAME AND ADDRESS Ford Motor Company, Dearborn, Mi 48121		10. PROGRAM ELEMENT, PROJECT, TASK AREA & WORK UNIT NUMBERS D/A Project: ARPA Order Number 1849 Agency Accession: DA OD 4733
11. CONTROLLING OFFICE NAME AND ADDRESS Army Materials and Mechanics Research Center Watertown, Massachusetts 02172		12. REPORT DATE September, 1974
		13. NUMBER OF PAGES 180
14. MONITORING AGENCY NAME & ADDRESS (if different from Controlling Office)		15. SECURITY CLASS. (of this report) Unclassified
		15a. DECLASSIFICATION/DOWNGRADING SCHEDULE
16. DISTRIBUTION STATEMENT (of this Report) Distribution limited to U.S. Government agencies only: Test and Evaluation data; Sept., 1974. Other requests for this document must be referred to the Director, Army, Materials and Mechanics Research Center, ATTN:AMXMR-PL, Watertown, Massachusetts 02172		
17. DISTRIBUTION STATEMENT (of the abstract entered in Block 20, if different from Report)		
18. SUPPLEMENTARY NOTES		
19. KEY WORDS (Continue on reverse side if necessary and identify by block number) Gas Turbine Engine Silicon Nitride Brittle Design Silicon Carbide Ceramics Non-Destructive Tests High Temperature Materials Mechanical Properties		
20. ABSTRACT (Continue on reverse side if necessary and identify by block number) (See reverse side)		

UNCLASSIFIED

SECURITY CLASSIFICATION OF THIS PAGE(When Data Entered)

ABSTRACT

The "Brittle Materials Design, High Temperature Gas Turbine" program is to demonstrate successful use of brittle materials in demanding high temperature structural applications. A small vehicular gas turbine and a large stationary gas turbine, each utilizing uncooled ceramic components, will be used in this iterative design and materials development program. Both the contractor, Ford Motor Company, and the subcontractor, Westinghouse Electric Corporation, have had in-house research programs in this area prior to this contract.

In the vehicular turbine project, three dimensional stress analysis programs are being developed and applied to turbine rotors and stators. Improvements have been made in the fabrication of duo density silicon nitride rotors. A major objective was reached with the completion of a 50 hour cyclic engine test of ceramic hot flow path components. A silicon carbide combustor tube was tested in a combustor rig for 50 hours, including 6 hours at an outlet temperature of 2500°F. Non-destructive evaluation techniques have been applied to the fabrication of ceramic components resulting in the elimination of defective parts at an early stage in processing.

In the stationary turbine project, considerable design effort was expended on the modification of the rotating test turbine for the high temperature testing to meet program objectives. The static test rig was rebuilt for 2500°F peak temperature operation, and five cycles were run to 2300°F to establish control parameters. Damage to the new ceramic duct section and to the mixer caused testing to be stopped. The silicon nitride and silicon carbide stator vane assemblies being tested were apparently undamaged. A rotor blade configuration was analyzed by the three dimensional stress analysis program and the results are presented.

UNCLASSIFIED

SECURITY CLASSIFICATION OF THIS PAGE(When Data Entered)